INVESTIGATIONS OF 3D PRINTED ORTHOPAEDIC CORTICAL BONE SCREWS TO IMPROVE BIOMECHANICAL PULLOUT STRENGTH

Submitted in partial fulfilment of the requirement for the award of the degree

of

Doctor of Philosophy

Submitted by

Raj Agarwal

Roll No.: 901908013

Under the Supervision of

Dr. Vishal Gupta
(Assistant Prof., MED)

Dr. Jaskaran Singh
(Assistant Prof., MED)



THAPAR INSTITUTE OF ENGINEERING & TECHNOLOGY, PATIALA

FEBRUARY 2023

DEDICATED TO

MY PARENTS

(Mrs. Madhu Agrawal and Mr. Yashpal Agrawal)

For their love, support, and encouragement

Certificate

This is to certify that the thesis entitled **'Investigations of 3D printed orthopaedic cortical bone screws to improve biomechanical pullout strength'** submitted by **Mr. Raj Agarwal** to the **Thapar Institute of Engineering and Technology Patiala** for the award of the degree of ***Doctor of Philosophy***, is a record of the original bonafide research work carried out by him under our guidance and supervision of **Dr. Vishal Gupta** (Assistant Professor) and **Dr. Jaskaran Singh** (Assistant Professor). The results contained in it have not been submitted in part or full to any other institute or university for the award of any degree/diploma.

09-06-2023

Dr. Vishal Gupta

Mechanical Engineering Department

TIET, Patiala, Punjab, India

Jaskaran Singh 09/06/2023

Dr. Jaskaran Singh

Mechanical Engineering Department

TIET, Patiala, Punjab, India

Acknowledgements

This thesis symbolizes an important milestone in the journey of my life. I would like to express my deep sense of gratitude and sincere thanks to my thesis supervisor ***Dr. Vishal Gupta*** and ***Dr. Jaskaran Singh***. Their excellent guidance, constant encouragement and optimistic outlook have been a source of inspiration for me throughout this work. The knowledge of the subject and wealth of experience motivated me to complete the work. I have benefited immensely from their devotion to research, and ability to see things that are not obvious.

Very special thanks to ***Dr. Hitesh Kumar Mehtani***, Assistant Professor, Department of Mechanical Engineering at Thapar Institute of Engineering and Technology, Patiala for his valuable suggestions and comments to carry out this work. Many thanks to ***Dr. Sanjai Saxena***, Professor, and ***Ms. Ramandeep Kaur***, Research Scholar, Department of Biotechnology at Thapar Institute of Engineering and Technology, Patiala for their valuable suggestions and suggestions preparation of biological solutions, preservation of bone-screw samples.

I owe many thanks to ***Dr. Asit Ranjan Mridha***, Professor, Department of Pathology, All India Institute of Medical Sciences (AIIMS) New Delhi for the histopathological analysis and the preservation of specimens. Gratitude is also given to ***Dr. Aman Bansal***, Department of Radiology, Amar Hospital Punjab for providing the DEXA scans facility to monitor the bone mineral density of porcine bones and for his valuable suggestions to carry out this work.

Gratitude is also given to ***C.A. Milli Pamnani*** and ***Mr. Rajat Kumar*** for their enthusiastic assistance, unlimited support, and motivation during the preparation of this dissertation.

I am also thankful to my doctoral committee ***Dr. Tarun Kumar Bera*** (HOD), ***Dr. Dheeraj Gupta*** (Professor), ***Dr. Vivek Jain*** (Associate Professor), ***Dr. Vishal Srivastava*** (Associate Professor) at TIET, Patiala and ***Dr. Sanjeev Soni*** (Sr. Principal Scientist) at CSIO, Chandigarh for their constructive suggestions and valuable guidance during the present research.

Many thanks are given to my friends and research scholars at TIET, Patiala, ***Dr. Kunal Arora***, ***Ms. Shrutika Sharma***, ***Mr. Faheem Faroze***, ***Mr. Khalid***, and co-research scholars/friends at TIET Patiala who were always there to lend a helping hand when it mattered most and for the camaraderie that took away all the pressures and made research work more enjoyable. I am thankful to staff members of the Department of Mechanical Engineering, TIET, Patiala for providing me with essential aids to complete experiments.

I am indebted to my mother, ***Mrs. Madhu Agrawal***, and father, ***Mr. Yashpal Agrawal*** for their blessings, and motivation, providing me moral support, and taking care of many social responsibilities and constant support throughout this period. I appreciate the love and support of my family members who helped me focus on my work.

Above all, I owe it all to my ***Almighty Khatu ShyamJi*** for granting me the wisdom, health, and strength to undertake this research task and enabling me to its completion.



(Raj Agarwal)

Abstract

Bone fractures are a common hazard due to external forces acting on the bone, causing misalignment, or breakage of bones. Bone drilling is imperatively required for fractured bone fixation used during orthopaedics surgeries, joint replacement, plate implantation, and total knee arthroplasty. The fractured bone is repaired with bone screws and implants to secure and retain the accurate position of fracture parts for early mobilization and early union. Bone screws are used in almost every orthopaedic surgery, as they provide inter-fragmentary compression to support the fractured bone.

The success of osteosynthesis is affected by bone-screw interface holding power, type of screw used, screw purchase strength, the number of screws used and bone mass available for fixation, the orientation of screws and bone mineral density. The poor pullout strength and holding power at the bone-screw interface may lead to intolerable pain, screw loosening and implant failure at the fracture site can cause reoperation and revision surgery. These orthopaedic bone screws are made up of metallic biomaterials such as titanium, and stainless steel that are strong, ductile, fatigue-resistant, and highly biocompatible. However, due to the high stiffness and high strength of metallic screws, they may cause stress corrosion, the stress-shielding effect, tear and wear in the surrounding tissues. Further, strong integration at the bone-screw interface by sharp threads and soft bony tissues complicates the post-operative revision surgery while removing the metallic screws. This problem can be solved with biodegradable bone screws.

Three-dimensional (3D) printing technology provides the ideal tailor-made solution for different orthopaedic applications. Various researchers used this technology for the fabrication of patient-specific prosthetics and customized implants. Limited research is reported for the fabrication of orthopaedic bone screws using 3D printing technology. To overcome the aforesaid problems associated with surgical metallic bone screws, a novel 3D-printed bone screw is introduced. In the present work, fused filament fabrication-based 3D printing technology is used to fabricate orthopaedic cortical bone screws. The influence of different process parameters on the mechanical strength of 3D-printed cortical screws was monitored. The fracture and fatigue crack propagation at the bone screw interfaces were observed at the microscopic level. The process parameters of 3D printing technology are optimized with different machine learning (ML) models. A total of 100 data points were used for the training and testing of different predictive ML models. Ensemble ML models were also leveraged to improve the robustness and accuracy of base learning ML models.

The bone drilling experiments were performed using rotary ultrasonic-assisted bone drilling (RUABD) and conventional bone drilling (CBD) to monitor the biomechanical pullout strength at the bone-screw interface. The influence of various drilling angles or inclination angles was observed on the pullout strength of bone screws. The micrographs at the bone-tool interface and drilled hole morphology were also observed to estimate the initial screw stability and holding strength at the bone-screw interface.

The in-vitro degradation behaviour of 3D-printed cortical screws was observed in different biological solutions. Three different biological solutions were used that have similar ion concentrations to human blood plasma. The influence of different process parameters of 3D printing technology was observed on the degradation rate. The compressive strength of 3D-printed screws was tested before and after 24 weeks of preservation to understand the effect of degradation rate on the compressive strength of 3D-printed screws.

So, it can be concluded that 3D-printed bone screws can be used for fracture fixation of small bones or anterior cruciate ligament fixation. Also, it can reduce the stress-shielding effect and eliminate the problem of post-operative revision surgery.

Keywords: 3D printing, Biomechanical pullout strength, Bone screw, Bone mineral density, CBD, Cortical screw, Ensemble models, Inclination angle, Histopathology, Machine learning, Microcracks, Osteosynthesis, RUABD.

Contents

Particulars	Page No.
Certificate	I
Acknowledgements	III
Abstract	V
Contents	VII
List of Figures	XIII
List of Tables	XXI
Abbreviations	XXIV
Chapter 1: Introduction	**1-12**
1.1 Background	1
1.2 Bone fracture and its treatment methods	2
1.3 Bone drilling and its drawbacks	4
1.4 Bone screws and their types	5
1.5 Aim and objective of the present work	9
1.5.1 Aim and motivation of the study	9
1.5.2 Research goal	10
1.5 Outline of the Thesis	11
Chapter 2: Literature review	**13-35**
2.1 Introduction	13
2.2 History of bone screws	13
2.3 Review of 3D printing techniques and biomaterials used for bone screw fabrication.	14
2.3.1 Metallic biomaterials	16
2.3.1.1 Electron beam melting (EBM) technique	18
2.3.1.2 Direct metal laser sintering (DMLS) technique	20
2.3.1.3 Selective laser melting (SLM) technique	20
2.3.1.4 Comparing different metal 3D-printing techniques.	23
2.3.2 Polymeric biomaterials	25
2.3.2.1 Stereolithography (SLA) technique	28
2.3.2.2 Selective laser sintering (SLS) technique	28

2.3.2.3 Polyjet 3D printing technique 29
2.3.2.4 Fused deposition modelling (FDM) technique 30
2.3.2.5 Comparing different polymeric 3D-printing techniques 31
2.4 Summary 33
2.5 Research gaps 34
2.6 Problem Formulation 35
2.7 Research objectives 35
Chapter 3: Fabrication of orthopaedic cortical screws using 3D printing 36-50
3.1 Introduction 36
3.2 Details of design and fabrication of cortical screws 37
3.2.1 Design of cortical screws 37
3.2.2 PLA polymer details 37
3.2.3 Experimental design and process parameters 39
3.2.4 Mechanical characterization 40
3.2.5 Microscopic fracture observation 41
3.3 Results and discussion 41
3.3.1 Compression testing 41
3.3.2 Tensile testing 44
3.3.3 Morphology of different patterned screws 45
3.3.4 Fractography of cortical screws 48
3.4 Conclusions 49
Chapter 4: Machine learning based approaches for predicting compressive strength and optimization of process parameters 51-76
4.1 Introduction 51
4.2 Experimentation details 52
4.2.1 Fabrication procedure 52
4.2.2 Process parameters 53
4.3 Background of Machine Learning Models Employed 57
4.3.1 Decision trees (DT) 57
4.3.2 Random Forest (RF) 58
4.3.3 Support vector regression (SVR) 58
4.3.4 k-nearest neighbour (kNN) 59

4.4 Grid search algorithm with K-fold cross-validation 60
4.5 Data Visualization and Interpretation 61
4.6 Application of ML models 65
4.7 Ensemble ML models 70
4.7.1 GradientBoost 71
4.7.2 AdaBoost 72
4.7.3 XGBoost 73
4.8 Adequacy of ensemble ML models 73
4.9 Conclusions 76
Chapter 5: Effect of drilling techniques on the biomechanical pullout strength **77-97**
5.1 Introduction 77
5.2 Experimental procedure 78
5.2.1 Workpiece information 78
5.2.2 Drilling parameters selection 79
5.2.3 Experimental investigation 81
5.2.4 Pullout strength testing 82
5.3 Result and Discussion 83
5.3.1 Measurement of induced cutting force 83
5.3.2 In-situ temperature monitoring 86
5.3.3 Biomechanical pullout strength of cortical screws 89
5.3.4 Morphology of drilled holes 91
5.3.5 Micrographs at bone-tool interface 94
5.4 Conclusion 97
Chapter 6: Degradation behaviour and Histopathological evaluation **98-130**
6.1 Introduction 98
6.2 Run order and characterization of 3D-printed screws 99
6.2.1 Process parameters and run order for 3D-printing of screws 99
6.2.2 Biological assessment 103
6.2.3 Mechanical characterization 105
6.3 Sample preparation of histopathological examination 106
6.4 Histopathological examination 108
6.4.1 Decalcification of bone 108

6.4.2 Tissue processing 109
6.4.2.1 Dehydration and cleaning 110
6.4.2.2 Infiltration and impregnation 110
6.4.3 Tissue embedding 111
6.4.4 Tissue sectioning 112
6.4.5 Slide staining and cover-slipping 113
6.5 Results and discussion 114
6.5.1 In-vitro degradation behaviour 114
6.5.1.1 Influence of infill pattern on different solutions at different weeks 115
6.5.1.2 Influence of infill percentage on different solutions at different weeks 117
6.5.1.3 Influence of layer height on different solutions at different weeks 119
6.5.1.4 Influence of wall thickness on different solutions at different weeks 121
6.5.2 Surface morphology 122
6.5.3 Compressive strength of cortical screws 123
6.5.4 Histopathological evaluations 125
6.6 Conclusions 130
Chapter 7: Effect of bone mineral density on the biomechanical pullout strength **131-148**
7.1 Introduction 131
7.2 3D printing of Ti6Al4V screws and their characterization 131
7.2.1 Porcine femur bone detailing 131
7.2.2 Bone mineral density measurement 132
7.2.3 3D printing of Ti6AL4V cortical screws 135
7.2.4 Drilling of porcine femur bones 135
7.2.5 Biomechanical pullout strength setup 137
7.3 Results and Discussions 137
7.3.1 Micromorphology of different cortical screws 137
7.3.2 Analysis of hydroxyapatite formation 139
7.3.3 Elemental analysis of hydroxyapatite coating 140

7.3.4 Biomechanical pullout strength of cortical screws 142
7.3.4.1 Effect of BMD on pullout strength of cortical screws 142
7.3.4.2 Effect of gender on pullout strength of cortical screws 143
7.3.4.3 Effect of biomaterials on pullout strength of cortical screws 143
7.3.4.4 Effect of immersion period on pullout strength of cortical screws 145
7.3.5 Fractured bone morphologies after screw extractions 145
7.4 Conclusions 147
Chapter 8: Summary, conclusions, and the future scope **149-151**
8.1 Summary 149
8.2 Conclusions 149
8.3 Future scope 151
Reference 152
List of publications from the present work 174

List of Figures

Figure No.	Caption	Page No.
Figure 1.1	Structure of bone (reprinted with permission from Elsevier [4]).	1
Figure 1.2	Method to treat a fractured bone (a) indirect method, (b) direct method.	3
Figure 1.3	Drilling on the bone for surgery (reprinted with permission from Elsevier [11]).	4
Figure 1.4	Various types of orthopaedic bone screws used for different applications within the human body.	6
Figure 1.5	Various types of bone screws: (a) Cortical screw, (b) Cancellous screw, (c) Hip screw [13], (d-e) Bio-absorbable screw [14], (f) Acutrak screw [15], (g) Cannulated screw [16], (h) Pedicle screw [17], (i) Herbert screw [15] [all the images are reprinted with permission from Elsevier [13–17]].	7
Figure 1.6	Bone-screw-related complications observed in the literature.	9
Figure 2.1	Evolution of research in orthopaedic bone screws.	14
Figure 2.2	Comparison of after push out of (a) EBM fabricated Ti6Al4V ELI screw with (b) conventional screw, SEM images of bone-screw (a1-a4) EBM ELI screw with (b1-b4) conventional screw, histological images of (a5,a6,a7) EBM screw with (b5,b6,b7) conventional screw [Reprinted with permission from Elsevier [41]].	19
Figure 2.3	(a) Pedicle screws with different re-entrant angles and auxetic units, (b) SEM images of screw bodies with auxetic units, (c) FEM and boundary conditions, (d) schematic of the test specimen, (e) maximum pullout force interactions with different designs of auxetic structures [Reprinted with permission from Elsevier [45]].	21
Figure 2.4	Micro-CT images of the (a) controlled screw, (b) 3D-printed bone screw; histological analysis of (c) control screw, (d) 3D-printed screw, 6-month specimens for bone formation evaluation of (e) control screw, (f) 3D-printed screw; B: bone, S: screw [no permission is required according to the journal policy [36]].	22

Figure 2.5	Comparison of control screw and 3D-printed screw in rabbit animal for (a) total bone-volume fraction, (b) bone surface density, (c) on-growth bone volume fraction, (d) in-growth bone volume fraction [no permission is required according to the journal policy [36]].	23
Figure 2.6	3D-printed biodegradable implants (screws, pins, plates) using PLA biomaterial [no permission is required according to the journal policy [40]].	27
Figure 2.7	(a) CAD design of cortical screw, (b) STL file, (c) 3D printed screw, (d & e) pitch length measurement, (f & g) uniform layers of the screw, fill density of (h) 25%, (i) 45%, (j) 65%, (k) pore distribution, (l) biodegrading profiles of porous and solid screws, (m) alizarin red-stained screw, histopathological of tissue surrounding of (n) porous screw, (o) solid screw [no permission is required according to the journal policy [31]].	31
Figure 3.1	(a) CAD model of the cortical screw; (b) X-ray view in Ultimaker Cura; (c) Slicing format; (d) Single extrusion Ultimaker 2+ Connect printer; (e) Printer head with fabricated screw; (f) Ultimaker PLA silver metallic filament with cam switch and updated-geared feeder.	38
Figure 3.2	(a) Universal testing machine to monitor the (b) compression testing, and (c) tensile testing of 3D-printed cortical screws.	40
Figure 3.3	Influence of (a) infill percentage, (b) wall thickness, and (c) layer height on the compressive strength of 3D-printed cortical screws.	42
Figure 3.4	(a) Compressive strength of the different patterned 3D-printed screws, (b) compression testing of triangular and honeycomb structured cortical screws.	43
Figure 3.5	(a) Tensile strength of the different patterned 3D-printed screws, (b) tensile testing of triangular and honeycomb structured cortical screws.	45
Figure 3.6	(a) Thread profile of 3D printed cortical screw, (b) layer by layer deposited PLA materials layers from screw head to threads.	46

Figure 3.7	SEM micrographs and microstructure with the different magnification of different infill patterns of the cortical screws (a) triangular, (b) grid, (c) concentric, and (d) honeycomb.	47
Figure 3.8	SEM Micrographs of the fracture surface of cortical screws (a) triangle-patterns (b) honeycomb-pattern.	48
Figure 4.1	Procedure for fabrication and mechanical testing of screws.	53
Figure 4.2	(a) DT, (b) RF, (c) SVR, (d) kNN.	59
Figure 4.3	(a) grid search representation, (b) 5-fold cross-validation.	61
Figure 4.4	The box-whisker plot of input process parameters on compressive strength.	62
Figure 4.5	Fractured images of different patterned 3D-printed cortical screws.	63
Figure 4.6	Pair-plot of independent parameters and compressive strength.	64
Figure 4.7	Predicted and true values of training data for compressive strength.	66
Figure 4.8	Predicted and true values of testing data of 20 data points for compressive strength.	67
Figure 4.9	Residual plot of different ML models.	68
Figure 4.10	Error metrics of ML models for (a) training data, and (b) testing data.	69
Figure 4.11	The methodology followed for mechanical strength prediction.	71
Figure 4.12	(a) GradientBoost model, (b) AdaBoost model.	72
Figure 4.13	Taylor diagram for evaluating the performance of different models for (a-b) training data and (c-d) testing data.	74
Figure 4.14	Predictive performance of different ML algorithms for (a) AdaBoost, (b) GradientBoost, (c) XGBoost, (d) decision tree, (e) random forest.	75
Figure 5.1	(a) drilling setup, (b) perpendicular drilling, (c) inclined drilling for porcine femur bones.	81
Figure 5.2	Biomechanical pullout strength testing setup.	82
Figure 5.3	The influence of process parameters on induced cutting force (a) inclination angle vs force, (b) feedrate vs force, (c) rotational speed vs force.	85

Figure 5.4	Infrared thermograms during RUABD at different run order of (a) ID 20, (b) ID 19, (c) ID 10, (d) ID 15, (e) ID 1, (f) ID 5.	86
Figure 5.5	Infrared thermograms during CBD at different run order of (a) ID 15, (b) ID 14, (c) ID 5, (d) ID 10, (e) ID 3, (f) ID 1.	87
Figure 5.6	Schematic for perpendicular and inclined bone-screw samples.	89
Figure 5.7	Effect of (a) inclination angle, (b) feedrate, and (c) rotational speed on the biomechanical pullout strength.	90
Figure 5.8	SEM micrographs of inclined drilled holes during (a) RUABD, (b) CBD.	92
Figure 5.9	SEM micrographs of drilled holes during CBD of the porcine femur bone.	93
Figure 5.10	SEM micrographs of drilled holes during RUABD of the porcine femur bone.	94
Figure 5.11	(a) Burnt bone chips agglomerated in the conventional surgical twisted drill bit, (b) micrographs of bone-tool morphology, (c) adhered bone chips in flutes of the surgical tool, (d) EDS of the surgical tool after drilling.	95
Figure 5.12	(a) Bone debris clustered within the diamond-impregnated drill tool, (b) micrographs of bone-tool morphology, (c) agglomerated bone debris, and (d) EDS of the diamond tool after drilling.	96
Figure 6.1	3D-printed cortical screws based on run order by varying different process parameters (S1 to S16); (a) for SBF solution, (b) for PBS solution, (c) for HBSS solution.	102
Figure 6.2	(a) SBF immersed 16 cortical screws, (b) PBS preserved 16 cortical screws, and (c) HBSS immersed 16 cortical screws, (d) (e) Eppendorf micro-centrifuge tubes immersed cortical screws in various biological solutions.	105
Figure 6.3	Compressive strength testing setup for 3D-printed cortical screws fixed in screw holding fixture.	106
Figure 6.4	Surgical metallic (Ti and SS) and 3D-printed PLA bone-screw samples.	107
Figure 6.5	Methodology for the histopathology procedure.	108
Figure 6.6	Porous cassettes with the specimen.	109

Figure 6.7	(a) Automatic tissue processing unit for dehydration, (b) clearing processing unit.	110
Figure 6.8	Tissue embedding unit.	111
Figure 6.9	Tissue embedding procedure.	111
Figure 6.10	Actual images of tissue embedded in the wax mould.	112
Figure 6.11	Rotary microtome used for sectioning.	112
Figure 6.12	Automatic staining unit.	113
Figure 6.13	Images of final slides for the microscope examination.	113
Figure 6.14	Micrographs and EDS elemental analysis of 3Dprinted PLA cortical screws: (a) (b) un-treated surface, (c) (d) SBF immersed cortical screw surface, (e) (f) PBS immersed surface of screw, (g) (h) HBSS immersed screw surface shows the presence of Ca, Na, Cl, P.	115
Figure 6.15	Degradation behaviour of different infill patterns in different solutions at (a) 6 weeks, (b) 12 weeks, (c) 18 weeks, (d) 24 weeks.	116
Figure 6.16	Comparison of the degradation rate of variation in infill patterns of cortical screws at different weeks on different solutions.	117
Figure 6.17	Degradation behaviour of different infill percentages in different solutions at (a) 6 weeks, (b) 12 weeks, (c) 18 weeks, (d) 24 weeks.	118
Figure 6.18	Comparison of the degradation rate of variation in infill percentage of cortical screws at different weeks on different solutions.	119
Figure 6.19	Degradation behaviour of different layer heights in different solutions at (a) 6 weeks, (b) 12 weeks, (c) 18 weeks, (d) 24 weeks.	120
Figure 6.20	Comparison of the degradation rate of variation in layer height of cortical screws at different weeks on different solutions.	120
Figure 6.21	Degradation behaviour of different wall thicknesses in different solutions at (a) 6 weeks, (b) 12 weeks, (c) 18 weeks, (d) 24 weeks.	121
Figure 6.22	Comparison of the degradation rate of variation in wall thickness of cortical screws at different weeks on different solutions.	122
Figure 6.23	Elemental mapping of different elements present in cortical screw preserved in SBF solution.	123

Figure 6.24	Compressive strength of cortical screws based on (a) variation in infill pattern, (b) variation in infill percentage, (c) variation in layer height, and (d) variation in wall thickness.	124
Figure 6.25	The scanner view of the bone surface after extraction of titanium cortical screws (a) at 500 µm [haematoxylin and eosin (H&E)] and (b) at 200 µm (H&E).	126
Figure 6.26	The scanner view of bone surface after extraction of stainless-steel cortical screws (a) at 500 µm [haematoxylin and eosin (H&E)] and (b) at 200 µm (H&E).	127
Figure 6.27	The scanner view of bone surface after extraction of 3D-printed cortical screws (a) at 500 µm [haematoxylin and eosin (H&E)] and (b) at 200 µm (H&E).	127
Figure 6.28	Bone surface after extraction of titanium cortical screw [H & E].	128
Figure 6.29	Bone surface after extraction of stainless-steel cortical screw [H & E].	129
Figure 6.30	Bone surface after extraction of 3D-printed PLA cortical screw [H & E].	129
Figure 7.1	Porcine male bones with X-ray micrographs and DEXA scan micrographs with measured bone density for (a) (a1) (a2) (a3) 6-months old, (b) (b1) (b2) (b3) 24-months-old, (c) (c1) (c2) (c3) 48-months-old femur bones.	133
Figure 7.2	Porcine female bones with X-ray micrographs and DEXA scan micrographs with measured bone density for (a) (a1) (a2) (a3) 6-months old, (b) (b1) (b2) (b3) 24-months-old, (c) (c1) (c2) (c3) 48-months-old femur bones.	134
Figure 7.3	(a) Titanium powder for 3D printing of cortical screw, (b) experimental bone drilling setup, (c) 3D-printed titanium, titanium, and stainless-steel cortical screws, (d) different cortical screws insertion in female and male femur bones with different densities, (e) immersion of male/female bone-screws specimens in SBF solution, (f) preservation of samples in an incubator for 60 days, (g) different screws immersed in SBF solution for biological assessment.	136

Figure 7.4	Micrographs of untreated cortical screws (a) 3D-printed titanium cortical screw, (b) surgical titanium cortical screw, (c) surgical stainless-steel cortical screw; SBF immersed cortical screws (d) 3D-printed titanium cortical screw, (e) surgical titanium cortical screw, (f) surgical stainless-steel cortical screw.	138
Figure 7.5	Micrographs of HA accumulation in (a) 3D-printed titanium cortical screw, (b) surgical titanium cortical screw, (c) surgical stainless-steel cortical screw; elements present in accumulated HA in (d) 3D-printed titanium cortical screw, (e) surgical titanium cortical screw, (f) surgical stainless-steel cortical screw.	140
Figure 7.6	Elemental area mapping of the tip of cortical screws for (a) untreated, (b) SBF immersed for 3D-printed titanium screws; (c) untreated, (d) SBF immersed for surgical titanium screws; (e) untreated, and (f) SBF immersed for surgical stainless-steel screws.	141
Figure 7.7	Untreated bone-screws pullout strength at 1st day for (a) surgical SS screws, (b) surgical Ti-screws, (c) 3D-printed titanium screws; SBF immersed bone-screws pullout strength at 60th day for (d) surgical SS screws, (e) surgical Ti-screws screws, and (f) 3D-printed titanium screws.	144
Figure 7.8	Fractured bone morphologies after push-out of cortical screws from bone periphery for 6 months, 24 months and 48 months old for (a) (d) (g) surgical SS screws, (b) (e) (h) surgical Ti-screws, (c) (f) (i) 3D-printed titanium cortical screws.	146

List of Tables

Table No.	Caption	Page No.
Table 2.1	Recent development for bone screw fabrication via 3D printing techniques.	15
Table 2.2	Specifications of metals used in orthopaedic screw fabrication [46, 47, 49, 53].	17
Table 2.3	Gold standard metallic biomaterials for orthopaedic bone implants.	17
Table 2.4	A comparison of metal-based 3D printing technology.	24
Table 2.5	Specifications of various polymers used in orthopaedic screw fabrication.	26
Table 2.6	A comparison of polymer-based 3D printing technology.	32
Table 3.1	Specifications and parameters of the cortical screw.	37
Table 3.2	Process parameters with various levels for experimental design.	39
Table 4.1	Input parameters range used for 3D printing.	54
Table 4.2	Input process parameters and their corresponding compressive strength for fabrication of 100 cortical screws by 3D printing.	54
Table 4.3	Error metrics of different ML models for comparing means and standard deviation of the training data set.	70
Table 4.4	Error metrics of different ML models for comparing means and standard deviation of the testing data set.	70
Table 5.1	Process parameters used for experimental investigation.	79
Table 5.2	Specifications of drilling tools used during RUABD and CBD.	80
Table 5.3	Run order followed to perform RUABD and CBD experiments.	80
Table 5.4	Cutting force during RUABD and CBD techniques.	84
Table 5.5	Temperature elevations during RUABD and CBD techniques.	88
Table 5.6	Biomechanical pullout strength during RUABD and CBD techniques.	91
Table 6.1	Run order and experimental trial for fabrication of cortical screws.	99
Table 6.2	Comparison of ion concentrations of solutions concerning human blood plasma.	103
Table 6.3	Chemical reagents contribution for preparing 1000 ml of SBF, PBS, and HBSS solution.	104

Table 6.4 Input process parameters used for 3D printing for screw fabrication. 107

Table 6.5 Drilling parameters used during bone drilling for the histopathological examination. 107

Abbreviations

3D	Three dimensional
AI	Artificial intelligence
ANOVA	Analysis of variance
ASIF	Association for the Study of Internal Fixation
BMD	Bone mineral density
CAD	Computer-aided design
CT	Computed tomography
CD	Conventional drilling
CNC	Computer numerical control
DMLS	Direct metal laser sintering
EBM	Electron beam melting
FEM	Finite element method
FDA	Food and Drug Administration
FDM	Fused Deposition Modelling
ML	Machine learning
PCL	Polycaprolactone
PEEK	Polyether-ether-ketone
PEG	Polyethylene glycol
PGA	Poly-glycolic acid
PHB	Poly hydroxyl-butyrate
PLA	Poly-lactic acid
PLGA	Poly lactic-glycolic acid
PMMA	Poly-methyl-methacrylate
PPF	Polypropylene fumarate
RUABD	Rotary ultrasonic-assisted bone drilling
SEM	Scanning electron microscopy
SLM	Selective Laser Melting
STL	Standard Tessellation Language
UV	Ultraviolet

Chapter I

Introduction

Chapter 1

Introduction

1.1 Background

Bones are an essential part of all vertebrate species as they provide stability, strength, the ability to move, and scaffolding for muscles. Bone is the infrastructure of the human body, it provides a rigid framework that offers protection and support, as well as attachment sites for muscles that are essential for locomotion and movement [1]. Bones are living, metabolically active and growing soft fibrous material that has dense connective tissues [2]. The 206 distinct bones in the human body come in four basic shapes: long bone, short bone, flat bone, and irregular bone. Bone tissue is composed of distinct types of soft tissues, hard tissues, bone marrow, protein fibres and bone cells [3]. The properties of bone are hard, brittle and have poor thermal conductivity. A typical structure of the bone is presented in Figure 1.1.

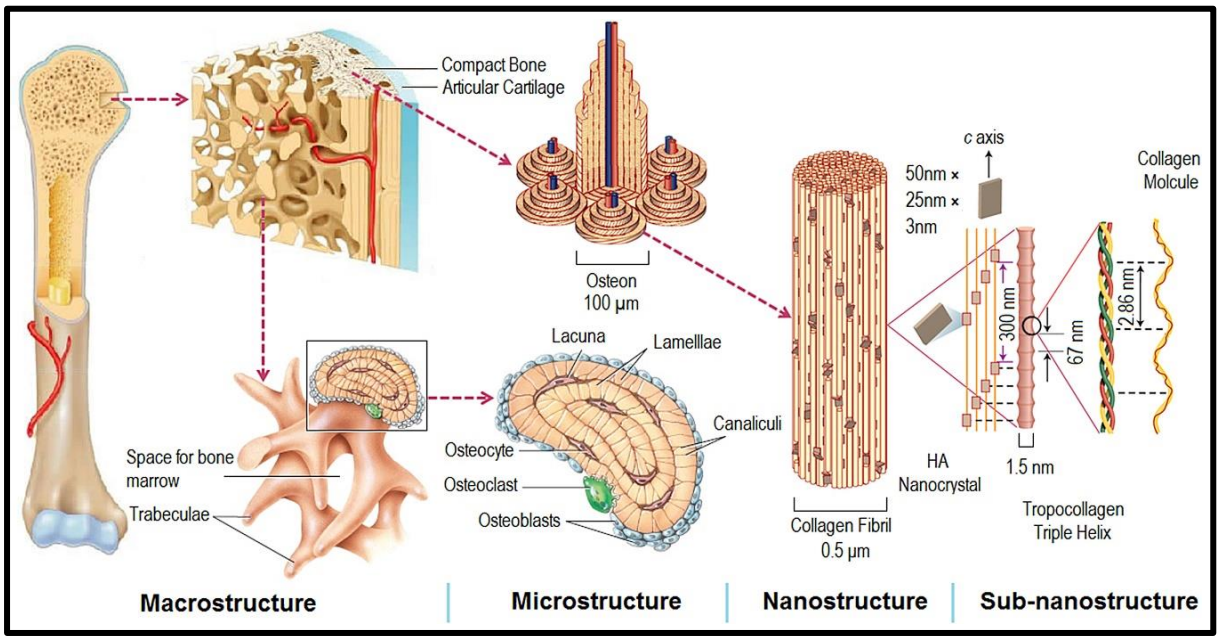


Figure 1.1: Structure of bone (*reprinted with permission from Elsevier* [4]).

Bone is a composite tissue having a hard outer layer made of crystalline calcium phosphate (hydroxyapatite) with small amounts of other mineral substances, covering a soft spongy structure made of the protein collagen [5]. There are three sections of a bone, proximal epiphysis, diaphysis, and distal epiphysis as shown in Figure 1.1. The outer layer of bone gives strength and the inner honeycomb-like structure containing a matrix gives the flexibility required by the body. The exterior outer layer is known as cortical bone and the inner spongy

surface is known as cancellous bone. With the task of structurally supporting the body, 80 percent of the weight of a human skeleton is due to cortical bones, and they are very dense compared to cancellous bones. Both cortical and cancellous bone contains living cells, which help make repairs when bones are broken or injured.

The soft tissue and hard tissue are covered by a spongy layer (cancellous) and a hard layer (cortical bone) [Figure 1.1]. The bone marrow is present inside the tubular part of the bone [Figure 1.1]. The hard tissue consists of an inter-cellular calcified material. The outer surface of the bone marrow which is lined with the inner surface of bone consists of endosteum layers. The bones are stiffer and stronger at higher strain rates, which is a way to compensate for the higher loads and stresses imposed by vigorous activity or super physiological loading. For the growth and repair of the bone, these layers (periosteum and endosteum) provide the vascular system which is used to supply nutrients and oxygen.

1.2 Bone fracture and its treatment methods

As the bone helps to strengthen the body, so the mechanical behaviour of bone is exceedingly important for estimating fracture risks. Some part of the body is constantly under compressive loads, which may increase the risk of fracture. The fracturing of bone is a common issue because of sports injuries, age factors, age, osteoporosis, industrial and transport accidents, etc. At the time of fracture, bones break, or bone alignments may be dislocated. A bone fracture occurs at the point where the physical force exerted on the bone is much stronger than the bone itself. It is a medical condition where the continuity of the bone is broken partially or completely. When a bone is broken, the periosteum (connective tissue) and endosteum (bone marrow tissue) provide bone-forming cells, which endeavour to bridge the fracture. During fracture, bone breaks or does not align with each other. Fractured bones can heal by producing new bone-forming cells and blood vessels at the fractured site.

The treatment of bone fracture usually involves restoring fractured bone to its initial position and immobilizing it until restoration and reconstruction take place. There are two main methods for the treatment of bone fractures: direct and indirect. The indirect method is a time-consuming process, during which the body part is immobilized from the outside and its movement is relatively restricted [3]. For outer fixing of bone, plaster casts, body casts and orthopaedic casts are used, as depicted in Figure 1.2 (a). There are a few disadvantages to the indirect method, such as difficulty in aligning the fractured parts, wrong bone alignment and a lengthy process of healing [3]. The indirect method is also known as the conventional method.

To overcome these limitations, a direct method has been introduced by orthopaedic surgeons where the fractured bone is treated internally and directly by surgical procedure to reposition and secure the bones. The direct method implies the fixation of the fractured part of bone by exposing the skin and fixing the fractured bone with the help of implants, wires, pins, and screws, as illustrated in Figure 1.2 (b). During the direct approach, a surgical procedure is required for the repair and reconstruction of fractured parts of bones [6]. Fast recovery is one of the main advantages of this process, and the problems associated with the conventional approach can be avoided. Bone drilling is performed to create holes at the right position on fractured sites and an implant is fixed. In this approach, immobilization is done by fixation of bone with implants and screws. Early mobilization and early union of bone fractures are the primary goals of internal fixation.

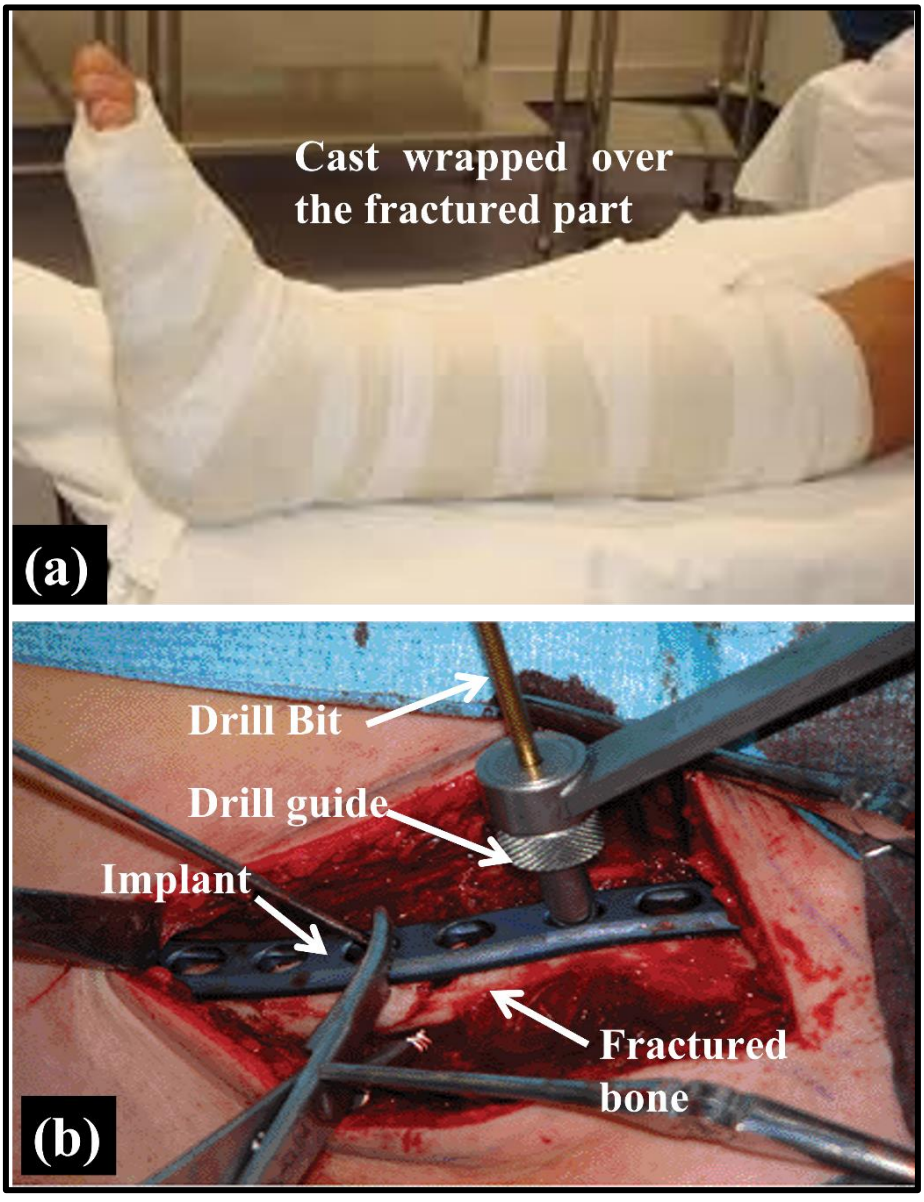


Figure 1.2: Method to treat a fractured bone (a) indirect method, (b) direct method.

Nowadays, surgeries like orthopaedics, dental, neurosurgery, and reconstructive, craniomaxillofacial surgeries require the cutting of bone. These surgeries are the most commonly performed operations in clinical practice. In the United States alone, approximately 719,000 knee surgeries and 332000 hip replacement operations were performed in 2010. In the United States alone, more than 10.2 million bone fracture surgeries are reported annually [7, 8]. In orthopaedic and trauma surgery, various bone-cutting techniques are used, namely drilling, sawing, boring, grooving, grafting, and shearing. Out of these drilling of bone is the most common surgical operation.

1.3 Bone drilling and its drawbacks

Bone drilling is a thermomechanical indispensable procedure imperatively leveraged for the treatment and alignment of fractured bone. During the drilling of bone, the surgeon applies the axial force on the rotating drill that penetrates inside the bone surface and removes the area of bone for screw insertion [9]. The bone drilling procedure is generally utilized for fixation of the fractured bone, joint replacement, plate implantation, craniotomy in neurosurgery, total knee arthroplasty and other orthopaedic applications [10]. After the drilling of bone, fractured parts of bones are immobilized by joining and aligning with screws, plates, wires, and implants to support the fractured part of the bone as illustrated in Figure 1.3.

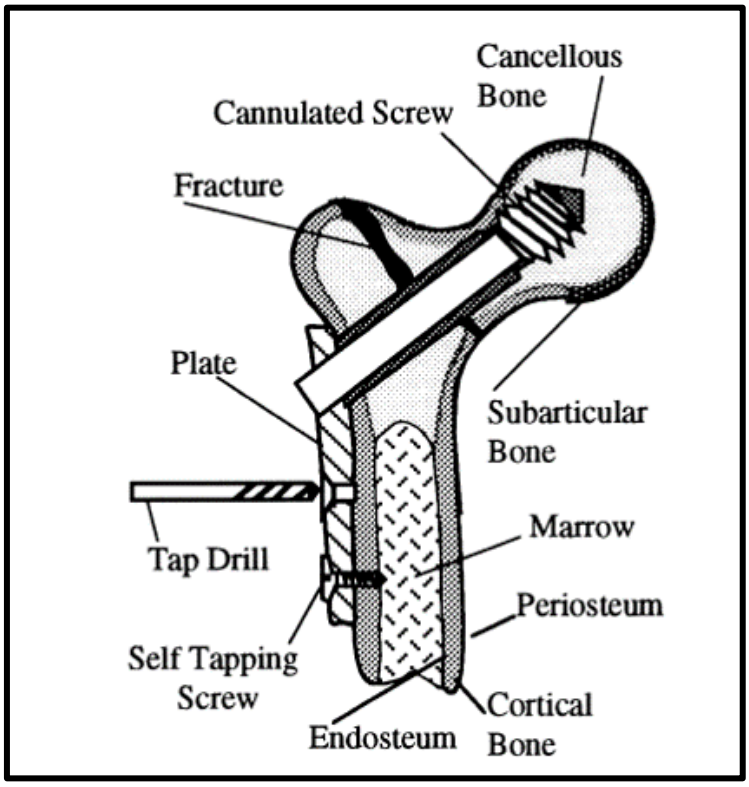


Figure 1.3: Drilling on the bone for surgery (*reprinted with permission from Elsevier* [11]).

Figure 1.3 shows a typical schematic diagram of drilling in femur surgery, where a fractured part of the bone was aligned with the help of a plate and screws, and to insert the screw in the bone drilling was performed. The purpose of bone drilling is to provide support to the fractured part at the direct level and helps the healing of the bone fracture faster. This orthopaedic drilling of bone is very much similar to a mechanical drilling process that results in to increase in the reactive forces, torque, microcracks, delamination and temperature of surrounding bone material. As the fractured bone gets healed simultaneously it will cause the generation of microcracks on the surface of the bone and heat generation during the drilling of the bone. The heat is generated due to friction between the drill bit and the bone surface, which is the cause of cell death, and change in the natural properties of bone. When the temperature is elevated above the threshold value, bone resorption may occur due to thermal exposure, which results in thermal necrosis. The temperature rise in bone drilling above the thermal threshold (around 47°C for 1 minute or 40°C for 7 minutes) is a prime concern [12]. The success of osseointegration is highly dependent upon thermal injuries, interlayer delamination, higher cutting force, hole inaccuracy, poor pullout strength, microcracks in the surrounding soft tissues, bone-chip coagulation, low insertion torque, immediate loading at the implant site, lack of initial implant stability and insignificant bone volume. The holding power at the bone-screw joint depends on anchorage strength and pullout strength between the screw and bone. Damaged bones with microcracks are not able to hold the screws and implants for a very long period leading to implant failure. "*The poor pull-out strength and holding strength at the bone-screw interface may lead to intolerable pain, screw loosening and implant failure at the fracture site and affect the reliability of surgery causing reoperation and revision surgery*".

1.4 Bone screws and their types

Bone screws are used in almost every orthopaedic surgery to fix fractured parts of the bone for accelerating the healing and mobility of injured tissues. The recovery of fractured parts majorly depends upon the selection of suitable implant and bone screws, as the cortex of a bone is the hard outer shell covering the entire bone. Internal fixation can be achieved using devices like orthopaedic bone screws, fixation plates, pins, wires, spinal fixation devices, intramedullary rods, and nails. A bone screw is a biomedical implant that converts rotational motion into linear motion and is a very efficient implant for repairing a fracture using inter-fragmentary compression, or for fixing a splinting device such as a plate, nail, or fixator. Bone screws are specifically designed to function effectively in the bone into which they are installed. Early

mobilization and early union of fracture is the primary goal of internal fixation. The fixation stability at the bone-screw interface is affected by bone-screw interface holding power, type of screw used, screw purchase strength, wound location, fracture type, number of screws implanted, the orientation of screws and bone mineral density.

Bone screws can be classified into different types based on their application and the location of fractured bones. There are various types of bone screws available commercially that are used for fixing different fractured human bones as illustrated in Figure 1.4.

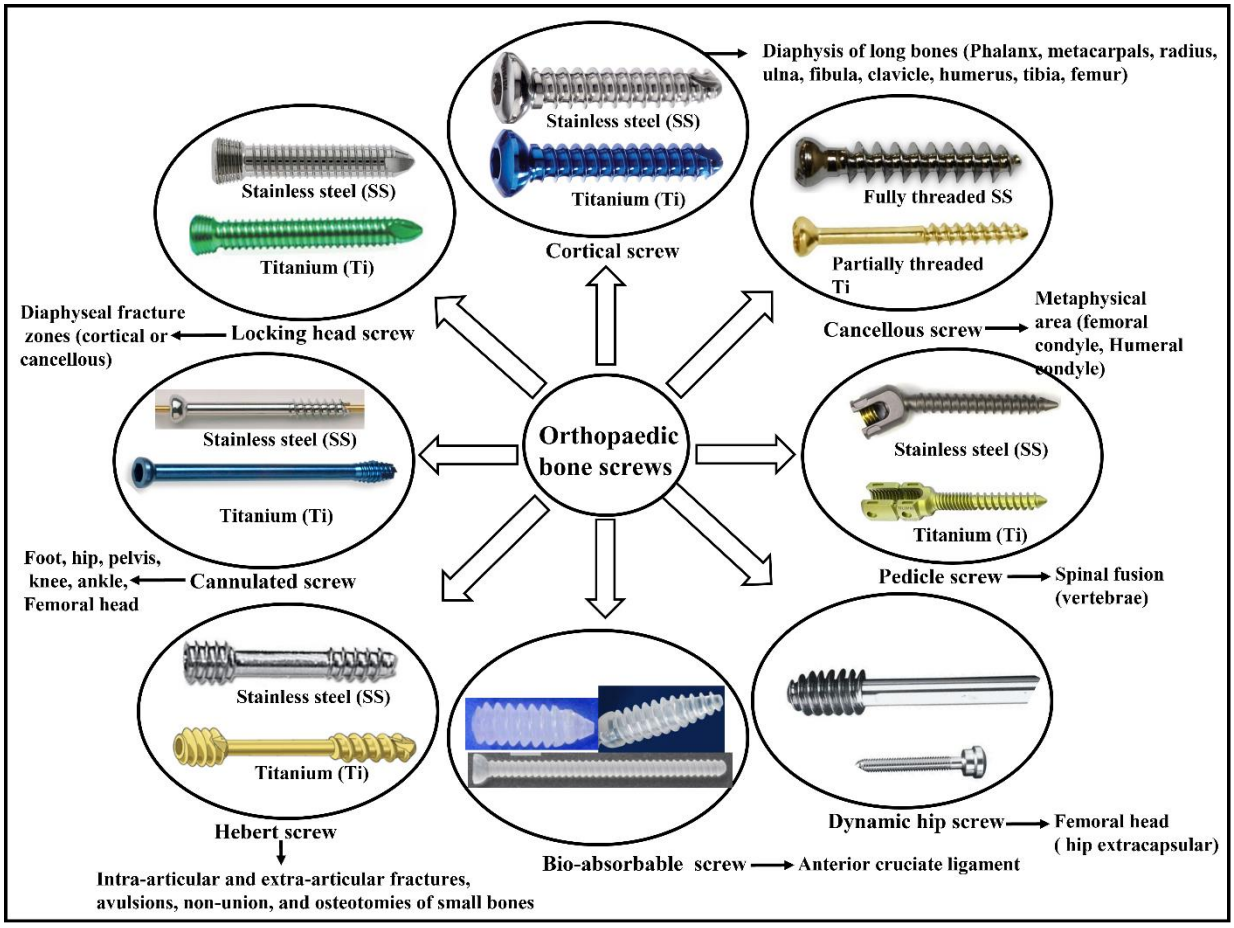


Figure 1.4: Various types of orthopaedic bone screws used for different applications within the human body.

The X-ray radiographs of different types of bone screws with their application in the human body are presented in Figure 1.5. Hebert screws are used for intra-articular and extra-articular fractures, cannulated screws are used for the treatment of foot, knee, ankle, pelvis, and femoral head fractures. Mostly used bone screws are pedicle screws used for spinal fusion, cancellous screws used in the metaphysical area and cortical screws used in the diaphysis of long bones. Cortical screws are mostly used bone screws in most of human bones.

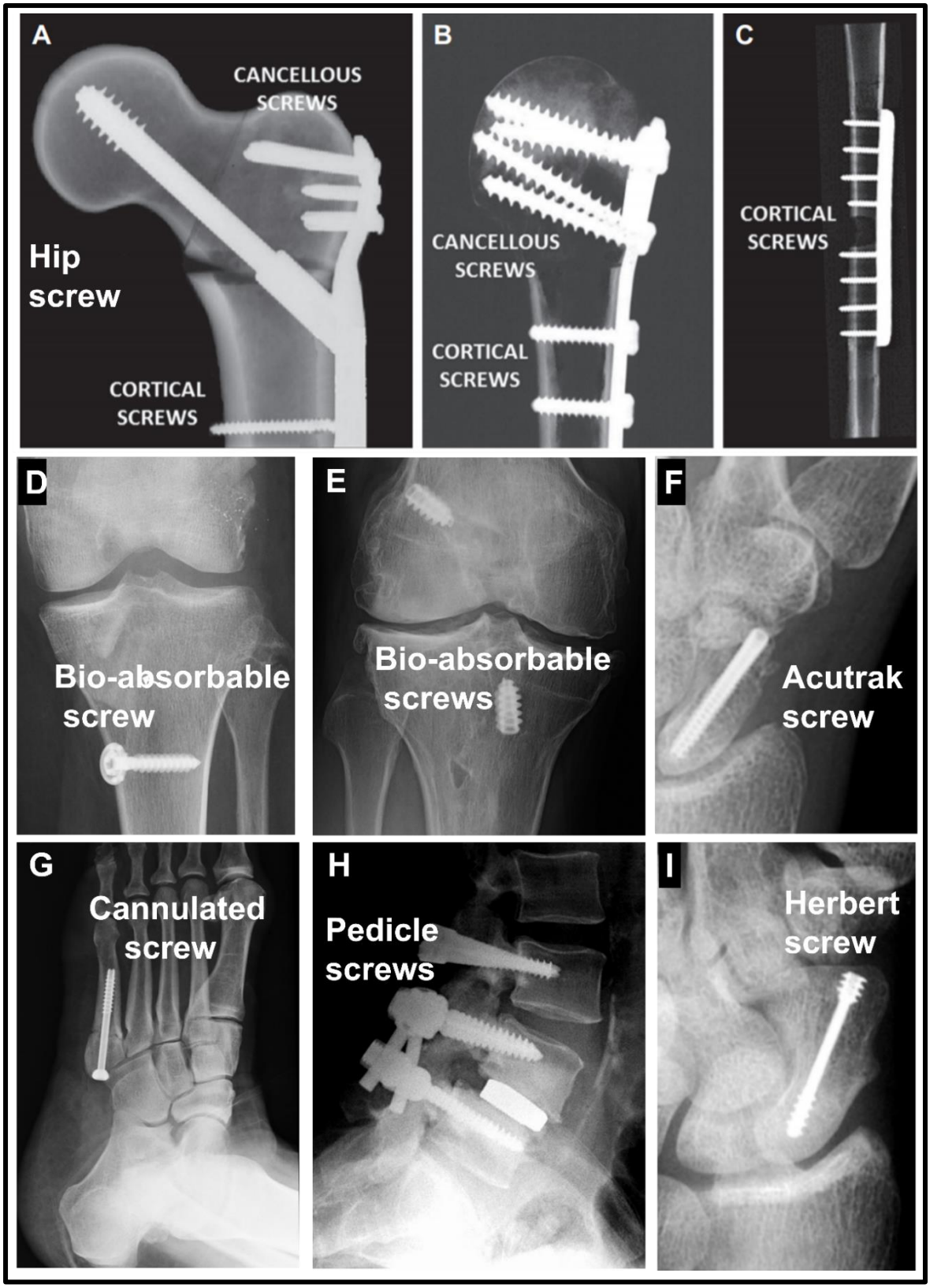


Figure 1.5: Various types of bone screws: (a) Cortical screw, (b) Cancellous screw, (c) Hip screw [13]**, (d-e) Bio-absorbable screw** [14]**, (f) Acutrak screw** [15]**, (g) Cannulated screw** [16]**, (h) Pedicle screw** [17]**, (i) Herbert screw** [15] ***[all the images are reprinted with permission from Elsevier*** [13–17]***].***

The most commonly used bone screws for osteosynthesis in veterinary orthopaedics are cortical and cancellous [18]. Cortical and cancellous screws are classified by the layers of bone that they interact with. The cortical screw is designed for the diaphysis bone as they have smaller threads, a lower pitch for higher holding power in cortical bone and large core diameter. It is recommended that the screw diameter should not exceed 40% of the diameter of the bone [19]. Cancellous bone screws have a larger outer diameter, a deeper thread, and a larger pitch than cortical screws [18], therefore, cortical screws are a preferable choice in metaphysical or epiphyseal bone [18, 20]. The design of cortical screws consists of several geometrical parameters like head shape, shaft length, outer diameter, inner diameter, screw thread angle, thread type, pitch, tip, and length of the screw. The design of cortical screws varies based on their application for fixation according to the length and thickness of fractured bone. It must be noted that geometric parameters such as thread pitch, diameter and length of the cortical screw are highly variable among the available orthopaedic screws in the market [21]. Different screw designs have different initial contact and surface area, dissipation, and distribution of stress forces at the bone-screw interface and increased pull-out resistance to load. Bone screws are made of stainless steel and titanium that has the disadvantage of stress corrosion, notch sensitivity, and poor wear characteristics. However, various diameters and lengths of cortical screws are available, but they are standardized and common for every patient with fractured bone (for children, teenagers, and adults).

From ancient civilizations to the 21st century, material properties and design parameters of bone screws have been modified to reduce bone-screw-related complications, such as stress shielding effect, pullout strength of bone-screw, screw perforation and screw purchase failure. The stress shielding effect occurs due to the incongruity of elastic moduli between the screw and bone [22]. Pullout strength is defined as the force required for pulling a screw out of its foundation in bone [23]. Lower pullout strength of the bone screw is the primary reason for bone loss during healing and screw loosening [24]. Screw perforation is the failure at the bone-screw interface that leads to screw tip penetration through the subchondral bone into the joint [25]. Screw purchase failure occurs at the bone-screw interface without macro-displacement of the bone segment or screw [25]. Screw perforation [25] and screw purchase failure [18, 26, 27] of the articular cartilage may lead to problems like avascular necrosis, delayed union, lower bone-screw interface holding strength, and non-union [22, 25]. These problems cause unbearable pain and may increase the chances of revision surgery. Another major complication is the excessive load at the fracture site which mainly affects the bone screw and causes

breakage of the bone screw leading to revision surgery [27, 28]. All the discussed bone screw complications are summarized in Figure 1.6.

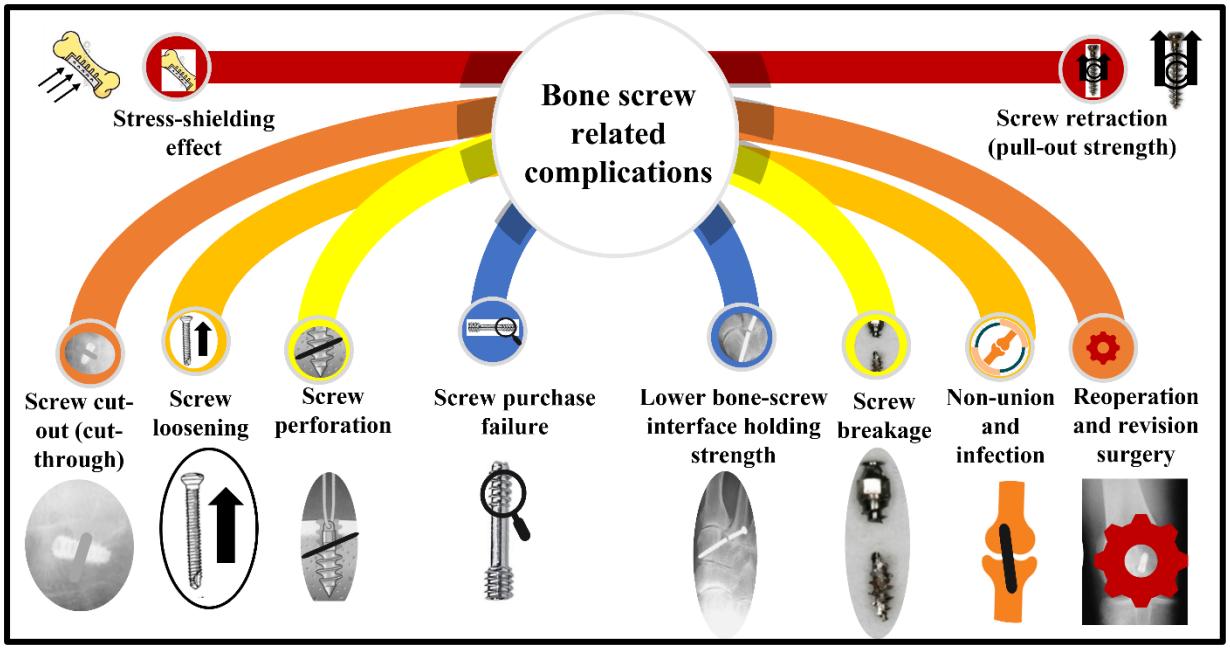


Figure 1.6: Bone-screw-related complications observed in the literature.

In order to reduce the bone-screw-related-complications, biodegradable bone screws may reduce the stress-shielding effect as they can degrade and absorb in the body after a period of time which also eliminates the complex post-operative surgery required for removal of the implanted screw. Also, patient-specific bone screws fabricated by three-dimensional (3D) printing techniques may improve the bone-screw holding strength and grasping power. The customized bone screw would have porous lattice structures, which are expected to significantly enhance the pull-out strength.

1.5 Aim and objective of the present work

1.5.1 Aim and motivation of the study

In the United States alone, more than 10.2 million bone fracture surgeries are reported annually [7, 8]. It was estimated that by 2050, total hip fractures of 500,000 will be occurring annually in the United States only [29]. The treatment of fractured bones imperatively requires a bone drilling technique for fixing the fractured bone with orthopaedic bone screws and plates. The treatment of osteoporotic fractures is challenging for orthopaedic surgeons, as with osteoporotic bones the bone quality and density of bone decrease. Approximately 200 million people worldwide are affected by osteoporosis [30]. Every year osteoporosis affects 8.9 million

individuals globally resulting in an osteoporotic fracture every 3 seconds [31], moreover, this number is expected to be doubled by 2040 [30]. Osteoporotic fractures are associated with high rates of morbidity and mortality and the overall cost of treatment is estimated to reach $18 billion globally [30]. Screw loosening and loss of implant stability may also occur, due to osteoporosis [32]. It has been reported that nearly one-third of the treated fractures with locking plates have complications; 11% have screw-related complications [25]. The reported rate of screw misplacement pedicle fixation ranges from 21 to 40% [32]. The stability of fixation is determined by compression across the fracture site that is affected by bone-screw interface holding power, type of screw used, screw purchase strength, the number of screws used and bone mass available for fixation, the orientation of screws, and bone mineral density. To improve the holding power and biomechanical pullout strength at the bone-screw interface, the customized biodegradable bone screw can be investigated.

Therefore, a biodegradable cortical screw design would be explored using three-dimensional (3D) printing techniques where the geometrical parameters would be optimized to appropriately support osteoporotic bones. The customized screw designs would have porous lattice structures, which are expected to significantly enhance the pull-out strength. Various machine learning algorithms can be used to optimize the input process parameters. Moreover, the insertion angle for screw implantation will be optimized for the maximum pullout strength of bone screws. It needs to be noticed that the idea of using bio-absorbable screws is expected to diminish the post-operative revision surgery to extract the inserted screw. Overall, the current implant failure rate would be reduced and the holding strength at the bone-screw interface would be improved.

1.5.2 Research goal

The major goal of the present research work has been *investigating 3D-printed orthopaedic cortical bone screws to improve biomechanical pull strength* which can eliminate the stress-shielding effect, post-operative revision surgery for screw extraction and improve biomechanical pullout strength at bone-screw interface. The goal has been achieved by the following research objectives.

1) To fabricate cortical bone screws using rapid prototyping technology.
2) To optimize the process parameters during the fabrication of cortical bone screw in view of maximizing the strength of screw using machine learning algorithms.

3) To compare the pull-out strength with conventional bone drilling and inclined bone drilling.
4) To examine the histopathological analysis to observe the bone-screw interface.

1.6 Outline of the Thesis

The present in vitro study is organized into 8 chapters as discussed below:

Chapter 1 presents an introduction to the basic approach related to bone fractures, bone drilling, application of bone screws, and various bone-screw-related complications associated with conventional bone screws. This chapter also gives an overview of the research problem, objectives, methodology and thesis organization.

Chapter 2 describes the current state-of-the-art literature in the intended direction of research. This chapter presents a comprehensive and up-to-date review of the different 3D printing techniques used, characteristics, merits and demerits of the prominent biomaterials used for orthopaedic bone screw fabrication. Based on the literature review, the research gaps have been presented to formulate the research problem.

Chapter 3 focuses on designing and fabricating orthopaedic cortical screws using fused filament fabrication-based 3D printing technology. The details of process parameters and their ranges used to fabricate cortical screws are described. The influence of 3D printing process parameters on the mechanical strength of fabricated screws was observed. The surface morphology and fracture micrography was also observed.

Chapter 4 discusses the details of the applications of different machine learning and ensemble machine learning models leveraged for predicting mechanical strength and optimizing different process parameters of 3D printing technology for the maximum mechanical strength of fabricated bone screws.

Chapter 5 presents the experimental setup for performing rotary ultrasonic-assisted drilling and conventional drilling of porcine bone. The chapter presents in-situ monitoring of temperature elevations and cutting force during bone drilling techniques. The influence of

inclination angle on the biomechanical pullout strength during inclined and conventional bone drilling is presented.

Chapter 6 deals with the biodegradation of 3D-printed cortical bone screws in different biological solutions (simulated body fluid, phosphate-buffered solution, and Hank`s balanced Salt Solution). Also, histopathological evaluation at the bone surface after the extraction of surgical metallic screws and 3D-printed cortical screws is examined.

Chapter 7 presents the fabrication of Ti6Al4V cortical bone screws using selective laser melting based 3D printing technology. For the biological assessment of bone-screw samples, SBF solution was used. Bone mineral density (BMD) of male and female porcine femur bones was monitored. For the biological assessment of bone-screw samples, SBF solution was used. The influence of immersion period, gender and BMD was monitored on the biomechanical pullout strength of 3D-printed Ti6Al4V and surgical metallic cortical screws.

Chapter 8 summarizes the major outcome of the present research work. The future scope of the work has also been highlighted in this chapter.

Chapter II

Literature review

Chapter 2

Literature review

2.1 Introduction

The major goal of the present in-vitro study is to design and develop an orthopaedic cortical bone screw using 3D printing technology to promote the biomechanical pullout strength and holding power at the bone-screw interface. This chapter presents the state-of-the-art literature survey in the direction of the history of bone screws, types of bone screws, application of 3D printing technologies, characteristics, merits, and demerits of the prominent biomaterials explored until the 21st century for the fabrication of bone screws. The effect of bone mineral density and inclination angle on the cutting temperature, force, microcracks, hole quality, and pullout strength at the bone-screw interface has been discussed. The important literature available in this field has been reviewed as under.

2.2 History of bone screws

Orthopaedic bone screws have been used for the internal fixation of bone fractures for more than 100 years. In 1912, **William O. Sherman** [33] introduced the orthopaedic screw as the most dependable and efficient means of securing and retaining the accurate position of fracture parts. In 1949, **Robert Danis** [34] designed the compressive plate and modified the machined screw by reducing the thread surface, altering the thread diameter, and introducing a buttress thread design to improve the pullout strength of the screw. In 1958, **Maurice Muller** [34, 35] and a group of Swiss surgeons established the Association for the Study of Internal Fixation (ASIF) to study the effect of internal fixation and bone healing. In the same year, **Bagby and Janes** [35] designed impacting bone plates with oval-shaped holes that allowed eccentric screw placement for intra-fragmentary compression through tightening. This design, with slight modification, remains in use today. From the introduction of stainless steel in 1926 to test on titanium alloys introduced in 1970 [34], innovation and research continued to modify the material properties and design parameters of orthopaedic bone screws for better stability and holding capacity of screws.

In the following decades, screw geometry based on the number of threads, pitch, shape, diameter variations etc., was optimized for a variety of bone types, quantities and pathologies [35]. As a result, the modification in bone screws has attracted more attention from academic

research to clinical applications. As presented in Figure 2.1, with the participation of modern technology in the fabrication of bone screws, the research and innovation related to orthopaedic bone screws are constantly growing and evolving. The milestones of evolution in orthopaedic bone screws are illustrated in Figure 2.1. The most recently developed orthopaedic bone screws are being manufactured via 3D printing techniques.

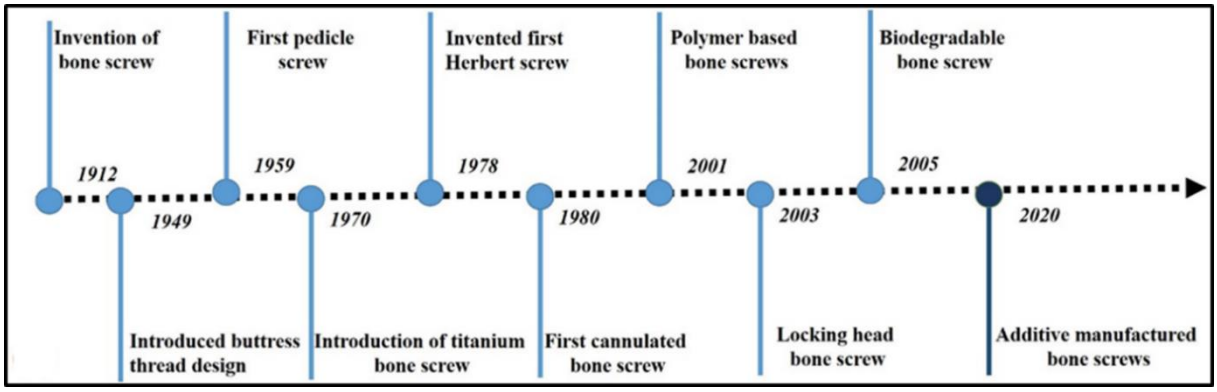


Figure 2.1: Evolution of research in orthopaedic bone screws.

2.3 Review of 3D printing techniques and biomaterials used for bone screw fabrication.

The role of 3D printing technologies in the fabrication of orthopaedic bone screws is becoming vital and popular as this technology provides incredible customizability, efficient speed, high accuracy, and freedom to design anything using CAD models. With the advancement in the 3D printing technique, patient-specific customized orthopaedic bone screws can be fabricated. 3D printing technology can provide the porous auxetic structure to the surface of the bone screw to enhance the bone in-growth through the screw body, improving the bone-healing contact and the Osseo-integration process. 3D-printed bone screws can produce rough and irregular geometry to the screw surface that may influence bone regeneration.

As 3D printing technology provides high accuracy, safety, great customizability, and less wastage in by-products. The recent development in the bone screw fabricated via 3D printing technology is presented in Table 2.1. The 3D-printed bone screws have the advantage of higher bone-screw contact, excellent implant stability, capability to provide porous structure in the screw body to promote Osseo-integration and vascularization over traditional manufacturing of bone screws. The porosity in orthopaedic bone screws produced with 3D printing technology could improve tibia graft fixation and enhance the biomechanical performance of the bone-tendon-screw interface [36]. The literature based on 3D-printed orthopaedic bone screws is presented in Table 2.1. This table presents the recent advancement in orthopaedic bone screws using different 3D printing techniques.

Table 2.1: Recent development for bone screw fabrication via 3D printing techniques.

Publication	Year	Process Used	Screw type	Material Properties			Remarks
				Metallic screws	Bio-absorbable	Porous structure	
[37]	2017	-	Cortical	✓	✓	×	The metal screw provides higher fixation strength than the bio-absorbable screw.
[38]	2018	Metal powder bed fusion	-	✓	✓	×	3D printing can influence the internal fixation of implants. The open pores can increase flexibility and can improve screw-level fixation.
[26]	2019	-	Pedicle	✓	×	×	Double dual-threaded screws exhibited better pullout biomechanics in osteoporotic bone with bi-cortical bone.
[39]	2019	Custom designed mould	Bone screw	×	✓	×	The highest mechanical strength properties were obtained with 10% MgO and 20% silk composite over PCL.
[40]	2019	FDM	Screws, pins, plates	×	✓	×	Hybrid fabrication for adsorbing during osseous fixation devices can be achieved using 3D printing.
[41]	2020	E0BM	Eli	✓	×	×	Higher bonding force and bone-implant contact was observed in 3D-printed screw.
[42]	2020	3D printing	Cancellous Screw	✓	×	✓	Different auxetic structures have additional tensile stiffness and strength.
[36]	2020	3D printing	Cortical	✓	×	✓	3D printed improves bone ingrowth and enhanced biomechanical performance.
[43]	2020	SLM & EBM	-	✓	×	×	The milling group presents a higher screw loosening value than the 3D printing
[31]	2020	FDM	Cortical		✓	✓	The porous screws have better interaction and increased vascularization as compared to solid screws.
[44]	2020	EBM	Bone screw	✓	×	✓	10 and 100 μg/ml of Ti6Al4V particles may improve osteogenic differentiation.
[45]	2021	SLM	Pedicle	✓	×	✓	Auxetic pedicle screw can improve the bone–screw fixation by radial expansion of the screw body under tensile force to resist the pulling out of the screw from the bone surface by the re-entrant unit cell pores.

2.3.1 Metallic biomaterials

Metals are the primarily used biomaterials in orthopaedic, dental, and joint replacement surgeries due to their excellent strength, high fracture toughness, hardness, and biocompatibility [46, 47]. The gold standard metallic biomaterials for the fabrication of orthopaedic implants (bone screws) are titanium, stainless steel, and cobalt-based alloys [48]. It has been observed that titanium-based biomaterials have excellent biocompatibility and ductility. Although titanium-based implants are fatigue resistant with poor wear characteristics [49, 50]. Moreover, cobalt-based alloys are highly considered due to their superior strength and property resistance [51]. Table 2.2 and Table 2.3 provide a comprehensive detailed mechanical property, specifications, indigent percentage of metals, advantages, disadvantages, and application of metallic biomaterials in orthopaedics. Table 2.2 provides a summarised mechanical property of metallic biomaterials currently used in orthopaedic bone screw fabrication. Moreover, the detailed comparison of different metallic biomaterials is presented in Table 2.3. This table could help select suitable biomaterials based on the application and usage of metallic biomaterials.

Titanium is highly reported in the literature as a suitable biomaterial for bone screw fabrication utilizing different 3D printing techniques. **Huang et al.** [36] fabricated titanium screws using 3D printing technology. The bioactive surface modification of porous titanium was observed with preservation in simulated body fluid for seven days. The surface-modified bone screws were implanted in rabbits to monitor the ultimate pullout strength. It was observed that ultimate pullout load failure was significantly higher in 3D-printed screws.

Lee et al. [52] used 3D printing technology to fabricate titanium ELI screws and performed an in-vivo study on rabbits. It was witnessed that the 3D-printed screw has higher bonding strength and shows higher bone-to-implant contact, indicating a higher Osseo-integration rate than the conventionally machined screw. Active osteogenesis and new bone formation were significantly higher in 3D-printed titanium bone screws. **Yao et al.** [45] enhanced the geometry of titanium pedicle screws by providing an auxetic structure with the help of 3D printing technology to resist the loosening of the pedicle screw. The auxetic structure of bone screws results in the better anti-pullout performance of pedicle screws with excellent screw-bone fixation. 3D-printed titanium bone screws can reduce screw loosening by improving holding power and pullout strength at the bone-screw interface. There are various 3D printing techniques used to fabricate metallic parts as discussed in the further section.

Table 2.2: Specifications of metals used in orthopaedic screw fabrication [46, 47, 49, 53]**.**

Material	Young`s modulus (GPa)	Elastic modulus (GPa)	Density (g/cm^3)	Yield strength (MPa)	Ultimate tensile strength (MPa)	Elongation (%)	Fatigue strength (MPa)
ASTM 316L Stainless steel	195-200	202	8	250 (hf) 310 (cw)	550 (hf) 655 (cw)	40-50	379-414 (cf) 414-448 (cw)
ASTM 22-13-5 Stainless steel	193-200	200	7.88	827 (hf) 993 (cw)	1069 (hf) 1262 (cw)	35	414 (hf) 483 (cw)
Titanium alloy Ti-6Al-4V	113	110-114	4.4	795-895	985	12	520
Cobalt chrome F5262	230-240	220	8.5	950-1000	1200	10-30	207

Note cf- cold forging, cw- cold worked, hf- hot forged.

Table 2.3: Gold standard metallic biomaterials for orthopaedic bone implants.

Metal	Type	Ingredients percentage	Advantages	Disadvantages	Usage
Stainless steel (SS)	316L SS (3% molybdenum, 16% nickel & L= Lower carbon content)	Iron (59.8-68.97%)	Biocompatible [46]	Susceptibility to crevice and stress corrosion [47]	Used in plates, screws, Intramedullary (IM) nails, external fixators etc. [46, 47].
		Chromium (16-18%)	Strong [47]		
		Nickel (10-16%)	Relatively ductile [49]	Stress shielding effect [46]	
		Molybdenum (2-3%)	Relatively Cheap [47]		
		Nitrogen (0.1%)	Reasonable corrosion resistance [51]	Poor wear resistance [51]	
		Carbon (0.03%)		High Young`s modulus(200 G Pascal) [46, 49]	
Titanium (Ti) alloys	TITANIUM 64 (Ti-6Al-4v)	Titanium (89%)	Excellent biocompatibility [48]	Poor wear characteristics [50]	Used in internal fixators, screws, plates, vertebral spacers, halos, IM nails etc. [46, 47, 51].
		Aluminium (6%)	MR scan compatible [49]	Relatively expensive [46]	
		Vanadium (4%)	Corrosion resistance [51]	Notch sensitivity [47]	
		Others (1%)	Ductile [51]	Systematic toxicity-vanadium [51]	
			Fatigue resistance [47]	Can be brittle (less ductile) and have more metal debris generation than cobalt alloys [47, 49]	
			High Osseo integration [48]		
			Low Young`s modulus [47]		

Cobalt chrome alloys	Co-Cr	Primarily cobalt (30-60%)	Excellent long-term biocompatibility with soft tissues and blood [54]	Risk of stress shielding [51]	Usually used for bearing surfaces, artificial joints including knee and hip joints, arthroplasty implants, dental implants and orthopaedic implants [46, 47, 51].
		Chromium (20-30%)	High osteointegration [47]		
			Incredible strong strength [51]	Nickel sensitivity [51]	
		Molybdenum (5-7%)	High wear resistance [51]	Expensive [47]	
		Elements like 1% iron, manganese, tungsten, nitrogen, phosphorus etc.	Excellent resistance to corrosion compared to SS and Ti alloys that reduce complications with surrounding tissues [49, 51]	Very high Young`s modulus [47]	
			Excellent castability and toughness [46]	Workability and plasticity are low as compared to SS and Ti alloys [46]	

2.3.1.1 Electron beam melting (EBM) technique

EBM is an advanced 3D printing technology majorly used to fabricate metal parts. The build plate is coated with a layer of metal powder placed under a high vacuum (1×10^{-4} Torr) and fused using the melting of material by an electron beam (heat source) controlled by electromagnetic coils [55]. The maximum build part can be fabricated of dimensions 350 x 350 x 380mm^3 with a tolerance of ± 0.2mm and minimum layer thickness of 0.5mm [56, 57]. The EBM machine reads the 3D CAD model and then successfully lays down powdered material layers. After one layer is complete, the build platform is moved down and continues the process for the next layer [58]. The semi-sintered powder is removed for post-processing to get the fabricated metal part [59, 60]. EBM uses materials like copper, bulk metallic glass, stainless steel, pure titanium, Ti6Al4V, CoCr, and Inconel [44, 59, 61]. EBM technology has a faster printing speed due to the electron beam, which is more potent than laser. EBM is ideal for manufacturing lightweight, durable, high-quality metal parts with high density (99.9%) and high strength of dense end parts [43, 58, 62]. This technology has an edge for building complex geometric structures to achieve a weight reduction of fabricated parts and a low risk of deformation with good mechanical properties. This technology is used in biomedical applications for implants, acetabular cups, prostheses, and bone screw fabrication [43, 58, 61, 63]. Due to its high energy density and scanning method, this technology has a unique build rate. However, it has a little less accuracy than SLM [56]. The material removal rate is a very

slow process. EBM technology is a costly process and uses expensive materials that only suit industrial applications [64].

The EBM technology can be used to fabricate various biomedical instruments and implants for orthopaedic applications. **Lee et al.** [41] used EBM technology to fabricate ELI bone screws and compared them with conventional machined screws, as depicted in Figure 2.2. EBM machined bone screws and conventional screws were implanted in the rabbit tibia for two weeks and then pushed out to observe the holding strength at the bone-screw interface. The strained histological analysis, SEM micrographs and elemental analysis were conducted on the pushed-out screws. It was observed that EBM fabricated bone screw has a higher adhered bone in the surface of the screw as depicted in Figure 2.2(a) compared to negligible bone attached in conventional bone screw. The result revealed higher bone-to-implant contact interaction and higher push-out strength of EBM-fabricated ELI screws than conventionally machined screws.

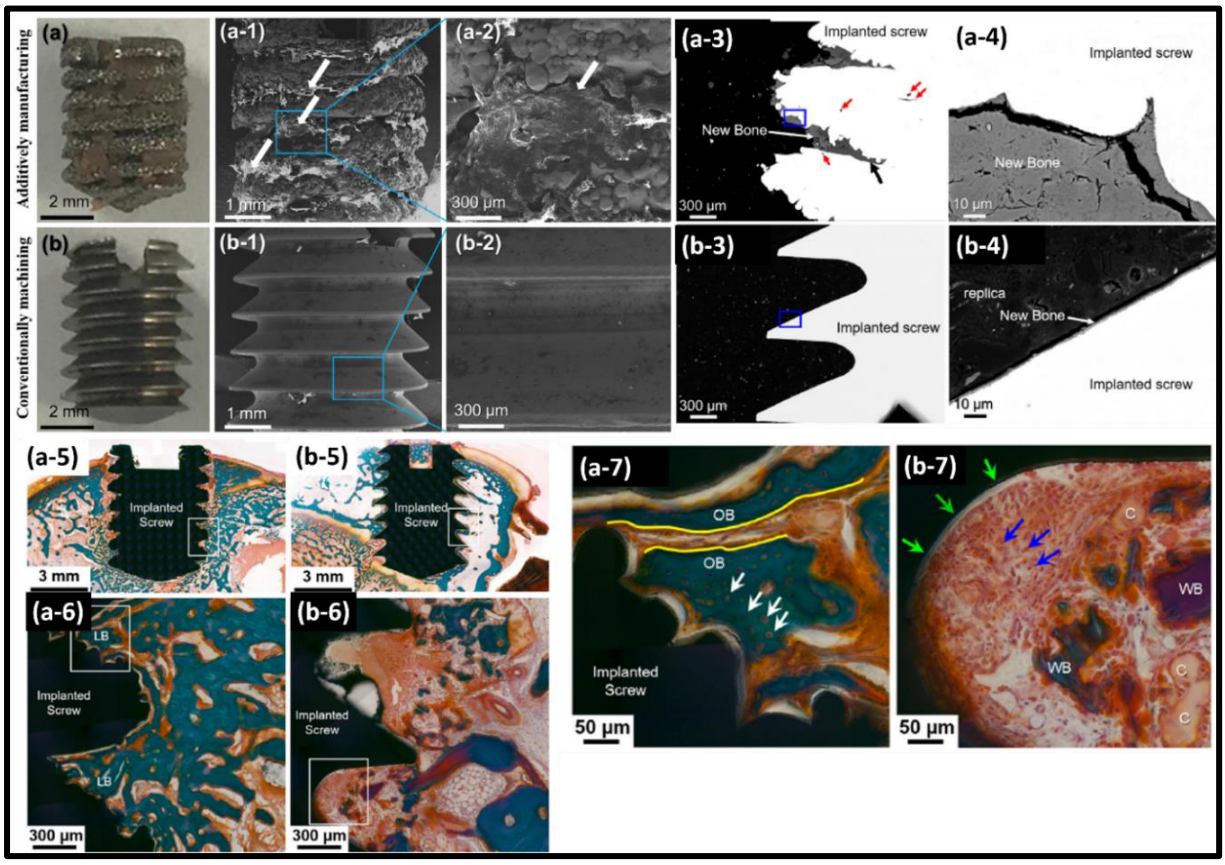


Figure 2.2: Comparison of after push out of (a) EBM fabricated Ti6Al4V ELI screw with (b) conventional screw, SEM images of bone-screw (a1-a4) EBM ELI screw with (b1-b4) conventional screw, histological images of (a5,a6,a7) EBM screw with (b5,b6,b7) conventional screw *[Reprinted with permission from Elsevier* [41]*].*

2.3.1.2 Direct metal laser sintering (DMLS) technique

DMLS is a laser-based technology that utilizes a high-powered laser as a power source to sinter and fuse layers of metallic powder together by pointing the laser and outlining the object in a layer-by-layer format to build up the design of a 3D cad model [55, 65]. Parts are printed in an enclosed build chamber with argon gas. The maximum part resolution of 250mm×250mm×300mm with a layer thickness of 0.02mm to 0.06mm and tolerance of ± 0.1mm can be achieved [14, 38, 82, 85]. When the build finishes, the post-processing requires an initial brushing to remove the slack powder, and the part is removed.

The materials used in DMLS technology are aluminium (AlSi10Mg), stainless steel (316L), titanium (Ti64), cobalt chrome (Co28Cr6Mo), copper (CuNi2SiCr), and nickel alloy 625 [49, 55, 64–67]. Titanium-based implants fabricated using DMLS technology have a survival rate of 97% and biological complications of 7% [49]. DMLS technology prints durable, lightweight, and precise, detailed metal parts with excellent quality, high accuracy, strong mechanical strength, creep resistance and fatigue characteristics pretty much the same as products machined from comparable wrought, forged, or cast material [68–70]. This technology creates complex structures, intricate detailing, and delicate features [71]. The major disadvantage of DMLS is a relatively slow process with expensive post-processing.

2.3.1.3 Selective laser melting (SLM) technique

SLM is a metal printing (powder bed fusion) technology that utilizes metallic powder and a high-intensity laser as an energy source that fuses high-temperature metallic powder in a layer-by-layer format based on a 3D CAD model [72]. The layers are continuously to be combined and deposited one over the other until the completion of the part. The most commonly used metallic powder for the SLM process are titanium, ferrous alloys, cobalt-chrome, aluminium, copper, magnesium, zinc, and tungsten [50, 66, 68].

The significant advantage of SLM technology is to fabricate any complex lattice-structured metallic implants with high fracture toughness and mechanical strength that may promote bone ingrowth, vascularization, and the process of Osseo-integration [50, 73–75]. The manufacturing of critical structures, customized metallic design with high dimensional precision and good surface integrity is the key advantage of this technology [66]. The only limitation of SLM technology is that the conduction and diffusion of laser heat cause unwanted fusion of neighbouring powder particles, limiting the resolution of final features [76–78].

SLM technology is widely used in literature for bone screw fabrication. **Yao et al.** [45] used SLM to fabricate auxetic structured pedicle bone screws, as depicted in Figure 2.3. The pedicle screws were manufactured with SLM technology with different re-entrant angles and auxetic units, as presented in Figure 2.3(a). These various re-entrant angles and wall thickness of fabricated pedicle screws are morphologically monitored by micrographs as shown in Figure 2.3(b). The pullout strength of the screw was monitored with a FEM and experimentally using sawbones as depicted in Figure 2.3(c) and Figure 2.3(d), respectively. It was concluded that varying the wall thickness and re-entrant angles of the auxetic structure may support the pullout strength of pedicle screws, as presented in Figure 2.3(e).

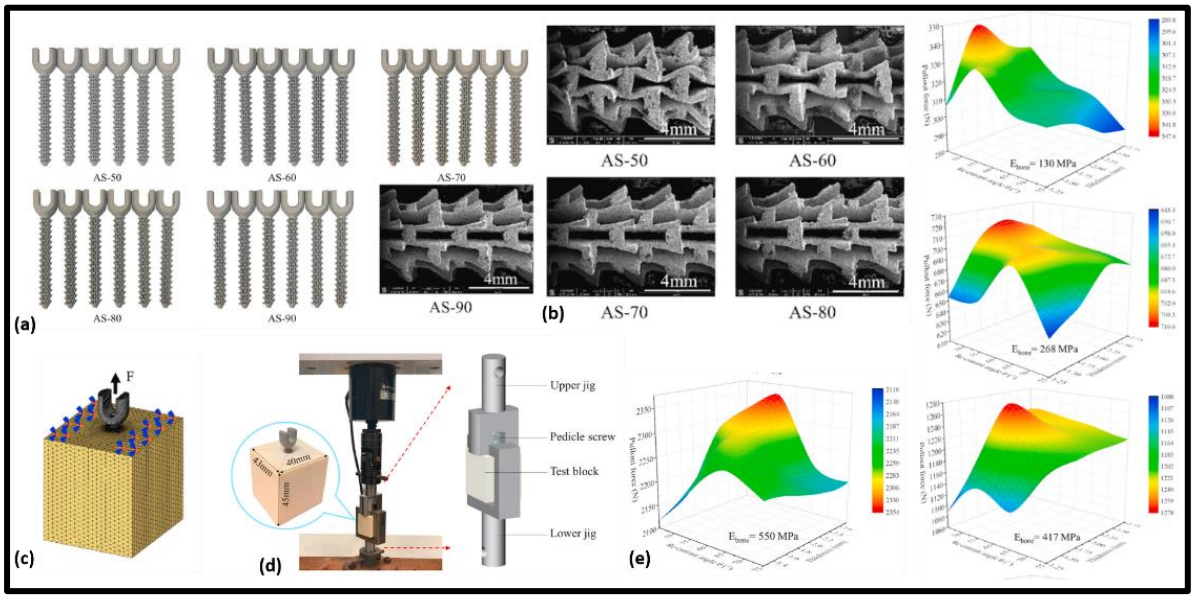


Figure 2.3: (a) Pedicle screws with different re-entrant angles and auxetic units, (b) SEM images of screw bodies with auxetic units, (c) FEM and boundary conditions, (d) schematic of the test specimen, (e) maximum pullout force interactions with different designs of auxetic structures *[Reprinted with permission from Elsevier* [45]*].*

Huang et al. [36] used SLM technology to fabricate titanium bone screws and compared them with a conventional screw in rabbit animals for 6 months. Micro-CT examination of implanted control screw and 3D-printed screw is presented in Figure 2.4(a) and Figure 2.4(b) to monitor tissue volume and bone volume fraction. Histological analysis of the bone screw was conducted for monitoring bone ingrowth as depicted in Figure 2.4(c) and Figure 2.4(d). The 3D-printed screw has a rough surface that quickly promotes bone ingrowth. After 6 months of implantation, the bone screw construct was monitored. It was witnessed the hat 3D-printed screw has higher woven bone and a wider gap at the interface as compared to controlled screw as illustrated in Figure 2.4(e) and Figure 2.4(f) respectively.

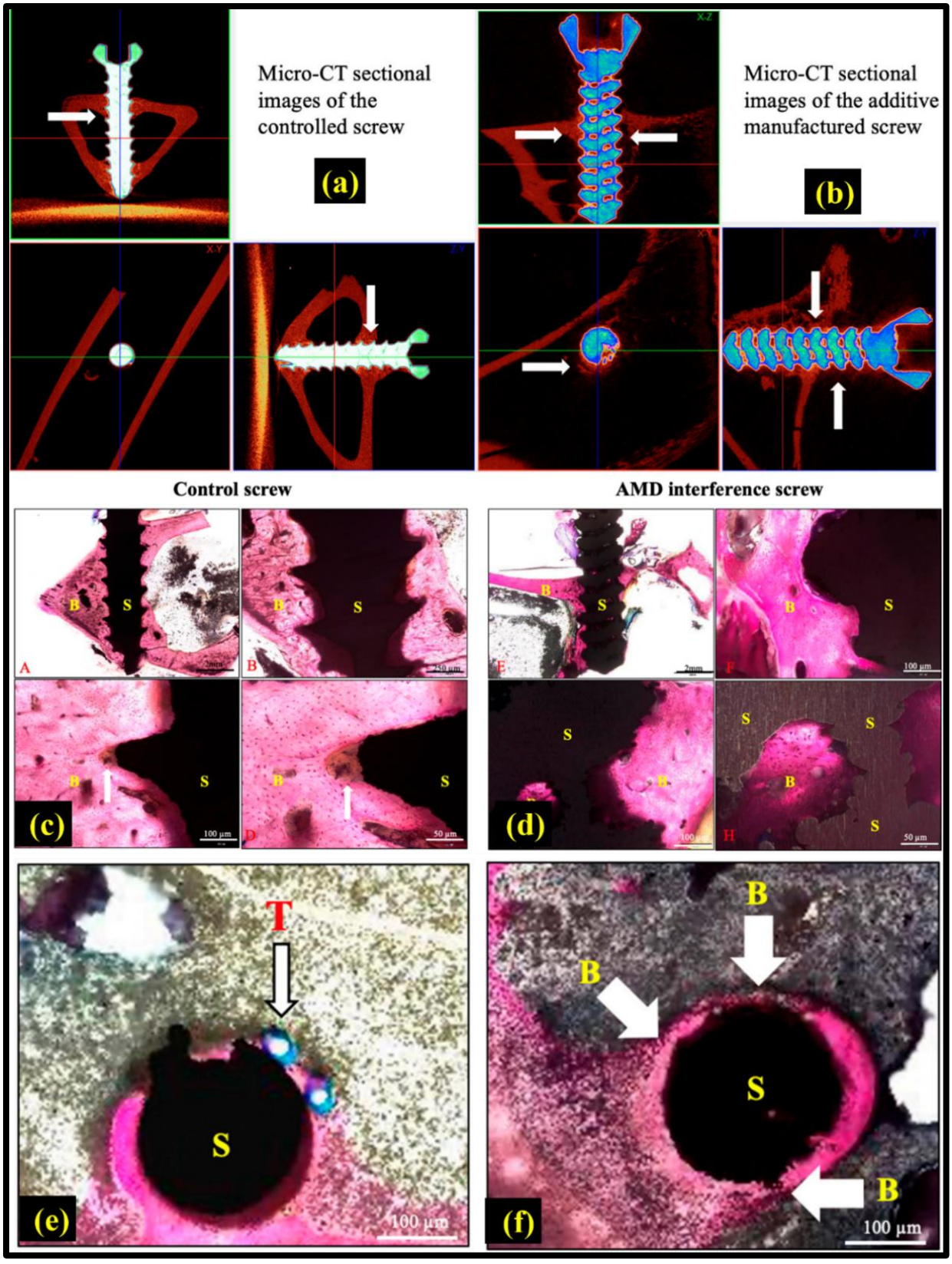


Figure 2.4: Micro-CT images of the (a) controlled screw, (b) 3D-printed bone screw; histological analysis of (c) control screw, (d) 3D-printed screw, 6-month specimens for bone formation evaluation of (e) control screw, (f) 3D-printed screw; B: bone, S: screw ***[no permission is required according to the journal policy*** [36]***].***

The analytical data charts for evaluation of bone volume fraction, bone surface density, on-growth and ingrowth bone volume fraction of the control screw and 3D-printed screw are illustrated in Figure 2.5. It was witnessed that the 3D-printed interference screw has significantly higher bone volume fraction, surface density, and ingrowth bone volume fraction as compared to the controlled bone screw as presented in Figure 2.5. Therefore, the 3D-printed bone screw is preferred over the control screw. As 3D-printed screws have the potential for surface modification, design customization, and patient-specific screw over the conventional screw.

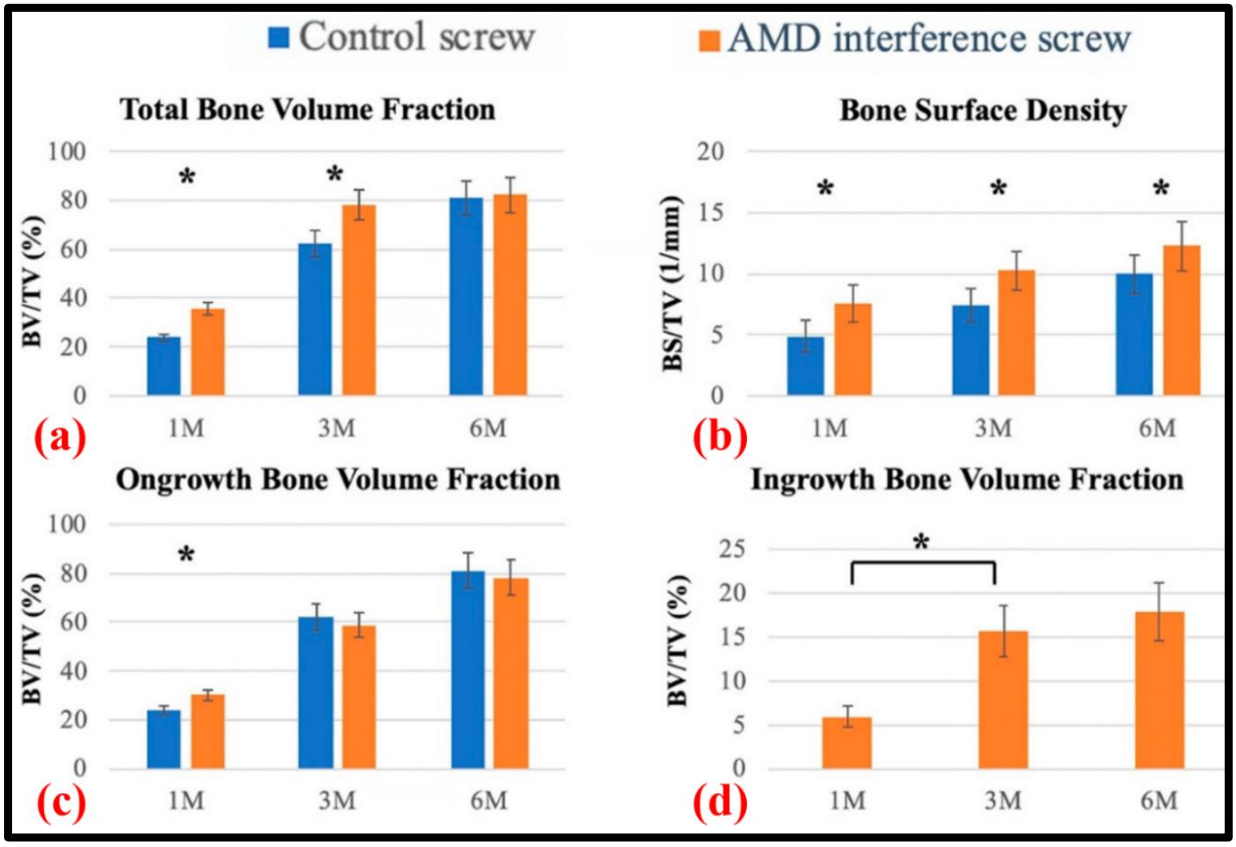


Figure 2.5: Comparison of control screw and 3D-printed screw in rabbit animal for (a) total bone-volume fraction, (b) bone surface density, (c) on-growth bone volume fraction, (d) in-growth bone volume fraction *[no permission is required according to the journal policy* [36]*].*

2.3.1.4 Comparing different metal 3D-printing techniques.

Metal-based 3D-printing techniques for the fabrication of orthopaedic implants, including bone screws, are the new era of research trends of the present generation. Most metal-based 3D-printing techniques use powder bed fusion technology that employs either a laser or electron beam to fuse the metallic powder into a solid model. Literature reports the maximum utilization

of titanium as a promising metallic biomaterial for orthopaedic bone screw fabrication using different metallic 3D-printing techniques. The most used metallic 3D-printing techniques are electron beam melting, selective laser melting and direct metal laser sintering. Table 2.4 provides a concise summary and comparison of different metal-based 3D-printing techniques used in the biomedical domain to fabricate metallic orthopaedic implants (bone screws). The comparative summary of different metal-based AM techniques is helpful for other researchers, medical practitioners, and professionals to select the suitable 3D-printing technique based on their choice of material, resolution, part size and application.

Table 2.4: A comparison of metal-based 3D printing technology.

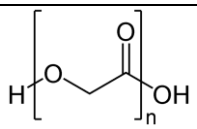
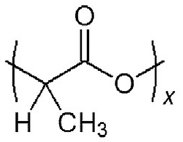
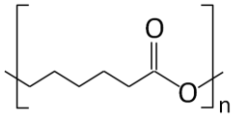
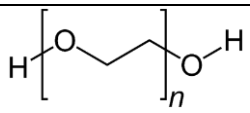
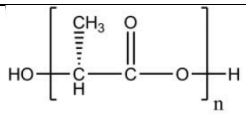
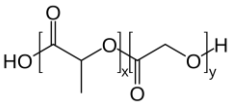
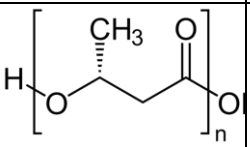
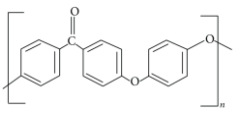
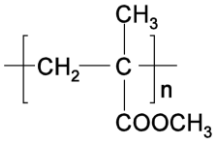
3D-printing Technique	Biomaterial Usage	Processing Parameters	Advantages	Limitations
SLM	Ti alloys	Powder size (10–45μm)	Complex lattice structure fabrication with ease	The conduction and diffusion of laser heat originate from the unwanted fusion of neighbouring powder particles and limit the resolution of final features.
	Stainless steel	Laser sintering (intensity 100 W-1 kW)	Customized design with high accuracy	
	Aluminium, Copper	Layer thickness (30–90μm)	Diversity of printable metallic biomaterials	
	Ni-Ti alloy	Scanning strategy (unidirectional or bidirectional)	No requirement for support	Porous lattice structures require a post-printing process
	Cobalt-chromium	Nd-YAG laser (1.064μm)/fiber -laser (1.09μm)	High utilization (unsintered powder can be reused and removed)	Acute size restrictions
	Ferrous alloy			
	Magnesium, zinc, tungsten	An inert environment	Good surface integrity	Expensive
EBM	Ti alloys	High vacuum (1× 10-4 Torr)	Range of printable metallic biomaterials	Slightly lesser accuracy compared to SLM
	Cobalt-chromium	Layer thickness (50–100μm)	High accuracy (tolerance ± 0.2mm)	Expensive powder materials

	Stainless steel	Freedom of size of build part (350 x 350 x 380mm^3)	Low risk of deformation with decent mechanical strength	The cost of the printing process is significantly higher
	Bulk metallic glass	Scanning strategy (unidirectional or bidirectional)	The un-sintered powder can be recycled (High utilization)	Porous structures require the post-processing of fabricated parts
	Inconel, copper		High-quality metal parts with tuneable strength and density	
DMLS	Aluminium, Copper	High-power laser (intensity 200 W-1000 W)	Range of printable metallic biomaterials	A fine range of layer thickness
	Ti alloys	Layer thickness (20–50μm)	Low level of internal defects	Costly process
	Cobalt-chromium	Feature size (250mm×250mm×300mm)	Strong mechanical strength	The quality of parts varies depending on resolution and material
	316L Stainless steel		Complex structures with intricate detailing	
	Inconel	High accuracy (tolerance limit ± 0.1-0.2mm)	High quality with great accuracy and detailed metal parts	Post-processing required for fabricated parts

2.3.2 Polymeric biomaterials

Polymers are highly considered biomaterials for implant fabrication due to their superb processability and are the first material to be used by 3D-printing techniques. Polymers consist of the replication of multiple units of a basic sequence (monomer). They are divided into two categories: natural and synthetic polymers. Natural polymers like collagen, chitosan, cellulose, and starch have been studied for different applications in modern medicine [79, 80]. Synthetic polymers are widely reported for biomedical applications because of their thermomechanical and chemical properties. Various polymeric biomaterials used for biomedical applications have different chemical structures, diverse degradation time intervals, specific thermal and mechanical properties as depicted in Table 2.5 [81–93]. These polymers can be used orthopaedic applications as implant material for fabrication of orthopaedic implants and bone screws.

Table 2.5: Specifications of various polymers used in orthopaedic screw fabrication.

Material	Chemical structure*	Melting point (^{0}C)	Density (g cm^{-3})	Glass transit temperature (^{0}C)	Ultimate tensile strength (MPa)	Tensile modulus (GPa)	Degradation time
PGA		220-230	1.53	34-40	57	6-7	6-12 months
PLA		170-180	1.210-1.430	55-60	53	3.5	2-5 years
PCL		59-64	1.11-1.15	-60	10.5-16.1	0.4	>2-3 years
PEG		62.2	1.12	-63	61	2	>1 year
PLLA		170-180	1.25	60	61-70	3.6	24 months
PLGA		240-280	1.3	37	4.3-12.9	1.31	5-6 months
PHB		170-180	1.25	5-14.85	40	3.5	1 month
PEEK		343	1.31	143	110	4.5	-
PMMA		160	1.18-1.2	110	71	1.7	-

* x, y, n indicates the number of times each unit repeats.

Polymethylmethacrylate (PMMA) as bone cement for prosthesis fixation is widely used as a void filler [94]. Synthetic polymers like Polyether-ether-ketone (PEEK) have similar mechanical properties to the bone, excellent radiolucency, and chemical resistance [95, 96]. Polycaprolactone (PCL) [39, 97], polylactic acid (PLA) [31, 73, 96, 98], poly-l-lactic acid (PLLA) [31, 57, 73, 96, 97] and polyglycolic acid (PGA) [98–101] are the most used synthetic polymer in the field of orthopaedic as biodegradable materials. Various other polymers like polyethylene glycol (PEG), poly lactic-glycolic acid (PLGA), poly hydroxyl-butyrate (PHB), and polypropylene fumarate (PPF) are used in the orthopaedic and dental field for fabricating the scaffolds, vascular tissues, and hydrogels [87, 96, 102, 103]. Figure 2.6 provides a recent development in biodegradable (polymeric) implants fabricated with the help of the 3D-printing technique. However, future research can explore other biodegradable polymers with 3D-printing technology for orthopaedic bone screw fabrication. There are various 3D-printing techniques used for polymeric parts as discussed in the further section.

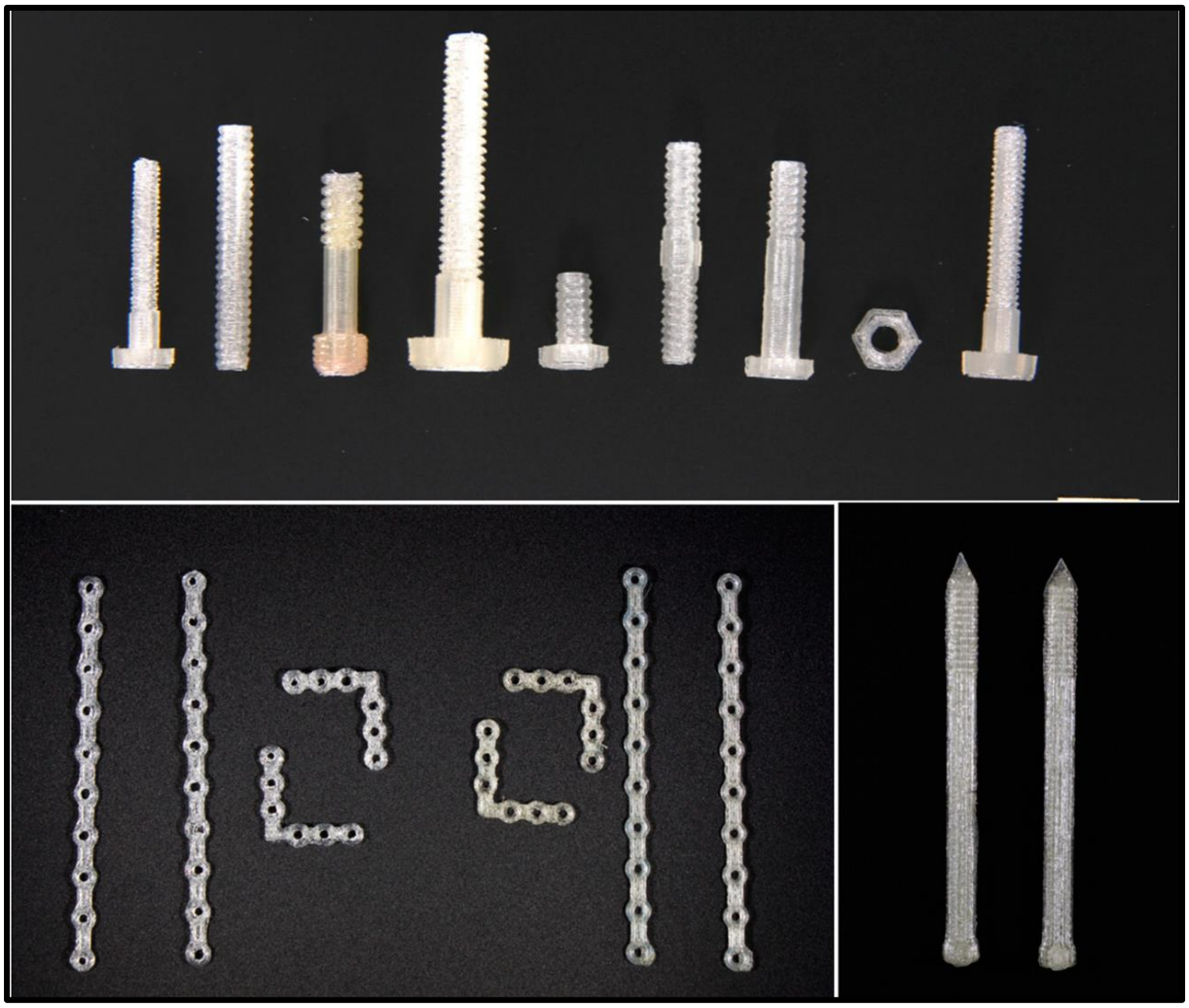


Figure 2.6: 3D-printed biodegradable implants (screws, pins, plates) using PLA biomaterial *[no permission is required according to the journal policy* [40]***].***

2.3.2.1. Stereolithography (SLA) technique

SLA was the first 3D-printing process to be theorized and was developed in the late 1980s. SLA uses a photopolymer resin with a thin layer that a UV laser can cure [55]. The resin solidifies into a single two-dimensional layer of the CAD model. After every layer is cured, the platform moves down in the bottom-up approach with the attached cured structure and other layers of uncured resin spread over the top for solidification [104]. After building the model, the non-polymerized liquid resin can be collected and reused by draining. Draining helps in the removal of liquid non-polymerized resin after building the structure. The kinetics of curing reactions is a critical area that affects layer thickness polymerized and curing time. This can be controlled with the help of scanning speed, light source power, amount of monomer and chemistry present within the monomers. Apart from this, the depth of polymerization can be controlled by the addition of UV absorbers.

The advantages of this fast fabrication process of SLA technology are creating complex shapes with auxetic internal structure, the comfort of abstraction of unpolymerized resin, functional prototyping, patterns, and high-resolution part (~0.2 µm) with accuracy **[**[105]. The drawback of SLA technology is that photo-polymerized resin with poor mechanical properties essentially is provided for tissue engineering. Comprehensive support structure removal may be difficult.

2.3.2.2. Selective laser sintering (SLS) technique

In the process of SLS, a laser source with high power is used for the fusion of small metallic, ceramic, and thermoplastic particles or glass powders [55]. The surface of polymer powdered particles is scanned by laser in a two-dimensional pattern for heating of powder above the glass transition temperature. After the deposition of every layer, the bed is lowered and a fresh layer of powdered material is deposited over the top surface [55]. The un-sintered, unbound, loose powder works as a support material removed after the part is completed. In practice, due to the single melting point of all powder, the melting is relatively easy to achieve, with the detailed resolution, no extra support is required as the powder work as the support material [106, 107]. Materials for the SLS process are limited to thermoplastic polymers [56]. The incredible resolution of features is determined by the particle size of the powder, the diameter of a focused laser beam, and heat transfer in the powder bed. Moreover, fast sintering and poor spreading of powder may cause edge inaccuracies. The porosity in models fabricated with SLS technology is limited as the particle size of the powder may vary the size of pores in the model.

The drawback of too small particles of powder material may result in poor spreading and can also cause powder clumping [56].

The surface of powdered particles is scanned by laser to sinter by heating them above the glass transition temperature. After the deposition of one layer, the piston with the fabricated part is lowered and fresh powdered material is rolled across the surface [55]. This leads to the formation of a subsequent layer strongly bonded to the previous layer. The particle size of the powder, heat transfer on the powdered bed and diameter of the focused laser beam plays an important role in determining the resolution of features of this process. Quick sintering and poor spreading of powder results in edge inaccuracies. However, this process cannot be used for materials with a smaller pore size as created pores highly depend on powder particle size. Poor spreading from the clumping of powder is another reason for limiting powder particles to a large size.

2.3.2.3. Polyjet 3D printing technique

Polyjet technology works similarly to traditional inkjet printing. A carriage with four or more inkjet heads deposits tiny droplets of photopolymer in a liquid state on the build tray and ultraviolet (UV) lamp that solidifies the material [108]. Multiple jetting heads allow different materials (too in multi-colour format) to be ejected at the same time enabling this technology to produce the object with various levels of flexibility [55, 109]. With a minimum wall thickness of 1mm, microscopic layer resolution of 16 microns (0.016 mm), and accuracy up to 0.1-0.3 mm can be obtained [105]. The polyjet 3D printer offers polished, smooth surfaces, exceptionally detailed and precise prototypes using the broadest range of materials with accuracy, precision, and excellent detailing [104]. This technology can achieve complex geometries, delicate features, and intricate details. The main part of this technology is the usage of the widest variety of colours and materials in an individual model. An essential application of polyjet 3D printers is in the healthcare sector which enables surgeons to produce a replica of organs that need to be replaced. Prosthetic limbs, joint replacement, and customized implant fabrication are the potential of this technology. The process can produce structures with complicated geometries and thin walls such as implant models, realistic teeth, and maxillofacial models with excellent accuracy, detailing and precision.

The polyjet 3D printer offers polished, smooth surfaces, and exceptionally detailed prototypes that can convey the aesthetics of the final product. It helps in the manufacturing of

fixtures, jigs and tools with high accuracy. This technology can fabricate highly complex shapes with delicate features and intricate details. The technique holds the primary feature of the usage of a variety of materials and colours into a single model with high efficiency.

2.3.2.4. Fused deposition modelling (FDM) technique

FDM or fused filament fabrication technology works by extruding a thermoplastic polymer through a heated extrusion head that heats the polymer to a semi-molten state and immediately bonds to the laydown pattern on a build stage [110, 111]. Two nozzles are used for the deposition of thermoplastic polymer into a semi-liquid state [112]. The layers are fused to build the part in a layer-by-layer style [113]. The material must have a low melting temperature, heat transfer characteristics, and rheology for FDM material selection criteria [114–116]. This technology can produce high porosity models due to the laydown pattern [117]. This technology is the most affordable, cost-effective, and budget-friendly 3D printing technology for fabrication of complex structures [118]. The laydown pattern providing high porosity along with good mechanical properties distinguishes FDM from other processes [119, 120]. However, this process is limited to thermoplastic materials possessing viscosity that is low for the extrusion process and high enough for structure building [121]. FDM is not limited to the geometrical complexity of structures using industrial materials with optimal thermal and rheological properties [122, 123].

The FDM technology can be used as most budget-friendly, easy to use 3D printing technology for fabrication of orthopaedic implants and instruments. **Dhandapani et al.** [31] used PLA polymer to fabricate porous biodegradable cortical screws using FDM-based 3D printing technology. The CAD model with dimensions (Figure 2.7(a)), STL file (Figure 2.7(b), printed screw (Figure 2.7(c)), and micrographs of the cortical screw are presented in Figure 2.7(d-g), respectively. PLA screw incubated in simulated body fluid solution shows osteoblast-like cells in the form of calcium. PLA-based solid and porous screws were implanted in rats to observe mineralization and vascularization. Micro CT sections determine the porosity of screws as shown in Figure 2.7(h-k) respectively. The weight loss was higher in the porous screw than the solid screw when preserved in simulated body fluid, as shown in Figure 2.7(i) and Figure 2.7(m). These screws were inserted in rats to observe the in-vivo behaviour via histopathological analysis. The results of histopathological examination witnessed that porous screws have higher neovascularisation and low immunogenicity around the screw compared to non-porous screws, as presented in Figure 2.7(n) and Figure 2.7(o).

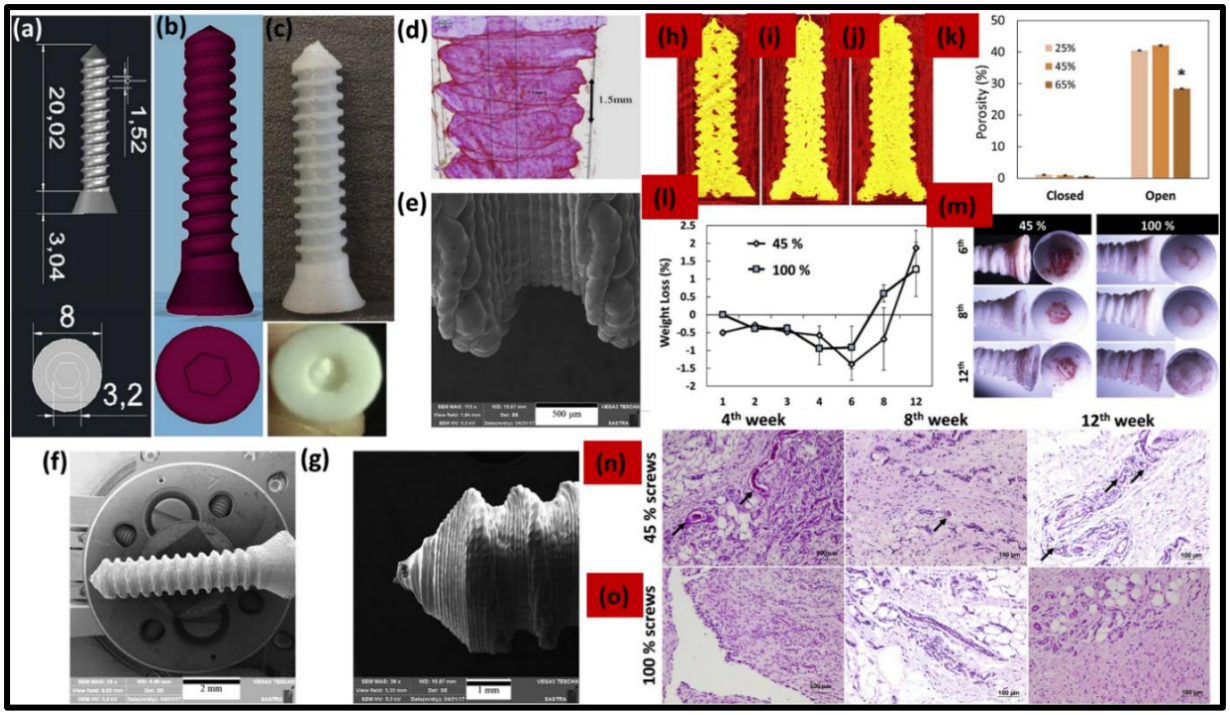


Figure 2.7: (a) CAD design of cortical screw, (b) STL file, (c) 3D printed screw, (d & e) pitch length measurement, (f & g) uniform layers of the screw, fill density of (h) 25%, (i) 45%, (j) 65%, (k) pore distribution, (l) biodegrading profiles of porous and solid screws, (m) alizarin red-stained screw, histopathological of tissue surrounding of (n) porous screw, (o) solid screw *[no permission is required according to the journal policy* [31]*].*

2.3.2.5. Comparing different polymeric 3D-printing techniques

Polymer-based 3D-printing techniques for the fabrication of orthopaedic bone screws are the new era of research trends of the present generation. Literature reports maximum utilization of PLA as a promising polymeric biomaterial using FDM-based 3D-printing technology. A comparison of polymer-based 3D-printing technologies is presented in Table 2.6. It was elucidated from Table 2.6 that FDM-based 3D printing technology has various advantages over other polymeric-based 3D-printing techniques. FDM is one of the most adequate, precise, and cost-effective 3D-printing technology used to fabricate biomedical prototypes. **Dhandapani et al.** [31] fabricated porous biodegradable cortical screws using FDM-based 3D printing technology. PLA screw incubated in simulated body fluid solution shows osteoblast-like cells in the form of calcium. PLA-based solid and porous screws were implanted in rats to observe mineralization and vascularization. It was observed that PLA porous screws fabricated by 3D printing technology show higher human mesenchymal stem cell adhesion, mineralized matrix synthesis, and enhanced mineralization than solid PLA screws.

Table 2.6: A comparison of polymer-based 3D printing technology.

Observation	Polyjet technology	FDM technology	SLA technology	SLS technology	Reason
Operations					
Type	UV cured extrusion	Material extrusion	Vat polymerization	Powder bed fusion	The operation techniques of various polymer-based 3D printing technologies use different binding strategies to fabricate the final product from the 3D cad model.
Process Time	↑↑↑	↑↑	↑↑	↑↑	
Pre-process	↑↑	↑↑↑	↑↑	↑	
Post-process	↑↑↑	↑↑↑	↑↑	↑↑↑	
Office Environment	↑↑↑	↑↑↑	↑↑↑	↑↑↑	
Ease of Use	↑↑↑	↑↑↑↑	↑↑↑	↑↑↑↑	
Parameters					
Layer thickness (mm)	0.1-0.3	0.05-0.127	0.05-0.015	0.05-0.01	Every technique has its concept of fabrication that is limited to various input parameters and binding volumes.
Minimum wall thickness (mm)	1	1	5	0.8	
Build volume (mm)	294x192x148.6	1000x1000x1000	1500x650x550	550x550x750	
Support	Required	Required	Required	Not required	
Characteristics					
Surface Finish	↑↑↑	↑↑↑	↑↑↑↑	↑↑↑↑	The characteristics of various techniques have different outputs
Feature Detail	↑↑↑	↑	↑↑↑↑	↑↑↑	
Accuracy	↑↑	↑↑↑	↑↑↑↑	↑↑↑	

Size	↑	↑↑↑	↑↑↑↑	↑↑	based on their usage and cost.
Cost	↑↑	↑	↑↑	↑↑↑	
Materials					
Rigid	↑↑↑	↑↑↑	↑↑↑	↑↑↑	Different techniques consume different materials (may use different colours as well) based on the application of usage.
Flexible	↑↑↑	↑	↑	↑	
Durable	↑↑	↑↑↑	↑↑↑↑	↑↑↑	
Transparent	↑↑↑	↑	↑	↑↑	
High-performance	↑↑	↑↑↑	↑↑↑↑	↑↑↑↑	

As the PLA polymer has lesser mechanical strength, **Suryavanshi et al.** [39] used composite biomaterial (PCL-MgO-silk fiber) to fabricate biodegradable bone screws to apply bone-soft tissue fixation. These composite bone screws were implanted in rats to monitor cell viability and tissue adhesion. It was witnessed that composite biomaterial has excellent cell viability, tissue adhesion and hemocompatibility. The MgO nanoparticles contribute to enhancing the tensile strength of the bone screw, whereas silk fiber provides higher stability, modulus and imparts a synergistic effect on the mechanical performance of the bone screw. **Singh et al.** [124] enhanced the shear strength and morphological features of PLA material, by 3D printing almond skin powder-reinforced matrix of PLA biomaterial. The various depth of insertion of the cancellous screw was observed in different infill patterns. It was witnessed that the honeycomb printing infill pattern and 100% insertion of the cancellous screw have maximum shear strength.

2.4 Summary

The recent advancement in 3D printing technologies for the fabrication of orthopaedic bone screws has been progressively advancing and evolving. The advantages of 3D-printed orthopaedic bone screws over conventional bone screws have been monitored based on bone growth, biodegradability, bone-implant contact, pullout strength, tensile stiffness, bone surface density and bone volume fraction in the literature.

Insufficient fixation strength and less holding power of cortical screw is the reason for implant failure. The strength of screw pull-out can result in loss of reduction, mal-union and non-union. Pull-out strength majorly depends upon the quality and shear strength of the bone,

the major diameter of the screw, the length of thread engagement, the method of drilling of bone, microcracks present during drilling and higher insertion torque. Screw loosening and screw migration including cut-out, pull-out, cut-through, back-out and screw breakage are the major bone screw problems faced by an orthopaedic surgeon. Also, gripping strength, fusion rate, future vertebral fractures, neurological, infection, and reoperation to remove the screw are other drawbacks of orthopaedic bone screws.

Recently, fast-rapid growth has been observed in the 3D-printed biodegradable implants both in clinical and research usage, but still there exists the need for improvement. The search for suitable polymers for superior safety, biocompatibility, and bio-absorbance (degradability) with enough mechanical properties is ongoing. 3D printing technology is the game-changing and better alternative as compared to conventional manufacturing to fabricate orthopaedic implants as it allows easier fabrication, porous lattice structures, precise shapes and fine-tuning of topography.

It is possible to create custom-made patient-specific implants by using 3D modelling software and 3D printing technology that can design and print any complex structure using different materials such as polymers, ceramics and metals has allowed for the adaptation of this technology in biomedical applications [65]. These materials have specific mechanical and material properties, chemical and thermal properties, processing methods, cell-material interactions, and FDA approval [125]. However, most commonly bone screws are made of stainless steel, titanium alloys and cobalt alloys [52, 53].

2.5 Research gaps

The literature survey presented in the above sections revealed that most of the researchers studied the method of fabrication of screws and modification in the material of screws for better Osseo-integration of screws with the bone. Most of the research has been reported on basis of the absolute stability of screws, but very few studies have been reported on the relative stability or combined stability of cortical screws. Very few attempts have been made to measure the pull-out strength and insertion torque of the cortical screw at the bone-implant site. No attempt appears to be made up to the author's best knowledge where special screws based on the bone mass and density of bone for osteoporotic bone are designed. Therefore, it is planned to fabricate various cortical screws based on variations in their patterns and infill percentage for improving the pull-out strength, better contact and holding power of screw and reducing insertion torque of cortical screw. After analysing the literature gap, it can be concluded that:

- Majority of the research has been conducted on the material improvement and method of fabrication of cortical screws.
- No study is focused on the modification of cortical screw design based on bone mineral density, bone quality and bone mass available especially for osteoporotic bone.
- Research related to improving the biomechanical pull-out strength based on the cortical screw design and fabricating method is scantly reported in the literature.
- Studies related to variation in input parameters of 3D printing technology for cortical screw fabrication and its benefit are very scarcely reported.
- The role of artificial intelligence in predicting the pull-out strength of cortical screws is scantly reported in the literature.

2.6 Problem Formulation

According to a literature survey, the incidence of screw loosening of bone screws ranges from 0.6% to 11% and it might be even higher in osteoporotic spines [126]. It had been reported that the implant failure rate for the lower leg is around 2.1-7.1% [127] and it is even higher than the failure rate for the upper limbs because of the physiologic stress during locomotion.

Keeping in mind the literature gap and analysis, also due to the failure rate of cortical screws, the present dissertation is focused on "Investigations of 3D printed orthopaedic cortical bone screws to improve biomechanical pull strength".

2.7 Research Objectives

- To fabricate cortical bone screws using rapid prototyping technology.
- To optimize the process parameters during fabrication of cortical bone screw in view of maximizing the strength of screw using machine learning algorithms.
- To compare the pullout strength with conventional bone drilling and inclined bone drilling.
- To examine the histopathological analysis to observe the bone-screw interface.

Chapter III

Fabrication of orthopaedic cortical screws using 3D printing

Chapter 3

Fabrication of orthopaedic cortical screws using 3D printing

3.1 Introduction

The previous chapter [chapter 2nd] discussed complications caused by metallic orthopaedic bone screws like stress-shielding effect, screw loosening, screw migration, higher density difference, painful reoperation and revision surgery for screw extraction can be overcome with the bioabsorbable bone screws. 3D printing technology provides the ideal tailor-made solution for different orthopaedic applications [128]. This technology offers various merits and functionalities such as precision [122], ease of the process [73], less material wastage [57], personalization [129], degree of freedom [130], accuracy [131], biocompatibility [132], and customization [133] for the fabrication of complex structures used in biomedical applications. 3D printing technology is an innovative technique that has shown potential in several surgical innovations such as the fabrication of cost-effective orthopaedic screws. 3D printing technology can be used to fabricate customized patient-specific orthopaedic bone screws. Due to 3D printing technology's various advantages and benefits, it was used to fabricate orthopaedic cortical screws during the present work.

The present chapter discusses the design and fabrication of cortical screws using fused filament fabrication (FFF) based 3D printing technology. Polylactic acid (PLA) polymer was used for the fabrication of orthopaedic cortical screws. The influence of various process parameters like infill pattern, infill percentage, layer height, and wall thickness used during the fabrication of screws was observed on the mechanical strength of screws. The mechanical behaviour and fracture mechanism of different patterned cortical screws were observed based on compression testing and tensile testing of screws. Scanning electron microscopy (SEM) was used to observe the surface topographical features, fracture behaviour, and microstructure characterization of different patterned cortical screws. The post-yielding fracture mechanics of 3D-printed polymer-based orthopaedic cortical screws by various infill patterns were monitored. Based on the SEM micrographs, mechanical characterization of compression and tensile testing shows the propagation of stress, fractures and fatigue cracks at the bone screw interfaces. The details of fabrication set-up using FFF based 3D printing technology, process parameters, mechanical testing, SEM micrographs, microcracks, and fracture behaviour of 3D-printed screws have been discussed below.

3.2 Details of design and fabrication of cortical screws

3.2.1 Design of cortical screws

The cortical bone screw was designed in Creo parametric 7.0, with similar dimensions to commercially available stainless steel cortical screws. Specifications and parameters of the cortical screw are presented in Table 3.1. The dimensions of the screw computer-aided design (CAD) model are depicted in Figure 3.1(a). The stereolithographic file of the CAD model is imported in the Ultimaker Cura application for an X-ray view and slicing format as presented in Figure 3.1(b), (c). The FFF-based 3D printing technology was used to fabricate the cortical screws using a full touch screen single extrusion printer (Ultimaker 2+ Connect) with a build volume of 223x220x205 mm as depicted in Figure 3.1(d). Cam switch with an updated geared feeder exerts more force on the filament, reduces heat exposure from the motor and makes it easy to load and unload the filament, as shown in Figure 3.1(f). A nozzle diameter of 0.25 mm, nozzle temperature of 180-260 ^{0}C, build speed lesser than 24 mm^{3}/s, and nozzle heat-up time of less than 2 minutes is used to fabricate cortical bone screws.

Table 3.1: Specifications and parameters of the cortical screw.

Serial No.	Parameters	Specifications
1	Major diameter	4.5 mm
2	Minor diameter	3.5 mm
3	Head diameter	8 mm
4	Pitch	1.75 mm
5	Screw length	20 mm
6	Hexagonal socket depth	3.2 mm
7	Socket depth	3 mm

3.2.2. PLA polymer details

Polylactic acid (PLA) is broadly employed in the biomedical domain as an implant material due to its outstanding biocompatibility, high strength, excellent transparency biodegradability, and thermomechanical properties [134, 135]. PLA is a clinically approved polymer by Food and Drug Administration (FDA, USA) for various health applications like implantable devices [136–138]. Ultimaker PLA silver metallic filament (code-RAL9006) was chosen as it is safe, reliable, has incredible tensile stiffness with detailed surface quality and is easy to print at high printing speed. Ultimaker PLA biopolymer (filament diameter of 1.75 ± 0.03 mm, melting temperature of 145-160 ^{0}C) was used to fabricate cortical screws.

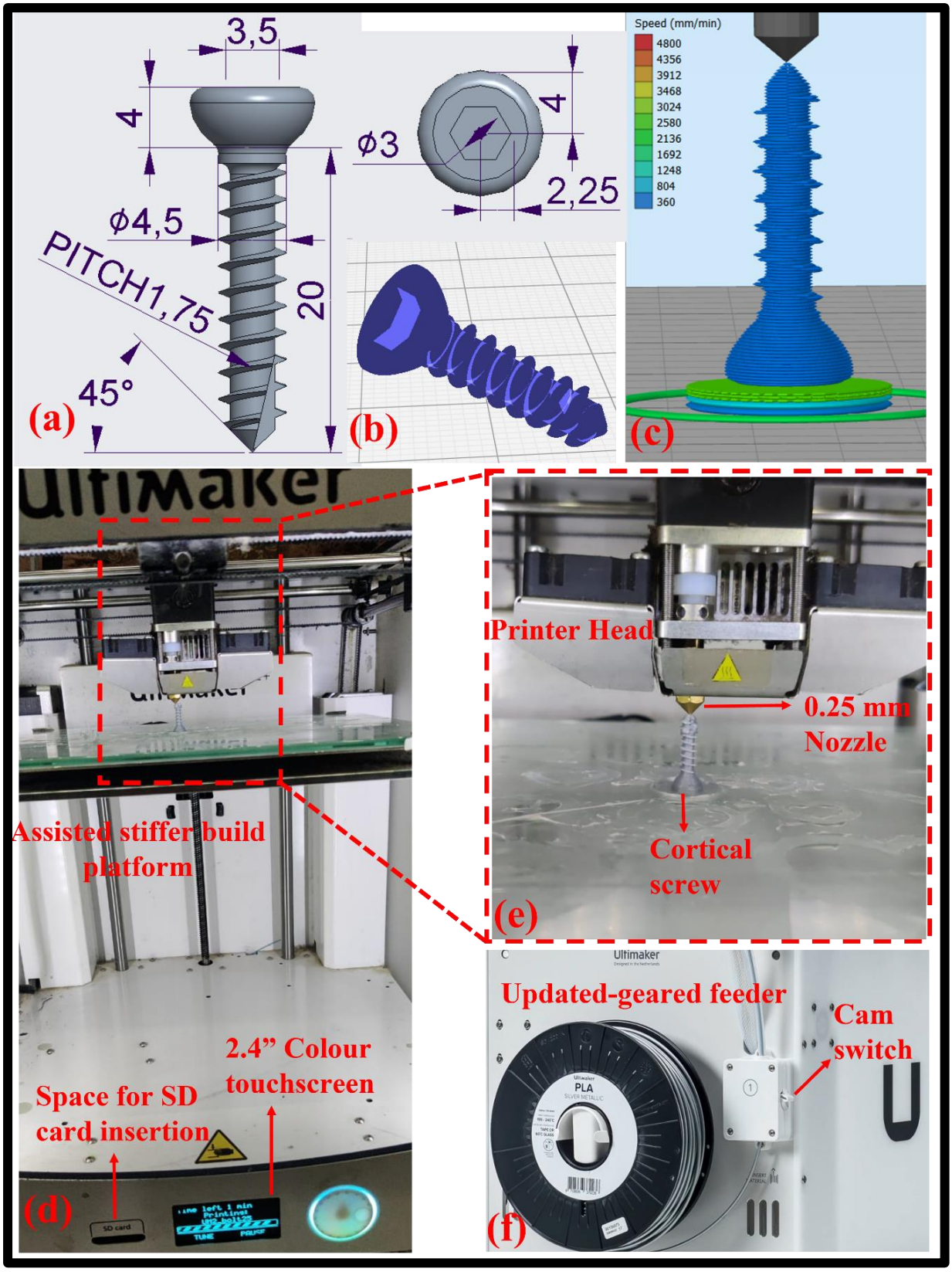
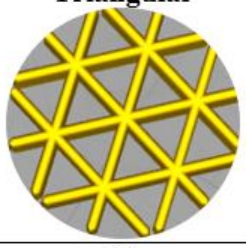
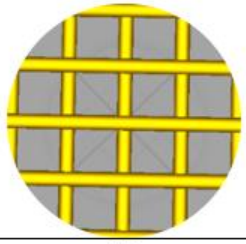
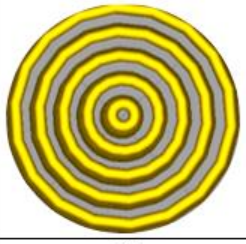
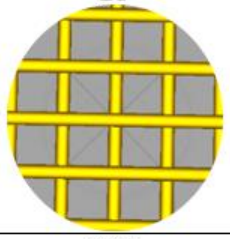
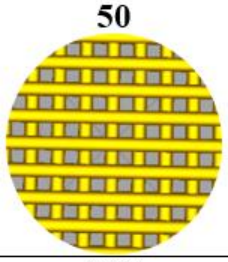
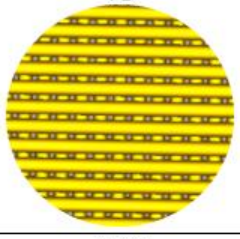
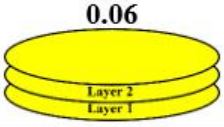
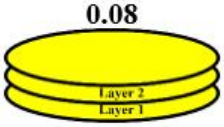
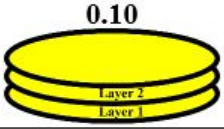
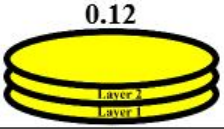
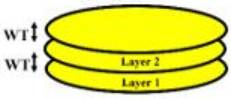
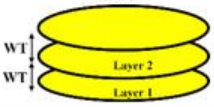
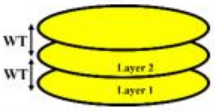


Figure 3.1: (a) CAD model of the cortical screw; (b) X-ray view in Ultimaker Cura; (c) Slicing format; (d) Single extrusion Ultimaker 2+ Connect printer; (e) Printer head with fabricated screw; (f) Ultimaker PLA silver metallic filament with cam switch and updated-geared feeder.

3.2.3. Experimental design and process parameters

The selection of process parameters has a vital role in fabricating bone screws. The process parameters used during the fabrication of bone screws must determine the strength of the screw to support the load-bearing fracture sites. The input process parameters have been selected based on the literature that has significant effects on the 3D-printed parts [31, 124, 139]. Four major process parameters were selected and varied up to four different levels, as presented in Table 3.2. The porosity of the bone screw is controlled by infill percentage (percentage of porous structure) and the filling pattern of the inside portion of the screw is controlled by infill pattern. Layer height is the height of the individual layer of the fabricated model. Wall thickness is provided to define the width of a single layer of the bone screw. These four process parameters are controlled by the servomotor as per the direction provided in the Ultimaker Cura software and contribute to building timing for the screw fabrication. To observe the influence of each process parameter separately, the single variable study was conducted where one process parameter was varied (keeping other parameters constant).

Table 3.2: Process parameters with various levels for experimental design.

Process parameters	Level 1	Level 2	Level 3	Level 4
Infill pattern	Triangular 	Grid 	Concentric 	Honeycomb 
Infill percentage (%)	25 	50 	75 	100 
Layer height (mm)	0.06 	0.08 	0.10 	0.12 
Wall thickness (mm)	0.25 	0.50 	0.75 	1 

3.2.4 Mechanical characterization

As 3D-printed cortical bone screws should have adequate mechanical strength for supporting load-bearing fracture sites. The mechanical strength of fabricated cortical screws was monitored based on mechanical characterization in terms of their tensile strength and compression strength. The failure mechanism and mechanical strength of 3D-printed cortical screws were monitored based on mechanical characterization, compression testing, and tensile testing of different 3D-printed bone screws. The compression testing of 3D-printed cortical screws is important as the major role of bone screws is to provide interfragmentary compression across the fractured bone site.

The compression testing of different cortical screws was performed using a universal testing machine (DAK system UTM-series 7200) at a constant deformation rate of 1.5 mm/min according to ASTMD-695 as presented in Figure 3.2. The red arrow indicates the axial load direction of 5 kN applied on the cross-section of the tip of the cortical screw during compression testing as depicted in Figure 3.2. The tensile testing of different patterned cortical screws was monitored following the ASTMD-638 standards. Data were monitored at a frequency of 20 Hz. The unconfined compressive strength and tensile strength of cortical screws were observed with high-speed microprocessor-based control in MPa and considered the final strength of cortical screws.

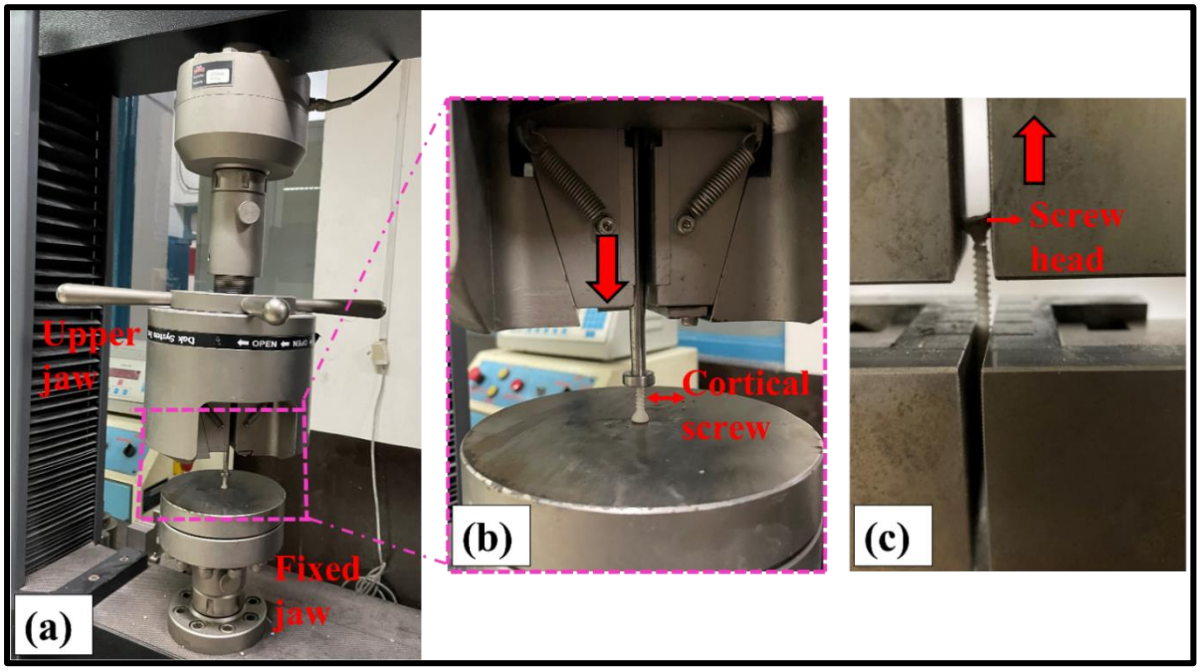


Figure 3.2. (a) Universal testing machine to monitor the (b) compression testing, and (c) tensile testing of 3D-printed cortical screws.

3.2.5 Microscopic fracture observation

The morphology, microstructure, and surface topographical feature of 3D-printed cortical screws were observed using scanning electron microscopy (SEM). The fractography was performed on tensile samples on Zeiss^{TM} Sigma 500 Field emission gun electron microscope. SEM analysis was performed at a high vacuum. To avoid charging, these samples were coated with gold using Gold Sputter Q150R PlusTM.

3.3. Results and discussion

3.3.1. Compression testing

The ASTMD-695 standard was followed for the compression testing of different 3D-printed cortical screws. The literature observed that strain rate and temperature are the leading cause of change in fracture mode from brittle to ductile [140]. Compression testing was done at room temperature as per the application of these cortical screws in the orthopaedics and biomedical domains. The influence of infill percentage, wall thickness, and layer height on the mechanical compressive strength of 3D-printed cortical screws was monitored as illustrated in Figure 3.3. It was observed that with an increase in infill percentage, the compressive strength of 3D-printed screw increases as depicted in Figure 3.3(a). This is due to an increase in material consumption during fabrication and a reduction in porosity. At 100% of the infill percentage the cortical screw is almost solid and with maximum compressive strength of 284MPa.

With increasing the wall thickness of the 3D-printed screw, the compressive strength of the screw increases as depicted in Figure 3.3(b). This is due to an increase in the number of layers with increasing the wall thickness of 3D-printed cortical screws. The variation in wall thickness from 0.25 mm to 1 mm, changes the compressive strength by 5%. The change in wall thickness does not influence the compressive strength of 3D-printed screw much.

The change in layer height varies the compressive strength of the 3D-printed cortical screw. As the layer height increases, the number of layers decreases that reducing the compressive strength of the cortical screw, as depicted in Figure 3.3(c). The increase in layer height increases the extrusion rate and void densities of the 3D-printed screw, which results in reducing the material consumption and weight of the screw. Hence, by increasing the layer height, the mechanical compressive strength of the 3D-printed cortical screw reduces.

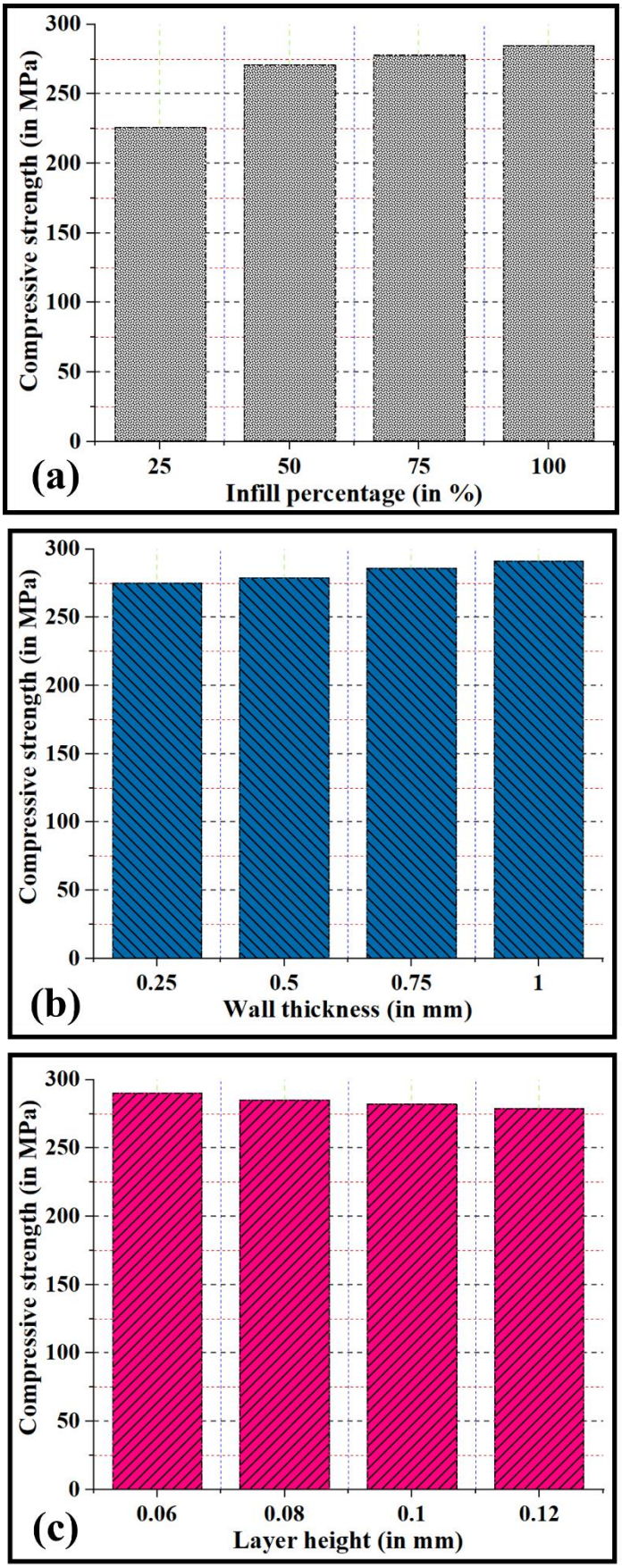


Figure 3.3: Influence of (a) infill percentage, (b) wall thickness, and (c) layer height on the compressive strength of 3D-printed cortical screws.

Different infill-patterned cortical screws were placed at the lower fixed jaw of the UTM machine, and the axial load was applied from the tip of the screw. The ultimate compressive strength of 3D-printed screws was calculated concerning the surface area of the cortical screw. The compressive strength was monitored as the highest peak value of the load graph for the maximum load-bearing capacity at the fractured site. The compressive strength of different patterned cortical screws is presented in Figure 3.4.

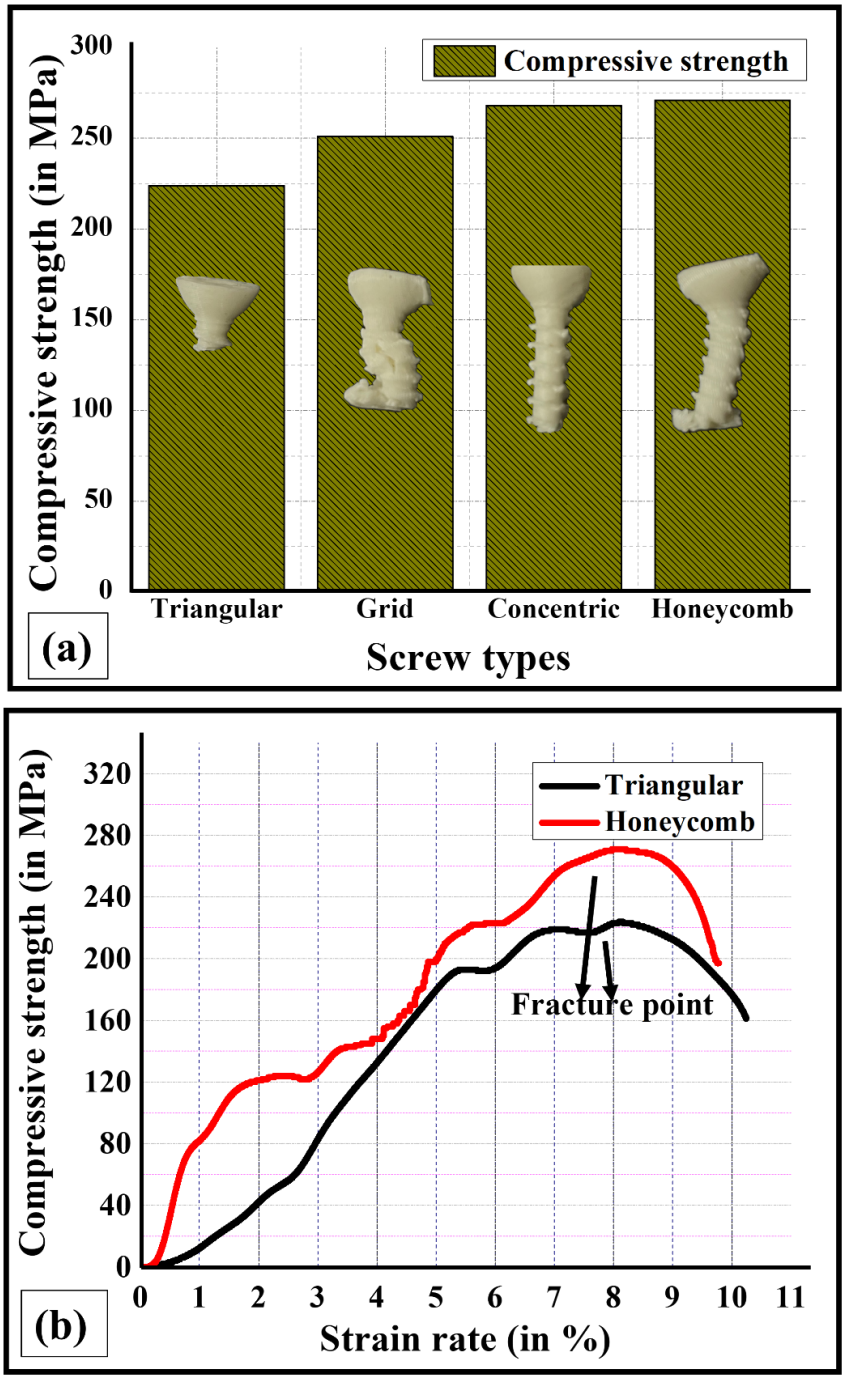


Figure 3.4: (a) Compressive strength of the different patterned 3D-printed screws, (b) compression testing of triangular and honeycomb structured cortical screws.

It was observed that the infill patterns significantly influence the compressive strength of 3D-printed cortical screws. The results revealed that the triangular pattern has a minor compressive strength of 224 MPa as compared to the grid (G), concentric (C) and honeycomb (H) with 251 MPa, 268 MPa and 271 MPa, respectively. The triangular (T) pattern possesses less molecular bonding between monomers of the respective layer due to the material packaging and the morphology of the triangular pattern. The grid and concentric patterned cortical screws have higher strength than the triangular pattern due to the higher number of layers and different patterned structures. Additionally, the morphology of the honeycomb-patterned cortical screw has the maximum compressive strength compared to other patterns of cortical screws. Hence, the honeycomb-patterned cortical screw is the most suitable and favoured infill pattern of cortical screws for maximum compressive strength of 3D-printed cortical screws.

3.3.2. Tensile testing

The ASTMD-638 standard was followed for the tensile testing of different patterned cortical screws as depicted in Figure 3.5. The experimental investigation of the tensile behaviour of cortical screws was done in the universal testing machine at room temperature. The mechanical response was based on the tensile testing of cortical screws; the uniaxial tensile test was conducted on different infill patterns of cortical screws. The maximum tensile strength of cortical screws was monitored as highest value of load graph and screw failure.

The tensile strength of different patterned cortical screws is presented in Figure 3.5. The tensile strength of the triangular cortical screw has a minor tensile strength of 114 MPa compared to the grid pattern of 138 MPa and the concentric pattern of 152 MPa. This is due to bonding strength between the correlated and nearby layers as compared to other patterns of cortical screws. The grid and concentric patterned screws have higher tensile strength than the triangular patterned screw and lower than the honeycomb-patterned screw. This is due to patterned morphology and molecular bonding between the layers. It was observed that the honeycomb pattern cortical screw has the highest tensile strength of 163 MPa compared to other cortical screws. This is because the honeycomb pattern cortical screw has higher bonding strength between the molecules and has a higher weight-to-area ratio that exhibits higher tensile strength than other patterned cortical screws. Therefore, honeycomb pattern cortical screws are preferred as the optimum infill pattern of cortical screws for maximum tensile strength of 3D-printed cortical bone screws.

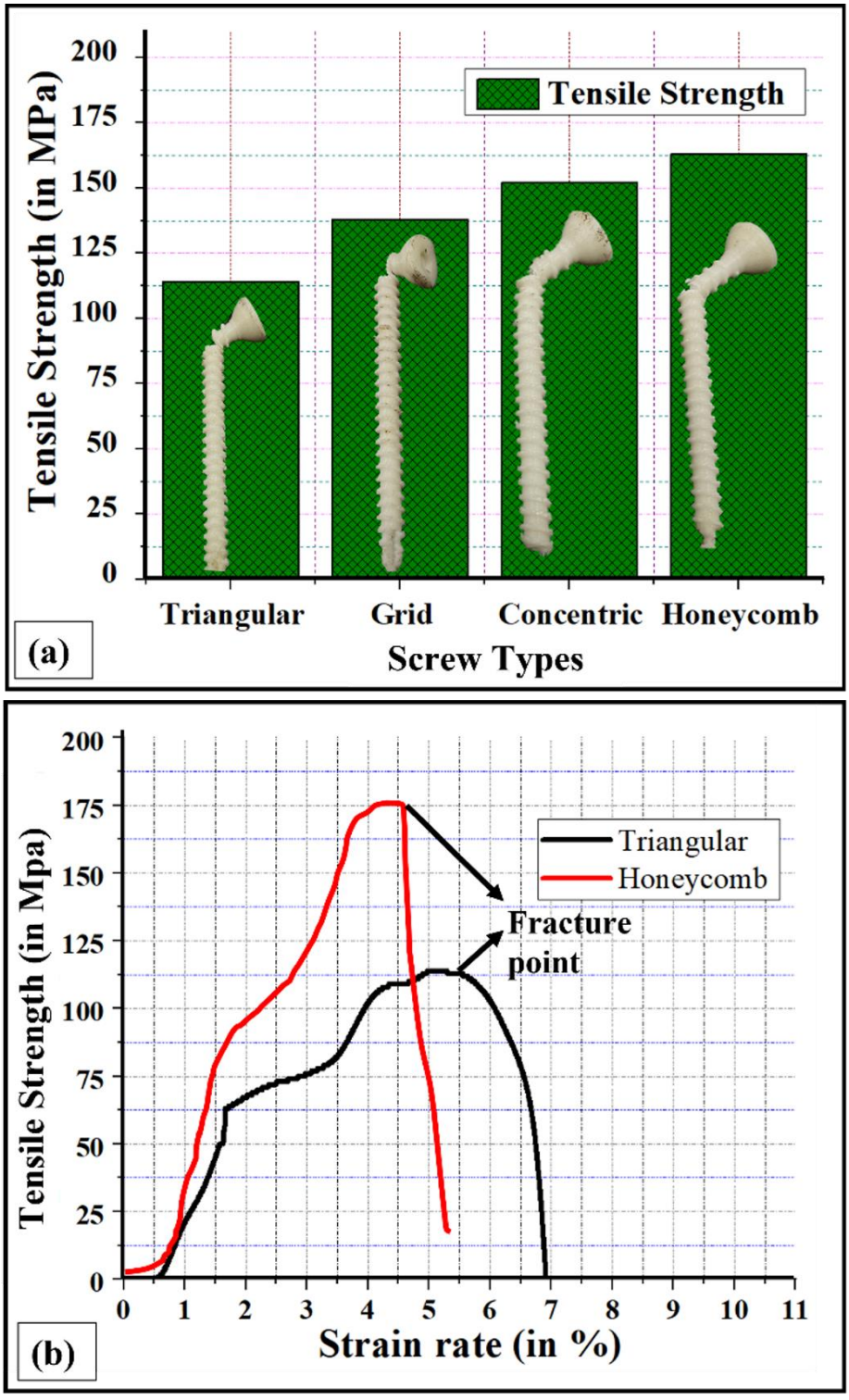


Figure 3.5: (a) Tensile strength of the different patterned 3D-printed screws, (b) tensile testing of triangular and honeycomb structured cortical screws.

3.3.3. Morphology of different patterned screws

The morphology and microstructure of different infill patterned cortical screws were observed at the microscopic level to understand the fractography and mechanism of failure of cortical

screws. The SEM micrographs of different patterned cortical screws show a similar structure with layer-by-layer addition of PLA polymer as depicted in Figure 3.6(a). The screw head, threads and screw body show similar structures as illustrated in Figure 3.6(b). Different patterns of 3D-printed cortical screws were also observed for microscopic observations. After the mechanical failure of different patterned screws, the micromorphology is expected to change as they have different filling patterns during the fabrication of the screws.

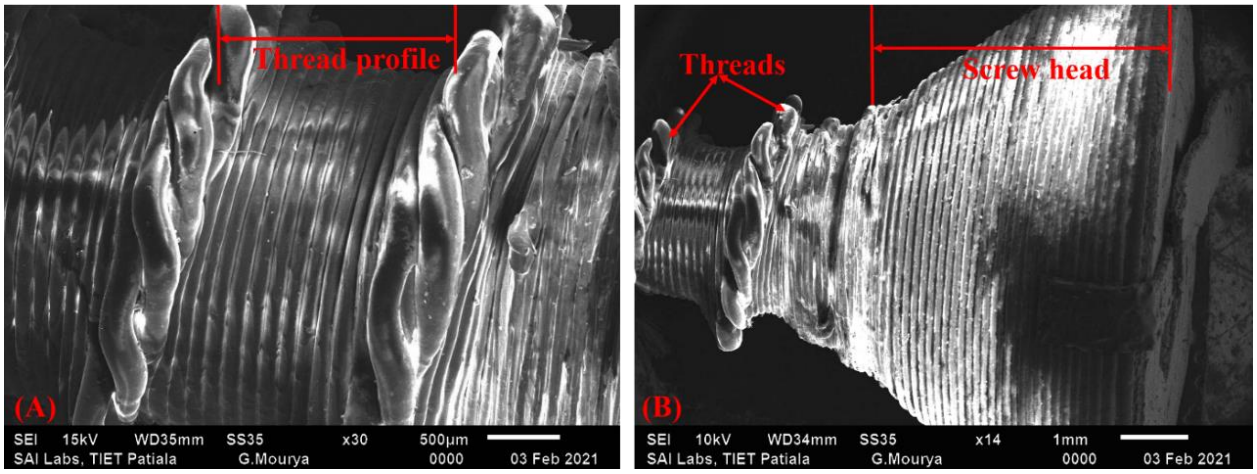


Figure 3.6: (a) Thread profile of 3D printed cortical screw, (b) layer by layer deposited PLA materials layers from screw head to threads.

It was observed that the mechanical (compressive and tensile) strength of cortical screws varies with the change in the infill pattern of cortical screws. The morphology and failure mechanism of the different patterned cortical screw is analysed at microscopic levels using scanning electron microscopy, as presented in Figure 3.7. The microstructure of different infill patterns of screws is magnified at the microscopic level from 500X to 1000K X of magnification and scale from 400µm to 200nm. Micrographs showed an appreciable difference in the morphology and microstructure of infill patterns of cortical screws. These micrographs are the primary reason for variation in the mechanical strength of different patterned cortical screws. The triangular-pattern cortical screw shows higher voids are present inside the consequent layers, as shown in Figure 3.7(a). This is the leading cause of lower mechanical strength during compression and tensile testing. The strength of the screw is inversely proportional to the voids of cortical screws. The grid-pattern cortical screw has higher strength than the triangular-pattern screw [Figure 3.4]. The higher compressive strength on grid-patterned screw is due to lower voids present on the consequent layers as compared to triangular-patterned screw as witnessed in Figure 3.7(b). Less microcracks and voids are the main reason for higher compressive strength in grid-patterned cortical screw.

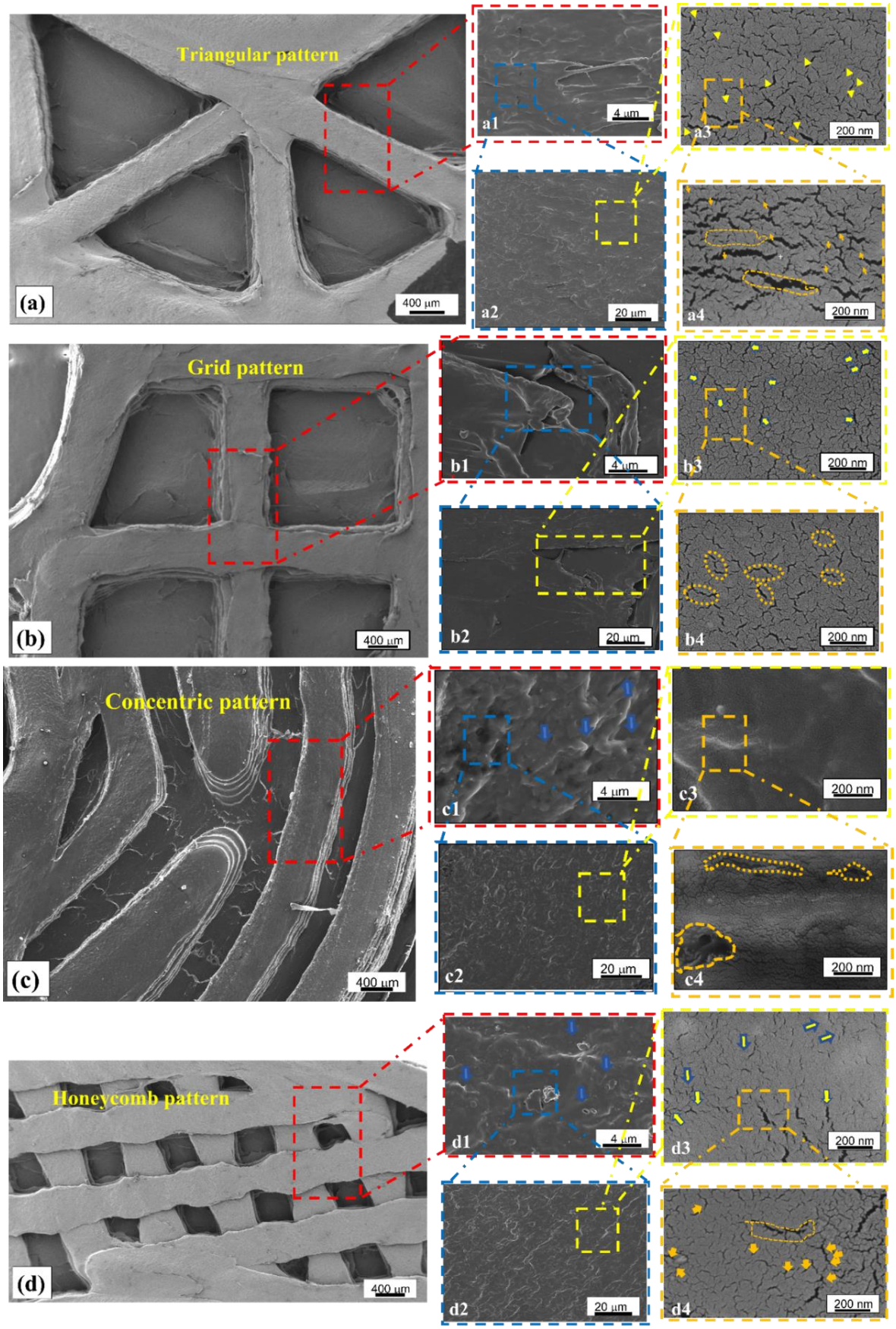


Figure 3.7: SEM micrographs and microstructure with the different magnification of different infill patterns of the cortical screws (a) triangular, (b) grid, (c) concentric, and (d) honeycomb.

The concentric pattern cortical screw has higher strength due to the lesser void present in the screw, as observed in Figure 3.7(c). The major reason for the strength of screws depends on the voids and defects present during the fabrication of cortical screws. The honeycomb pattern combines hexagonal cells with a high stiffness-to-weight ratio, relatively narrow cell structure, and cell length [141–143]. The honeycomb-patterned cortical screw (Figure 3.7(d)) depicts higher uniformity and smooth surface structure compared to other infill patterns of 3D-printed cortical screws due to the structural stability of the honeycomb pattern. It was also revealed that the strong bonding between the raster and microstructure, showed fewer flaws and voids in the honeycomb structure, as illustrated in Figure 3.7(d). The presence of large voids and porous for other patterns justifies the inferior mechanical properties of the other printed screws. Moreover, honeycomb cells increase the curve path due to their structure to promote mechanical strength.

3.3.4. Fractography of cortical screws

The microscopic images of the fracture surfaces of the screw are presented in Figure 3.8. The fracture behaviour of the cortical screw depends on the fabrication of the cortical screw. Two different fracture behaviour were identified: ductile to brittle after yielding.

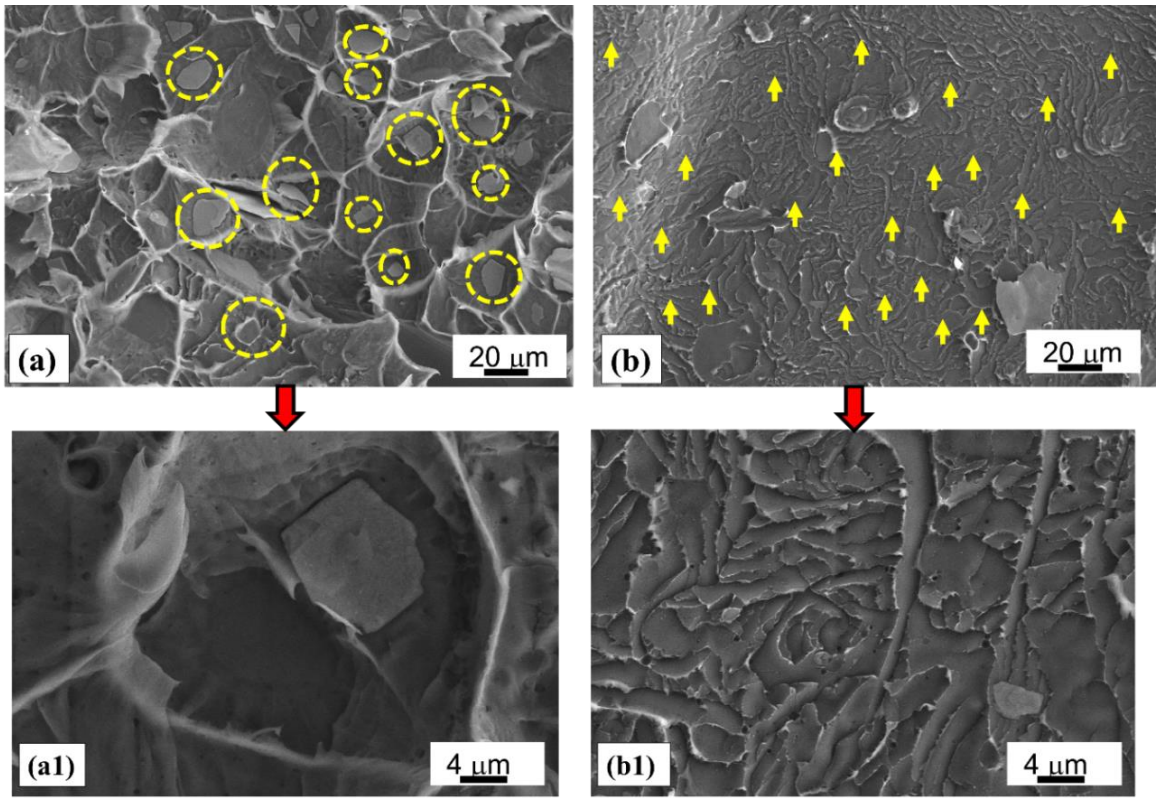


Figure 3.8: SEM Micrographs of the fracture surface of cortical screws (a) triangle-pattern, (b) honeycomb-pattern.

The fracture surface morphology revealed the presence of voids, indicating microscopic stress whitening in the specimen. Figure 3.8(a) showed more fraction of fracture patches which is also one of the types of evidence of ductile fracture. There was clear evidence of plastic yielding and stable crack propagation, as shown in Figure 3.8(a). These shreds of evidence were also observed in stress-strain data, in Figure 3.5(b). The honeycomb screw exhibits brittle failure as judged by the stress-strain curve shown in Figure 3.5 and the cracked feature of the broken specimen. The fracture surface showed typical signs of catastrophic failure through the number of crack planes, as shown in Figure 3.8(b), and this is clear evidence of brittle failure. Other than the honeycomb, all other samples showed different modes of failure. The change in different patterns of fabricated cortical screws caused a difference in the strength and fracture propagation model.

3.5 Conclusions

In this chapter, the orthopaedic cortical bone screws were fabricated using fused filament fabrication-based 3D-printed technology. The influence of various process parameters such as infill pattern, infill percentage, layer height and wall thickness used during the fabrication of cortical screws were observed on the mechanical behaviour, failure behaviour and microstructure was studied. Based on the experimental outcomes, the following conclusions have been made.

- The variation in infill pattern from triangular to honeycomb increases the mechanical compressive strength of the 3D-printed screw.
- The fracture mechanism of ductile to brittle fracture was observed with variation in the infill pattern of the bone screw.
- Honeycomb-structured cortical screws have approximately 17% higher compressive strength than the triangular patterned cortical screw due to higher bonding surface area and structural stability at the intercalated layers.
- The microscopic feature represents the initiation and deformation of the craze voids that grow in the crack and stretch more than the extension rate representing the molecular flexibility of 3D-printed cortical screws.
- An increase in infill percentage from 25% to 100%, increases the compressive strength due to an increase in material consumption and a reduction in porosity.
- With increasing the layer height decreases the mechanical compressive strength of the 3D-printed screw.

- As the layer height increases, the number of layers decreases that reducing the compressive strength of the cortical screw.
- With increasing the wall thickness increases the compressive strength of 3D-printed PLA cortical screws.

Chapter IV

Machine learning based approaches for predicting compressive strength and optimization of process parameters

Chapter 4

Machine learning based approaches for predicting compressive strength and optimization of process parameters

4.1 Introduction

In the last chapter, the cortical bone screws were fabricated using fused filament fabrication-based 3D printing technology. The influence of various input process parameters of 3D printer such as infill pattern, infill percentage, layer height, and wall thickness was observed on the mechanical strength of fabricated screws. It was found that with variations in process parameters, the mechanical strength of 3D-printed cortical screw varies. To ensure that bone screws can provide adequate support for load-bearing fracture sites, it is crucial to determine the optimal process parameters for fabrication. However, due to the numerous 3D printing fabricating parameters, assessing the mechanical strength of 3D-printed cortical screws is an intricate and time-consuming process. Thus, monitoring the mechanical strength of these screws can be challenging, especially when multiple experiments with varying process parameters are needed to determine their corresponding mechanical strength.

In this context, a data-driven machine learning (ML) approach can be a viable solution for predicting the mechanical strength of 3D-printed screws. To achieve this goal, it is essential to carefully select and optimize the process parameters for the 3D printer. Some of these parameters may not significantly affect the mechanical strength of the 3D-printed parts, so optimizing them is crucial to ensure the strength of 3D-printed screws.

Leveraging ML models can help optimize the process parameters and predict the mechanical strength of 3D-printed cortical screws. Further exploration of these models can maximize the strength of 3D-printed cortical bone screws for use in orthopaedic or trauma surgery to provide the necessary support and rigidity across load-bearing fracture sites. The application of ML models is extensively used in modern Industry 4.0 for predicting uncertainty and managing big data [144, 145]. The ML approach pertains to the utilization of statistical and computational tools for predicting data and establishing relationships between features. Previous studies have suggested that ML represents an intelligent approach capable of enhancing the performance of 3D-printing techniques and the fabricated parts [146, 147]. ML models are widely reported in 3D-printing applications for material properties prediction [148],

object recognition [149], optimization of topological designs [150] and process parameters [146]. As the base learners of ML models lack the robustness necessary to comprehend the intricate relationship between process parameters and output response, more sophisticated and intricate predictive models are required to enhance the predictive ability of these base learning ML models and better understand the inter-correlation between influential parameters of 3D printing techniques. Ensemble ML techniques can improve the robustness and efficacy of ML models. These techniques have been applied to various applications such as prediction, diagnosis, recognition, identification, classification, intrusion detection, and sentiment analysis [151, 152]. Therefore, a variety of base learning ML models and ensemble ML models were utilized to predict mechanical strength and optimize independent process parameters.

This chapter discusses the utilization of various base learning ML models, including support vector regression, k-nearest neighbors, decision trees, and random forest, to predict the mechanical compressive strength of 3D-printed cortical screws. These predictive ML models were developed using independent parameters such as infill percentage, layer height, infill pattern, and wall thickness. To understand the intricate relationship between the features of 3D printing technology, ensemble ML models (specifically XGBoost, AdaBoost, and GradientBoost) were also utilized and compared with base learning ML models. The effectiveness of different ML models was assessed using a range of error metrics. The predictive performance of these models serves as an indicator of their robustness.

4.2 Experimentation details

4.2.1 Fabrication procedure

The procedure followed for screw fabrication is illustrated in Figure 4.1. There are five steps involved starting CAD modelling, conversion, slicing, fabrication, and mechanical testing. In the first step, the CAD model was designed in Creo parametric 7.0 with dimensions similar to the standard 4.5 mm surgical orthopaedic stainless steel cortical screw. In the second step, the designed cortical screw was converted into a standard tessellation language (STL) file and imported into the Ultimaker Cura software. The third step involves the tessellation and slicing of the model which is then converted into G-Codes using slicing software. The fused deposition modelling technology was utilized for the fabrication of cortical screws as depicted in step 4. The PLA polymer was chosen due to its thermomechanical and biocompatible properties. An automated geared-based feeder was used to exert the PLA filament from the PLA spool for

effortless feeding of PLA filament to the nozzle for the extrusion process. Through the extrusion of PLA polymer, the cortical screws were fabricated in a layer-by-layer format by successive material layer deposition. In the field of orthopaedic surgery, bone screws are utilized to provide support and stability to fractured sites through interfragmentary compression. The mechanical compressive strength of these screws is an important factor in ensuring their stability and durability. To this end, it is critical that 3D-printed screws possess sufficient mechanical compressive strength to support the fractured site. In order to monitor the compressive strength of 3D-printed orthopaedic screws, a universal testing machine, specifically the DAK system UTM-series 7200, was used. This testing was conducted in stage 5 of Figure 4.1. Cortical screws were compressed, and the maximum value of compressive stress was identified as the ultimate compressive strength of 3D-printed screws.

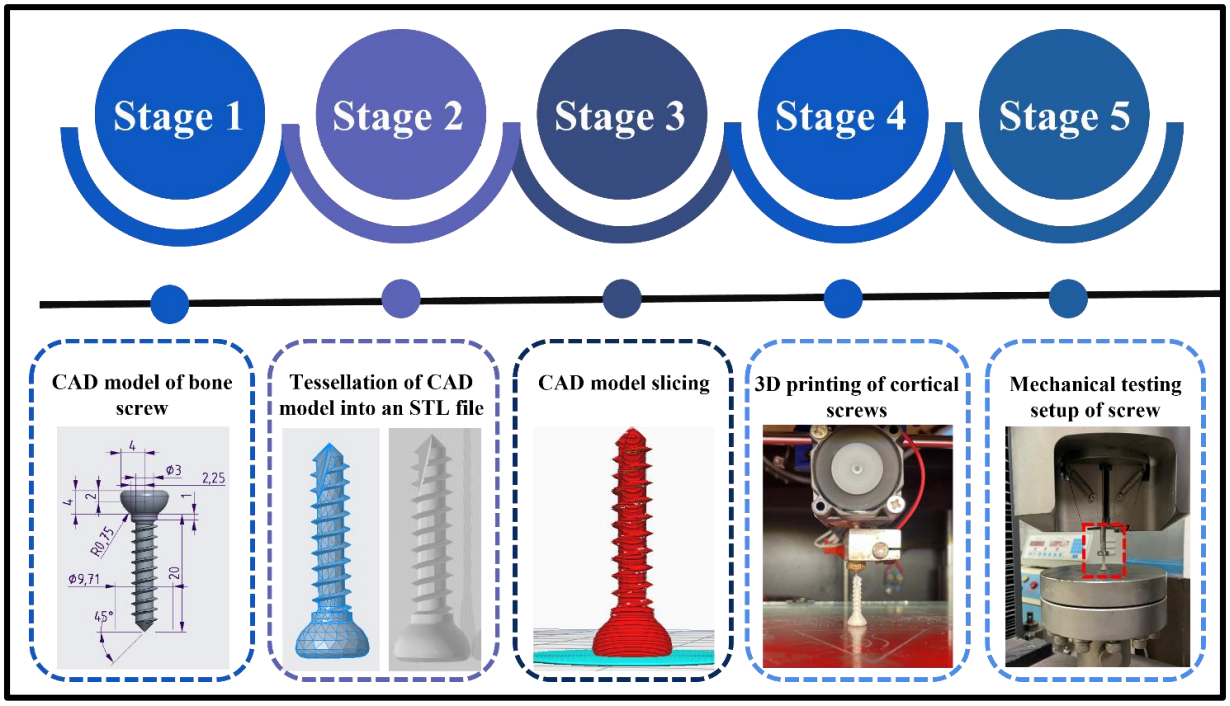


Figure 4.1. Procedure for fabrication and mechanical testing of screws.

4.2.2 Process parameters

The procedure for fabricating cortical screws by 3D printing technology was followed by varying different process parameters as represented in Table 4.1. These process parameters are infill pattern, infill percentage, layer height, and wall thickness. The process parameters were selected based on the pilot study and literature review [31, 124, 139]. Detailed definitions of these process parameters are provided in Chapter 3. These independent process parameters of the 3D printing technique were controlled by slicing software, the range of process parameters

is mentioned in Table 4.1. Layer height was varied from 0.06 mm to 0.12 mm, infill percentage was varied in the range from 25% to 100%, wall thickness was varied from 0.25 mm to 1 mm and different infill patterns were selected as presented in Table 4.1. By varying the different levels of these four process parameters, a total of 100 screws were manufactured by 3D printing technology. The detailed combination of process parameters and their corresponding mechanical compressive strength are presented in Table 4.2.

Table 4.1. Input parameters range used for 3D printing.

Independent parameters	**Range**	**Unit**
Layer height	0.06 to 0.12	mm
Infill percentage	25 to 100	%
Wall thickness	0.25 to 1	mm
Infill pattern	Triangular, Grid, Concentric, Honeycomb	

Table 4.2. Input process parameters and their corresponding compressive strength for fabrication of 100 cortical screws by 3D printing.

S. No.	**Infill pattern**	**Infill percentage (%)**	**Layer height (mm)**	**Wall thickness (mm)**	**Compressive strength (Mpa)**
1	Triangular	25	0.08	0.5	212
2	Grid	25	0.08	0.5	216
3	Concentric	25	0.08	0.5	221
4	Honeycomb	25	0.08	0.5	226
5	Triangular	50	0.08	0.5	224
6	Grid	50	0.08	0.5	251
7	Concentric	50	0.08	0.5	268
8	Honeycomb	50	0.08	0.5	271
9	Triangular	75	0.08	0.5	228
10	Grid	75	0.08	0.5	255
11	Concentric	75	0.08	0.5	272
12	Honeycomb	75	0.08	0.5	278
13	Triangular	100	0.08	0.5	232

14	Grid	100	0.08	0.5	260
15	Concentric	100	0.08	0.5	276
16	Honeycomb	100	0.08	0.5	285
17	Triangular	25	0.06	0.5	218
18	Triangular	25	0.1	0.5	209
19	Triangular	25	0.12	0.5	200
20	Grid	25	0.06	0.5	220
21	Grid	25	0.1	0.5	210
22	Grid	25	0.12	0.5	206
23	Concentric	25	0.08	0.5	226
24	Concentric	25	0.08	0.5	218
25	Concentric	25	0.08	0.5	214
26	Honeycomb	25	0.06	0.5	231
27	Honeycomb	25	0.1	0.5	221
28	Honeycomb	25	0.12	0.5	216
29	Triangular	50	0.06	0.5	230
30	Triangular	50	0.1	0.5	220
31	Triangular	50	0.12	0.5	216
32	Grid	50	0.06	0.5	255
33	Grid	50	0.1	0.5	245
34	Grid	50	0.12	0.5	240
35	Concentric	50	0.08	0.5	270
36	Concentric	50	0.08	0.5	264
37	Concentric	50	0.08	0.5	258
38	Honeycomb	50	0.06	0.5	275
39	Honeycomb	50	0.1	0.5	265
40	Honeycomb	50	0.12	0.5	260
41	Triangular	75	0.06	0.5	222
42	Triangular	75	0.1	0.5	233
43	Triangular	75	0.12	0.5	238
44	Grid	75	0.06	0.5	247
45	Grid	75	0.1	0.5	259

46	Grid	75	0.12	0.5	262
47	Concentric	75	0.06	0.5	274
48	Concentric	75	0.1	0.5	264
49	Concentric	75	0.12	0.5	258
50	Honeycomb	75	0.06	0.5	280
51	Honeycomb	75	0.1	0.5	274
52	Honeycomb	75	0.12	0.5	270
53	Triangular	100	0.06	0.5	235
54	Triangular	100	0.1	0.5	227
55	Triangular	100	0.12	0.5	222
56	Grid	100	0.06	0.5	263
57	Grid	100	0.1	0.5	257
58	Grid	100	0.12	0.5	252
59	Concentric	100	0.06	0.5	279
60	Concentric	100	0.1	0.5	270
61	Concentric	100	0.12	0.5	264
62	Honeycomb	100	0.06	0.5	280
63	Honeycomb	100	0.1	0.5	281
64	Honeycomb	100	0.12	0.5	283
65	Triangular	100	0.12	0.25	220
66	Triangular	100	0.12	0.75	226
67	Triangular	100	0.12	1	232
68	Grid	100	0.12	0.25	248
69	Grid	100	0.12	0.75	256
70	Grid	100	0.12	1	261
71	Concentric	100	0.12	0.25	260
72	Concentric	100	0.12	0.75	269
73	Concentric	100	0.12	1	273
74	Honeycomb	100	0.12	0.25	280
75	Honeycomb	100	0.12	0.75	289
76	Honeycomb	100	0.12	1	292
77	Triangular	50	0.12	0.25	204

78	Triangular	50	0.12	0.75	208
79	Triangular	50	0.12	1	215
80	Grid	50	0.12	0.25	230
81	Grid	50	0.12	0.75	237
82	Grid	50	0.12	1	243
83	Concentric	50	0.12	0.25	238
84	Concentric	50	0.12	0.75	248
85	Concentric	50	0.12	1	252
86	Honeycomb	50	0.12	0.25	261
87	Honeycomb	50	0.12	0.75	270
88	Honeycomb	50	0.12	1	272
89	Triangular	75	0.12	0.25	207
90	Triangular	75	0.12	0.75	214
91	Triangular	75	0.12	1	221
92	Grid	75	0.12	0.25	234
93	Grid	75	0.12	0.75	245
94	Grid	75	0.12	1	250
95	Concentric	75	0.12	0.25	248
96	Concentric	75	0.12	0.75	257
97	Concentric	75	0.12	1	262
98	Honeycomb	75	0.12	0.25	268
99	Honeycomb	75	0.12	0.75	281
100	Honeycomb	75	0.12	1	284

4.3. Background of Machine Learning Models Employed

The present study utilizes various ML models, including k-nearest neighbors (kNN), decision trees (DT), support vector regression (SVR), and random forest (RF) models. The next section describes the working principles of these models.

4.3.1 Decision trees (DT)

DT is a non-parametric supervised ML model that can perform classifications as well as regression analysis [153]. The DT is a flowchart-like structure that has leaves and branches known as leaf nodes and branching nodes as depicted in Figure 4.2(a). The branching node is

also known as the decision node which has further leaf nodes [153]. The model is trained using a classification tree, which has nodes that represent the predicted class and supply the characteristics along the way. The nodes represent the predicted class that provides the feature values along the path and the roots that takes a discrete set of values called the classification tree used for training the model. The internal nodes represent the features of a dataset, branches represent the decision rules, and each leaf node represents the outcome. DT is a graphical representation for getting all the possible solutions to a decision based on given conditions. The logic behind the decision tree can be easily understood because it shows a tree-like structure having decision nodes and leaf nodes.

4.3.2 Random Forest (RF)

RF is a supervised ML algorithm that is capable of performing both regression and classification analysis [154]. RF is a technique which detents the nonlinear relationships used to avoid overfitting. The schematics of the random forest model is presented in Figure 4.2(b). RF is an improved and further accurate ML model as compared to the decision tree model as it doesn't rely on a single decision tree. RF provides higher accuracy and reasonable prediction without hyperparameter tuning through the cross-validation of data. It utilizes an ensemble of regression trees that combines many classifiers to provide solutions to complex problems. RF is used for training the model consisting of nodes representing the predicted class and roots representing discrete values.

4.3.3 Support vector regression (SVR)

SVR is a supervised ML model leveraged for regression and classification analysis [155]. SVR is built based on the concept of a support vector machine. Despite its origins as a classification system, the support vector machine was extended to include regression later. The goal of SVR is to create an optimal decision boundary line, or hyperplane as depicted in Figure 4.2(c). By identifying the hyperplane and minimizing the difference between predicted and observed values, the SVR algorithm fits the data and reduces the error within a certain predetermined threshold. In an infinite-dimensional space, SVR creates a set of hyperplanes for regression and outlier detection as illustrated in Figure 4.2(c). The error between predicted values and observed values is reduced by determining the hyperplanes. The linear function (Figure 4.2(c)) followed by SVR is provided in Eq. (1), where function f(x) tolerates small errors in data set fitting and assumed w € R^n and b € R (w and b are coefficients to be adjusted).

$$f(x) = w^T + b \qquad \ldots\ldots\ldots\ldots\ldots\ldots\ldots\ldots (1)$$

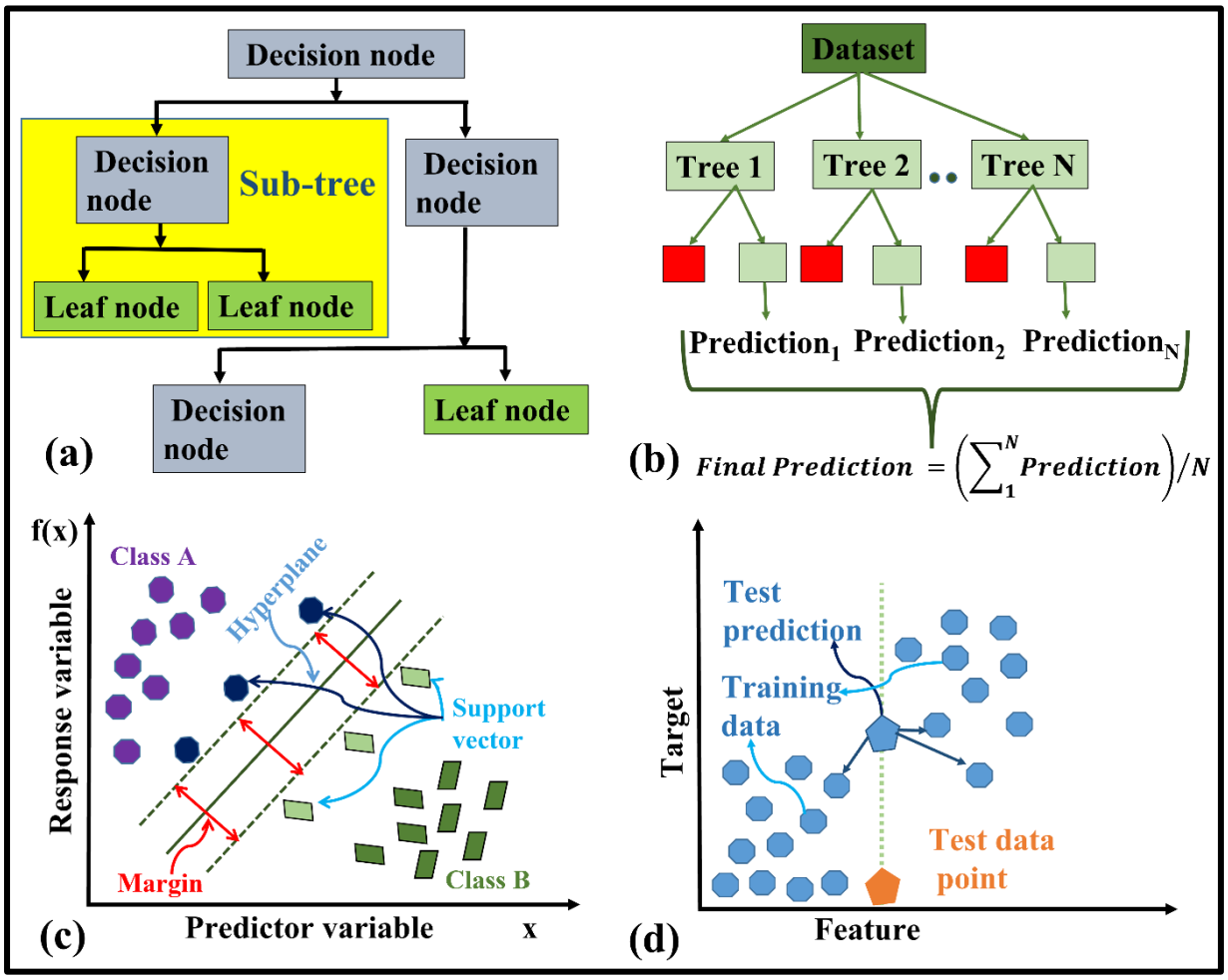


Figure 4.2. (a) DT, (b) RF, (c) SVR, (d) kNN.

4.3.4 k-nearest neighbour (kNN)

kNN is commonly used due to its simplicity and effectiveness for classification and regression issues. It is a non-parametric classification model that makes use of available data and classifies new data points using distance function similarity measures. As illustrated in Figure 4.2(d), covariates and associated variables are aggregated at the nearest distance to generate new observations from the existing data [156]. kNN is a non-parametric classification model to classify new observations of data points using the distance function. The new observation of a class of observation is obtained by closest distance or nearest neighbors using covariates as depicted in Figure 4.2(d). With the aid of Euclidean distance, which is computed as the square root of the sum of the squared differences among a new point (x) and an existing location (y), the distance between the query instance and each of the all-training points is determined as

described in Eq. (2). The closest distance is sorted, and the nearest neighbours of the data are discovered with the help of Euclidean distance.

$$\textbf{Euclidean distance} = \sqrt{\sum_{i=1}^{k} (x_i - y_i)^2} \qquad \ldots\ldots\ldots\ldots\ldots\ldots (2)$$

4.4. Grid search algorithm with K-fold cross-validation

Before implementing the ML models, the grid search with cross-validation algorithms was performed. The Grid search algorithm with cross-validation may increase the computational expense tremendously and automate the tuning of hyperparameters. Grid search builds a model for each possible combination of the hyperparameter values provided, evaluating each model, and selecting the architecture that produces the best results. Grid search assumes nothing about the model, and each trial can be run in parallel. The visual representation of a grid search is depicted in Figure 4.3(a). As a result of the grid search, every possible combination of hyperparameter values is tested, and the model that performs best is chosen. Parallel trials can be run within a grid search by multiple trials simultaneously because it does not assume anything about the model. Grid search optimization is performed to identify the optimal hyperparameters of the considered ML models.

K-fold cross-validation was used for the training of models to validate the shuffled data set multiple times to ensure an unbiased evaluation of predictive models. K-fold cross validation is a procedure used to estimate the skill of the model on new data. The visualization of cross-validation is depicted in Figure 4.3(b). The data set was shuffled in each of these K subsets, and the '1' testing sub-set was picked. The remaining 'K-1' bins are put together to develop a training set. In each split, the model is trained on the 'K-1' bins put together training data and tested on the remaining '1' testing data.

The critical aspect of cross-validation is validating the shuffled data set multiple times. The experiment has been repeated five times, which means five separate learning experiments were run for five significant sets (therefore K = 5). The performance of 5-fold cross-validation is then averaged by the values of different testing split sets computed in the loop. This emphasizes the assessment of learning algorithms more precisely and accurately. For specific predictive analysis and avoiding biases, a model is compared and chosen using the K-fold cross-validation technique.

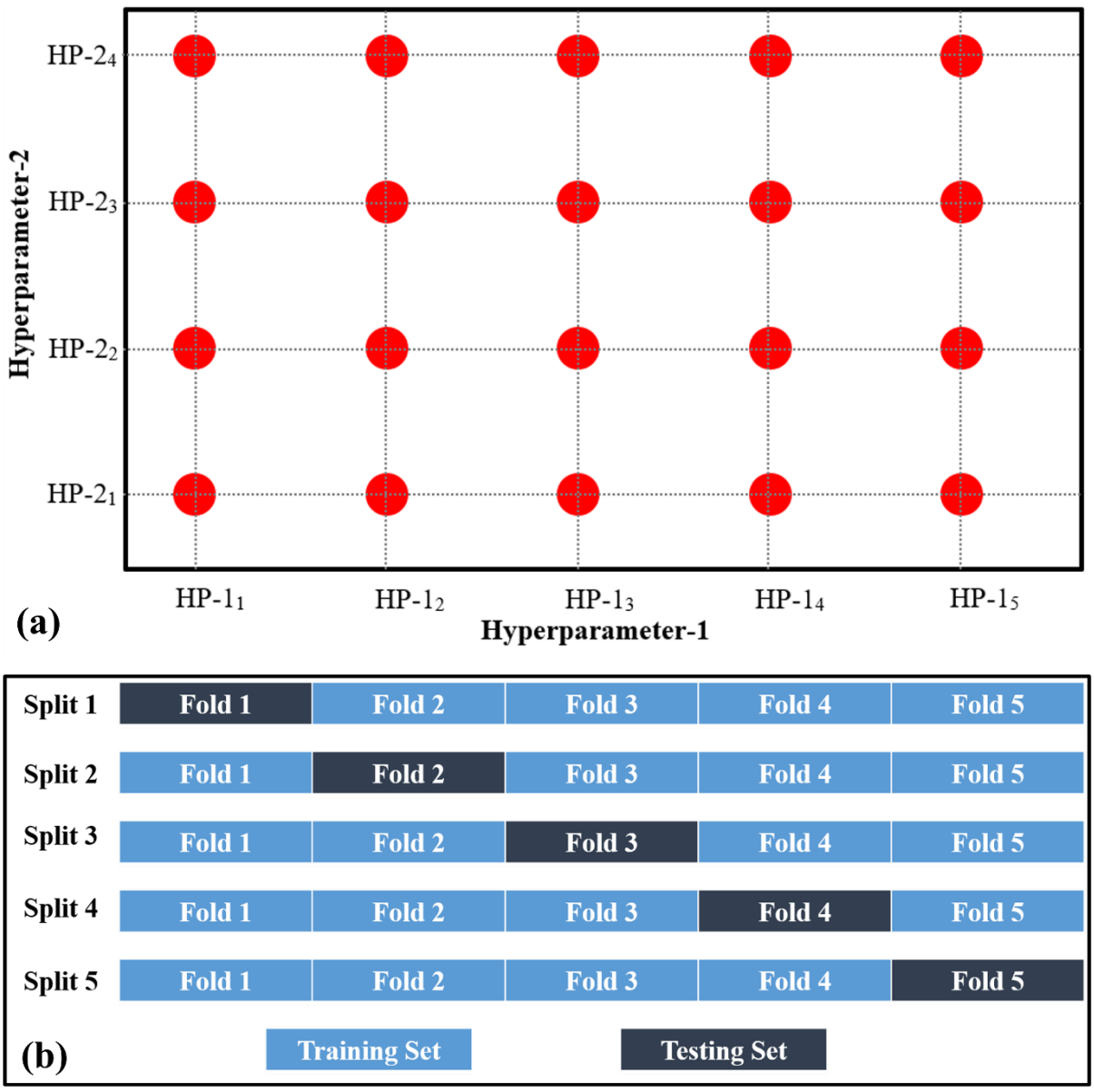


Figure 4.3. (a) grid search representation, (b) 5-fold cross-validation.

4.5 Data Visualization and Interpretation

For the training of ML models, a total of 100 cortical bone screws were fabricated with variations in four independent process parameters which are infill pattern, infill percentage, layer height and wall thickness. The compressive strength of 3D-printed cortical screws is represented in a box-whisker plot as depicted in Figure 4.4. It can be elucidated from Figure 4.4 that variation in different input process parameters influences the compressive strength of 3D-printed cortical screws. The most influential process parameter during the fabrication of orthopaedic cortical screws is the infill pattern and infill percentage as shown in Figure 4.4. With the variation in infill percentage from 25% to 100%, the compressive strength increases up to 17% (around 215 MPa to 262 MPa) as illustrated in Figure 4.4(a). As increasing the infill

percentage of the fabricated cortical screw, the porosity of the screw reduces which increases the weight and compressive strength of the 3D-printed screw.

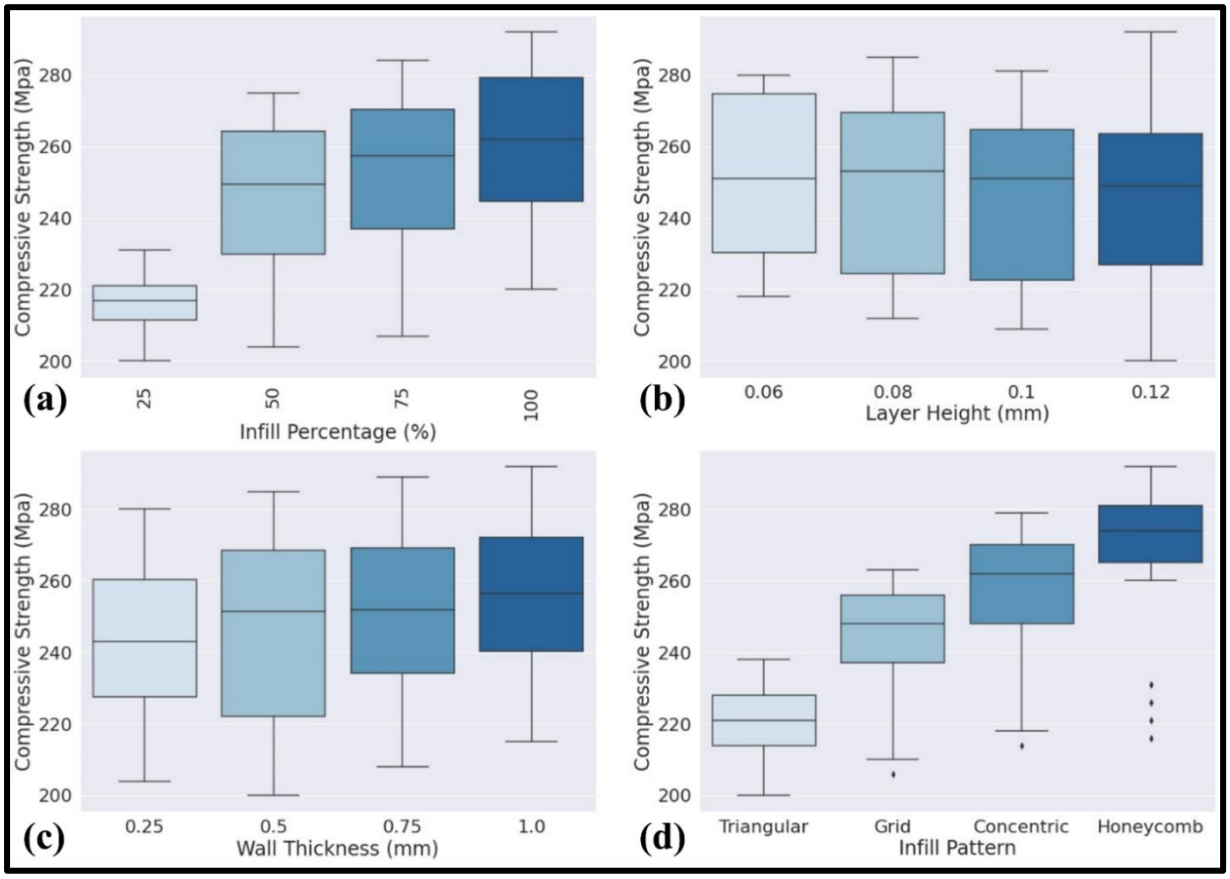


Figure 4.4. The box-whisker plot of input process parameters on compressive strength.

The influence of layer height does not affect the compressive strength of AM fabricated screws. It can be observed that increasing the layer height decreases the compressive strength of the screw as depicted in Figure 4.4(b). The increase in layer height increases the extrusion rate during the 3D printing of screw, which results in reducing the material consumption and weight of the screw. The variation in wall thickness influences the compressive strength of 3D-printed screws. The increase in wall thickness increases the compressive strength of AM-fabricated cortical screws as depicted in Figure 4.4(c). It was observed that honeycomb-patterned cortical screws have higher compressive strength compared to other infill patterns as shown in Figure 4.4(d). Varying the infill pattern from triangular to honeycomb pattern, the compressive strength increases up to 18% (around 220 MPa to 270 MPa) as illustrated in Figure 4.4(d). The honeycomb-patterned cortical screws have higher compressive strength as compared to other infill patterns due to the structural stability of the honeycomb pattern and higher bonding strength in the intercalated layers of fabricated cortical screws.

The fractured screws of different infill patterns along with their infill structures are illustrated in Figure 4.5. It was observed that by changing the pattern from honeycomb to triangular, the mechanical compressive strength and fracture stress of 3D-printed cortical screws decreased. Because in honeycomb-structured screws, the material packaging increases that enhancing the bonding surface area at the intercalated layers. Higher deformation and stress generation was witnessed in the honeycomb-patterned screw which indicates the highest compressive strength as depicted in Figure 4.5. From the box-whisker plot, it is elucidated that compressive strength is relatively less sensitive to changes in layer height and wall thickness compared to infill percentage and infill pattern.

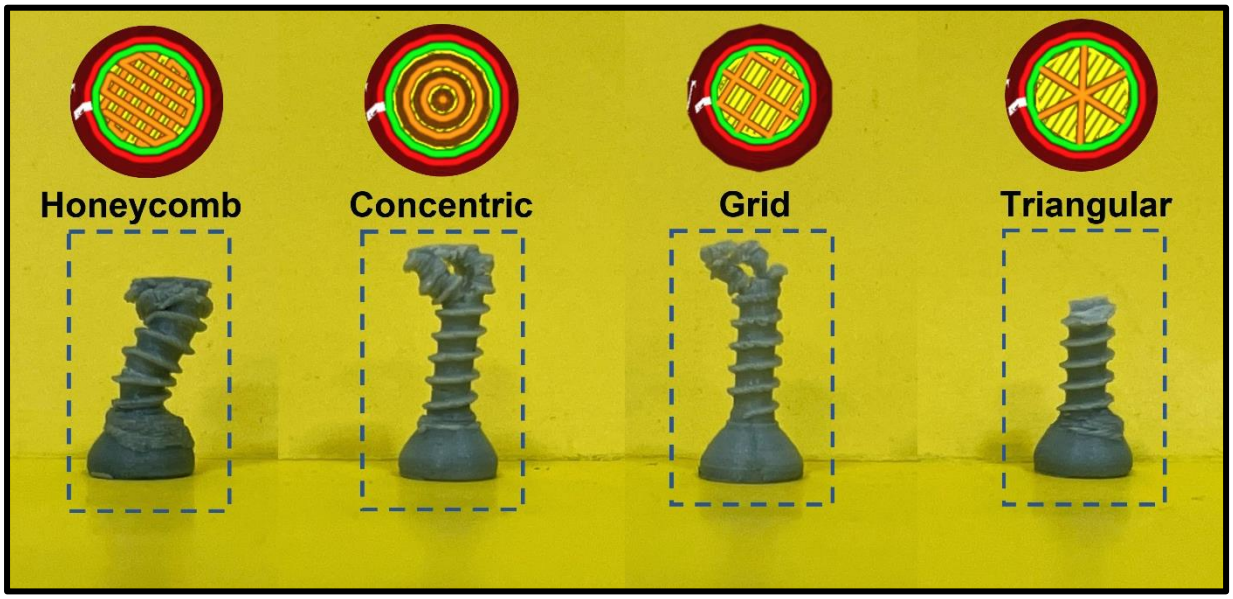


Figure 4.5. Fractured images of different patterned 3D-printed cortical screws.

A correlation pair-plot visualization of all independent parameters on the compressive strength of 3D-printed cortical screws is presented in Figure 4.6. This pair-plot graph provides data visualization that explains the pairwise relationship between the input process parameter with the output parameter. The interactive effect of input parameters on compressive strength can be understood with a correlation pair plot. Correlations are indicated by the direct or inverse relationship between input parameters and output response envisaged by a correlation pair plot. The pair plot explains the impact of the contribution and trend of influencing process parameters on the compressive strength of the bone screw. It was observed that infill pattern, infill density and wall thickness are positively correlated with compressive strength. Whereas layer height is negatively correlated with the compressive strength of the 3D-printed cortical screw. Increasing the layer height of 3D-printed cortical screws decreases the compressive strength of fabricated screws.

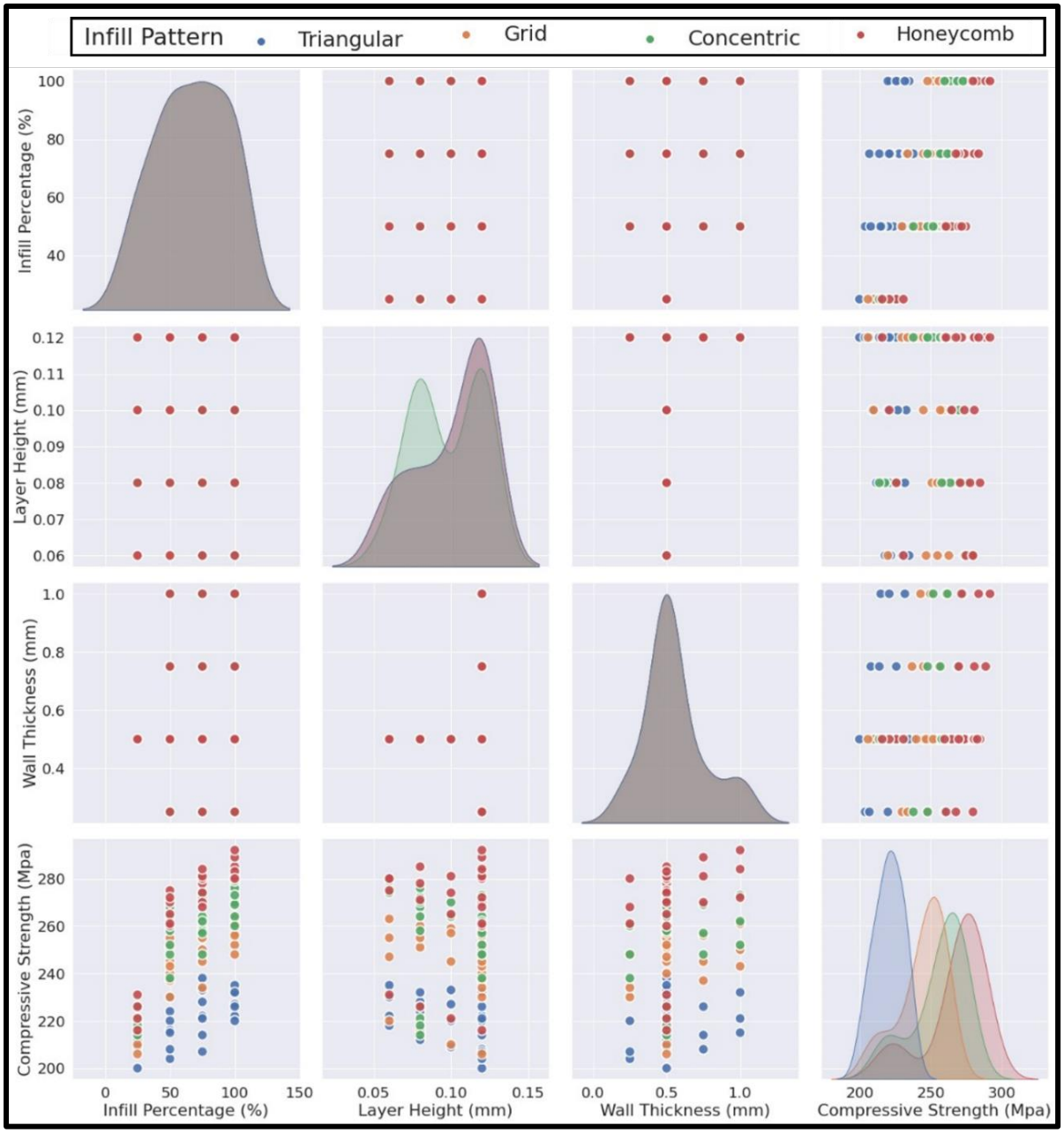


Figure 4.6. Pair-plot of independent parameters and compressive strength.

The correlation denotes the proportional relation between input parameters and output response, either directly or inversely proportional to each other. It was observed in pair-plot visualization (Figure 4.6) that changing the infill pattern and infill density of cortical screws significantly influences the compressive strength of 3D-printed cortical screws. The mechanical strength of 3D-printed screws is highly influenced by the interaction between the infill pattern and infill density as illustrated in Figure 4.6. An increase in the percentage of infill along with the infill pattern influences the mechanical compressive strength as compared to layer height and wall thickness of cortical screws. This is due to the higher contribution level of the infill pattern and infill percentage. Also, infill pattern and infill percentages significantly

influence the pattern of filling and porosity of 3D-printed screws which affects the weight and material consumption during screw fabrication. Hence, the mechanical compressive strength of the 3D-printed screw is significantly influenced by the infill pattern and infill percentage. The honeycomb-patterned screw offers higher mechanical strength due to structural morphology and higher bonding surface area at intercalated layers. At 100% of the infill percentage, the 3D-printed screw is an almost solid structure that contributes to the highest compressive strength. Hence, the honeycomb pattern with a 100% of infill percentage has the highest compressive strength of a 3D-printed cortical screw.

4.6 Application of ML models

A total of 100 cortical screws were fabricated by varying the input processing parameters (Table 4.1), implying 100 data points with their corresponding compressive strength. These 100 data points were distributed into 80 training and 20 testing data points to monitor the adequacy and performance of different ML models. Before implementing the ML models, the grid search with cross-validation algorithms was performed. The results of the training data by different ML models are presented in Figure 4.7. The green dots indicate the predicted values of compressive strength by the ML models and the red dots represent the experimental values of compressive strength. It was witnessed that the random forest-based ML model has higher accuracy as most of the predicted values of compressive strength overlapped with the true experimental values as observed in Figure 4.7. Whereas in the case of the kNN model, the predicted values of compressive strength deviate from the true (experimental) values of compressive strength.

Based on the training of data, the performance of testing data is defined and presented in Figure 4.8. Similar results were observed with testing data of 20 points, it was observed that random forest is the most accurate predictive ML model. At different points, the predicted value by the random forest model is almost overlapped with the true value as depicted in Figure. 4.8. Therefore, the random forest model is the most robust and accurate ML model for predicting the compressive strength of a screw. The SVR model predicts the nearby values as similar to true experimental values. The accuracy of the SVR model is consistently compared to kNN and DT. The most deviated results were shown by the kNN model. Based on the performance of training and testing data, it was observed that the random forest ML model is a precise and adequate predictive ML model for predicting the compressive strength of 3D-printed cortical screws.

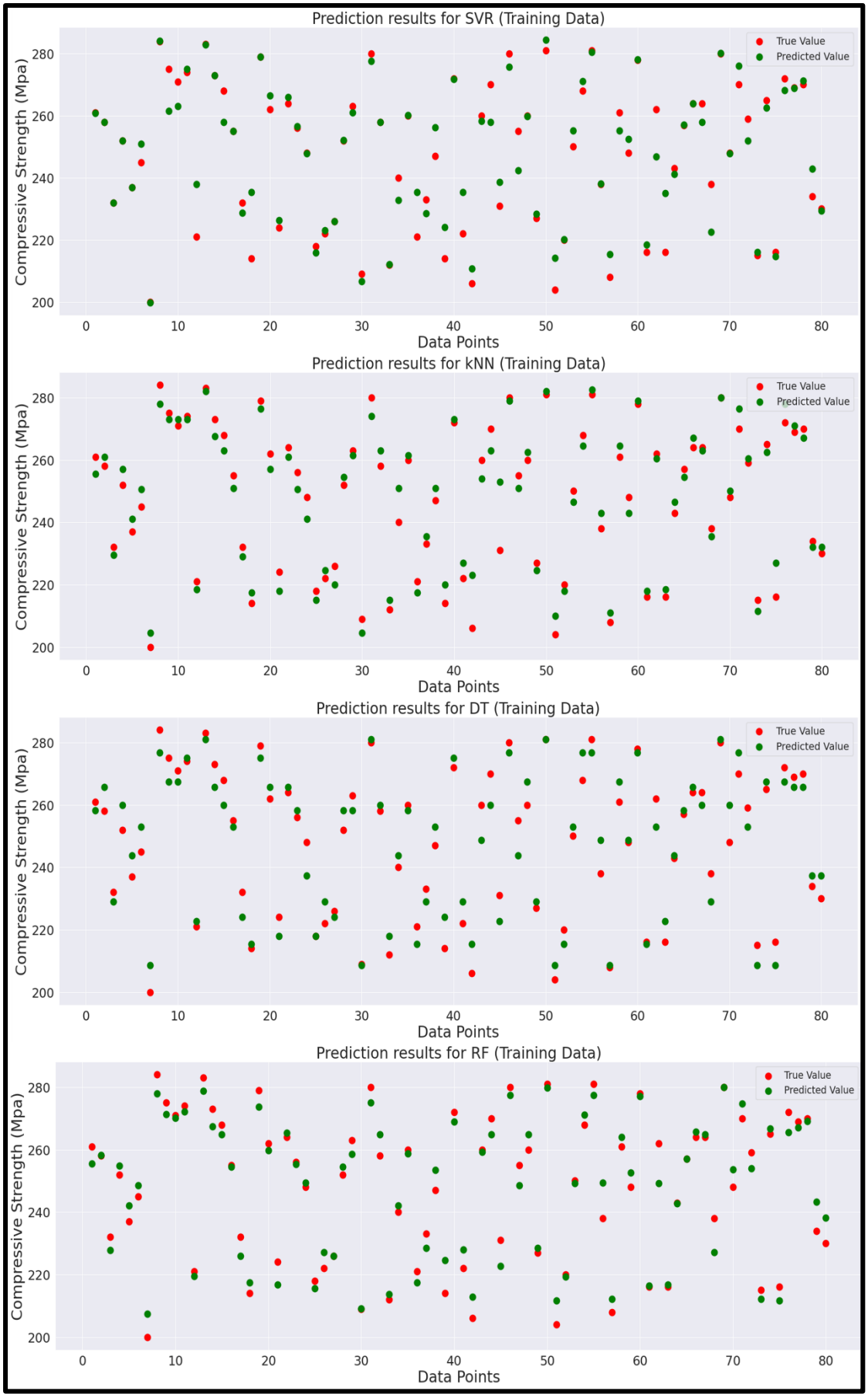


Figure 4.7. Predicted and true values of training data for compressive strength.

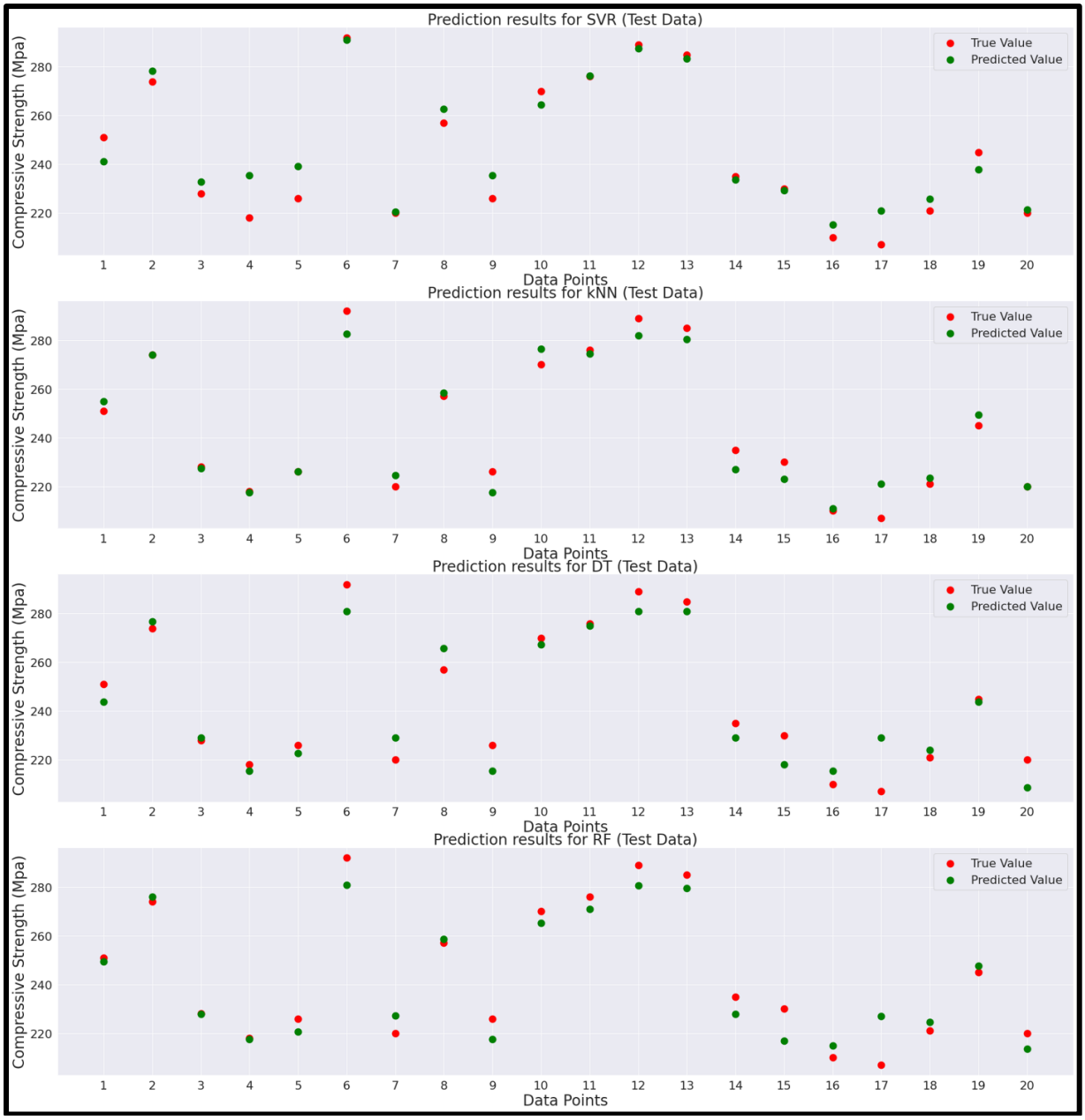


Figure 4.8. Predicted and true values of testing data of 20 data points for compressive strength.

To observe the performance of training data and testing data, the residual plot for different ML models was employed as illustrated in Figure 4.9. The residual plot is the relative residuals on the vertical axis, against the best estimate of the true value on the horizontal axis. It is useful to display the relationship between two paired variables using the same scale. The experimental values were presented in the horizontal axis in Figure 4.9. It was observed in the residual plot that the random forest ML model has most of the training and testing point difference lying in the range between -10 to 10, whereas higher variation was observed in the

kNN model. Therefore, the random forest ML model is the preferred predictive model as most of the difference between training and testing data points lies in the desired range.

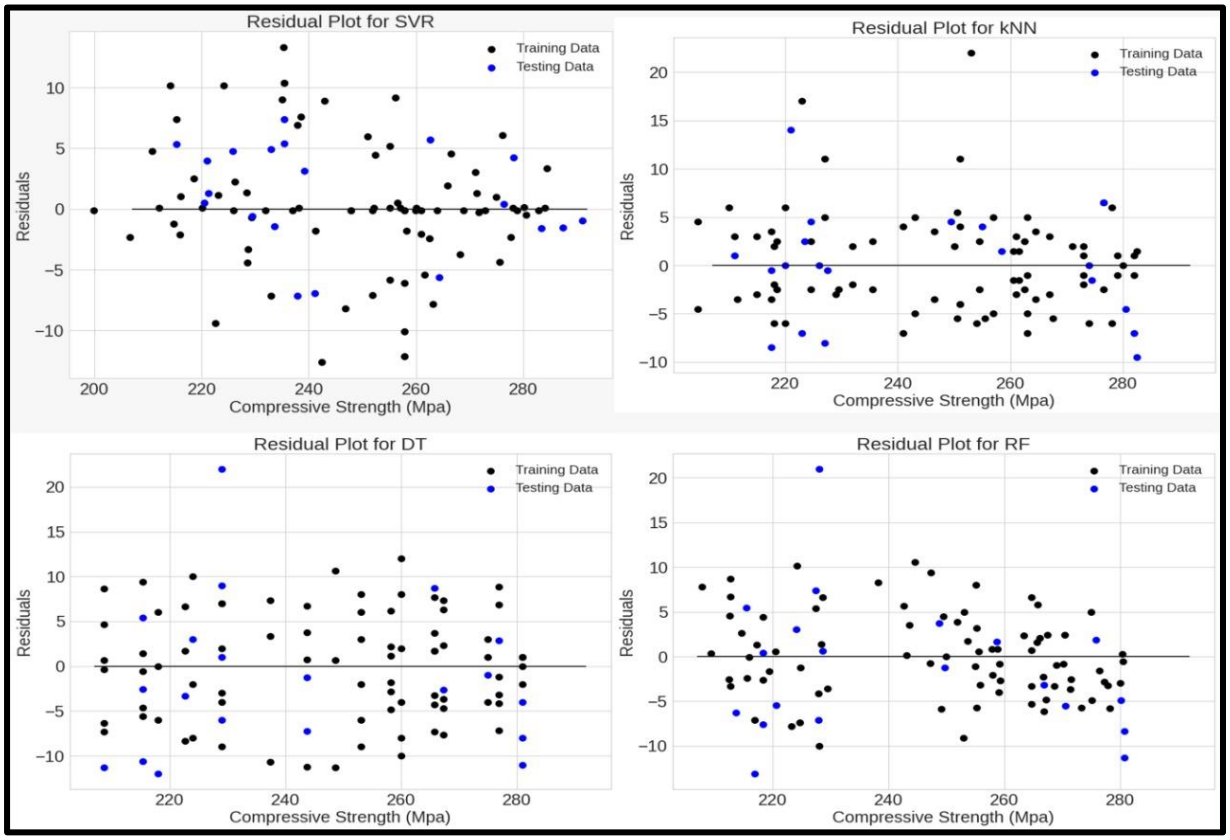


Figure 4.9. Residual plot of different ML models.

The adequacy of training and testing data points were defined as the least values of different error metrics. These error metrics are root mean square error (RMSE), mean absolute error (MAE) and coefficient of determination (R^2). The mathematical equations of various error metrics are provided in Eq. (3), Eq. (4), and Eq. (5). RMSE is calculated by Eq. (3), as the average of squared differences between each computed value and its corresponding correct value. MAE is calculated by Eq. (4), as the average of the difference between the predicted and actual value. R^2 is calculated by Eq. (5) as the difference between the samples in the dataset and the predictions made by the model. RMSE, MAE and R^2 define the adequacy and robustness of various predictive ML models used in the present work. Based on these three different error metrics, the adequacy of a predictive model is well-defined.

$$\mathbf{RMSE} = \sqrt{\sum_{i=1}^{n} \frac{(y_i - \overline{y_i})^2}{n}} \qquad \ldots\ldots\ldots\ldots\ldots\ldots (3)$$

$$\mathbf{MAE} = \frac{\mathbf{1}}{\boldsymbol{n}}\sum_{\boldsymbol{i=1}}^{\boldsymbol{n}} |\boldsymbol{y_i} - \overline{\boldsymbol{y_i}}| \qquad \ldots\ldots\ldots\ldots\ldots\ldots (\mathbf{4})$$

$$\mathbf{R^2} = \mathbf{1} - \frac{\sum_{i=1}^{n}(\overline{y_i} - y_i)^2}{\sum_{i=1}^{n}(\overline{y} - y_i)^2} \qquad \ldots\ldots\ldots\ldots\ldots\ldots (\mathbf{5})$$

Where, $\overline{\mathbf{y_i}}$ is the predicted points, $\mathbf{y_i}$ is the actual points, $\overline{\mathbf{y}}$ is the mean of actual points and $\boldsymbol{n}$ is the number of data points. The error metrics were monitored based on the mean and standard deviation of the predictive results by different ML models as illustrated in Figure 4.10. Error metrics of training data are presented in Figure 4.10(a). It was witnessed that the error metrics based on RMSE, MAE and R^2 for the mean and standard deviation of random forest are minimum in the case of training data as compared to other ML models as illustrated in Figure 4.10(a). The variability of independent variables and their relationships with other variables are described by R^2. The kNN model shows the highest error metrics as compared to other ML models for training data as depicted in Figure 4.10(a). The testing data-based error metrics are illustrated in Figure 4.10(b). The testing data shows the least error metrics of random forest in terms of the mean and standard deviation of predictive results as presented in Figure 4.10(b). The highest error metrics and least comparative predictive accuracy were observed in the kNN model as presented in Figure 4.10(b). The error metrics of the mean and standard deviation of training data of different ML models are presented in Table 4.3. The error metrics of mean and standard deviation of testing data of different ML models are described in Table 4.4. Therefore, based on the error metrics for training and testing data, it was witnessed that the random forest ML model is the most accurate predictive model for predicting the compressive strength of the 3D-printed cortical screws.

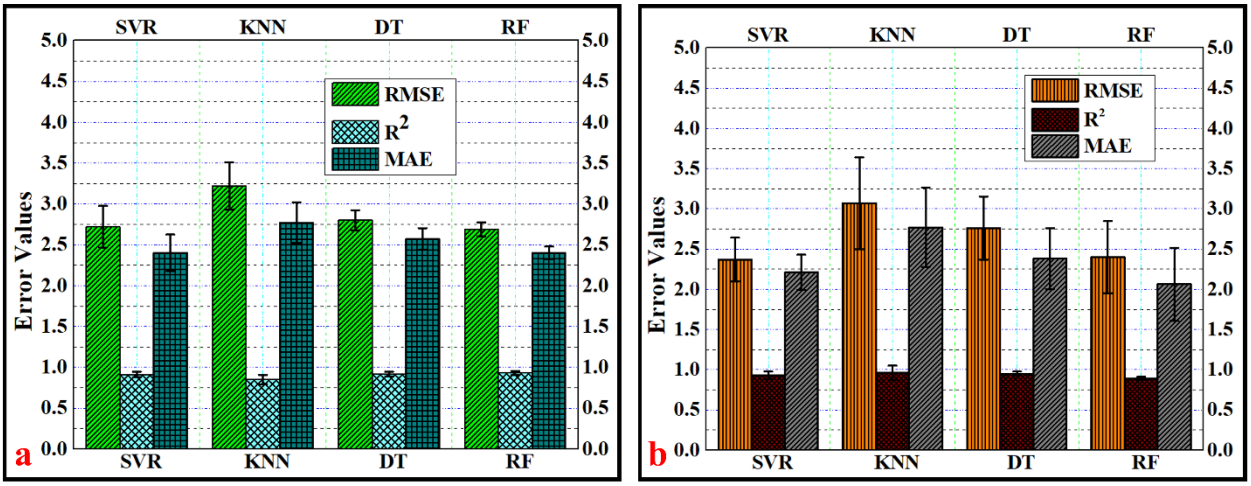


Figure 4.10. Error metrics of ML models for (a) training data, and (b) testing data.

Table 4.3. Error metrics of different ML models for comparing means and standard deviation of the training data set.

Error metrics	RMSE		MAE		R^2	
	Mean	SD	Mean	SD	Mean	SD
kNN	3.22	0.579	2.77	0.504	0.85	0.113
SVR	2.72	0.512	2.4	0.446	0.91	0.068
DT	2.8	0.248	2.57	0.267	0.916	0.058
RF	2.69	0.17	2.4	0.151	0.93	0.053

Table 4.4. Error metrics of different ML models for comparing means and standard deviation of the testing data set.

Error metrics	RMSE		MAE		R^2	
	Mean	SD	Mean	SD	Mean	SD
kNN	3.07	1.14	2.77	0.99	0.96	0.98
SVR	2.4	0.545	2.21	0.433	0.94	0.098
DT	2.76	0.78	2.38	0.754	0.93	0.05
RF	2.37	0.9	2.06	0.91	0.91	0.042

4.7. Ensemble ML models

After monitoring the error metrics, robustness and performance of base learning ML models, different ensemble ML models were leveraged. Advanced and complex predictive models are required to improve the predictive ability of base learning ML models and understand the intercorrelation between influencing parameters of 3D printing techniques. The robustness and effectiveness of ML models can be improved with ensemble ML techniques. The term "ensemble" presents a methodology in which two or more things work as a single unit. Ensemble methods create multiple models and combine them to improve the final prediction results [157–159]. The ensemble method lowers the spread of predictions and the proposed model to increase the predictive model's adequacy [160–162]. In this work, for the prediction of mechanical strength by different process parameters of 3D printing technology, ensemble

ML models such as XGBoost, AdaBoost, and GradientBoost were leveraged. The detailed methodology followed for leveraging ensemble ML models is presented in Figure 4.11. Different ensemble ML models were compared at different error metrics used to monitor the adequacy of base learning ML models.

4.7.1. GradientBoost

GradientBoost is an ensemble boosting ML algorithm that can be explained as an ensemble of decision trees used for classification and regression tasks [163]. Gradient-Boosted models are sequentially built trees to minimize the cost function. By using an additive regression model, this method predicts the desired outcome instead of building a single tree. During Gradient-Boosting several weak prediction models are produced and combined to generate one single strong model for predicting the accurate output response [164]. In each step of gradient boosting, a new function is added to the existing function to predict the output as illustrated in Figure 4.12(a). A decision tree is trained in each GradientBoost at different weights of training models based on the previous iterations to reduce the error [165].

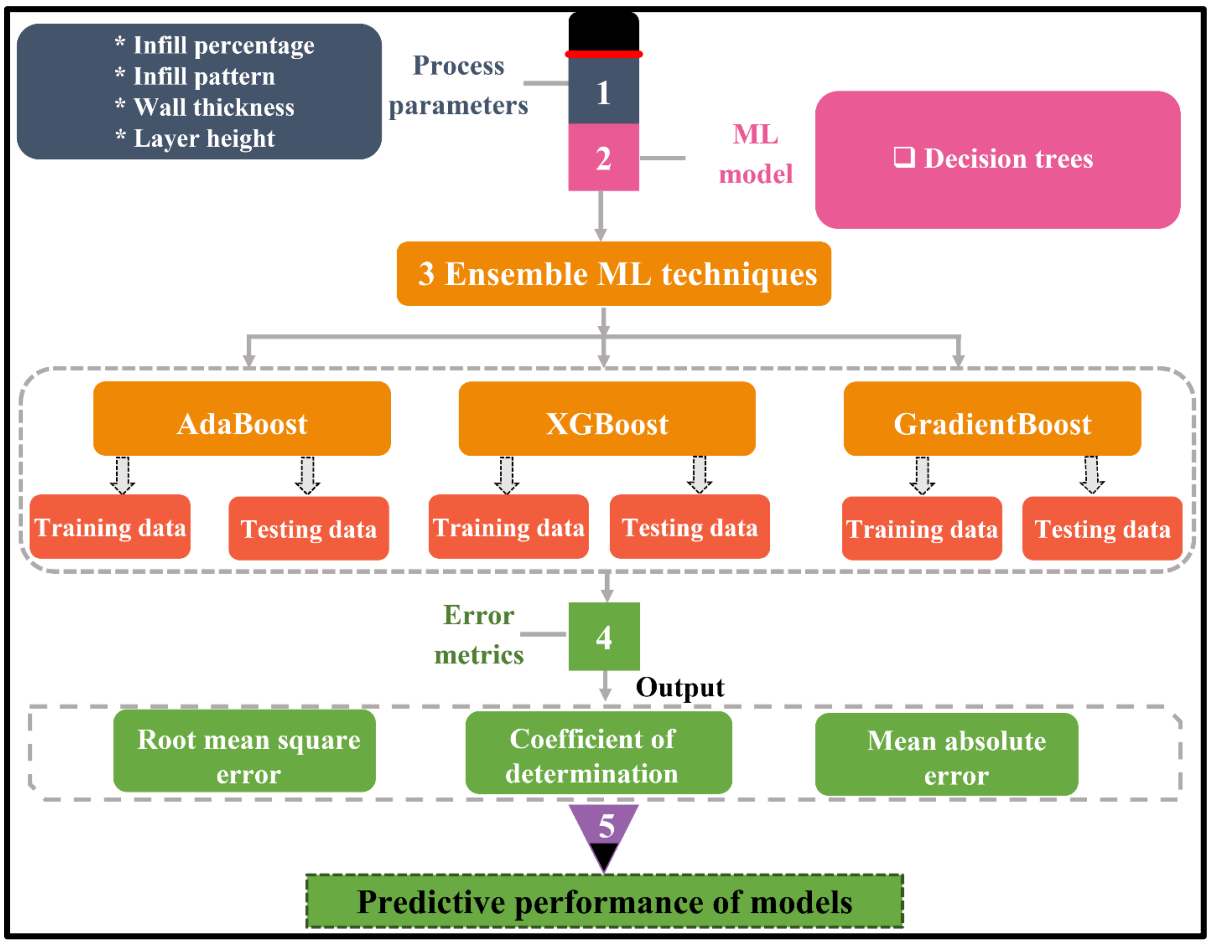


Figure 4.11. The methodology followed for mechanical strength prediction.

4.7.2. AdaBoost

An eminent boosting technique is AdaBoost leveraged for various applications such as regression and classification tasks [166]. In AdaBoost, different characteristics have been exploited for different purposes [167]. A node with two leaves is known as the stump. Each stump is made by previous stump mistakes as illustrated in Figure 4.12(b). This method modifies weight w_i in inverse proportion to the error ε_t and direct proportion to prediction accuracy. In addition, in the training phase, the accuracy of the classifier's predictions is weighted according to the final prediction. Every AdaBoost version trains a base learner based on weighted samples and performance associated with the earlier iterations.

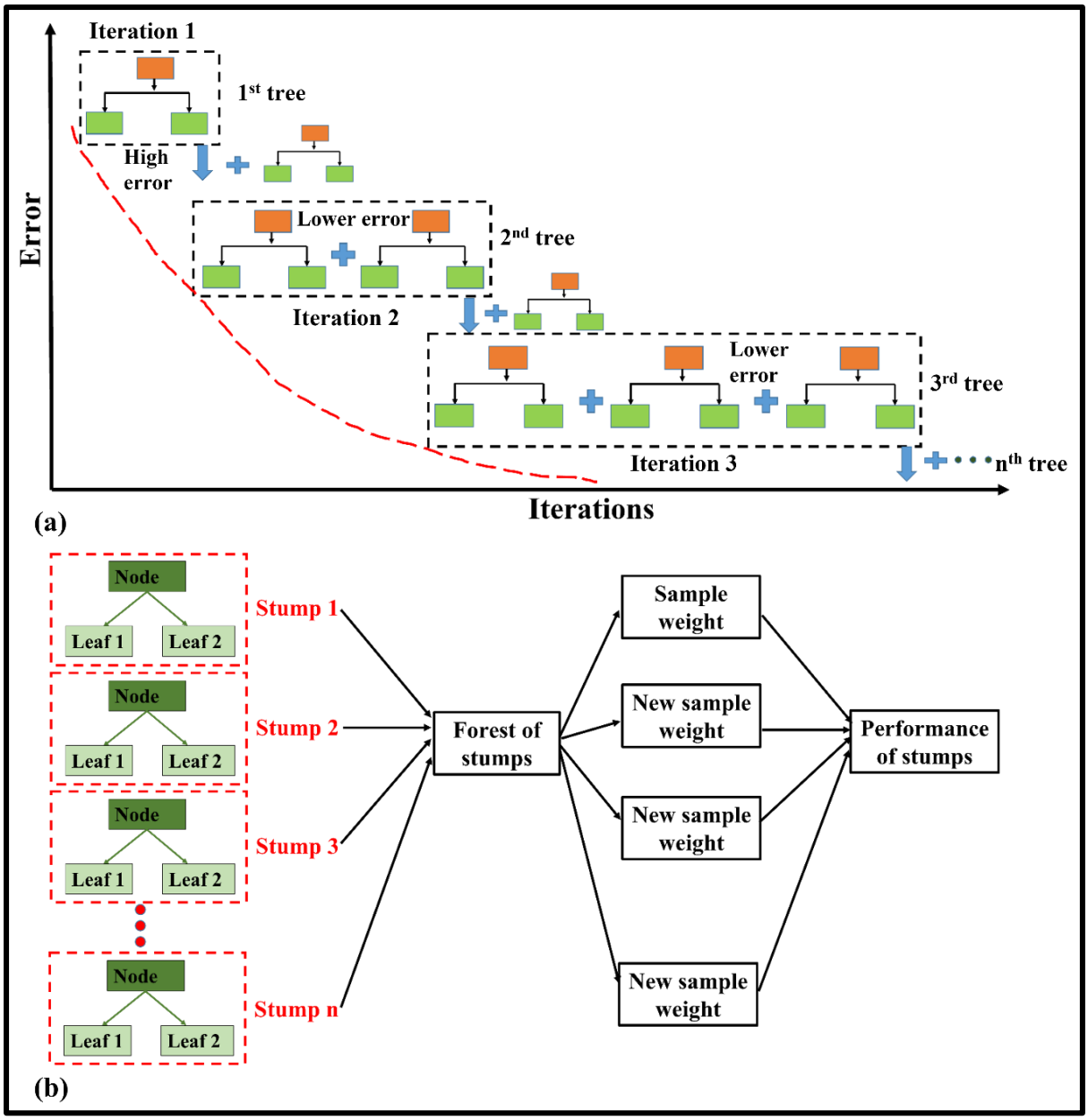


Figure 4.12. (a) GradientBoost model, (b) AdaBoost model.

4.7.3. XGBoost

XGBoost is an ensemble boosting technique used for classification and regression tasks [168]. For faster and more efficient decision trees, eXtreme Gradient-Boosting (XGBoost) decision trees are implemented using parallelized implementation [169]. XGBoost uses advanced regularization and in-built cross-validation that advances the model generalization capabilities. XGBoost uses a penalize complex model through regularization that helps in preventing overfitting, minimising the variance and controlling the complexity of the model [168, 170, 171]. XGBoost has higher computational efficiency and improved accuracy due to higher execution speed out of core computation [163].

4.8. Adequacy of ensemble ML models

The error metrics of different predictive ensemble ML techniques are envisaged with a Taylor diagram as illustrated in Figure 4.13. Taylor diagram is the mathematical diagram that identifies the most intuitive and comprehensive representation of error metrics of different models. The markers present in the Taylor diagram indicate different predictive ML models. The radial line of the Taylor diagram signifies R^2, horizontal and vertical coordinates of the Taylor diagram signify the RMSE of the predictive model.

Different error metrics were compared to monitor the adequacy of different ML models. The comparison of RMSE and R^2 for the training dataset is illustrated in Figure 4.13(a). Whereas MAE and R^2 of different ML models for the training dataset is represented in Figure 4.13(b). It was observed that XGBoost has the least values of RMSE and MAE as compared to other predictive models. The R^2 values of the XGBoost model was higher than 0.95 indicating higher accuracy compared to other predictive models. Hence, XGBoost is the most adequate ensemble model for the training dataset.

Similarly, for evaluating the performance of the testing dataset, RMSE and R^2, MAE and R^2 was observed as depicted in Figure 4.13(c) and Figure 4.13(d) respectively. The RMSE and MAE of XGBoost was comparatively lower in comparison to other predictive models for testing dataset also. The coefficient of determination was for XGBoost compared to other predictive models. Hence, based on the observation by the Taylor diagram, it was observed that the performance and robustness of the XGBoost ensemble ML model for training and testing dataset were most adequate for predicting the mechanical strength of 3D-printed screws.

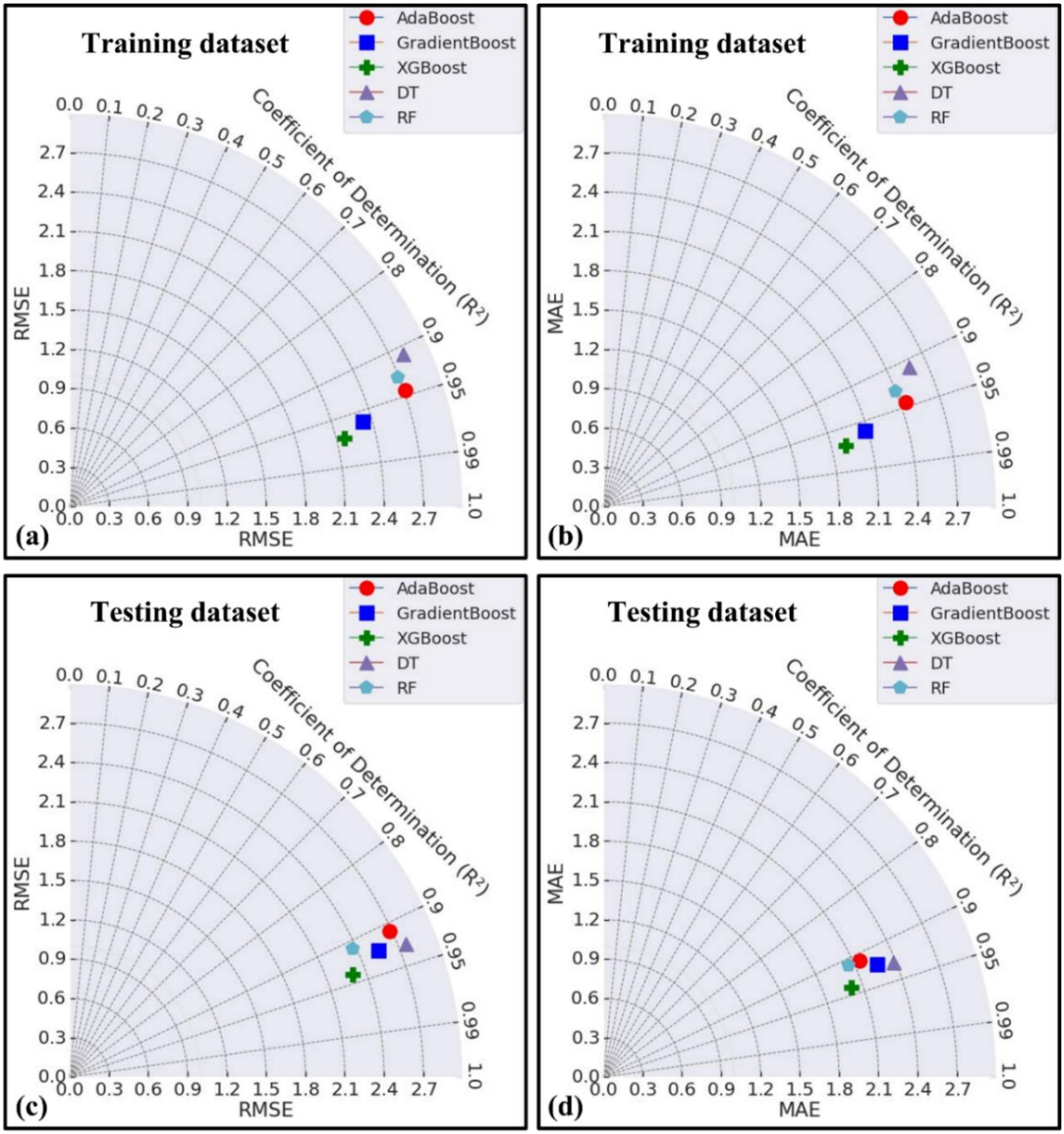


Figure 4.13. Taylor diagram for evaluating the performance of different models for (a-b) training data and (c-d) testing data.

After evaluating the error metrics of different ML models, the predictive performance of different ML models was observed via a scatter plot of experimental and predicted compressive strength values of 20 testing data points as depicted in Figure 4.14. The x-axis of the scatter plot represents the experimental values of compressive strength, and the y-axis represents the predicted values of compressive strength by different ML models. Each scatter plot graph consists of a 1:1 straight line indicating a perfect fit. Model fitting is more effective when scatter points are close to straight lines. The closeness of scatter points with straight lines represents better predictive performance and robustness of ML models.

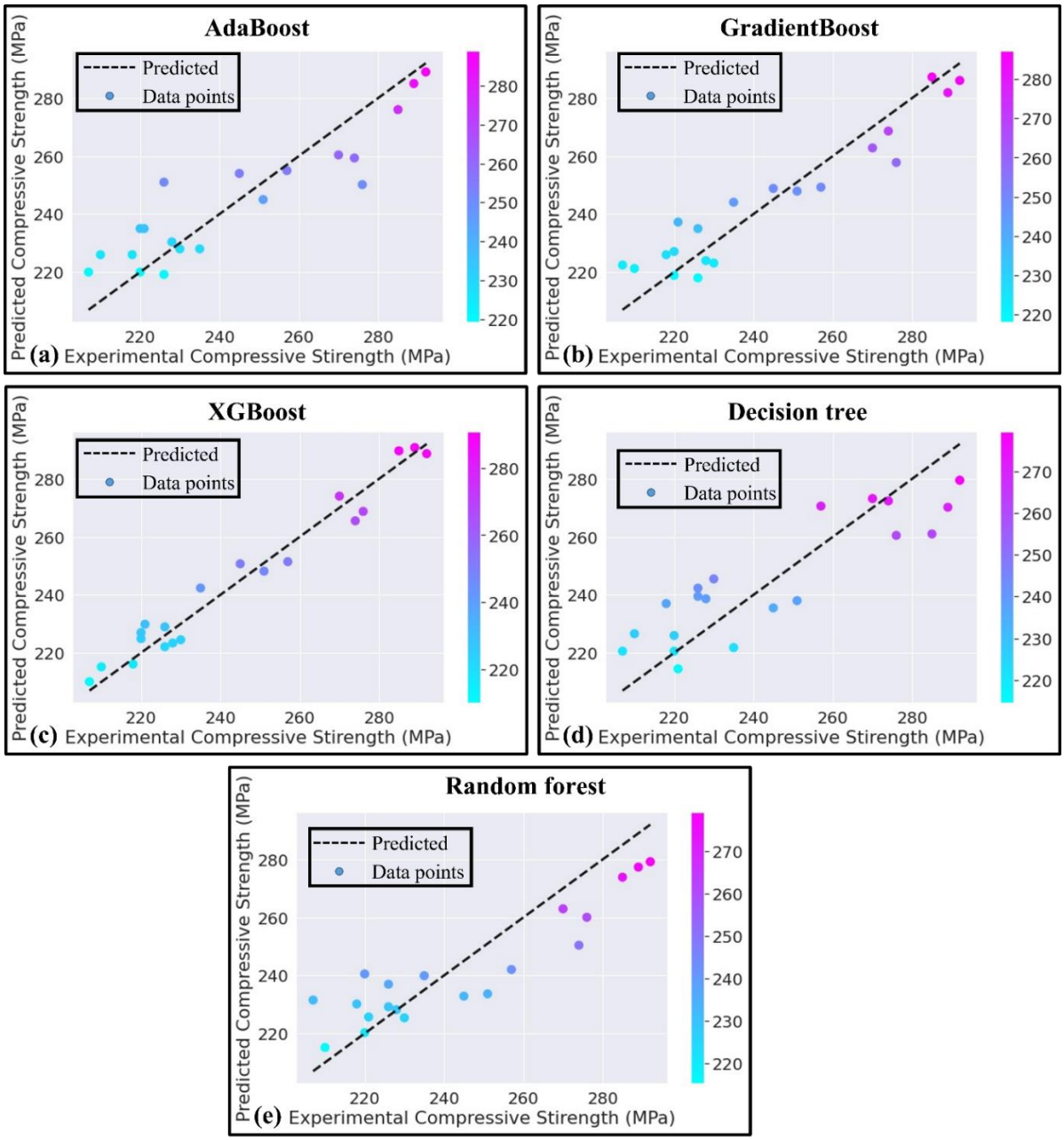


Figure 4.14. Predictive performance of different ML algorithms for (a) AdaBoost, (b) GradientBoost, (c) XGBoost, (d) decision tree, (e) random forest.

The AdaBoost algorithm represents the discrete distribution of predicted and experimental compressive strength values as illustrated in Figure 4.14(a). The GradientBoost perform better prediction compared to the AdaBoost model, as different data scatter points were close to a straight line as visualized in Figure 4.14(b). But very few scatter points were close to the straight line represent not an adequate predictive model. It was witnessed that the XGBoost ensemble model has an excellent and superior fit of scatter points experimental values of mechanical strength with the predicted compressive strength values as illustrated in Figure 4.14(c). The scatter points were separately distributed with the straight line during the

decision tree model as observed in Figure 4.14(d) representing not adequate predictive results. The predictive results by the random forest model show a better correlation of scatter points with a straight line as envisaged in Figure 4.14(e), but lower adequacy compared to ensemble ML models. Hence, it can be elucidated from the scatter plot that the XGBoost ensemble ML model has the highest accuracy with satisfactory predictive performance.

4.9. Conclusions

During the present chapter, 100 orthopaedic cortical screws were fabricated using fused filament fabrication-based 3D-printing technology by varying different process parameters. The influence of independent parameters on the mechanical strength of screws was evaluated. Different ML models (kNN, SVR, DT, and RF) with ensemble ML models AdaBoost, XGBoost and GradientBoost were leveraged to predict the compressive strength of 3D-printed cortical screw. Based on the accuracy of different ML models, the robustness and adequacy of ML techniques were defined by different error metrics. Based on the performance of different ML models, the following conclusions have been made.

- The error metrics of the random forest model were comparatively lower for training data with an MAE of 2.4 ± 0.151, RMSE of 2.69 ± 0.17, R^2 of 0.93 ± 0.053 and testing data with an MAE of 2.06 ± 0.91, RMSE of 2.37 ± 0.9 and R^2 of 0.96 ± 0.042.
- Ensemble ML models have higher adequacy and minimum error metrics compared to base learning ML models.
- XGBoost ensemble ML model has the least error metrics and the most adequate results for predicting compressive strength.
- The honeycomb pattern with 100% infill density has the highest mechanical strength.

Chapter V

Effect of drilling techniques on the biomechanical pullout strength

Chapter 5

Effect of drilling techniques on the biomechanical pullout strength

5.1 Introduction

Bone drilling is imperatively required for fractured bone fixation used during orthopaedics surgeries, joint replacement, plate implantation, total knee arthroplasty and various orthopaedic applications. The success of the surgery and level of post-operative discogenic pain is highly dependent upon poor holding power [172], pullout strength [173], interlayer delamination [174], initial implant stability [175], hole inaccuracy [3], microcracks in the surrounding soft tissues [176], and thermal injuries [12]. Drilling parameters used during orthopaedic surgeries significantly influence the holding power, initial implant stability and biomechanical pullout strength. Biomechanical pullout strength is defined as the force required for pulling a screw out of its foundation in bone [177]. Lower pullout strength [177] and insufficient holding strength [26] at the bone-screw interface is the primary reason for bone loss during healing [22] and screw loosening [24].

The preoperative and perioperative decision by the orthopaedic surgeon during fracture fixation decides the initial holding strength that influences the biomechanical pullout strength of bone screws. Various factors such as screw length, insertion depth, thread pitch, insertion torque, cannulation, screw diameter, screw reinsertion and insertion angle influence the pullout strength of orthopaedic screws [23, 178–182]. It can be observed from the literature that insertion angle, drill angle, or tilt angle is a significant factor that influences the holding power and pullout strength of implanted orthopaedic bone screw. The influence of ultrasonic-assisted drilling at different inclination angles on cutting force, temperature and pullout strength of bone screw is scantly reported.

Rotary ultrasonic-assisted bone drilling (RUABD) has achieved noteworthy interest in orthopaedic research and clinical applications due to the advantage of reducing thermal necrosis, cutting force, microcracks and enhancing the biomechanical pullout strength. In this chapter, bone drilling experiments are presented with varying drilling angles on porcine femur bone with RUABD and Conventional bone drilling (CBD). Porcine femur bones were selected for the drilling experiments owing to similar thermomechanical properties with human femur bones [183]. The influence of different drilling techniques at different inclination angles was

monitored on the temperature, microcracks, cutting force, and pullout strength. During the RUABD, a diamond-impregnated tool was used with various drilling parameters including ultrasonic actuation. Whereas, during CBD, the drilling experiments were performed with similar drilling parameters without ultrasonic vibrations with a surgical twisted drill bit to monitor pull-out strength, microcracks, cutting force and temperature elevations. Cutting force and temperature elevations were measured with the help of a dynamometer and thermal imaging camera respectively. Various bone screw samples were assessed for their biomechanical pullout strength in the universal testing machine as an indication of the maximum load applied until the screw was extracted from the bone. In this chapter the biomechanical pullout strength, microcracks, cutting force, and temperature elevations were monitored at different inclination angles during different drilling techniques (RUABD and CBD) on porcine femur bones.

5.2 Experimental procedure

Experiments were performed in two sets. In the first set of experiments, temperature elevations, microcracks and cutting force analysis were carried out for the RUABD and CBD processes while mechanical pullout strength was measured in the second set. The experiments were planned and performed according to the process parameters for both drilling processes, as listed in **Table 5.1**. A single variable study was used for drilling experimental investigation to understand the influence of each parameter separately. Suitable combinations of parameters which can show the effect of variable rotational speed and a variable feed rate with keeping other process parameters constant were used to study the biomechanical pullout strength of cortical screw.

5.2.1. Workpiece information

The thermal and mechanical properties of fresh porcine bones are homogenous and quite similar to that of human bones [23, 183]. No animals were sacrificed, as fresh porcine femur bones were obtained from the slaughterhouse. Four femur bones were harvested from each porcine. A total of sixteen femur bones were harvested from four male porcine of almost similar age and weight. The harvested femur bones were preserved in a buffered formalin solution (formalin, Sigma Aldrich) with a 10% concentration to maintain their biological properties. After removing the distal and proximal ends, the mid-diaphysis section was chosen as a drilling

location for bone drilling experimentation. The experiments were accomplished within 3 hours after the process of cleaning the bone samples to maintain the bone properties.

5.2.2. Drilling parameters selection

Based on the pilot study and literature review [184–186], the primary input process parameters have been chosen that affect most during the drilling process. Four major process parameters were selected and varied up to five different levels, as presented in Table 5.1. These drilling parameters are inclination angle, feedrate, rotational speed, and ultrasonic amplitude. The inclination angle is the variation of the angle from the drilling axis to the bone surface. During the present work, the inclination angle was varied from 0°, 10°, 20°, 30°, and 40°. These angles were finally selected as there were no significant differences after these drilling angles during the pilot study. The drilling tool's rotational speed refers to its rate of rotation which is essential for effective drilling during surgery. The range of rotational speed was varied from 600 to 3600 RPM for the current study as this range is widely used in the literature [184, 187–189]. Feedrate is another essential parameter that affects the drilling outcomes. The velocity at which a drill bit is introduced into the bone workpiece to make a precise hole is known as the drill feedrate. From the literature [184, 187–189], the range of 10-50 mm/min feedrate has been chosen for this in-vitro study.

With the use of vibrational ultrasonic amplitude, non-uniform contact between bone and tool surface can be obtained. The range from 0 to 20 µm was varied for ultrasonic amplitude during RUABD. The specifications of the drilling tools used during RUABD and CBD are presented in Table 5.2. Based on the variation in different drilling parameters, the run order for RUABD is followed as presented in Table 5.3. CBD experiments were performed without supplying ultrasonic amplitude as presented in Table 5.3.

Table 5.1. Process parameters used for experimental investigation.

Input parameters	Values	Units
Ultrasonic amplitude (UA)	0, 5, 10, 15, 20	µm
Inclination angle (IA)	0, 10, 20, 30, 40	Degree
Feedrate (FR)	10, 20, 30, 40, 50	mm/min
Rotational speed (RPM)	600, 1200, 1800, 2400, 3000, 3600	RPM

Table 5.2. Specifications of drilling tools used during RUABD and CBD.

Diamond-impregnated drill tool		**Surgical twisted drill tool**	
Abrasive grit size	120 µm	Helix angle	8.4°
Abrasive used	Diamond grits	Tool material	Stainless steel
Outer diameter	3.5 mm	Number of cutting lips	2
Inner diameter	2.5 mm	Point angle	120°
Wall thickness	1 mm	Diameter	3.5 mm

Table 5.3. Run order followed to perform RUABD and CBD experiments.

IDs	**RUABD**				**CBD**		
	UA	**IA**	**FR**	**RPM**	**IA**	**FR**	**RPM**
1	0	0	10	600	-	-	-
2	5	0	10	600	-	-	-
3	10	0	10	600	-	-	-
4	15	0	10	600	-	-	-
5	20	0	10	600	-	-	-
6	20	0	10	600	0	10	600
7	20	10	10	600	0	10	600
8	20	20	10	600	0	10	600
9	20	30	10	600	0	10	600
10	20	40	10	600	0	10	600
11	20	0	10	600	0	10	600
12	20	0	20	600	0	10	600
13	20	0	30	600	10	10	600
14	20	0	40	600	20	10	600
15	20	0	50	600	30	10	600
16	20	0	10	600	40	10	600
17	20	0	10	1200	0	10	600
18	20	0	10	1800	0	20	600
19	20	0	10	2400	0	30	600
20	20	0	10	3000	0	40	600

5.2.3. Experimental investigation

A computer numerical control (CNC) machine was used for the drilling of porcine femur bones. Ultrasonic actuation was provided by a piezoelectric transducer attached to the chuck of the CNC machine. As the bone has irregular geometry, a special fixture has been designed and fabricated. The drilling procedure was performed with a diamond-impregnated tool with a diameter of 3.5 mm. Through the CNC machine's control panel, the feedrate and rotational speed during drilling were controlled. The variation of vibrational ultrasonic amplitude (UA) was varied with the ultrasonic generator box.

To observe thermal variation during bone drilling infrared thermography technique is used. It uses a thermal imaging camera for monitoring temperature elevation during bone drilling as depicted in Figure 5.1(a). The infrared sensor detects the infrared energy emitted by the bone surface during the penetration of the drill bit into the bone surface. During the drilling of femur bones, the drilled hole quality was monitored with the Dino-light camera as illustrated in Figure 5.1(b). The microscopic observation of drilled holes during drilling illustrates the variation of surface morphology and bone debris formation during bone drilling. The inclination angle during bone drilling was changed with variations in special wooden blocks fabricated with different angles as depicted in Figure 5.1(c).

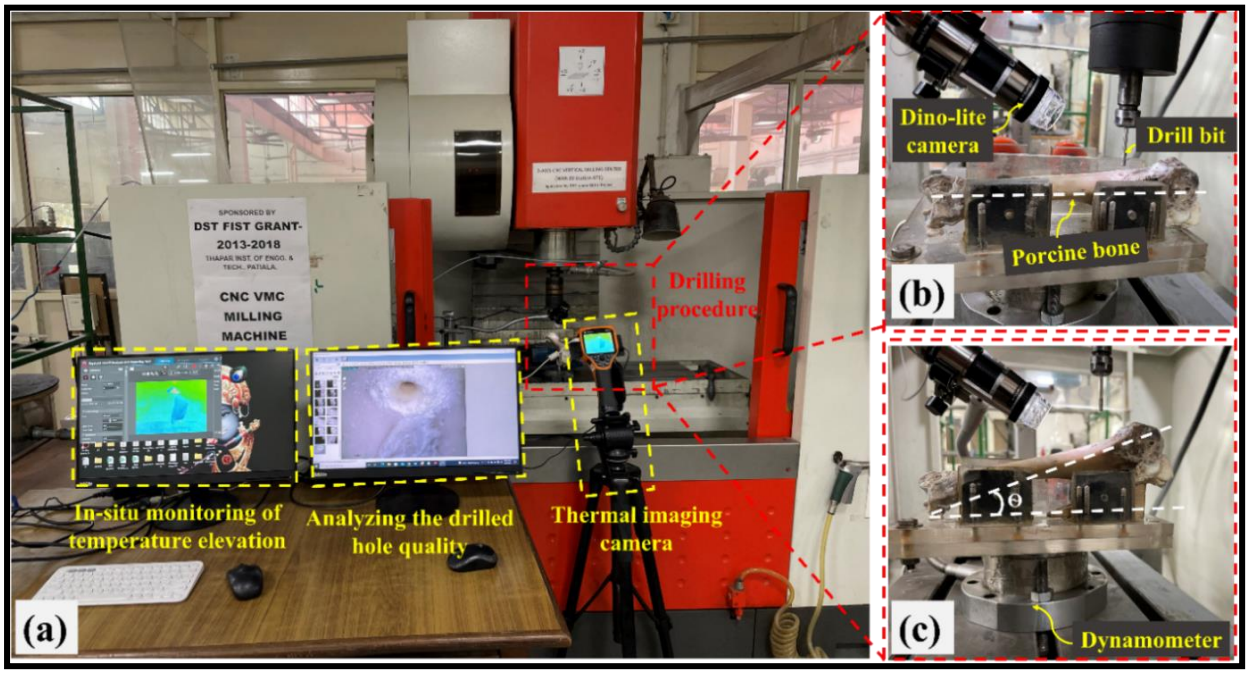


Figure 5.1. (a) drilling setup, (b) perpendicular drilling, (c) inclined drilling for porcine femur bones.

The cutting force generated at the drill site during the drilling experiments was measured with the help of a dynamometer (Kistler-type 9272) as depicted in Figure 5.1(c). Based on the run order of different IDs (Table 5.2), the experimentation for RUABD and CBD was performed to monitor the induced cutting force and temperature elevations. Further, bone was sectioned to examine their osteocyte track and drilling streaks using SEM micrographs.

5.2.4. Pullout strength testing

After monitoring the maximum temperature and cutting force, 4.5 mm surgical cortical screws were inserted carefully into the drilled bone samples. Further, the bone screw samples were prepared by slicing the bones sensibly and carefully perpendicular to the bone axis using a diamond surgical hacksaw for their mechanical characterization during pullout testing. The resisting holding strength and maximum required force to pull the cortical screws out from the bone surface were monitored using pullout testing setup as depicted in Figure 5.2.

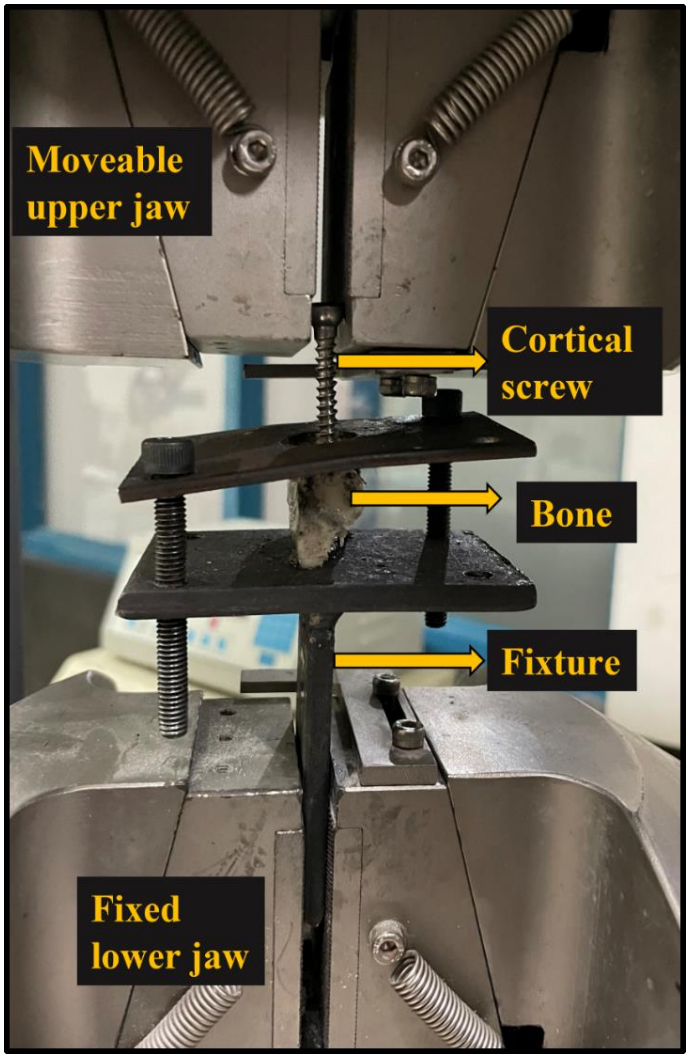


Figure 5.2. Biomechanical pullout strength testing setup.

Various bone screw samples were assessed for their biomechanical pullout strength in the universal testing machine (UTM) machine as an indication of the maximum load applied until the screw was extracted from the bone. In order to accommodate inclined bone-screw specimens, an in-house fabricated fixture was used to ensure adequate screw placement at the upper jaw of the UTM machine as depicted in Figure 5.2. The bone-screw specimens were held in the centre of the customized fixture, and both ends of the fixture rested in the upper jaw and lower jaw of the UTM machine.

5.3. Result and Discussion

5.3.1. Measurement of induced cutting force

The cutting force was measured during bone drilling using a *Kistler (Type 9272) 4-component Dynamometer*. The axial cutting force was measured perpendicular to the bone axis in the z-axis direction. The highest peak value of induced cutting force values based on different run orders is presented in Table 5.4. The change in percentage for cutting force during RUABD and CBD is also observed in Table 5.4. It was observed that cutting force during RUABD is significantly lower as compared to CBD of porcine femur bone. The RUABD technique reduces the cutting force by approximately 35% compared to CBD. This is due to non-uniform contact between the cutting tool and bone surface. Hence, RUABD technique can be used to reduce the induced cutting force during the drilling of porcine femur bones.

The influence of drilling parameters on the induced cutting force during RUABD and CBD is depicted in Figure 5.3. Maximum induced cutting force during the RUADB was observed to be higher as compared to CBD as illustrated in Figure 5.3. The influence of the inclination angle on the induced cutting force during bone drilling is presented in Figure 5.3(a). It can be observed that with an increase in inclination angle from 0^0 to 40^0 during bone drilling, the cutting force also increases. This is due to an increase in the contact area and friction at the tool-bone interface. The change in feedrate, influences the cutting force during drilling of porcine femur bones.

By increasing the feedrate during drilling, it can be observed that cutting force surges as illustrated in Figure 5.3(b). An intuitive explanation for this phenomenon is that a higher feedrate increases the surface contact at the bone-tool site. Also, with increasing the feedrate during drilling increases the material removal rate. The increase in material removal rate during

drilling increases the friction and centrifugal force. These results are also similar with the previous reported studies [185, 190].

With increasing rotational speed, cutting force was observed to be increasing during both the drilling techniques (RUABD and CBD) as illustrated depicted in Figure 5.3(c). It is due to the reason of burr loading at the bone-tool interface that influences the thermal energy and cutting force. With increasing drilling rotational speed, the friction at the bone-tool interface increases. These results are also similar with the previous reported studies [165, 173].

Table 5.4. Cutting force during RUABD and CBD techniques.

Run IDs	Cutting force (N)		
	RUABD	CBD	Change in %
1	62.2	-	-
2	56.3	-	-
3	50.5	-	-
4	42.1	-	-
5	37.0	-	-
6	37.0	48.5	31
7	43.6	57.8	32.5
8	50.2	67.5	34.5
9	56.8	77	35.5
10	67.7	92	35.8
11	37.0	48.5	31
12	49.6	66.3	33.6
13	58.1	78	34.2
14	63.9	86.5	35.3
15	66.3	90.5	36.5
16	37.0	48.5	31
17	44.3	59	33.1
18	51.1	69	35
19	58.4	80	36.9
20	68.7	95	38.2

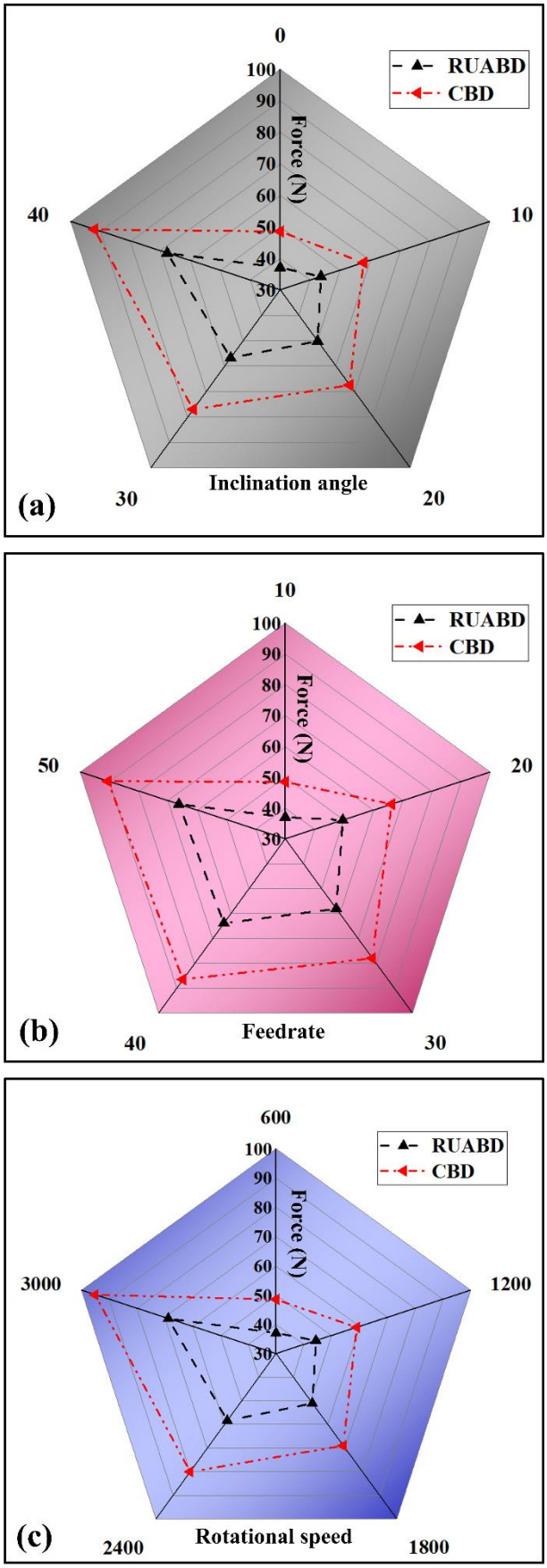


Figure 5.3. The influence of process parameters on induced cutting force (a) inclination angle vs force, (b) feedrate vs force, (c) rotational speed vs force.

5.3.2. In-situ temperature monitoring

The infrared energy emitted by the bone surface during drilling is detected by the infrared sensors of the thermal imaging camera. In-situ temperature monitoring during RUABD illustrates the variation in the thermal behaviour of bone represented by different thermograms as illustrated in Figure 5.4. During RUABD, ultrasonic actuations were provided at different amplitude levels that create non-continuous contact at the bone-tool interface. Due to less surface contact at the bone-tool interface, lower temperature elevations at the drill site were observed as depicted in Figure 5.4.

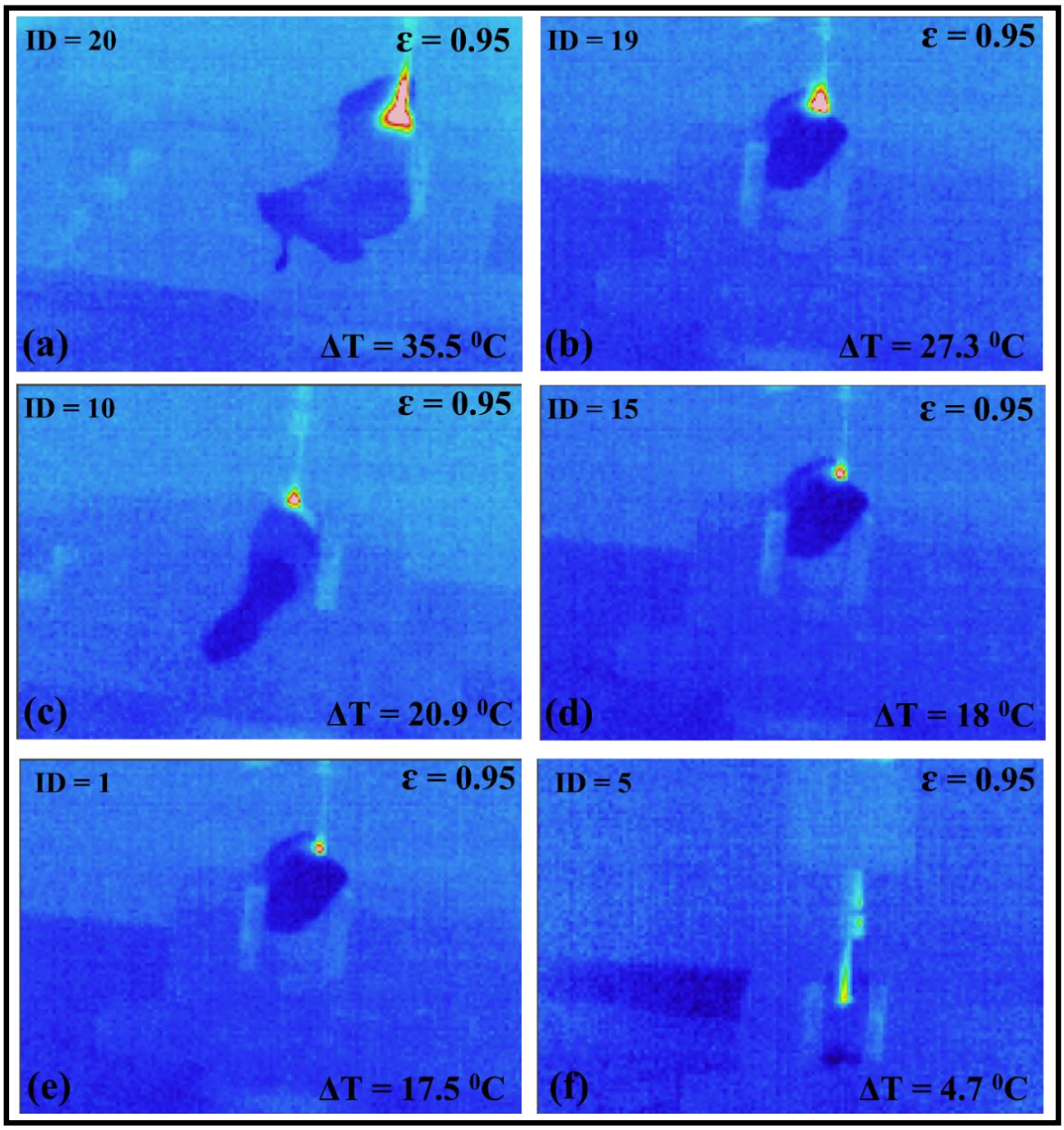


Figure 5.4. Infrared thermograms during RUABD at different run order of (a) ID 20, (b) ID 19, (c) ID 10, (d) ID 15, (e) ID 1, (f) ID 5.

Thermograms observed with CBD are illustrated in Figure 5.5. It was observed that CBD generates higher temperatures for similar run-order IDs without ultrasonic vibrations as compared to RUABD. Thermogenesis and thermal energy at the bone-tool interface instigate to increase with continuous engagement at bone and drilling tool. The continuous contact at bone-tool interface results to increase friction that increases the temperature elevations.

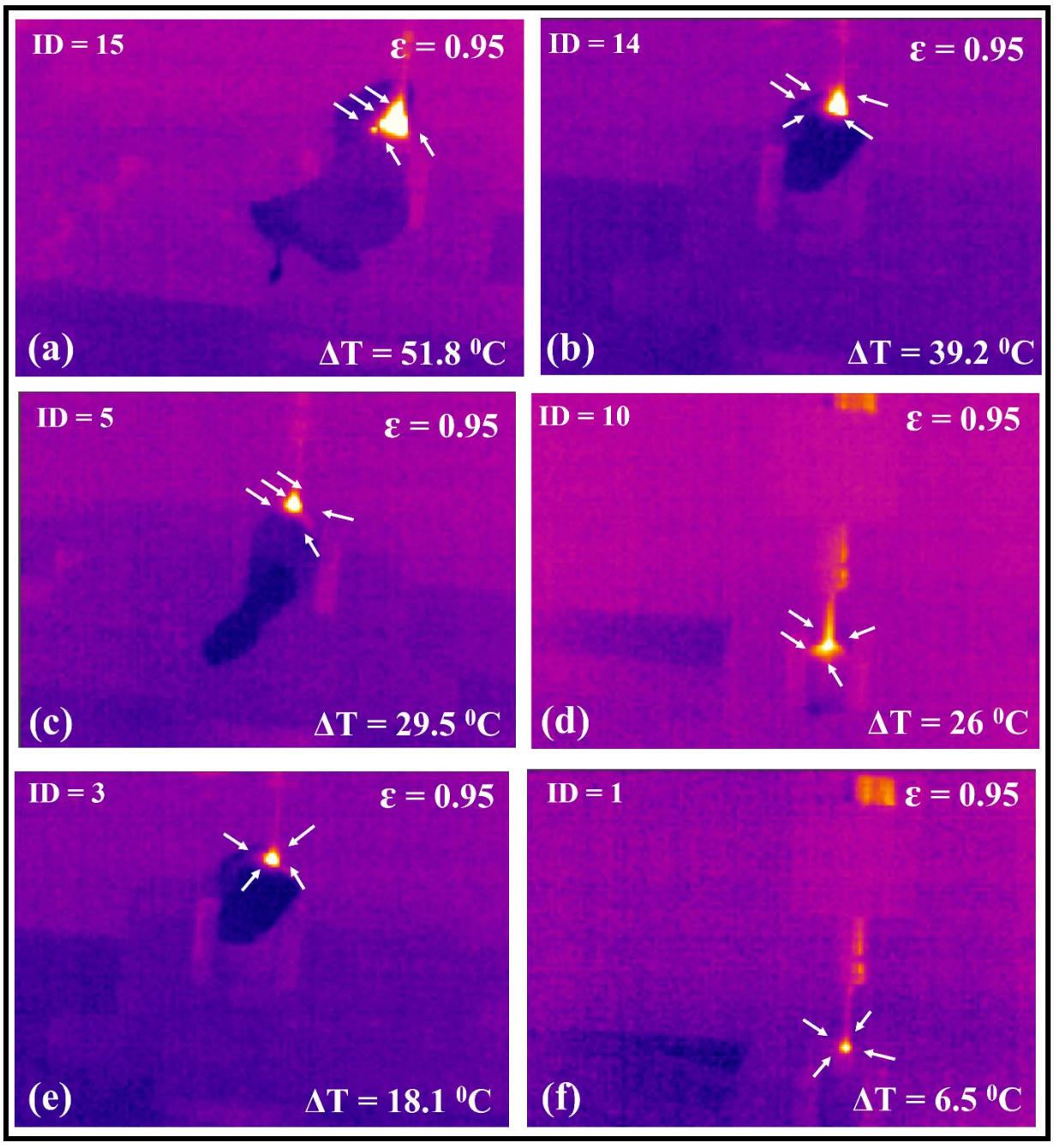


Figure 5.5. Infrared thermograms during CBD at different run order of (a) ID 15, (b) ID 14, (c) ID 5, (d) ID 10, (e) ID 3, (f) ID 1.

The temperature monitored with different drilling techniques are presented in Table 5.5. It was RUABD can reduce the temperature elevations by 30-40% as compared to CBD. It

was also observed that with variations in different process parameters during drilling, the temperature of bone varies. It was observed for both drilling techniques that with increasing rotational speed, the friction at the bone-tool interface increases. With increasing feedrate for both drilling techniques, the temperature was elevated. While varying the inclination angle from 0^0 to 40^0, it was observed that temperature elevates. This is due to an increase in the contact area and friction at the bone-tool interface during increasing the inclination angle. Hence, with increasing rotational speed, feedrate and inclination angle, temperature increases. Increasing ultrasonic vibrations reduce the temperature elevation at the bone-tool interface.

Table 5.5. Temperature elevations during RUABD and CBD techniques.

Run IDs	Temperature (in °C)		
	RUABD	**CBD**	**Change in %**
1	17.5	-	-
2	15.3	-	-
3	11	-	-
4	7.5	-	-
5	4.7	-	-
6	4.7	6.5	38.29
7	8.8	12.2	38.63
8	13	18.1	39.23
9	16.8	23.5	39.88
10	20.9	29.5	41.14
11	4.7	6.5	38.29
12	9.1	12.8	40.65
13	12.8	18.3	42.96
14	15.7	22.5	43.31
15	18	26	44.44
16	4.7	6.5	38.29
17	13.4	18.8	40.29
18	18.9	26.9	42.32
19	27.3	39.2	43.58
20	35.5	51.8	45.91

5.3.3. Biomechanical pullout strength of cortical screws

To evaluate the biomechanical pullout strength at the bone-screw interface, a universal testing machine was used. The biomechanical pullout testing setup to perform the push-out testing of bone-screw specimens. As there were different samples with different orientations of screws for inclination angle, the schematic for different bone samples is presented in Figure 5.6. The perpendicular bone-screw samples were easily placed in the fixture. The drilled hole morphology of both drilling techniques indicates the hole quality that can be correlated with the initial holding strength with the inserted bone screw.

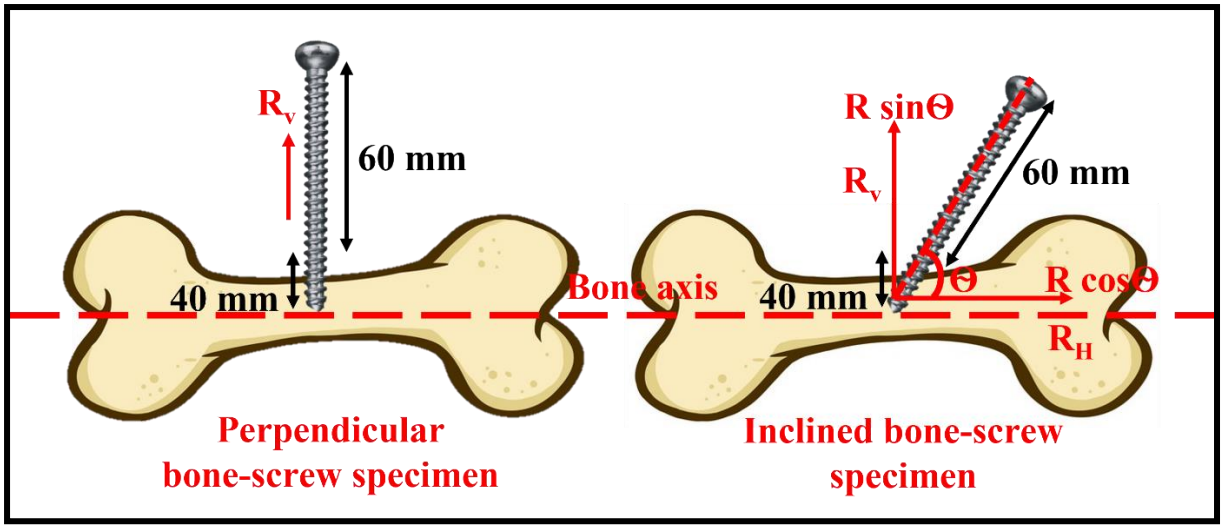


Figure 5.6. Schematic for perpendicular and inclined bone-screw samples.

The maximum value of pullout strength of cortical screws for different samples with different drilling techniques was monitored as depicted in Figure 5.7. It was observed that with increasing the inclination angle of drilling, the pullout strength is decreasing for both RUABD and CBD as presented in Figure 5.7(a). This decrease is due to the decrease in stiffness and increases in microcracks at the drill site. The influence of change in feedrate during drilling on the pullout strength at the bone-screw interface is shown in Figure 5.7(b). It was observed that with increasing feedrate, the pullout strength decreased because of an increase in material removal rate during bone drilling. With increasing rotational speed, the pullout strength also increased as represented in Figure 5.7(c). This is due to the decrease in cutting force and microcracks at the drill edge site. The monitored pullout strength for RUBAD and CBD is presented in Table 5.6. For different drilling parameters, the pullout strength by RUABD samples was significantly higher (approximately 50%) as compared to CBD samples due to precise cut and no microcracks at the drill site.

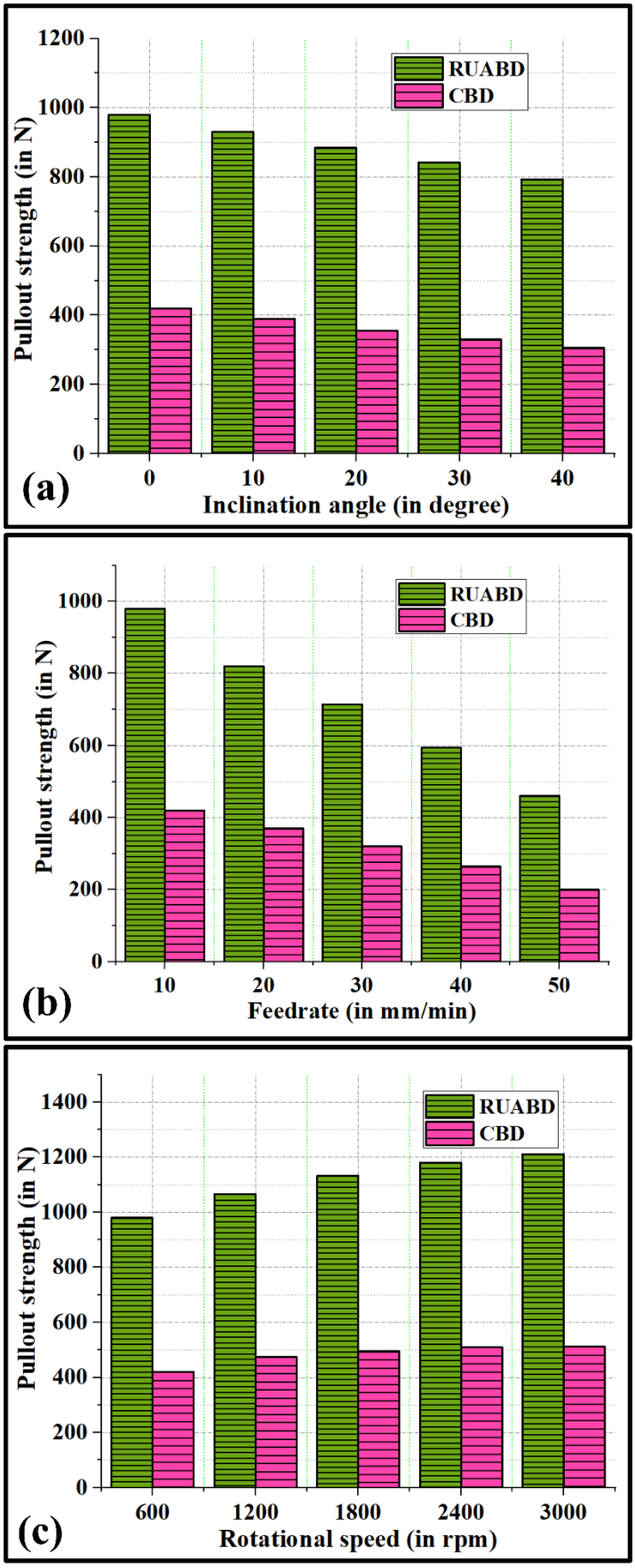


Figure 5.7. Effect of (a) inclination angle, (b) feedrate, and (c) rotational speed on the biomechanical pullout strength.

Table 5.6. Biomechanical pullout strength during RUABD and CBD techniques.

Run IDs	Biomechanical pullout strength (in N)		
	RUABD	CBD	Change in %
1	768	-	-
2	820	-	-
3	875	-	-
4	930	-	-
5	980	-	-
6	980	420	57.14
7	930	390	58.06
8	884	355	59.84
9	841	330	60.76
10	793	305	61.5
11	980	420	57.14
12	820	370	54.8
13	715	320	55.24
14	595	264	55.63
15	460	200	56.52
16	980	420	57.14
17	1066	475	55.44
18	1132	495	56.27
19	1180	510	56.77
20	1211	512	57.7

5.3.4. Morphology of drilled holes

The inclined drilled holes created by different drilling techniques were observed at microscopic level using SEM analysis. The microcracks presents at the drill site for both drilling methods indicates the holding strength with screw threads. It was observed that RUABD drilled hole shows a precise incline cut with no bone rupture and evident osteocyte track as illustrated in Figure 5.8(a). RUABD created holes with osteocyte track indicates higher holding strength at bone-screw interface. Whereas CBD hole quality indicates high bone rupture at the drill entrance with the delaminated bone periphery as depicted in Figure 5.8(b). No osteocyte track,

only microcracks were observed with CBD drilled bone surface. The bone surface morphology and drilled hole quality indicate the initial screw stability and holding strength at the bone-screw interface. Hence, RUABD drilled holes have higher biomechanical pullout strength as compared to CBD drilled holes.

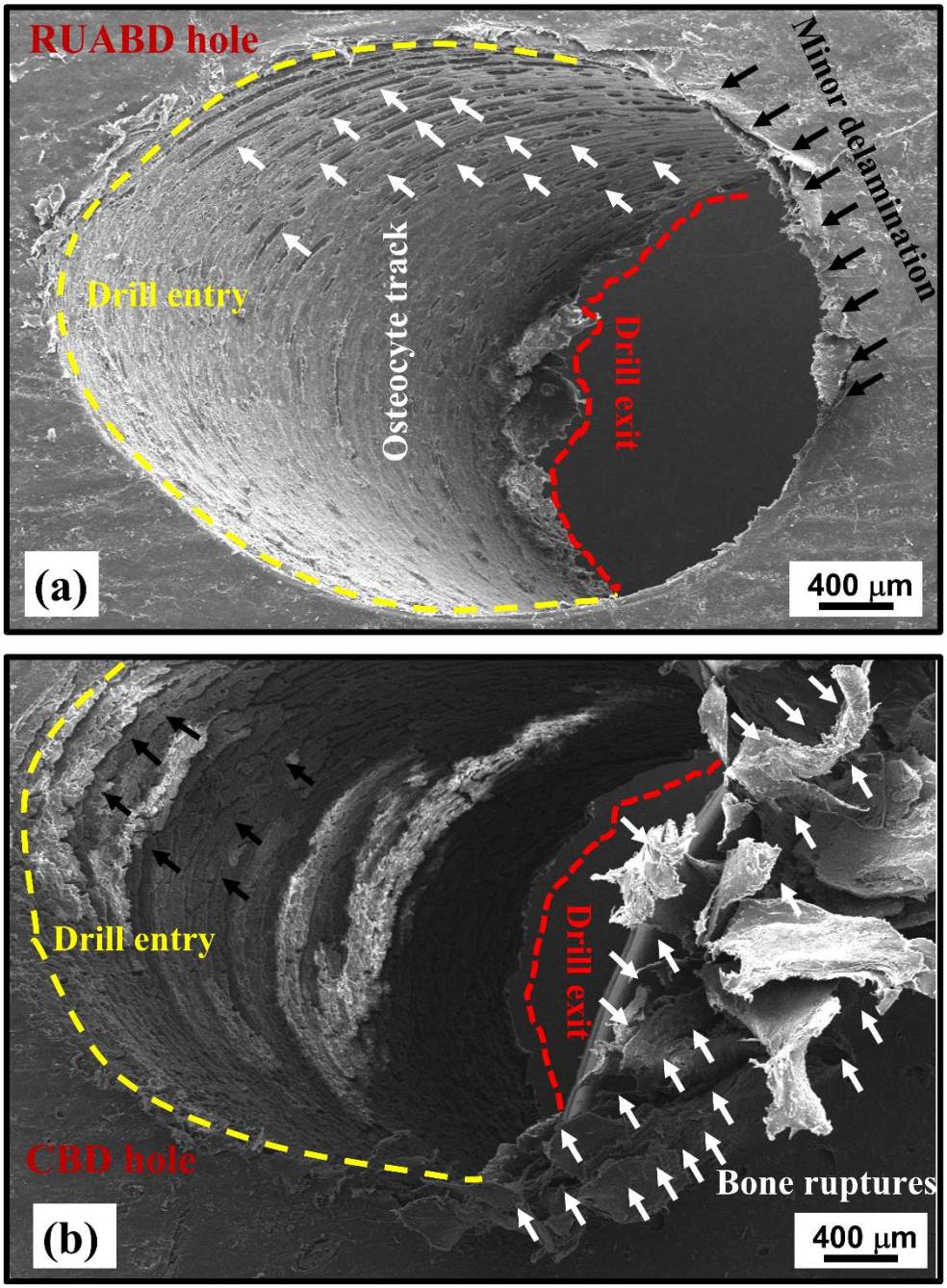


Figure 5.8. SEM micrographs of inclined drilled holes during (a) RUABD, (b) CBD.

The drilled bone surfaces of different drilling methods (CBD and RUABD) were sectioned using surgical hacksaw to observe at microscopic levels. The drilled hole by CBD technique is presented in Figure 5.9(a). With the CBD technique, no osteocyte track was

observed as represented in Figure 5.9(b). Due to continuous drilling and higher friction at drill site, higher microcracks were witnessed during CBD as depicted in **Figure 5.9(c)**. The surface morphology represents the holding strength at the bone-screw interface.

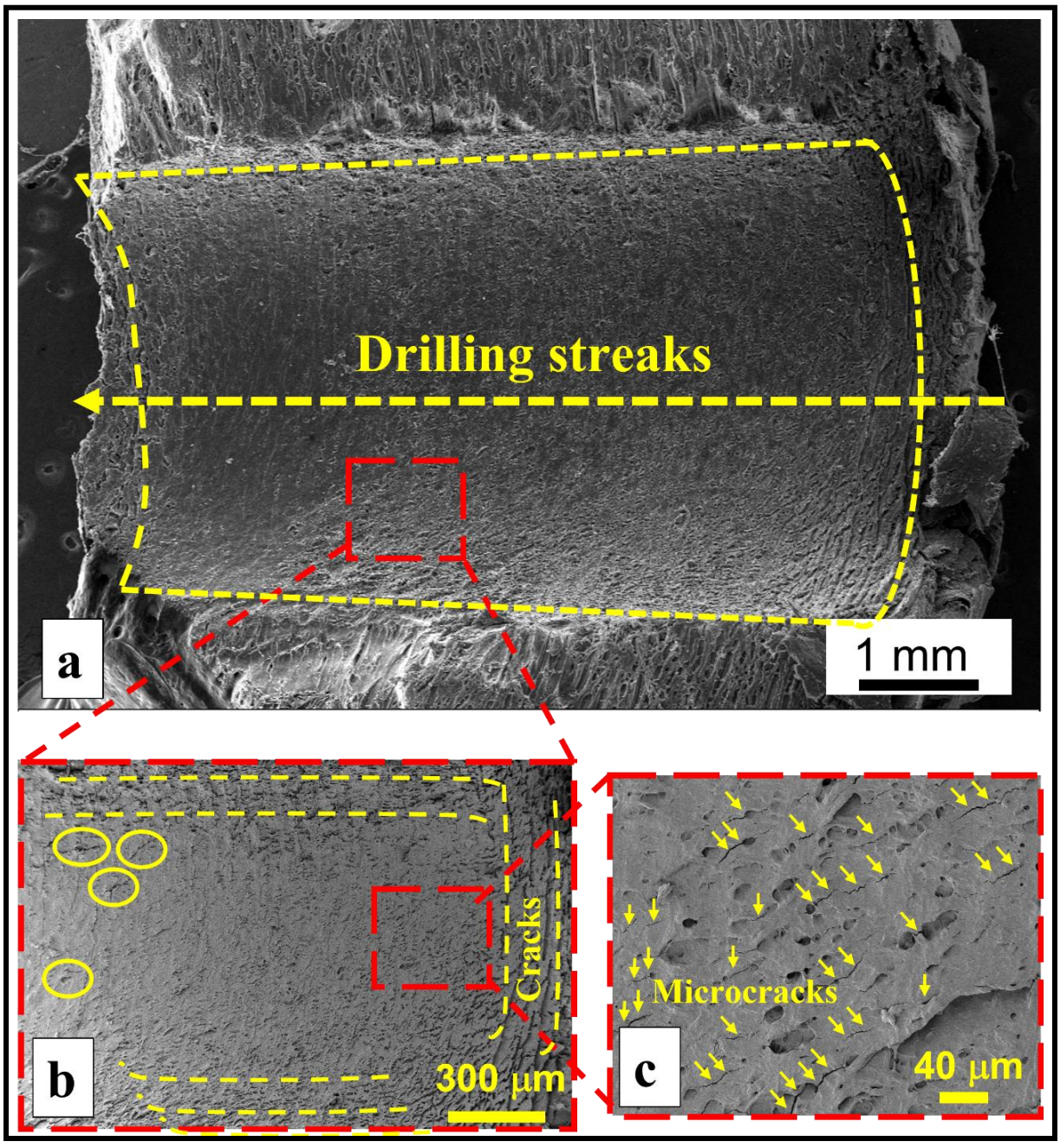


Figure 5.9. SEM micrographs of drilled holes during CBD of the porcine femur bone.

RUABD drilled hole surface show drilling streaks as presented in Figure 5.10(a). RUABD drilled hole is observed with osteocyte tracks indicating precise cut as illustrated in Figure 5.9(b). These evident osteocyte tracks were observed to have no microcracks as depicted in Figure 5.9(b). These visible osteocyte tracks without microcracks can improve the integration between threads of bone screw to improve the holding power and pullout strength.

This is also reported in the literature that with less microcracks at drill site, higher pullout strength of bone screw is observed [16, 155].

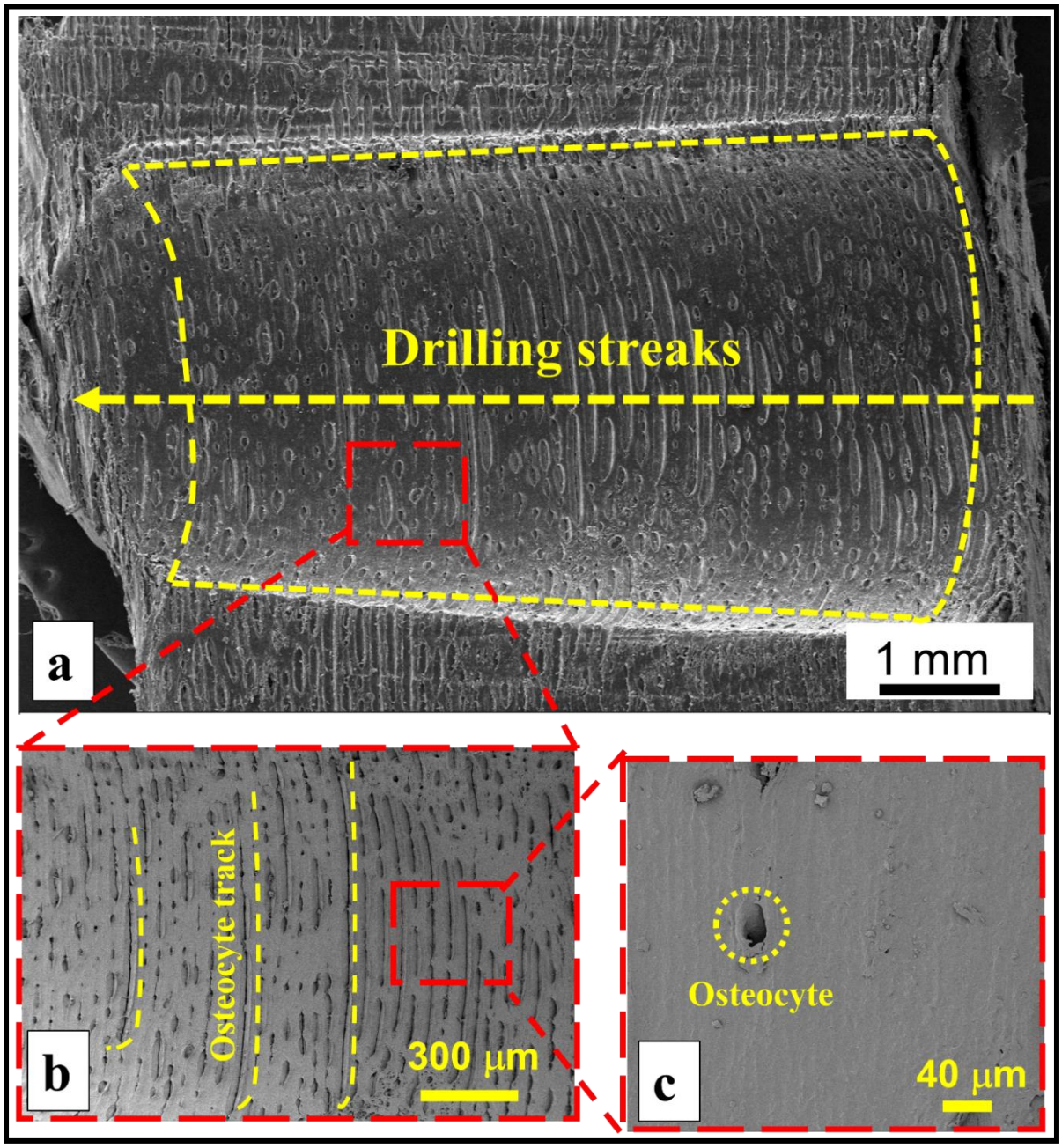


Figure 5.10. SEM micrographs of drilled holes during RUABD of the porcine femur bone.

5.3.5. Micrographs at bone-tool interface

The bone-tool morphology is also observed at microscopic level to understand the material removal during drilling with different techniques. With CBD, the burnt bone chips were adhered in the surgical twisted drill bit as presented in Figure 5.11(a). The micrograph of accumulated burnt bone chips in a conventional twisted drill bit is illustrated in Figure 5.11(b). Because of this agglomeration of bone chips (Figure 5.11(c)), friction at the bone-tool interface

increases owing to burr loading that lead to temperature elevations. The elements present in clustered bone at drill bit are presented in Figure 5.11(d). It was observed that high calcium percentage of 23.96% indicates higher bone accumulation at the drill tool. The burr loading and bone chip agglomeration at drill site indicates increase in induced cutting force.

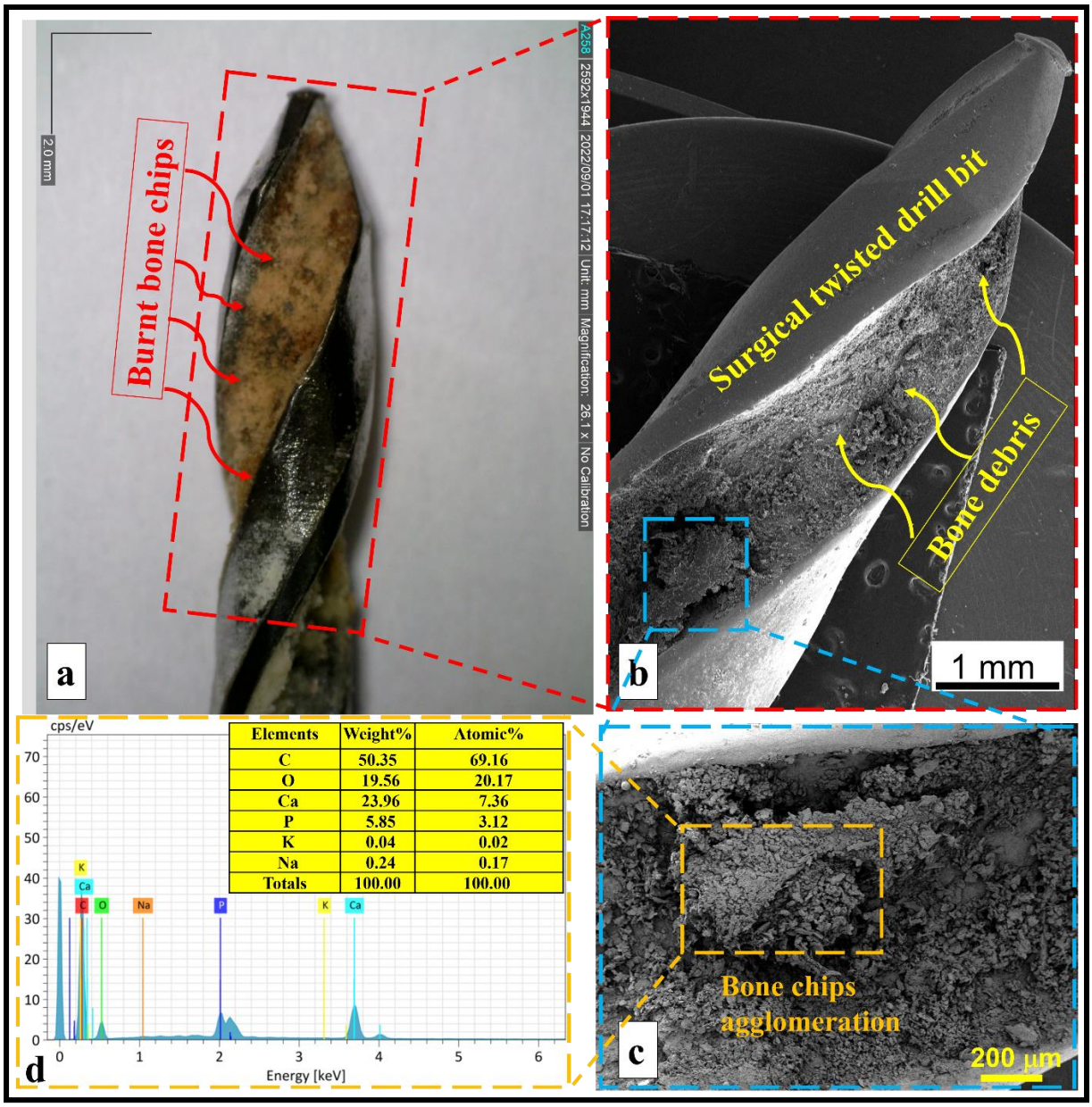


Figure 5.11. (a) Burnt bone chips agglomerated in the conventional surgical twisted drill bit, (b) micrographs of bone-tool morphology, (c) adhered bone chips in flutes of the surgical tool, (d) EDS of the surgical tool after drilling.

Whereas during RUABD, the diamond-impregnated tool was used. The clustered white bone debris with the diamond tool is presented in Figure 5.12(a). The powdered bone debris was clustered between the diamond grits of the drilling tool indicating no burning of the bone

surface as depicted in Figure 5.12(b). The enlarged view of clustered bone debris at the diamond-impregnated tool is illustrated in Figure 5.12(c). The elements present in clustered bone debris in the diamond tool are presented in Figure 5.12(d). A higher carbon percentage of 68.53% indicates diamond grits on the periphery of drill bit and a lower calcium percentage of 7.6% indicates minimal bone debris accumulation in diamond-impregnated tool. These powdered-shaped bone debris are expected to reduce the chip clogging, temperature elevations and induced cutting force at the drill site. Similar results were observed in the previous published researches [155, 161].

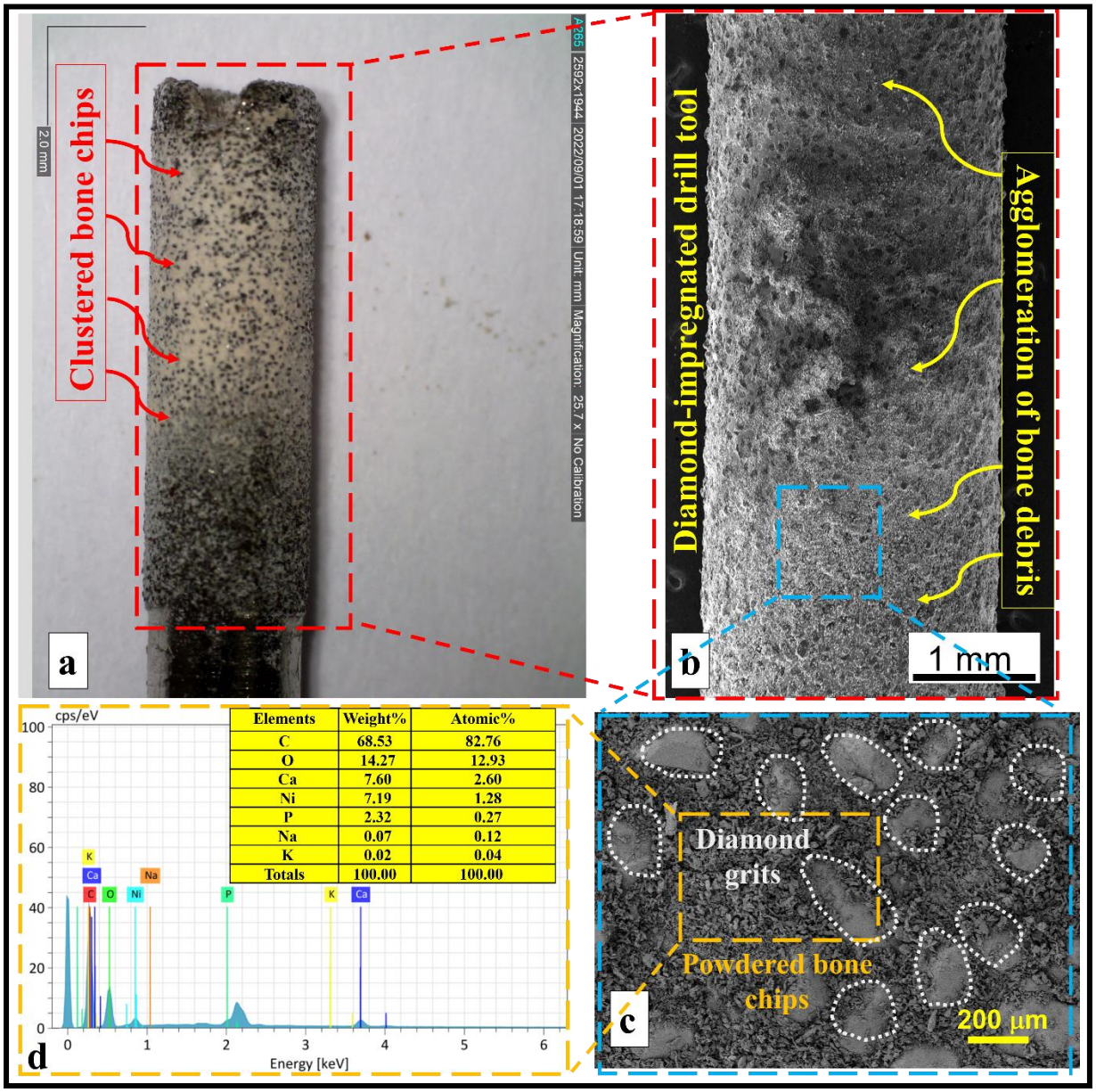


Figure 5.12. (a) Bone debris clustered within the diamond-impregnated drill tool, (b) micrographs of bone-tool morphology, (c) agglomerated bone debris, and (d) EDS of the diamond tool after drilling.

5.4. Conclusions

During the present chapter, bone drilling experiments were performed on the porcine femur bones using RUABD and CBD by varying different drilling parameters. Temperature elevations, cutting force, and microcracks were observed at the drill site during RUABD and CBD techniques. The influence of inclination angle, rotational speed and feedrate was monitored on the pullout strength of screws. Based on the bone drilling investigations, the following conclusions have been made.

- An increase in induced cutting force was observed to surge thermal energy and microcracks that lead to temperature elevations.
- Higher temperature elevations and cutting forces were observed during RUABD as compared to CBD.
- The SEM micrographs illustrate visible osteocyte tracks during RUABD, whereas no osteocyte tracks and microcracks were observed during CBD.
- RUABD with diamond-impregnated tool shows bone powdered debris, whereas during CBD clustered bone chips were observed.
- It was witnessed that with increasing the inclination angle, the biomechanical pullout strength at the bone-screw interface reduces. Changing the inclination angle from 0^0 to 40^0, the biomechanical pullout strength of cortical screws is reduced up to 18%.
- Higher pullout strength was witnessed with the drilling of bone at 0° due to an increase in stiffness that reduces microcracks at the bone-tool interface.

Chapter VI

Degradation behaviour and
Histopathological evaluation

Chapter 6

Degradation behaviour and Histopathological evaluation

6.1 Introduction

Surgical metallic bone screws are inserted to support the load-bearing fracture site to treat fractured bone. As mentioned in Chapter 1st, there are various bone-screw-related complications caused due to surgical metallic screws. One of the major drawbacks of metallic screws is the stress shielding effect caused due to the incongruity of elastic moduli between the screw and bone. Also, complex post-operative revision surgery is required to remove the implanted screw. It is important to observe the degradation behaviour of the 3D-printed cortical bone screws to reduce such bone-screw-related complications. After monitoring the degradation rate of the 3D-printed cortical screws, the feasibility and integration at the bone-screw interface are important to study. The histological evaluation may help understand surface damage, viable osteocytes, and tissue injuries at the bone-screw interface.

This chapter is divided into two parts. In the first part of the chapter, the in-vitro biodegradability of 3D-printed PLA cortical screws was examined. The influence of different process parameters of 3D printing technology was observed on the degradation rate. Three different biological solutions were used that have similar ion concentrations to human blood plasma [191]. These biological mediums are simulated body fluid (SBF), phosphate-buffered saline (PBS), and hank`s balanced salt solution (HBSS) used to preserve the 3D-printed screws for up to 24 weeks. The mechanical compressive strength of the screws was tested before and after 24 weeks of preservation in different biological solutions. The effect of the degradation rate of the PLA screw on the compressive strength of the screw was also examined.

In the second part of the chapter, 3D-printed PLA cortical screws were inserted in porcine femur bones for the histopathological procedure. The surgical metallic (titanium and stainless steel) cortical screws were also observed to monitor the bone surface after screw extraction. Bone-screw samples were preserved immediately after the experiment in 10% buffered formalin for histopathological evaluation. The samples were fixed overnight, and decalcification was done using a 10% Ethylene diamine tetraacetic acid (EDTA) chelating agent. The fresh EDTA solution was changed once every 2-week. After satisfactory decalcification, the samples were routinely processed for paraffin embedding and 5µ

deparaffinized tissue sections were stained with haematoxylin and eosin (H & E) for microscopic examination. Further, the tissue damage and surface damage after the extraction of screws from the bone surface were examined by histopathological evaluations.

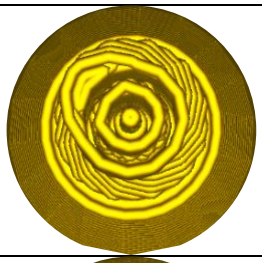
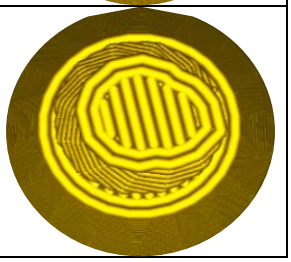
6.2 Run order and characterization of 3D-printed screws

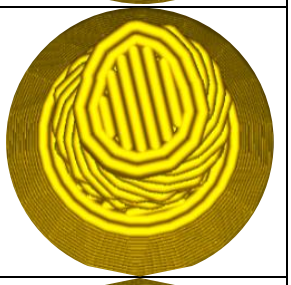
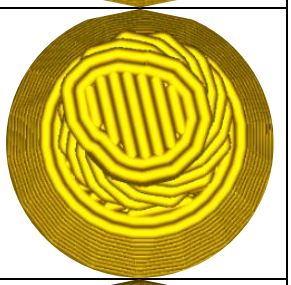
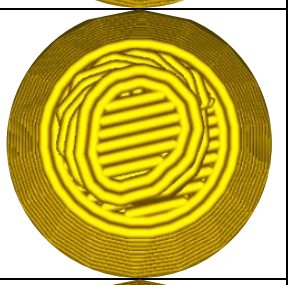
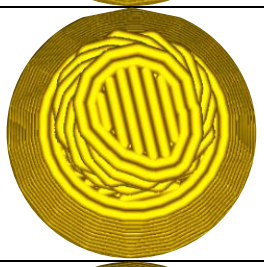
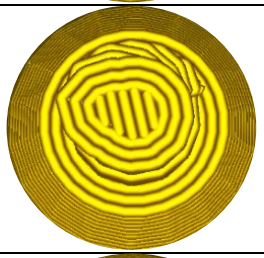
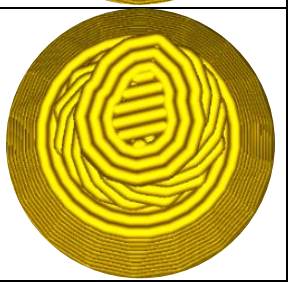
6.2.1. Process parameters and run order for 3D-printing of screws

Fused filament fabrication-based 3D printing technology is used to fabricate cortical screws. Various process parameters were varied at different levels to observe their influence on the degradation behaviour of 3D-printed cortical screws. These major process parameters include infill pattern (triangular, honeycomb, grid, concentric), infill percentage (25%, 50%, 75% and 100%), layer height (0.06 mm, 0.08 mm, 0.10 mm, 0.12 mm) and wall thickness (0.25 mm, 0.50 mm, 0.75 mm, 1 mm). A single variable study is performed to understand the influence of each parameter on the degradation rate. The run order for fabricating cortical bone screws is presented in Table 6.1. Each run order has a different interior design of the bone screw as presented as shown in Table 6.1. A number of cortical bone screws were fabricated for their biological assessment as depicted in Figure 6.1. The compressive strength of 3D-printed cortical screws was monitored before and after their biological assessment. The influence of the degradation rate on the compressive strength of cortical screws was also monitored.

Table 6.1: Run order and experimental trial for fabrication of cortical screws.

Run Order	Sample number	Infill pattern	Infill percentage (%)	Layer height (mm)	Wall thickness (mm)	The interior design of cortical screw
1	S_1	Triangular	50	0.08	0.5	
2	S_2	Grid	50	0.08	0.5	

3	S_3	Concentric	50	0.08	0.5	
4	S_4	Honeycomb	50	0.08	0.5	
5	S_5	Honeycomb	25	0.08	0.5	
6	S_6	Honeycomb	50	0.08	0.5	
7	S_7	Honeycomb	75	0.08	0.5	
8	S_8	Honeycomb	100	0.08	0.5	
9	S_9	Honeycomb	100	0.06	0.5	

10	S_{10}	Honeycomb	100	0.08	0.5	
11	S_{11}	Honeycomb	100	0.1	0.5	
12	S_{12}	Honeycomb	100	0.12	0.5	
13	S_{13}	Honeycomb	100	0.12	0.25	
14	S_{14}	Honeycomb	100	0.12	0.50	
15	S_{15}	Honeycomb	100	0.12	0.75	
16	S_{16}	Honeycomb	100	0.12	1	

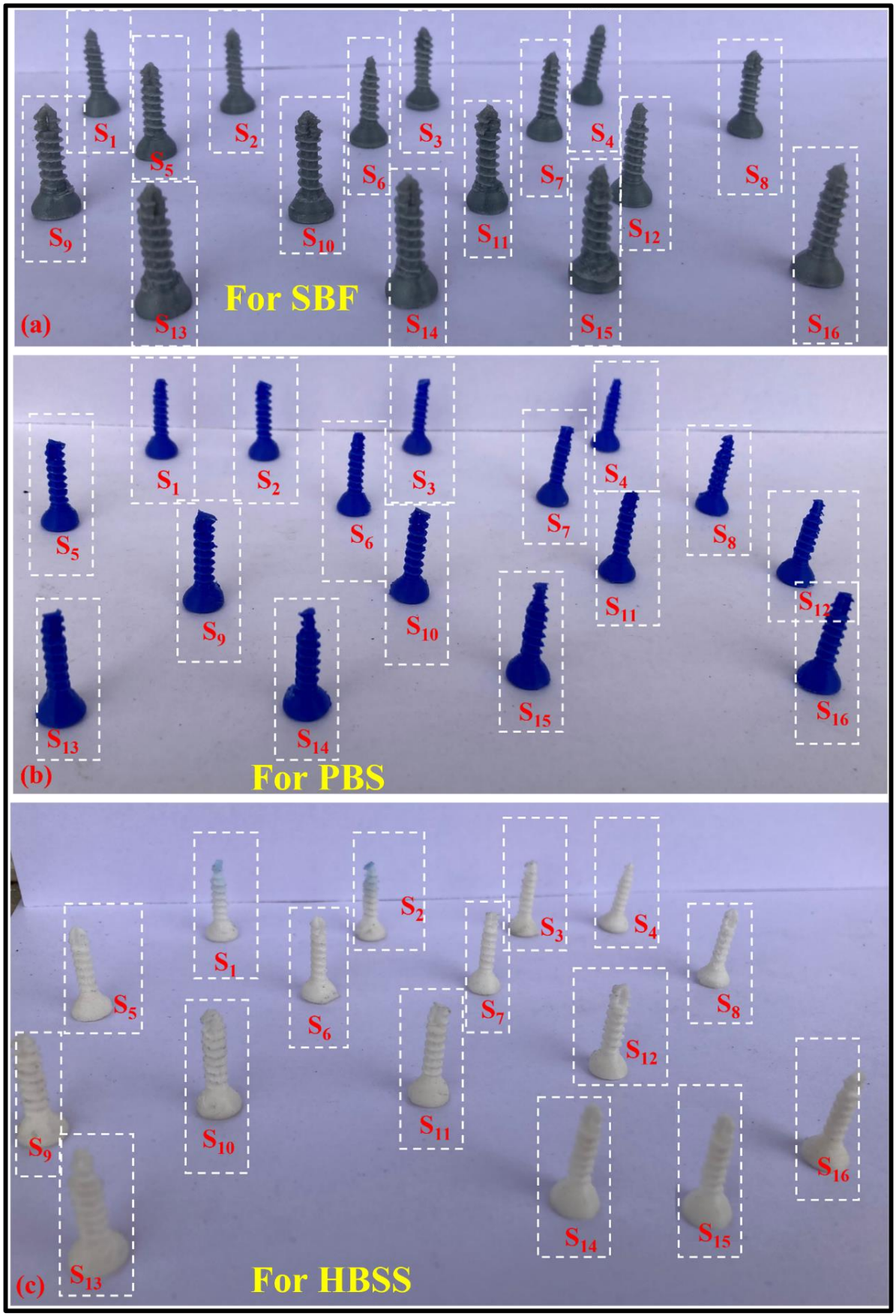


Figure 6.1: 3D-printed cortical screws based on run order by varying different process parameters (S_1 to S_{16}); (a) for SBF solution, (b) for PBS solution, (c) for HBSS solution.

6.2.2. Biological assessment

For in-vitro degradation behaviour and biological assessment of 3D-printed biomaterials, the samples can be preserved in different biological solutions to observe their biocompatibility and degradability [191–193]. The three most commonly used biological mediums reported in the literature are SBF, PBS, and HBSS which are used to mimic human biological conditions [191, 192]. These biological mediums have almost similar ion concentrations to human blood plasma, as presented in Table 6.2 [192].

Table 6.2: Comparison of ion concentrations of solutions concerning human blood plasma.

Ion	Human Blood Plasma	SBF	PBS	HBSS
Na^+ (mM)	142.0	142.0	157.0	142.0
K^+ (mM)	5.0	5.0	4.1	5.9
Mg^{2+} (mM)	1.5	1.5	-	0.8
Ca^{2+} (mM)	2.5	2.5	-	1.3
Cl^- (mM)	103.0	147.8	140	145
HCO_3^- (mM)	27.0	4.2	-	4.2
HPO_4^{2-} (mM)	1.0	1.0	11.5	0.8
SO_4^{2-} (mM)	0.5	0.5	-	0.8
Glucose (mM)	5	-	-	1
Tris (g L^{-1})	-	6.118	-	-
pH	7.2-7.4	7.40	7.40	6.8-7.2

3D-printed cortical screws were fabricated by following the same run order (Table 6.1) and the same polymer material of three different colours (metallic silver, navy blue, and pure white). These three sets of 3D-printed cortical screws were immersed in three different biological solutions SBF, PBS and HBSS, respectively. The biological solutions were prepared by different compositions of reagents as presented in Table 6.3. These three artificial fluids have several chemical reagents in different amounts that enable stoichiometric, bone-like apatite or calcium-deficient growth. A formation (crystal-chemical analogue to bone mineral) in cortical screws. After preparing biological solutions, the cortical screws were preserved in different biological solutions for different time interval.

Table 6.3: Chemical reagents contribution for preparing 1000 ml of SBF, PBS, and HBSS solution.

Reagents	SBF	PBS	HBSS
NaCl	8.035 g	8.0 g	8.0 g
$NaHCO_3$	0.355 g	-	0.35 g
KCl	0.225 g	0.2 g	0.4 g
$K_2HPO_4.3H_2O$	0.231 g	-	-
$MgCl_2.6H_2O$	0.311 g	-	0.10 g
1.0_M-HCl	39 ml	-	-
$CaCl_2$	0.292 g	-	0.14 g
Na_2SO_4	0.072 g	-	-
Tris	6.118 g	-	-
1.0_M-HCl	0-5 ml	-	-
Na_2HPO_4	-	1.42 g	0.048 g
KH_2PO_4	-	0.24 g	0.06 g
$MgSO_4.7H_2O$	-	-	0.10 g

For the preservation of cortical screws, Eppendorf (AG, Hamburg) smart lock micro-centrifuged tubes (made of polypropylene) were used. These centrifuged tubes were autoclaved (at 120 ^{0}C for 1 hour) before usage for immersion of solutions. Then, the 3D-printed cortical screws were preserved in 1.5 ml of SBF, PBS, and HBSS solutions respectively in Eppendorf micro-centrifuged tubes as presented in Figure 6.2. A number of samples (screw and biological solutions in Eppendorf tubes) were incubated at pH 7.4 and maintained at 36.5 ± 0.5^{0}C using an incubator for 24 weeks as depicted in Figure 6.2. The 1.5 ml of solutions were replaced every week with new solutions to prevent the biological medium's saturation.

To estimate the degradation rate of 3D-printed cortical screws, the initial weight of the screw (before immersion) and the final weight of the screw (after immersion) were monitored every two weeks. The degradation rate of the 3D-printed cortical screw was examined with the weight loss of individual screws that can be calculated using mathematical Equation 1. The SEM micrographs and EDS spectrum of the cortical screw were used for observing surface morphology and elemental analysis of the 3D-printed cortical screws.

$$Degradation\ rate = \frac{Initial\ weight\ of\ screw - Final\ weight\ of\ screw}{Initial\ weight\ of\ screw} \times 100 \quad \ldots\ldots\ldots\ldots (1)$$

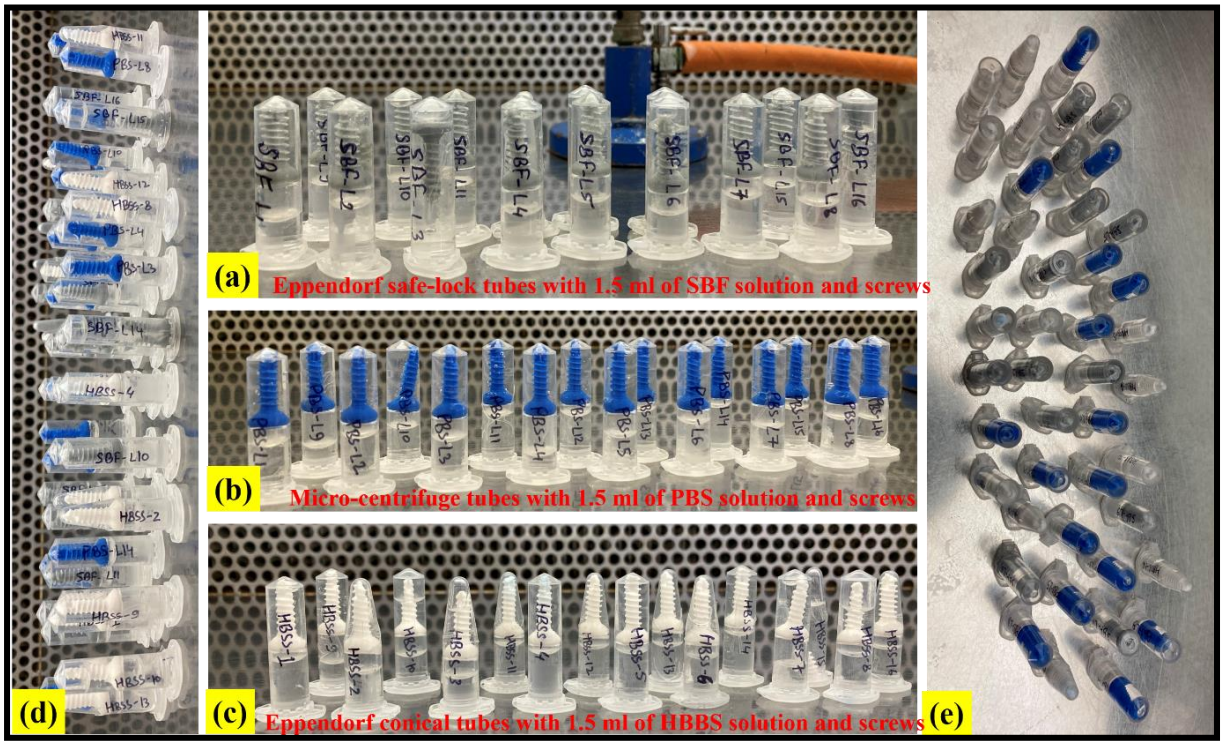


Figure 6.2: (a) SBF immersed 16 cortical screws, (b) PBS preserved 16 cortical screws, and (c) HBSS immersed 16 cortical screws, (d) (e) Eppendorf micro-centrifuge tubes immersed cortical screws in various biological solutions.

6.2.3. Mechanical characterization

A biodegradable cortical screw should have adequate mechanical strength for supporting load-bearing fracture sites. The mechanical strength of 3D-printed cortical screws was monitored based on the mechanical characterization of compression testing. The compression testing of different run orders of cortical screws was performed using a universal testing machine (UTM-series 7200, DAK system Inc, India) at a steady deformation rate of 1.5 mm/min, as presented in Figure 6.3. The black arrow indicates the axial load direction of 5 kN applied on the cross-section of the tip of the cortical screw. For uniformity of axial load on the cortical screw, a fixture was designed made up of composite material to fix the cortical screw. The cortical screws were set in the fixture for no relative motion on the cortical screw, as depicted in Figure 6.3. The maximum unconfined compressive strength of cortical screws was observed with high-speed microprocessor-based control in MPa and considered the final strength of cortical screws. The compressive strength of 3D-printed cortical screws was observed before and after 24 weeks of immersion of screws in biological solutions.

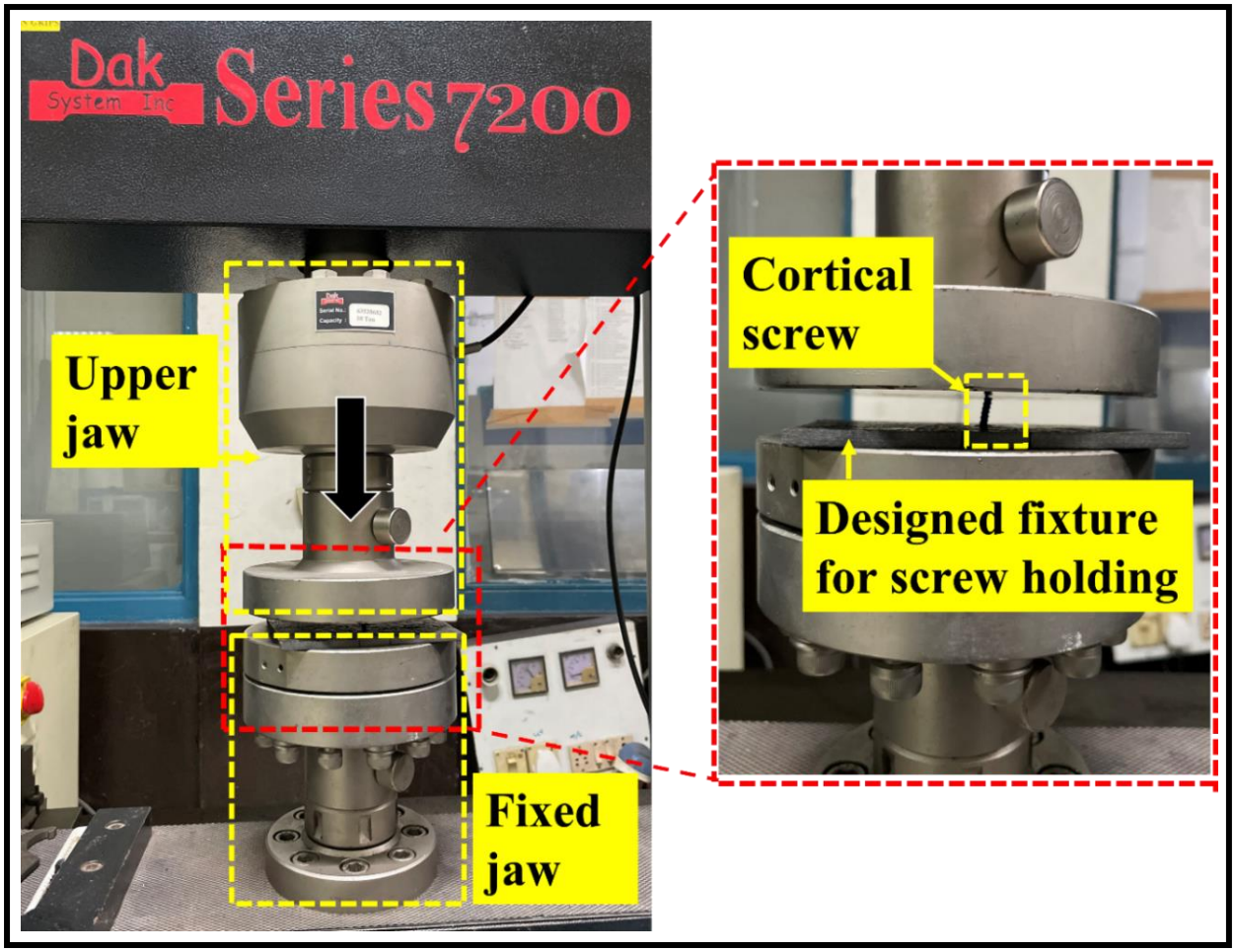


Figure 6.3: Compressive strength testing setup for 3D-printed cortical screws fixed in screw holding fixture.

6.3 Sample preparation of histopathological examination

After observing the degradation behaviour of 3D-printed cortical screws, histopathological evaluations were conducted. 3D-printed cortical screws were fabricated by maximum compressive strength parameters as listed in Table 6.4. After fabrication, bone drilling experiments were performed on porcine femur bone by drilling parameters that has maximum pullout strength as mentioned in Table 6.5 (from Chapter 5). Drilling experiments were performed within two hours after the cleaning process of porcine femur bones. Drilled bone samples were preserved immediately after drilling experimentation in fresh 10% buffered formalin solution after bone drilling experiments. 3D-printed PLA cortical screws and surgical metallic titanium (Ti) and stainless steel (SS) screws were inserted in the drilled bone samples. The bone-screw samples were preserved in a mixture of 10% buffered formalin solution and EDTA solution as shown in Figure 6.4 for the histopathological evaluation. All the experiments were conducted at room temperature on the same porcine cortical bone.

Table 6.4: Input process parameters used for 3D printing for screw fabrication.

Process parameters	Infill percentage	Infill pattern	layer height	wall thickness
Unit	%	Honeycomb	mm	mm
Values	100		0.06	1

Table 6.5: Drilling parameters used during bone drilling for the histopathological examination.

Rotational speed (rpm)	Feed rate (mm/min)	Inclination angle (°)	Drill diameter	Ultrasonic Parameters	
				Amplitude (µm)	Frequency (kHz)
3000	10	0	3.5	20	20



Figure 6.4: surgical metallic (Ti and SS) and 3D-printed PLA bone-screw samples.

6.4 Histopathological examination

Bone is different from metal or composite as it is a complex material in the form of layers containing soft tissue, hard tissue, bone marrow and protein fibres. Bones are hard in nature due to presence of calcium in them. For tissue sectioning in the histopathological examination of bones, the specimen should be calcium free. Therefore, decalcification of bone is a necessity for the sectioning of tissue. Histopathological examinations were carried out in the Bone and tissue pathology department All India Institute of Medical Sciences (AIIMS*) – New Delhi, India* under the supervision of *Dr. Asit R. Mridha* (Professor, Pathology Department AIIMS). The process flow chart which was used in this work for the histopathology procedure is given in Figure 6.5. In vitro bone drilling experiments were performed on porcine bone. Bone samples have been taken from the local butcher shop. Hence, no ethical permission was required for the procurement and cleaning of porcine bones.

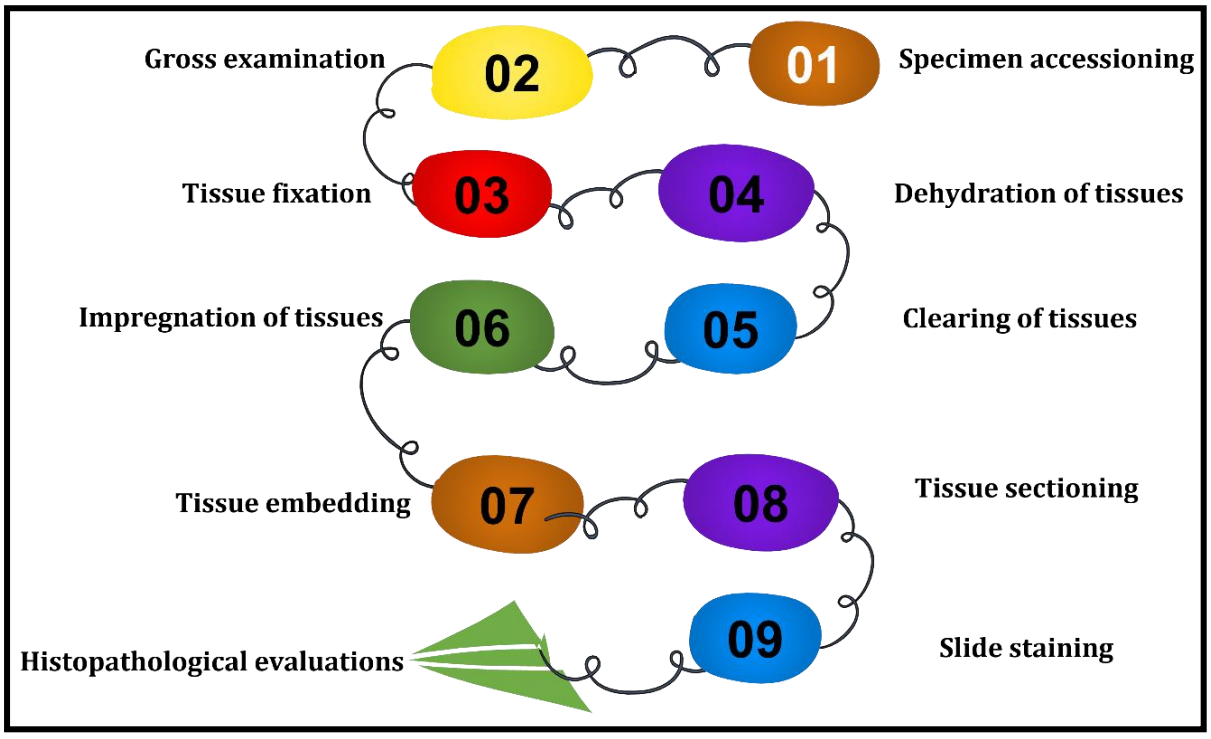


Figure 6.5: Methodology for the histopathology procedure.

6.4.1 Decalcification of bone

Calcified bone drilled samples were cut into small pieces for decalcification with a thin blade. It was taken into consideration that during this process the surrounding tissue near the drilled holes is not to tear and is in a safe position. Various methods are there in the medical field to decalcify the calcium from the bone which are:

1. Acid decalcification
2. Ion exchange resin
3. Electric ionization
4. Chelating method
    - Ethylene diamine tetraacetic acid (EDTA) solution
5. Surface decalcification

In the histopathological investigation, the EDTA method is widely used for the decalcification of bone, so in the present work it is used to decalcify the bone drilled holes samples. In order to provide thorough decalcification bone samples were kept separately. The endpoint of decalcification was carried out by physical testing of the specimen. The samples were fixed overnight, and decalcification was done using 10% EDTA of 5.5 gm chelating agent. The fresh EDTA solution was changed once every 2-week. After satisfactory decalcification, the samples were routinely processed for paraffin embedding and 5µ deparaffinized tissue sections were stained with haematoxylin and eosin for microscopic examination.

6.4.2 Tissue processing

It is a process of fixing the tissue on paraffin. Specimens with a maximum thickness of 5 mm were placed in the porous cassettes as shown in Figure 6.6, and after that processing of the tissue was carried out. Tissue processing is carried out in three stages:

1. Dehydration
2. Clearing
3. Impregnation



Figure 6.6: Porous cassettes with the specimen.

6.4.2.1 Dehydration and cleaning

In this step, water was removed from the bone specimen, and it is replaced by the dehydrating fluid. In our study, this was stopped when the specimen was almost 97% dehydrated. Samples were fixed overnight for dehydration on the automatic tissue processing unit as shown in Figure 6.7(a). Various dehydrant liquid solutions are available for the dehydration process such as ethyl alcohol, methyl alcohol, butyl alcohol and isopropyl alcohol and acetone. In this work, acetone was used as a dehydrants for the dehydration. It is the process of removal of dehydrants fluid with a miscible fluid. In this study acetone from the specimen was replaced by xylene which is a miscible fluid for dehydration as well as for embedding medium. The clearing process is performed on the clearing unit as shown in Figure 6.7(b).

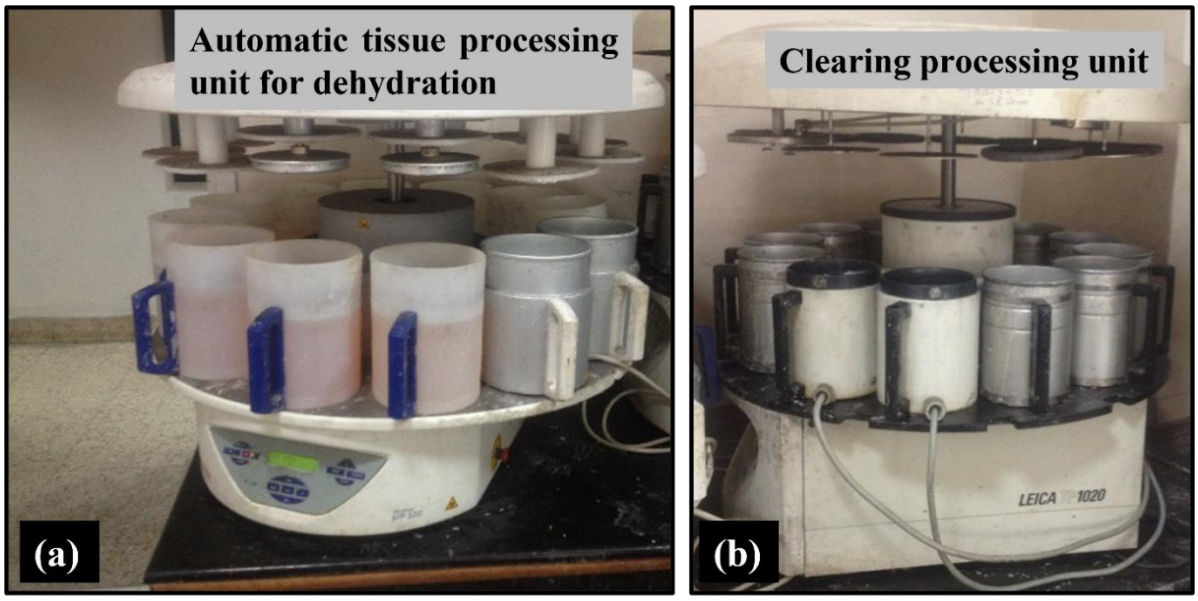


Figure 6.7.: (a) Automatic tissue processing unit for dehydration, (b) clearing processing unit.

6.4.2.2 Infiltration and impregnation

It is the process of replacing the xylene from the specimen with paraffin wax. In this tissue is transferred to paraffin wax for filtration and impregnation. This process is necessary for tissue embedding. Fixation of tissue on paraffin is a very complex chemical procedure. Various factors are affecting the fixation of tissue which are listed below:

1. PH
2. Temperature
3. Penitration of fixation
4. Voloueme of tissue

6.4.3 Tissue embedding

It is a process of embedding the tissue in the paraffin wax and it was done using the automatic tissue embedding machine as shown in Figure 6.8. In this work tissue embedding process was done in four steps as given in Figure 6.9. Firstly, the tissue cassette was placed in melted paraffin and the paraffin is filled with the mold. After that, the tissues were placed in the mold and allowed to cool for the sectioning of tissues. Figure 6.10 shows the actual images of the tissue embedded in the wax mould for the bone samples after the extraction of 3D-printed PLA and surgical metallic cortical screws.



Figure 6.8: Tissue embedding unit.

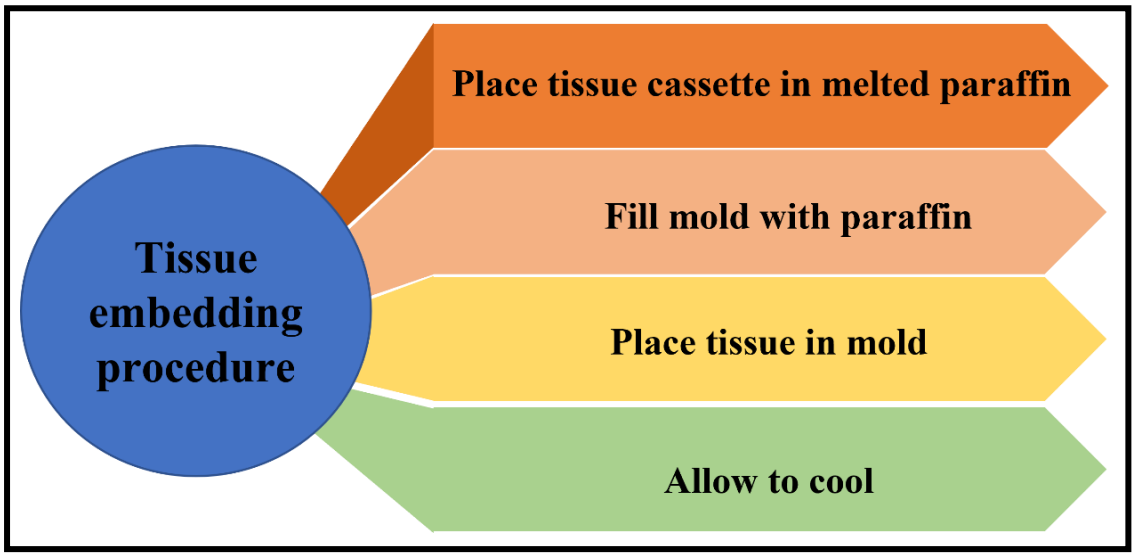


Figure 6.9: Tissue embedding procedure.

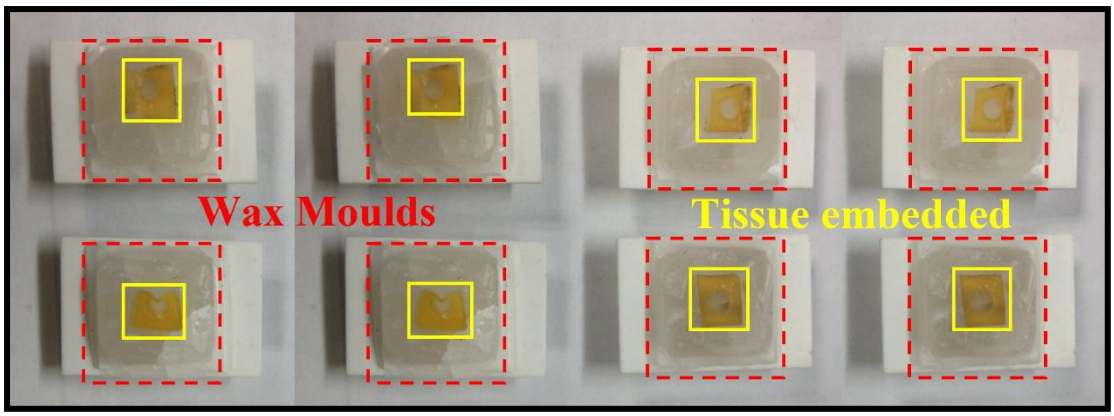


Figure 6.10: Actual images of tissue embedded in the wax mould.

6.4.4 Tissue sectioning

This process is also known as microtome where embedded tissue on paraffin wax was sliced for the sectioning into thick layers of 0.5 to 5 µ. These sections were further mounted on a glass sliced for staining. Various types of microtomes are there like rotary microtome, sledge microtome, cryo-microtome, ultra-microtome, vibrating microtome, saw microtome etc. but mostly rotary microtome is used for section. In our work also rotary microtome with a knife [Figure 6.11] was used and the layers were sliced of thickness 5µ. Further, these sliced layers were mounted on the microscopic glass slide for staining.



Figure 6.11: Rotary microtome used for sectioning.

6.4.5 Slide staining and cover-slipping

The slides which were prepared in the last section were colourless and difficult to appreciate the different components. Therefore, staining is required to examine the morphology of the tissue. It is done by using different types of coloured dyes which have the capability of identification for the specific components of the tissues. Various methods were used for this process, but in this work, H & E method was used for the staining on the automatic staining unit as shown in Figure 6.12. Coverslip slides were prepared using the mountain medium which was not miscible with water. In this work coverslip slides were prepared using the DPX as shown in Figure 6.13. The coverslip slides were observed for microscopic analysis.



Figure 6.12: Automatic staining unit.

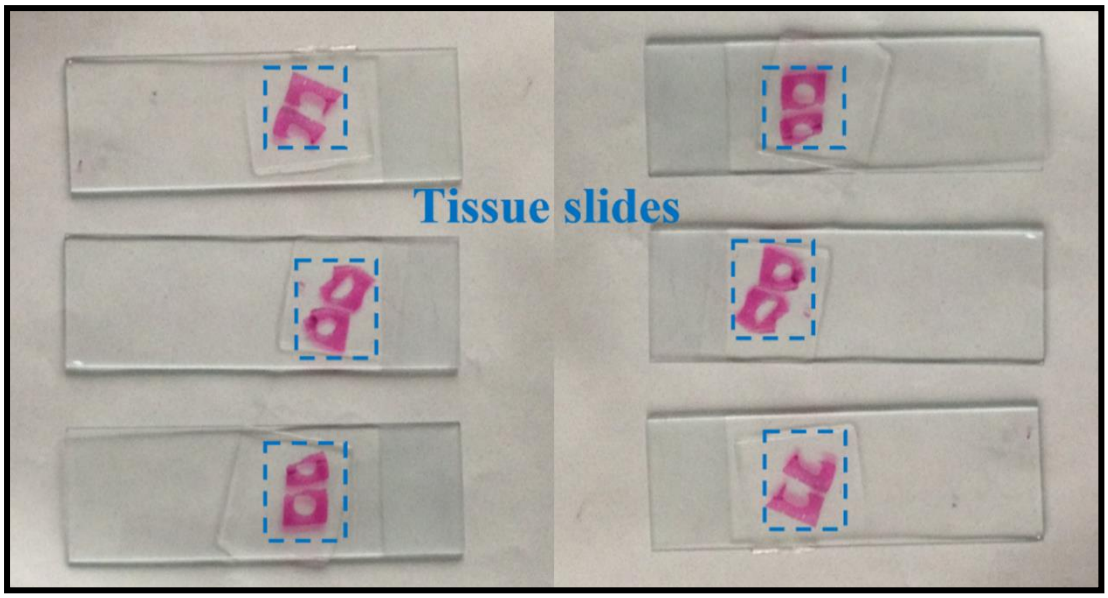


Figure 6.13: Images of final slides for the microscope examination.

6.5. Results and discussion

6.5.1. In-vitro degradation behaviour

The degradation rate of different cortical screws was observed during in-vitro monitoring of different cortical screws preserved in different biological solutions. The porous design of the cortical screw has a strong influence on the degradation rate due to the interior design of the bone screw. The initial weight of the cortical screw was taken after drying bone screws at 50 ^{0}C for one hour, and the final weight was taken after different time intervals. During the first week of immersion in biological solutions, apatite formation was observed on the threads of cortical screws. The apatite formation on the periphery of screws shows the biocompatible nature of PLA biopolymer and is witnessed using energy-dispersive spectroscopy (EDS).

Figure 6.14 shows the apatite formation on the threads of cortical screws when preserved in SBF, PBS and HBSS solutions. EDS provides information on elements present in the cortical screws fabricated by PLA polymer and the elemental morphology spectrums of Hydroxyapatite formatted during preservation in biological solutions. The preservation of cortical screws in SBF, PBS, and HBSS solutions leads to apatite formation containing carbon (C), oxygen (O_2), calcium (Ca), sodium (Na), phosphorus (P), magnesium (Mg), aluminium (Al), silicon (Si), chlorine (Cl), and potassium (K) elements as witnessed in Figure 6.14. The 'Ca' peaks present in the EDS spectrum confirm apatite deposition on threads of cortical bone screws. The SEM micrographs and EDS spectrum of the cortical bone screw before preservation (as fabricated) in biological solutions show base elements of C, O, and a negligible amount of Al as depicted in Figure 6.14(a) and Figure 6.14(b) respectively. The preservation of bone screws in SBF, PBS and HBSS solutions shows the biocompatibility of PLA polymer by apatite formation in all the biological solutions.

The change in the percentage of chemical reagents present in the various biological solutions is responsible for the difference in levels of apatite growth in cortical bone screws. Hydroxyapatite formation was observed during preservation in SBF solution as depicted in Figure 6.14(c). The higher growth of apatite formation in SBF solution is observed as illustrated in Figure 6.14(d) which increases the weight of the cortical screw after the first week of immersion. Moreover, less apatite is formed in the PBS solution due to different chemical reagents, as presented in Figure 6.14(f). Significantly less apatite formation was observed in the HBSS solution immersion, as depicted in Figure 6.14(h).

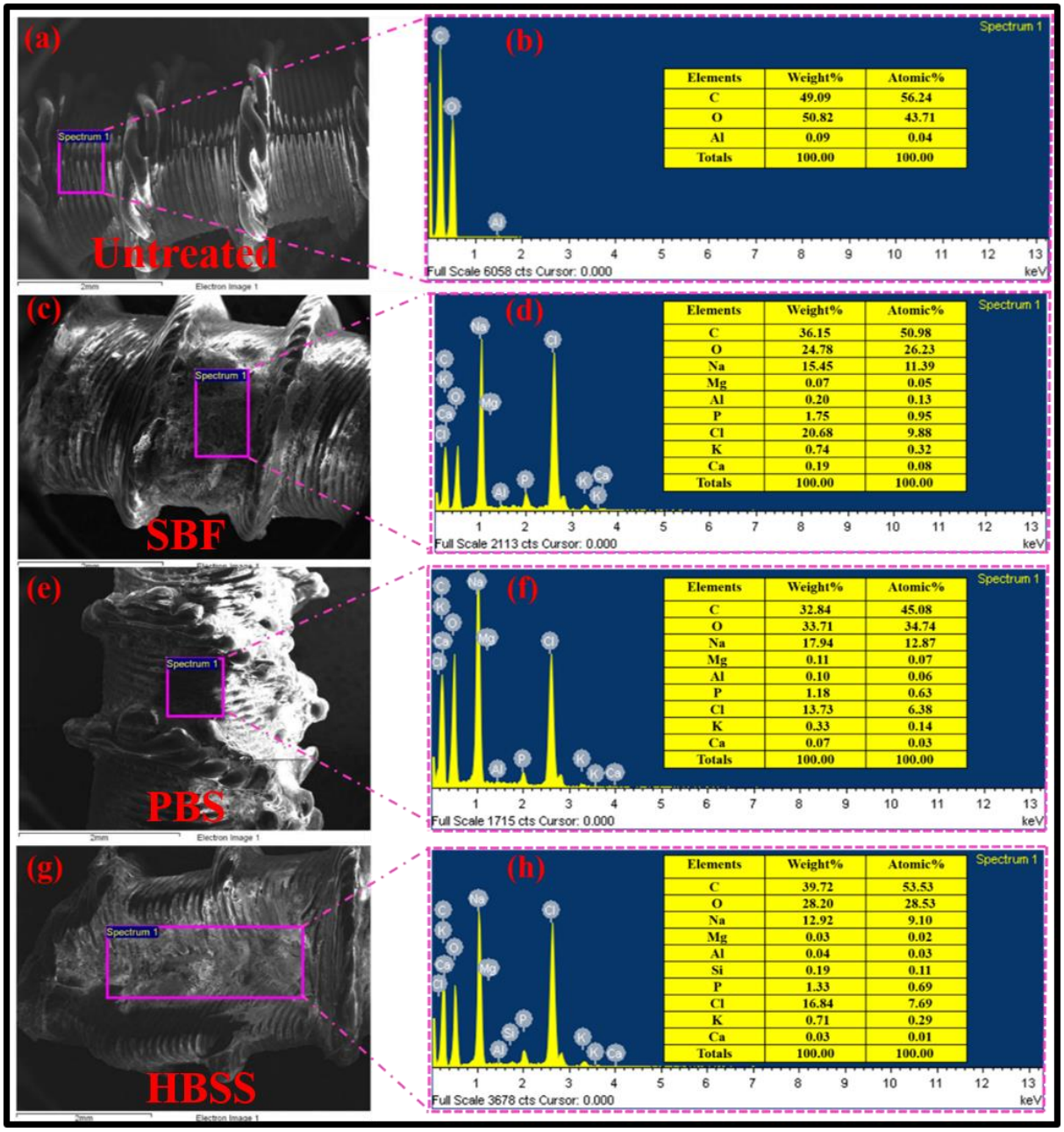


Figure 6.14: Micrographs and EDS elemental analysis of 3Dprinted PLA cortical screws: (a) (b) un-treated surface, (c) (d) SBF immersed cortical screw surface, (e) (f) PBS immersed surface of screw, (g) (h) HBSS immersed screw surface shows the presence of Ca, Na, Cl, P.

6.5.1.1. Influence of infill pattern on different solutions at different weeks

The influence of the infill pattern on the degradation behaviour of cortical screws is monitored with samples no. 1, 2, 3 and 4 from Table 6.1 (keeping other parameters constant). The in-vitro degradation rate of different infill patterned cortical screws was monitored every six weeks till 24 weeks, as presented in Figure 6.15. It was observed that the triangular infill pattern has a

higher degradation rate than the grid, concentric and honeycomb-patterned cortical screws, as illustrated in Figure 6.15(a). It was due to the infill structure of the cortical screw as material consumption during the fabrication of the cortical screw.

The triangular pattern consumes the least material compared to the concentric, grid and honeycomb-structured cortical screws. Moreover, the most negligible degradation was observed in the honeycomb-patterned cortical screw because of the complex shape of the honeycomb, layers overlapping, and higher material consumption during the fabrication of the cortical screw. A higher degradation rate was observed with increasing the time of preservation of cortical screws in biological solutions, as presented in Figure 6.15. The comparison of different solutions at different weeks of immersion on degradation rate is understood in Figure 6.16. It was witnessed that SBF solution has higher degradation rate with increasing the immersion time in terms of the number of weeks compared to PBS and HBSS solutions.

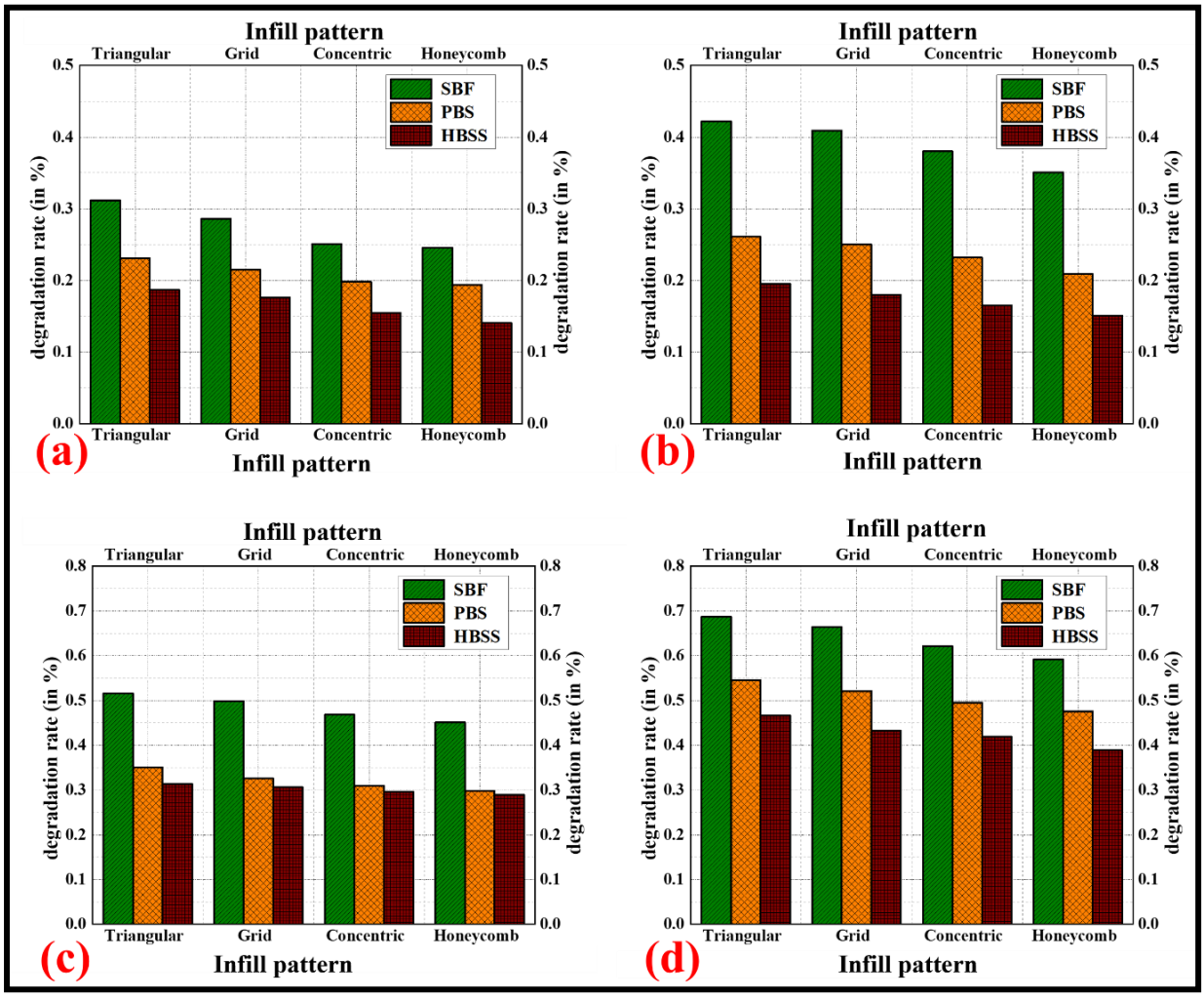


Figure 6.15: Degradation behaviour of different infill patterns in different solutions at (a) 6 weeks, (b) 12 weeks, (c) 18 weeks, (d) 24 weeks.

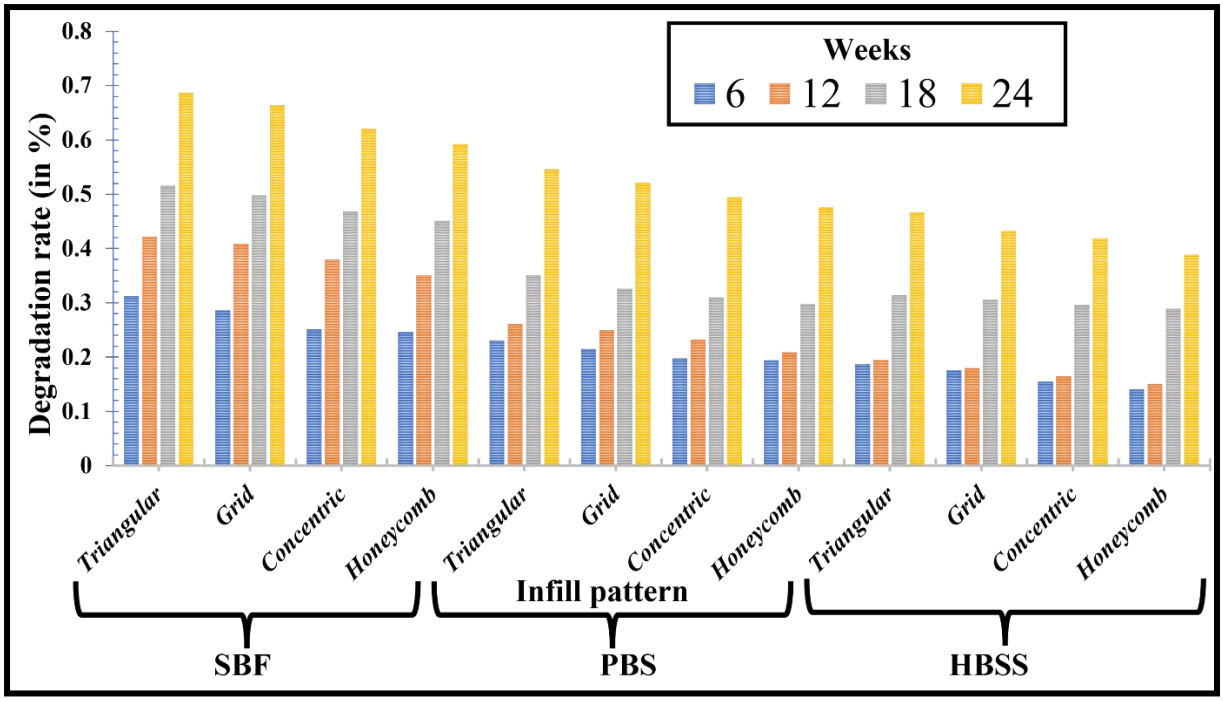


Figure 6.16: Comparison of the degradation rate of variation in infill patterns of cortical screws at different weeks on different solutions.

6.5.1.2. Influence of infill percentage on different solutions at different weeks

The change in infill pattern varies the porosity of cortical screws which influences the degradation behaviour of cortical screws. The effect of infill percentage is monitored by samples no. 5, 6, 7 and 8 from Table 6.1 (keeping other parameters constant). The in-vitro degradation rate of different infill percentages of cortical screws was monitored every 6 weeks till 24 weeks as presented in Figure 6.17. It was noted that the degradation rate increases with a decrease in infill percentage. It was observed that sample no. 5 with a 25% infill percentage is the most porous cortical screw with 75% porosity and showed the highest degradation rate compared to the infill percentage. This is due to the reason of porosity of the cortical screw. As the infill percentage decreases the porosity of the screw increases. With higher porosity, the biological solution gets a higher area for apatite formation and degradation behaviour of the screw. The increasing the infill percentage from 50% to 75%, the porosity of the screw decreases that reducing the degradation rate of the screw.

The highly porous bone screws (infill percentage 50%) after preservation in biological mediums show maximum apatite formation compared to other bone screws. This is because the increase in porosity increases the pore size to provide sufficient space for bone-like apatite to grow for proliferation, tissue growth, and adequate nutrient flow across the voids of cortical

bone screws to promote Osseo-integration to support the rigid fixation at the bone-fractured site.

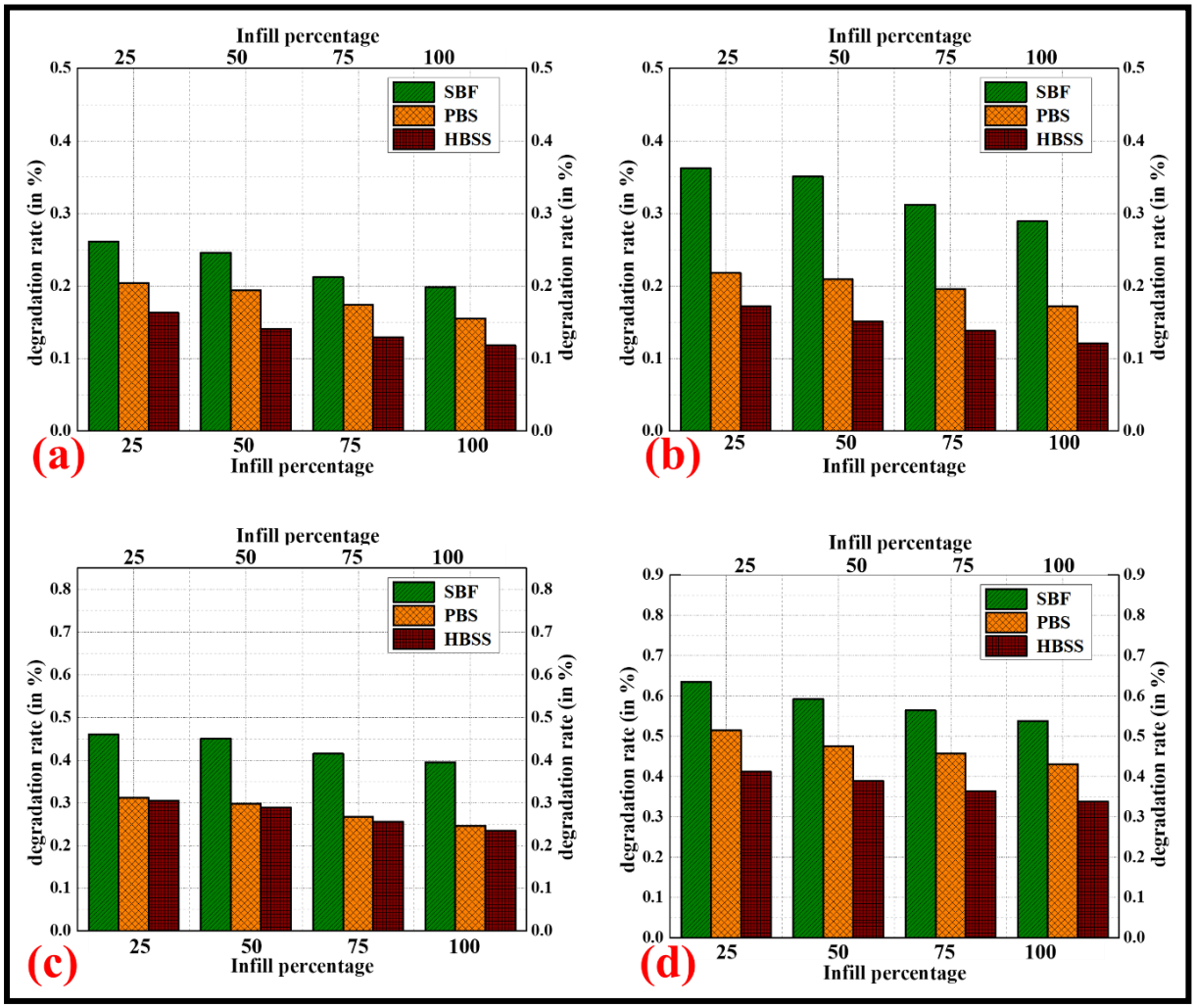


Figure 6.17: Degradation behaviour of different infill percentages in different solutions at (a) 6 weeks, (b) 12 weeks, (c) 18 weeks, (d) 24 weeks.

At 100% of the infill percentage, the cortical screw is mostly solid with no porosity that takes a long time to degrade from its initial stage. Moreover, the increase in infill percentage increases the molecular weight of the screw takes a longer time and slower the process of degradation. It was witnessed that the degradation of the screw increases with increasing the time of preservation in biological solutions. The SBF solution showed higher degradation of the screw as compared to PBS and HBSS due to changes in quantity and number of chemical reagents as depicted in Figure 6.17. The complete comparison of the impact of infill percentage for a different solution at different weeks on degradation behaviour is illustrated in Figure 6.18. The infill percentage of 25% with the highest porosity showed the highest degradation in SBF solution as compared to other biological solutions.

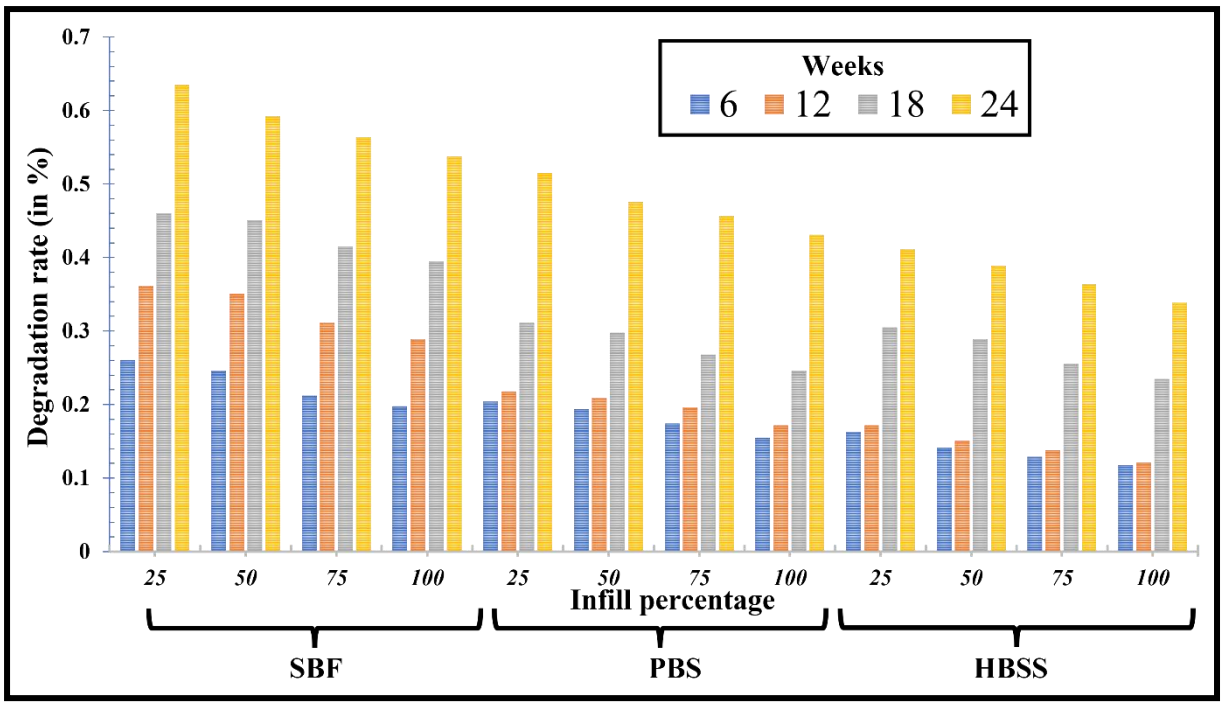


Figure 6.18: Comparison of the degradation rate of variation in infill percentage of cortical screws at different weeks on different solutions.

6.5.1.3. Influence of layer height on different solutions at different weeks

The change in layer height affects the degradation behaviour of cortical screws as the layer height is inversely proportional to the number of layers in the fabricated part. The degradation rate of cortical screws while varying the layer height (keeping other parameters constant) is monitored with samples no. 9, 10, 11 and 12 from Table 6.1. The in-vitro degradation rate of a different number of layered cortical screws was monitored every 6 weeks till 24 weeks as presented in Figure 6.19.

It was observed that as the layer height increases, the degradation rate of the cortical screw increases. This is due to the reason of increasing layer height, the extrusion rate, and the void densities of the fabricated part increase. The degradation of the cortical screw increases with increasing the preservation time in the biological solutions. It was witnessed that 24 weeks of immersion in biological solutions showed the highest degradation of cortical screws as compared to 12 weeks and 18 weeks as presented in Figure 6.19. The comparison of different weeks on different solutions for different layer heights of cortical screws the degradation is monitored and presented in Figure 6.20. It was observed that 0.12 mm of layer height showed the highest degradation at 24 weeks of preservation in the SBF solution as compared to other process parameters and biological solutions.

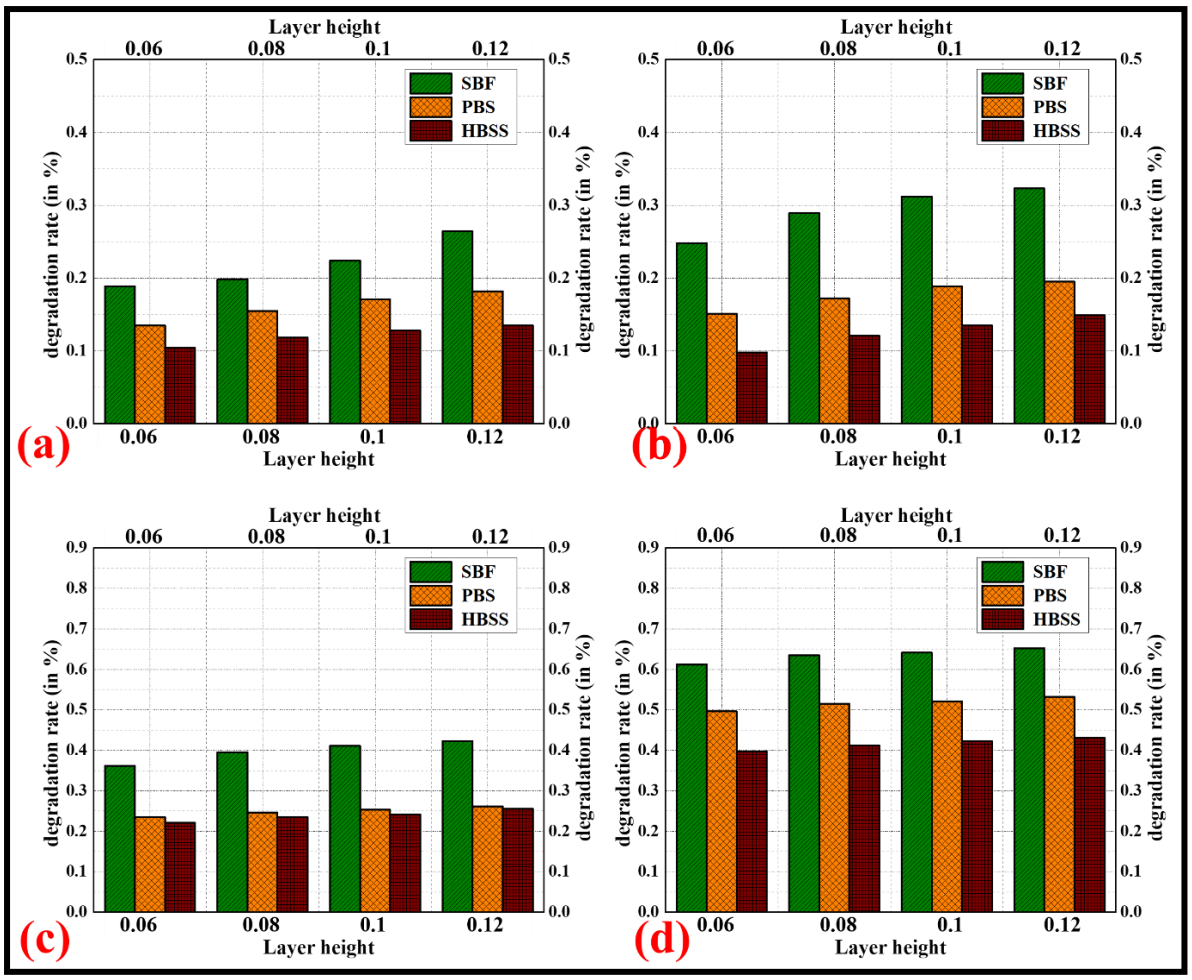


Figure 6.19: Degradation behaviour of different layer heights in different solutions at (a) 6 weeks, (b) 12 weeks, (c) 18 weeks, (d) 24 weeks.

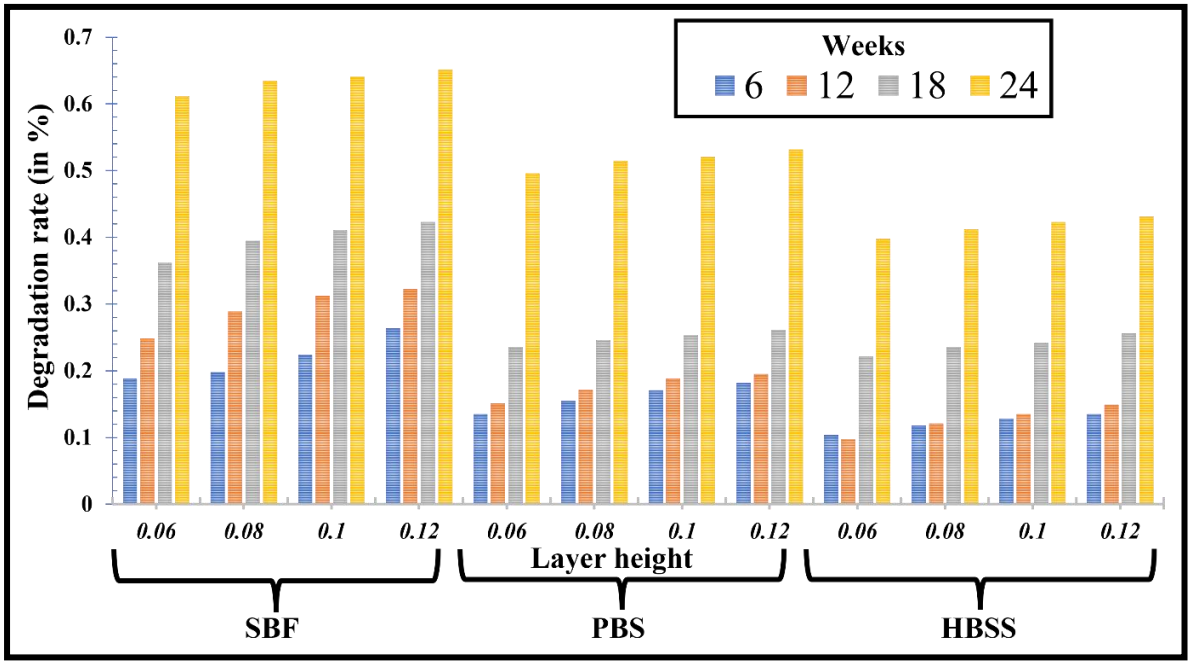


Figure 6.20: Comparison of the degradation rate of variation in layer height of cortical screws at different weeks on different solutions.

6.5.1.4. Influence of wall thickness on different solutions at different weeks

The effect of change in wall thickness on the degradation behaviour of cortical screws is monitored with samples no. 13, 14, 15 and 16 from Table 6.1 (keeping other parameters constant). The degradation rate of different infill patterned cortical screws was monitored every six weeks till 24 weeks, as presented in Figure 6.21. It was observed that wall thickness does not significantly affect the degradation rate of cortical screws.

As the wall thickness is the distance between one layer to another, it affects the degradation behaviour of cortical screw. The increase in wall thickness increases the distance between two consequent layers. The wall thickness of 0.25 mm exhibits minimum thickness between the layers increasing the number of layers in the fabricated part and increasing the weight of the cortical screw that reduces the process of degradation. Therefore, the wall thickness of 1 mm shows the maximum degradation rate as compared to other wall thickness.

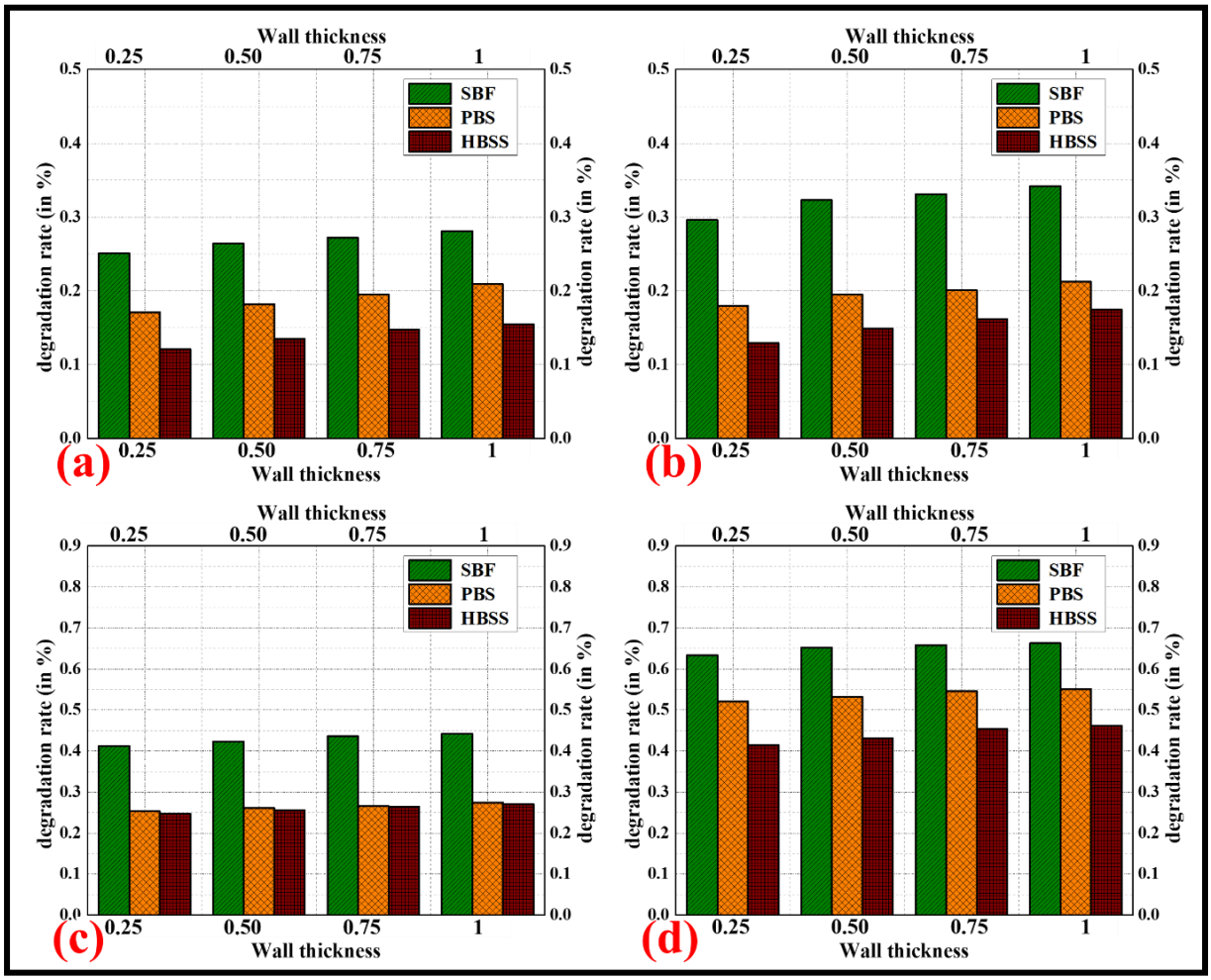


Figure 6.21: Degradation behaviour of different wall thicknesses in different solutions at (a) 6 weeks, (b) 12 weeks, (c) 18 weeks, (d) 24 weeks.

The complete comparison of different biological solutions at different weeks of immersion is illustrated in Figure 6.22. It was witnessed that the wall thickness of 1 mm at 24 weeks of immersion in SBF solution showed maximum degradation behaviour of cortical screw as compared to other wall thickness of cortical screws and other biological solutions.

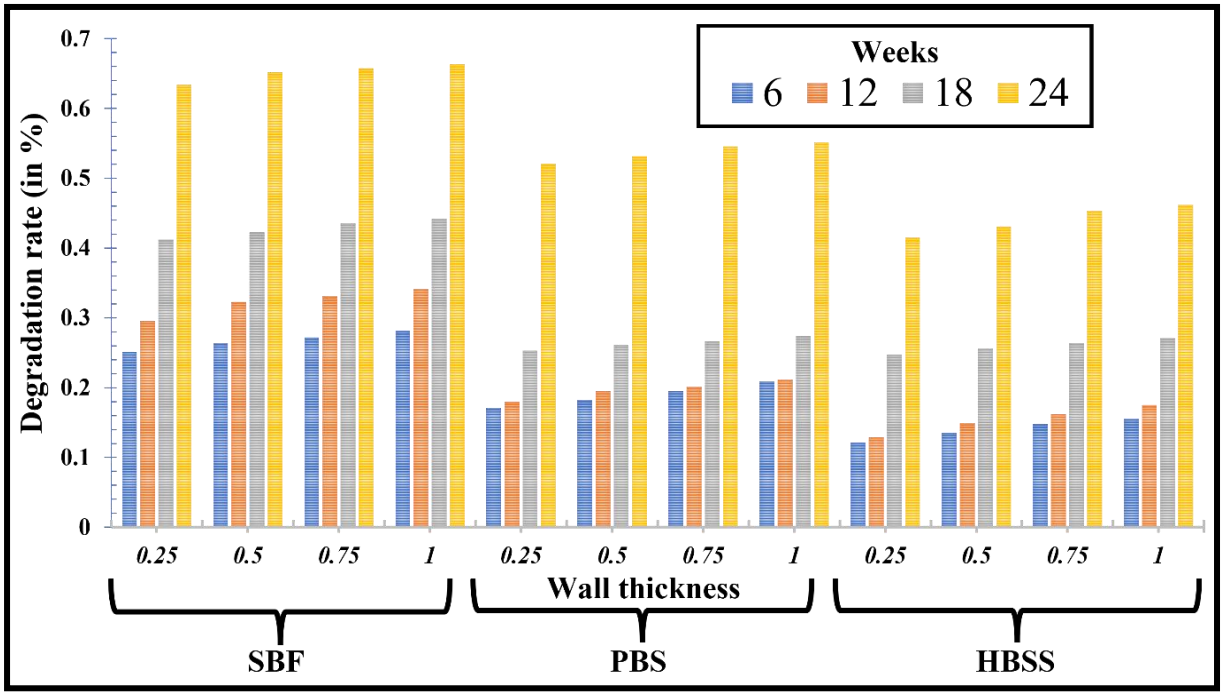


Figure 6.22: Comparison of the degradation rate of variation in wall thickness of cortical screws at different weeks on different solutions.

6.5.2. Surface morphology

The SBF solution showed higher apatite formation and the highest rate of degradation percentage compared to PBS and HBSS solutions. The microscopy and elemental mapping of the immersed cortical screw is done to observe the morphology of different elements present on the surface of the cortical screw. The higher apatite formation in the SBF solution influences the efficacy of cortical screws to enhance the Osseo-integration of bone-screw rigid fixation. The apatite growth is prejudiced and highly correlated with the porosity of the bone screw. The accumulation of apatite in the bone-screw geometry is witnessed in Figure 6.23. The elements present in the apatite are depicted with the help of elemental mapping, as presented in Figure 6.23. The elemental mapping of the cortical screw showed the presence of different elements on the surface of the cortical screw. Mostly higher elements adhesion was observed in the porous screws with less infill percentage. Therefore, the porous screw has the advantage over the solid cortical screws as they can support the callus formation and promote bone in-growth through pores in the screw body to resist the loosening of the screw.

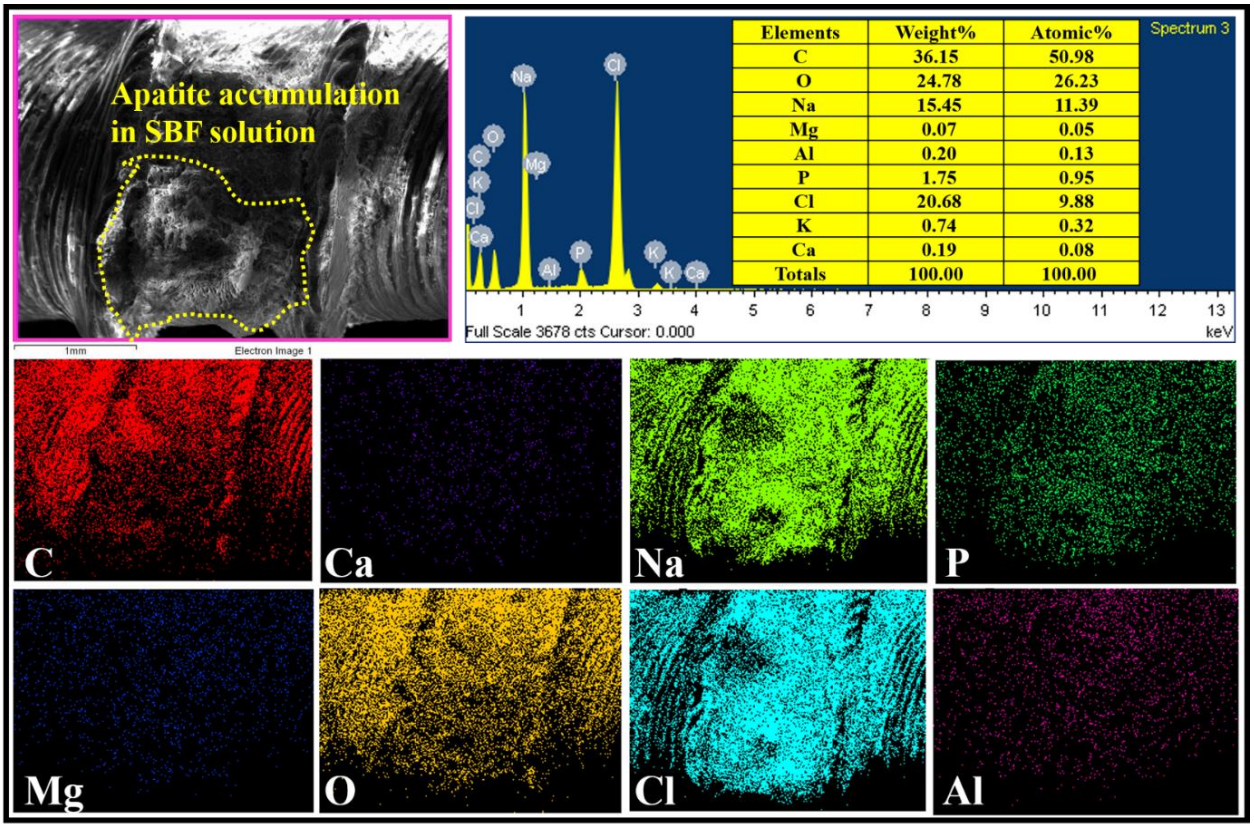


Figure 6.23: Elemental mapping of different elements present in cortical screw preserved in SBF solution.

6.5.3. Compressive strength of cortical screws

The mechanical compressive strength of cortical screws plays a significant role in orthopaedics at load-bearing fracture sites. The in-situ monitoring of the compressive strength of cortical screws was sensibly observed in the universal testing machine at room temperature. The initial compressive strength of different cortical screws was observed and compared with the compressive strength of screws after a degradation period of 24 weeks in different biological solutions. It can be expected that after the degradation behaviour of cortical screws, the compressive strength of screws may be reduced. The initial compressive strength of cortical screws with post-degradation compressive strength of screws in different biological solutions is presented in Figure 6.24.

It was observed that the compressive strength of sample no. 4 with honeycomb structured infill pattern has the highest compressive strength compared to other infill patterns, as illustrated in Figure 6.24(a). This is due to the complex honeycomb structure and higher material consumption during the fabrication of cortical screws. Moreover, a similar trend was observed in different biological solutions at 24 weeks of preservation. It was observed that

SBF-preserved cortical screws have lower compressive strength than PBS and HBSS solution, as depicted in Figure 6.24(a). This is due to the higher degradation rate in SBF solutions compared to other solutions.

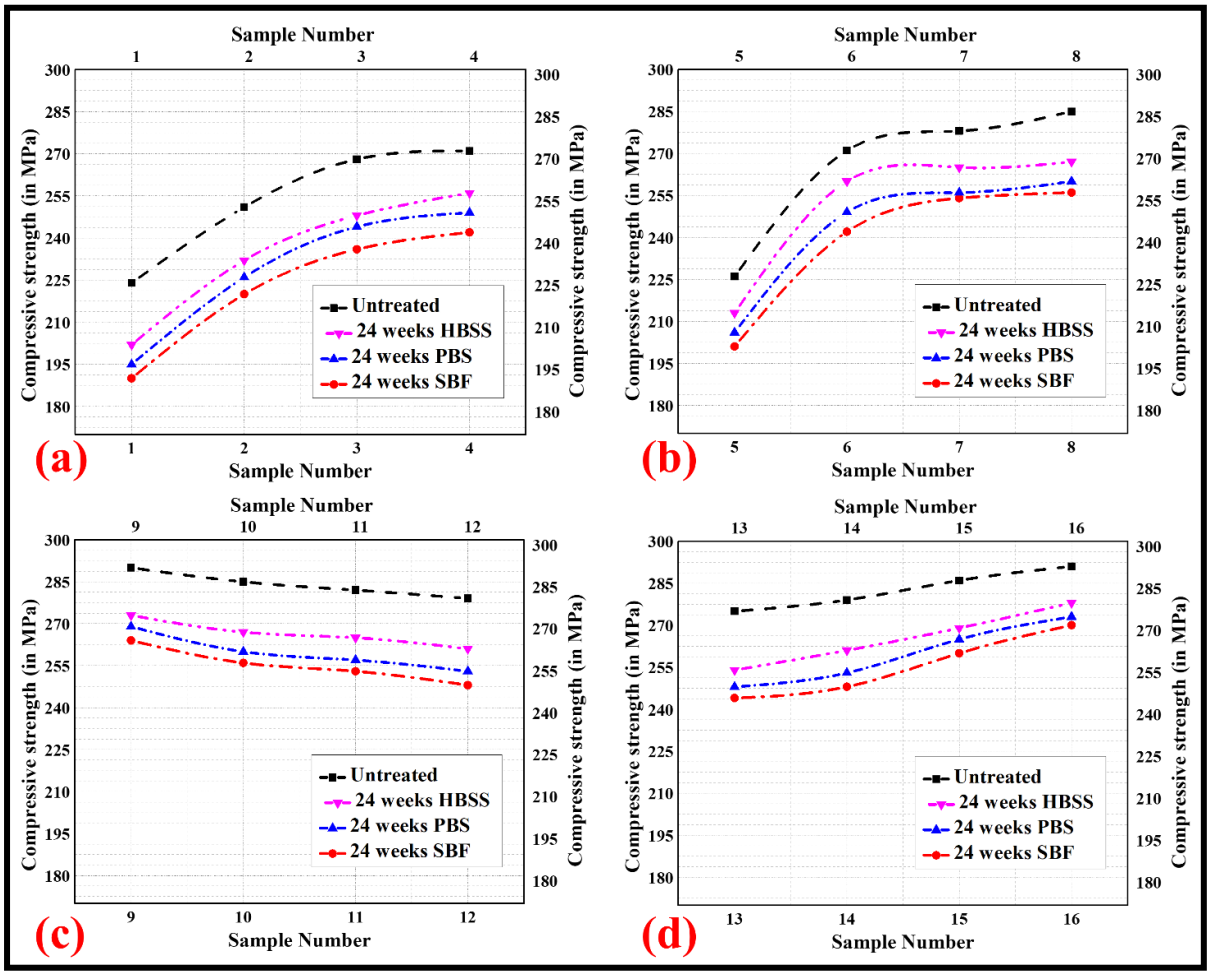


Figure 6.24: Compressive strength of cortical screws based on (a) variation in infill pattern, (b) variation in infill percentage**, (c) variation in layer height, and (d) variation in wall thickness.**

The influence of infill percentage or porosity level on the compressive strength of cortical screws is observed and presented in Figure 6.24(b). It was observed that with an increase in infill percentage, the porosity of the cortical screw decreases that significantly varying the compressive strength of the cortical screw. At an infill percentage of 100% (sample no. 8), the cortical screw is almost solid and promotes compressive strength to the maximum of 284MPa, as depicted in Figure 6.24(b). This is due to the higher infill percentage and low porosity of fabricated cortical screws. Moreover, similar trends were observed in different biological mediums after the immersion of 24 weeks. It was observed that HBSS solution preserved samples have higher compressive strength than other solutions due to less

degradation rate in the HBSS solution. However, the porous cortical screws with infill densities of 50% and 75% have the advantage of faster degradation than solid screws with an infill percentage of 100% without compromising the mechanical strength of the screw. Similar results were observed in the literature in that the infill percentage of 100% screws has higher compressive strength compared to 45% screws. Hence, porous cortical screws have an advantage over solid cortical screws.

The change in layer height varies the compressive strength of the cortical screw. As the layer height increases, the number of layers decreases that reducing the compressive strength of the cortical screw, as depicted in Figure 6.24(c). The increase in layer height increases the extrusion rate and void densities of the fabricated part, reducing the material consumption and weight of the screw which reduces the compressive strength of the cortical screw. Similar trends were observed in different biological solutions after a preservation period of 24 weeks. It was observed that a layer height of 0.06 mm (sample no. 9) has the highest compressive strength in the HBSS solution compared to other parameters, as presented in Figure 6.24(c). This is due to the low degradation rate of the HBSS solution.

The impact of wall thickness on the compressive strength of 3D-printed cortical screw is observed in the preservation of different biological solutions after 24 weeks. It was observed that 1 mm (sample no. 16) wall thickness has highest compressive strength in the HBSS solution, as shown in Figure 6.24(d). This is due to less degradation rate and a greater number of layers in the fabricated cortical screw. Through all these process parameters and different biological solutions, it can be concluded that with an increase in the degradation of the cortical screw, the compressive mechanical strength of the screw decreases. Hence, the degradation rate of the cortical screw is inversely proportional to the strength of the screw.

6.5.4. Histopathological evaluations

The prepared slides [Figure 6.13] were examined using the *BX43, Upright microscope, Olympus* for the histopathological observations. A slow decalcification process using a chelating agent (EDTA) was used to demonstrate the bone cell morphology. Acid decalcification often is associated with poor staining quality of the nuclei and tissue whereas EDTA decalcification does not affect staining quality. After satisfactory decalcification, the samples were stained with haematoxylin and eosin (H& E) for microscopic examination to evaluate the bone surface after the extraction of metallic surgical (titanium and stainless-steel)

and 3D-printed PLA cortical screws. The observation was done at different magnifications and scales to observe the bone surface and tissue damage. A magnification of 4X at a scale of 500 µm and 10X at a scale of 200 µm was used respectively for microscopic histopathological evaluations of the bone surface.

The scanner images of bone tissues after the extraction of the titanium cortical screw showed a ruptured hole edge with irregular numerous cracks in the hole edge quality as shown in Figure 6.25(a). The ruptured bone surface indicates higher bonding strength between the sharp threads of titanium cortical screws. The tissue damage and empty lacunas were witnessed after the pullout of titanium screws from the bone surface as depicted in Figure 6.25(b). The ruptured bone surface and empty lacunas indicate high surrounding tissue damage with bone during the extraction of surgical titanium cortical screws.

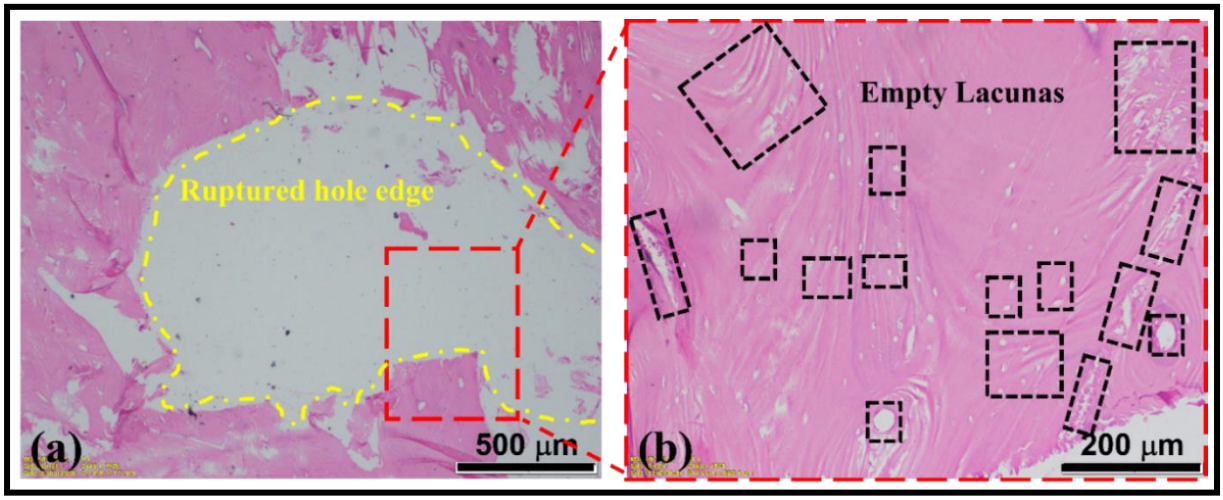


Figure 6.25: The scanner view of the bone surface after extraction of titanium cortical screws (a) at 500 µm [haematoxylin and eosin (H&E)] and (b) at 200 µm (H&E).

The bone surface after the removal of the stainless-steel cortical screw after the pullout testing is presented in Figure 6.26. The extracted surgical stainless steel bone surface depicts bone tissue damage and ruptured bone tissues as depicted in Figure 6.26(a). The evidence of gross tissue burns, and damaged bone tissues was demonstrated by microscopic examination as shown in Figure 6.26(b). This indicates higher holding strength with tissue damage during the separation of surgical stainless-steel cortical screw from the bone surface.

The scanner images of bone tissues after the extraction of the 3D-printed PLA cortical screw is shown in Figure 6.27. 3D-printed PLA-extracted bone surface revealed uniform sections with regular, smooth drilling edges as shown in Figure 6.27(a). This indicates less

surface damage with viable lacunas as demonstrated by microscopic examination as shown in Figure 6.27(b). Visible osteocytes were found near the bone surface after the extraction of 3D-printed PLA cortical screws indicating no tissue damage or cell death. This is due to less Young`s modulus of 3D-printed PLA screws as compared to surgical metallic (stainless-steel and titanium) cortical screws.

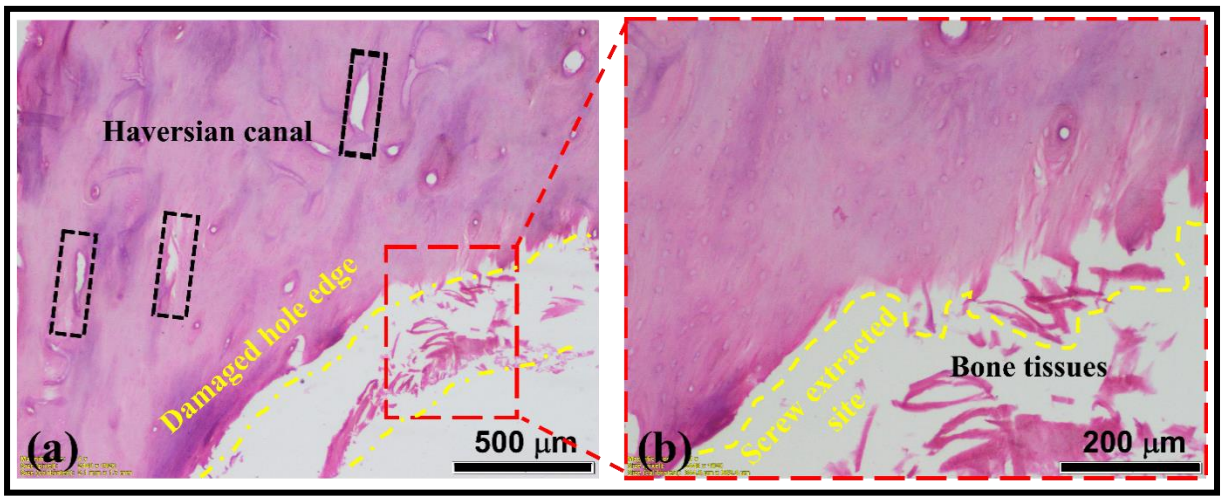


Figure 6.26: The scanner view of bone surface after extraction of stainless-steel cortical screws (a) at 500 µm [haematoxylin and eosin (H&E)] and (b) at 200 µm (H&E).

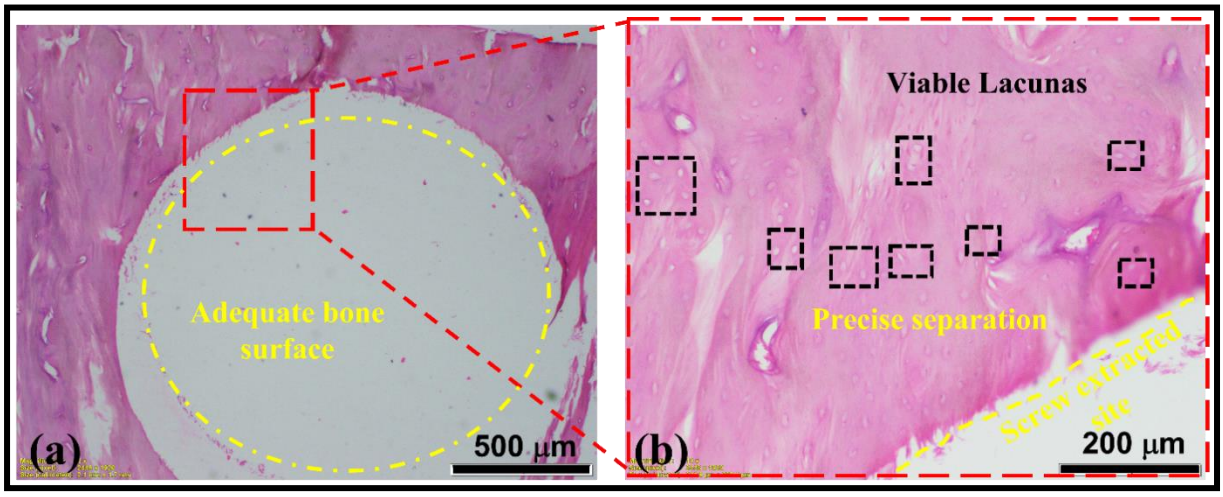


Figure 6.27: The scanner view of bone surface after extraction of 3D-printed cortical screws (a) at 500 µm [haematoxylin and eosin (H&E)] and (b) at 200 µm (H&E).

For observing the bone surface in detail after extraction of 3D-printed PLA and surgical metallic cortical screws, the microscopic images were magnified at 20X at a scale of 100 µm. The bone surface after the extraction of the titanium cortical screw represents empty lacunas with haversian canals as depicted in Figure 6.28. Haversian canals are series of tubes that forms a network in bone and blood vessels surrounded by lamellae. The higher haversian canal

represents tissue damage and injured surrounding cells. Empty lacunas after the extraction of titanium screws from bone surface represent the death of bone cells.

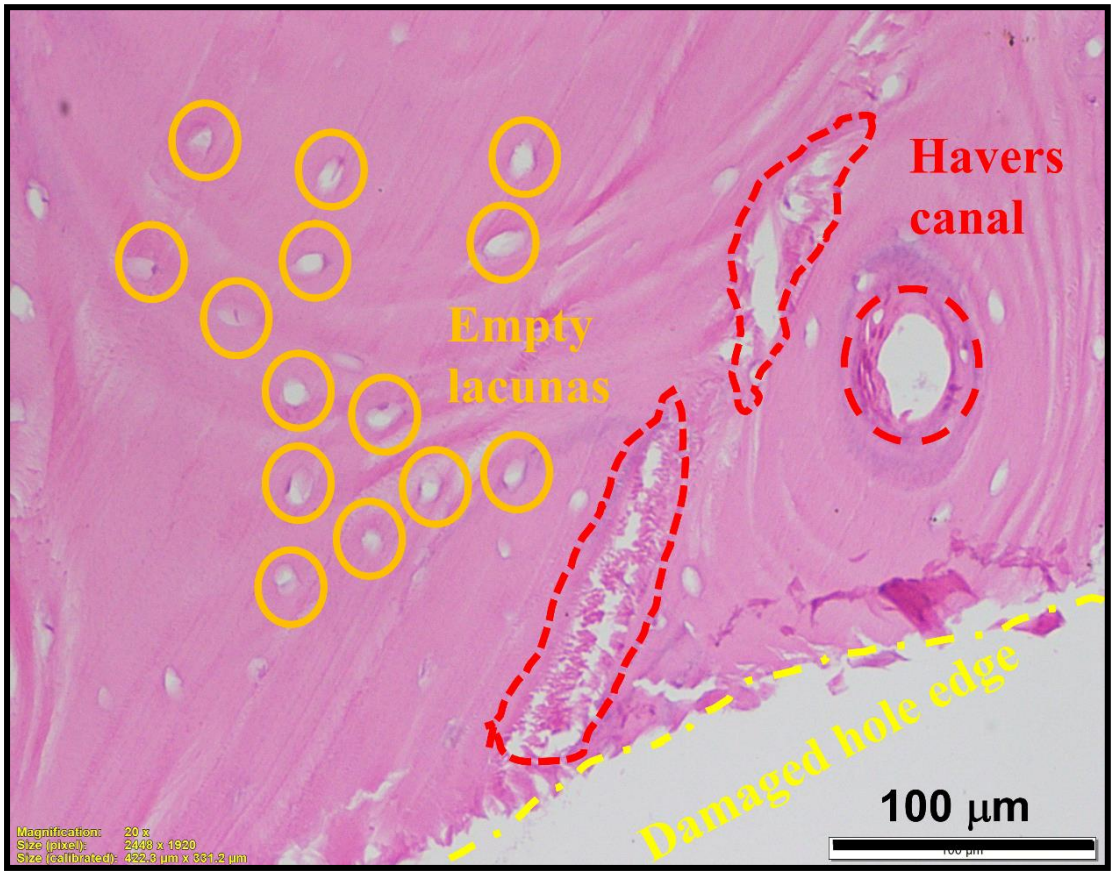


Figure 6.28: Bone surface after extraction of titanium cortical screw [H & E].

The histograms of bone surface after push-out of stainless-steel cortical screw illustrate the disrupted bone surface with empty lacunae without osteocytes as observed in Figure 6.29. This indicates high bone surface damage with harversian canals. The bone surface after the extraction of 3D-printed PLA cortical screws revealed uniform sections with no tissue damage as shown in Figure 6.30. No cell (osteocyte) loss and viable lacunas were seen after the separation of 3D-printed PLA screw from bone surface. The histologic features were consistent with the bone surface after removal of 3D-printed PLA cortical screw.

The histopathological evaluations indicate the disrupted and ruptured bone surface after the extraction of metallic cortical screws. Metallic cortical screws revealed gross cell death, high harversian canal, and tissue injury after the removal of screw from bone surface. But the proposed 3D-printed PLA cortical screw illustrates visible lacunas, no harversian canal with precise push-out of screw from bone surface without harming surrounding soft tissues. 3D-printed orthopaedic bone screws can be a vital solution to reduce tissue damage.

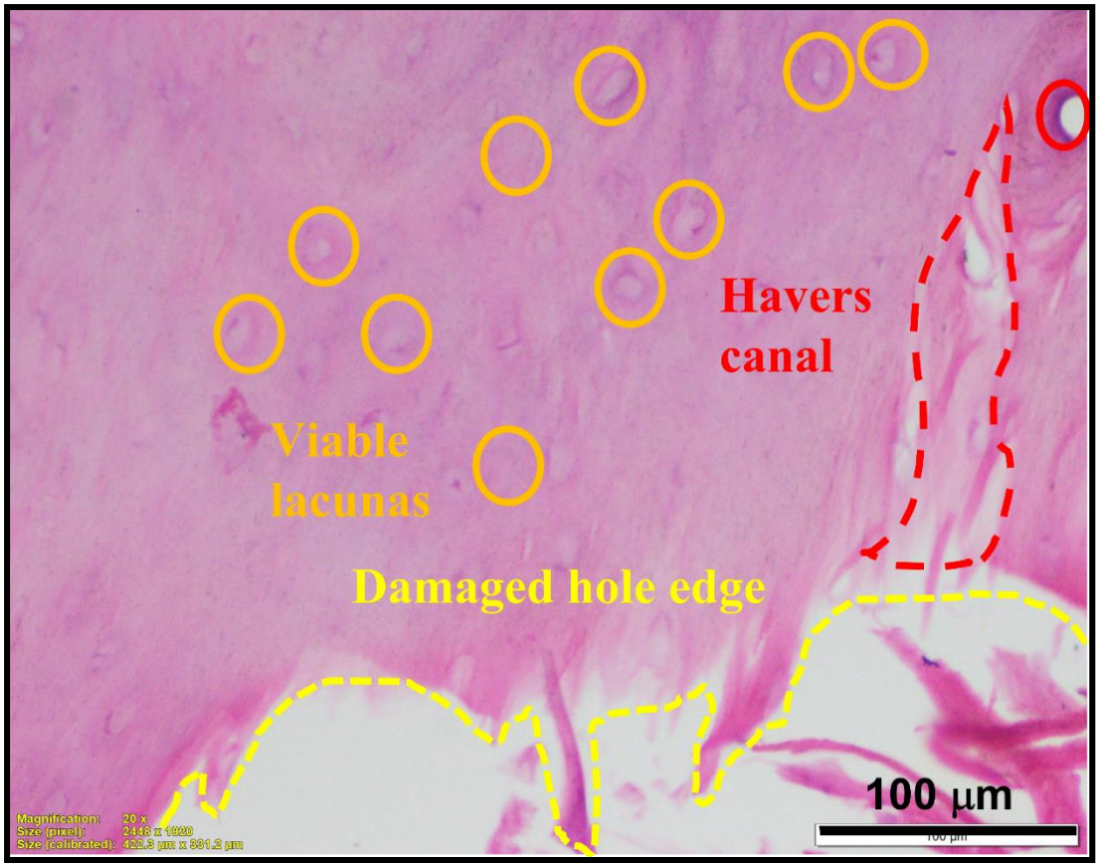


Figure 6.29: Bone surface after extraction of stainless-steel cortical screw [H & E].

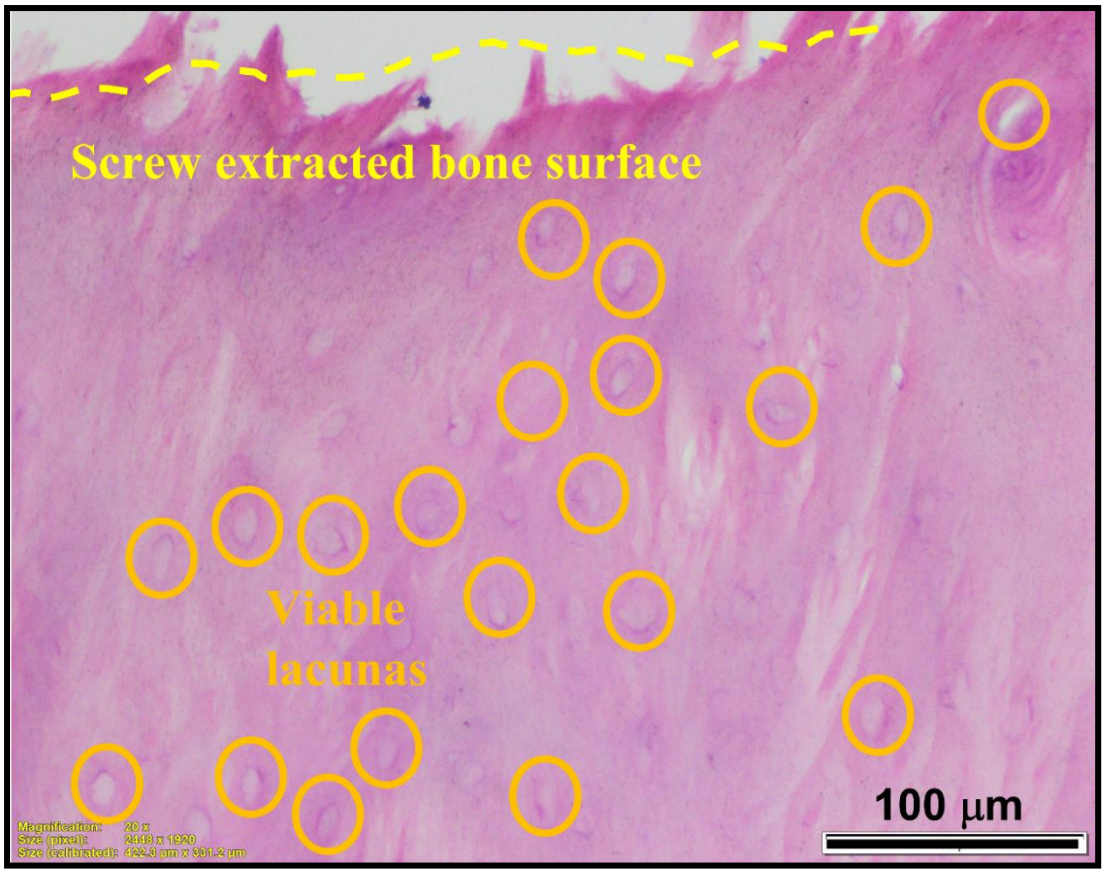


Figure 6.30: Bone surface after extraction of 3D-printed PLA cortical screw [H & E].

6.6 Conclusions

In the present chapter, the in-vitro degradation behaviour of 3D-printed cortical screws is investigated in different biological mediums. Three different biological solutions SBF, PBS, and HBSS solutions were used for the preservation of 3D-printed screws for 24 weeks. The influence of 3D printing process parameters was examined on the degradation rate of 3D-printed cortical screws. The mechanical compressive strength of various cortical screws is also observed before and after biological assessment. After their biological and mechanical characterisation, 3D-printed screws and surgical metallic screws were inserted in porcine femur bones for their histopathological evaluation. Following conclusions were made based on this chapter.

- Biological assessment of 3D-printed bone screws in different biological solutions illustrates biocompatible and biodegradable behaviour.
- The hydroxyapatite formation and degradation behaviour of 3D-printed PLA screws are higher in SBF solution compared to PBS solution and HBSS solution.
- The mechanical compressive strength of screw is inversely proportional to the degradation rate of the cortical screw.
- The hole edge quality after extraction of metallic (titanium, stainless-steel) cortical screws indicates ruptured bone surface, empty lacunas, tissue damage and high Haversian canals at bone surface.
- Histopathological evaluations at the drill edge site after the extraction of the 3D-printed PLA cortical screw illustrates less surface damage, no Haversian canals, and highly viable osteocytes at the bone-screw interface.

Chapter VII

Effect of bone mineral density on the biomechanical pullout strength

Chapter 7

Effect of bone mineral density on biomechanical pullout strength

7.1 Introduction

Osteoporosis is a disease and common health disorder characterized by decreased bone quality and mineral density, making the bone more susceptible to sustaining fractures [27]. Osteoporotic bones have low bone constructive and regenerative abilities due to a lack of bone mineral density (BMD). BMD is the amount of bone mineral in bone tissues used to measure the risk of fracture. The most prevalent risk factors for low bone density are due to low body weight, rheumatoid arthritis, vitamin D deficiency, severe obesity, patients with vertebral abnormalities and primary hyperparathyroidism [27, 30]. BMD is clinically measured as an indicator of osteoporosis and risk of bone fracture. The BMD and gender of bone may influence the biomechanical pullout strength and holding power at the bone-screw interface.

This chapter presents the measurement of BMD of male and female porcine femur bones of different ages. The influence of in-vitro bone densities with different ages and genders on the biomechanical pullout strength at the bone-screw interface. Selective laser melting-based 3D printing technology was leveraged for the fabrication of orthopaedic titanium cortical screws to improve the osseointegration in osteoporotic bones. The 3D-printed Ti6Al4V cortical screws were compared with the conventional metallic (titanium and stainless-steel) cortical screws. To check the biological assessment of different bone-screw samples, SBF solution was used for an interval of 60 days. The effect of BMD and gender of bone on the compressive strength of the screw was also examined.

7.2 3D printing of Ti6Al4V screws and their characterization

7.2.1. Porcine femur bone detailing

The porcine femur bones were selected, due to their similar properties to human bones [23, 183]. Porcine of different ages and gender were acquired from the slaughterhouse. The femur bones were harvested from male and female porcine with age groups ranging from 6 months, 24 months, and 48 months. It is expected that different ages of male and female femur bones may have variations in their BMDs. The harvested male and female bones were cleaned as illustrated in Figure 7.1(a, b, c) and Figure 7.2(a, b, c). These different aged bones for male and

female bones were observed for X-ray radiography as represented in Figure 7.1(a1, b1, c1) and Figure 7.2(a1, b1, c1). The harvested bones were cleaned and preserved in the 10% buffered formalin solution to maintain the biological and mechanical integrity of the bones. The drilling experiments were successfully performed on the same day after measuring the bone mineral density of different porcine femur bones.

7.2.2. Bone mineral density measurement

GE Healthcare's Prodigy DXA system was used to perform the dual-energy X-ray absorptiometry (DEXA) scans to monitor the level of osteoporosis in different aged porcine femur bones. It must be noted that usually the DEXA scans are used for human bones (above 20 years of age). Since the DEXA machine is not calibrated for measuring the bone density of porcine bones, therefore, the authors have performed calibration of porcine bones. The DEXA scan uses spectral imaging of bone to examine the bone composition and bone mineral density.

Different male and female femur bones of different ages were observed in the DEXA scan as depicted in Figure 7.1(a2, b2, c2) and Figure 7.2(a2, b2, c2). DEXA scans provide an in-depth analysis of fat tissue, muscle mass and density of bone using a T-score. The World Health Organization established the T-score value above -1 as normal bone density, between -1 and -2.5 as osteopenia with insufficient bone mass, below the range of -2.5 is referred to as osteoporotic bone.

The corresponding measured density of different aged male and female femur bones are presented in Figure 7.1(a3, b3, c3) and Figure 7.2(a3, b3, c3). 6-months old male femur bone was observed with osteopenia with BMD of 0.994 g/cm^3 as depicted in Figure 7.1 (a3). 24-month-old and 48-month-old male femur bones were observed in the range of normal density with different bone densities of 1.231 g/cm^3 and 1.736 g/cm^3 as shown in Figure 7.1(b3) and Figure 7.1(c3) respectively. It was observed that for with increasing the age of porcine femur bone, the BMD of bone also increased.

The 6-month-old female femur bone was observed as osteoporotic bone with a BMD of 0.844 g/cm^3 as demonstrated in Figure 7.2 (a3). 24-month-old female femur bone has a bone density of 1.091 g/cm^3 as depicted in Figure 7.2(b3). 48-month-old female femur bone with a BMD of 1.476 g/cm3 was observed in the normal density range as illustrated in Figure 7.2(c3). It was witnessed by DEXA scans that male femur bones for the same age group have higher BMD compared to female femur bones.

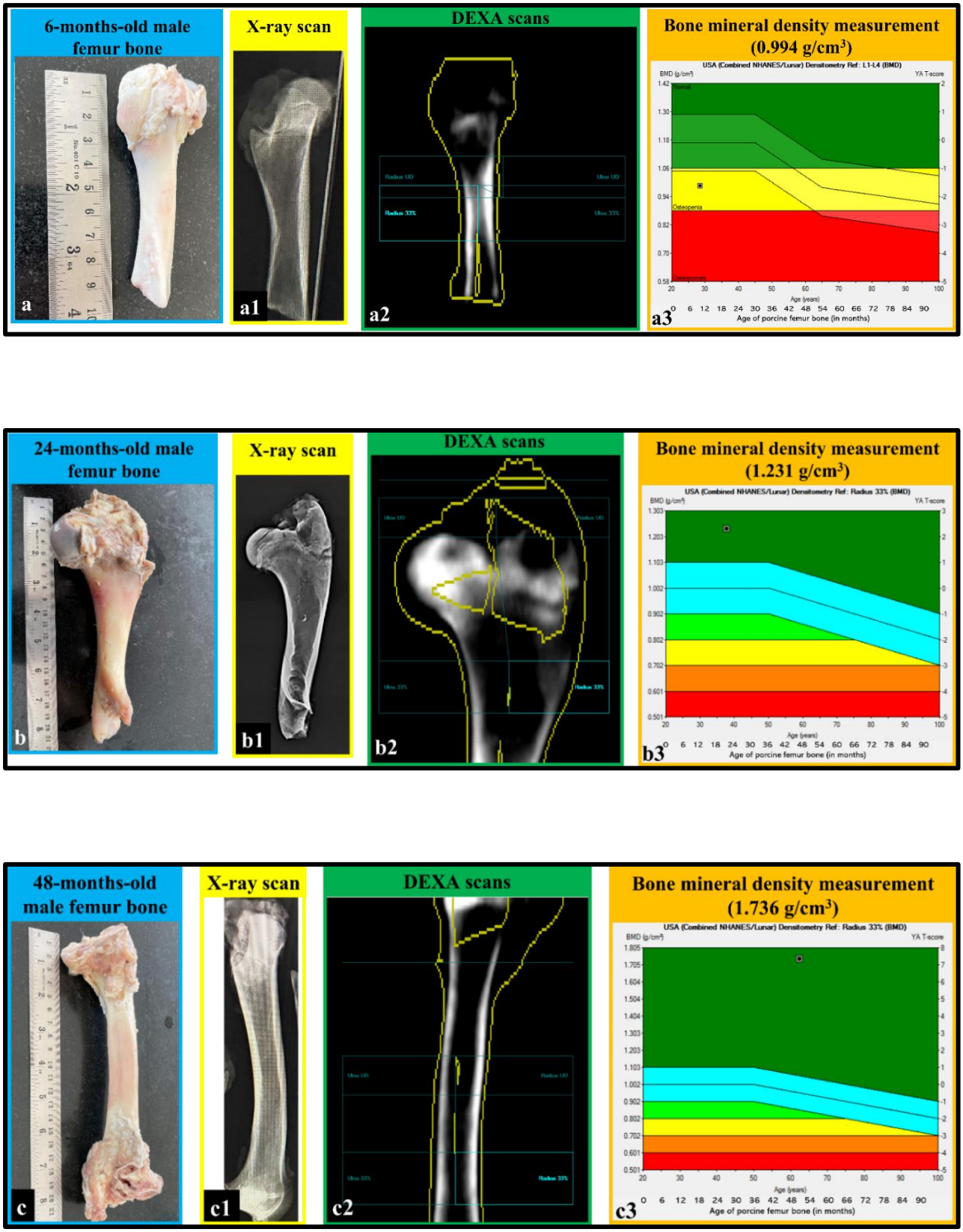


Figure 7.1. Porcine male bones with X-ray micrographs and DEXA scan micrographs with measured bone density for (a) (a1) (a2) (a3) 6-months old, (b) (b1) (b2) (b3) 24-months-old, (c) (c1) (c2) (c3) 48-months-old femur bones.

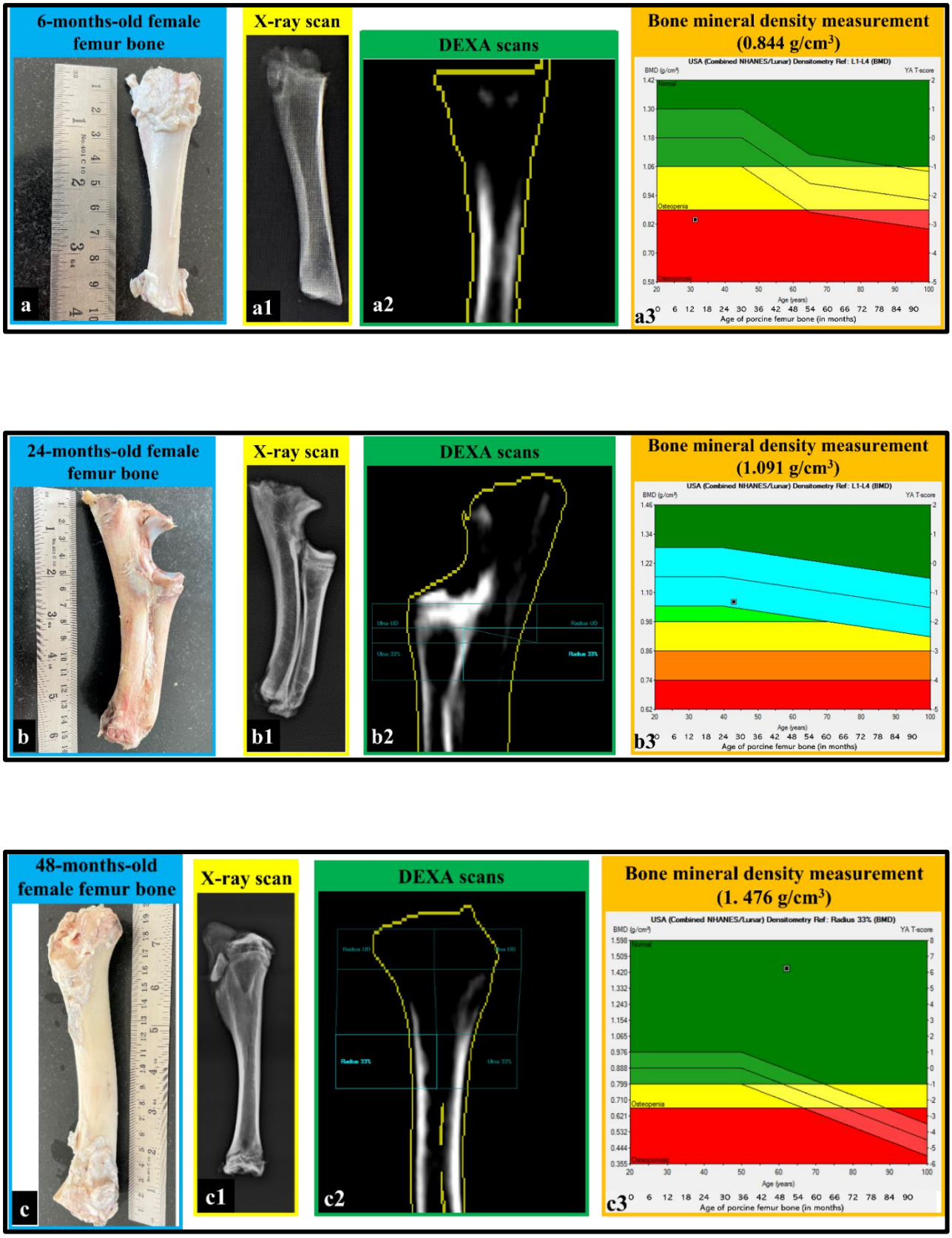


Figure 7.2. Porcine female bones with X-ray micrographs and DEXA scan micrographs with measured bone density for (a) (a1) (a2) (a3) 6-months old, (b) (b1) (b2) (b3) 24-months-old, (c) (c1) (c2) (c3) 48-months-old femur bones.

7.2.3. 3D printing of Ti6AL4V cortical screws

The conventional surgical cortical screws were compared with 3D-printed titanium cortical screws. For the fabrication of titanium cortical screws using 3D printing technology, the design of standard surgical titanium cortical screws was replicated in the designing software Creo parametric 7.0. The outer diameter, head diameter, pitch, length, and core diameter of the computer-aided design (CAD) were mimicked similar to the 4.5 mm surgical cortical screw. The 3D CAD model of the cortical screw was converted into standard tessellation language (STL) format for the fabrication of screws using selective laser melting (SLM) based 3D printing technology. Ti6Al4V powder was selected as a printing material with an average radius of 24 µm. The minimum powder radius of 14 µm and the maximum radius of Ti6AL4V powder of 37 µm, were calculated using Digimizer image analysis software as presented in Figure 7.3(a). During SLM technology, a high power-density laser was utilized to scan, melt, and fuse Ti6AL4V powder employing the fabrication of screws in a layer-by-layer structure. The unmelted powders surrounding the fabricated screw were reused for the fabrication of another cortical screw. After cleaning and post-processing of cortical screws, the structural morphology of the 3D-printed titanium screws was observed using scanning electron microscopy (SEM).

7.2.4. Drilling of porcine femur bones

The experimental setup for drilling different densities of porcine femur bones is demonstrated in Figure 7.3(b). *MTAB XLMILL (CNC 4640)* PC-controlled 3-axis vertical milling machine was used for drilling different aged porcine femur bones. The surgical twisted drill bit of diameter 3.5 mm and constant drilling parameters were used for the drilling procedure. These parameters were chosen based on a previously reported literature survey. The constant rotational speed of 1500 RPM and feedrate of 30 mm/min was provided through the auto mode PC-based G-codes for drilling of different densities and gender of porcine femur bones. After the drilling experiments, the 4.5 mm surgical titanium and stainless steel along with 3D-printed titanium cortical screws (Figure 7.3(c)) were inserted carefully in the drilled holes of different bone samples as depicted in Figure 7.3(d).

To observe the biocompatibility and mimic human biological conditions, the bone-screw specimens, and different cortical screws were preserved in SBF solution for 60 days of time intervals. SBF solution has numerous chemical reagents used in different amounts that

enable the growth of stoichiometric, bone-like apatite or calcium-deficient hydroxyapatite (HA) formation at biomaterials surface [194, 195]. The SBF-preserved bone-screw samples are illustrated in Figure 7.3(e). The SBF-immersed specimens were preserved in an incubator at 37 0C as illustrated in Figure 7.3(f) for 60 days. To understand the biochemical interaction and biocompatibility of 3D-printed screws and conventional screws, the biological treatment was assessed by following the same procedure. The cortical screws were preserved in SBF solution using Eppendorf centrifuged tubes in an incubator at 370C as illustrated in Figure 7.3(g). The SBF solution changed every week to avoid SBF solution contamination and saturation. It is expected that the biological assessment of cortical screws depicts a similar biological behaviour as SBF-preserved bone-screw specimens.

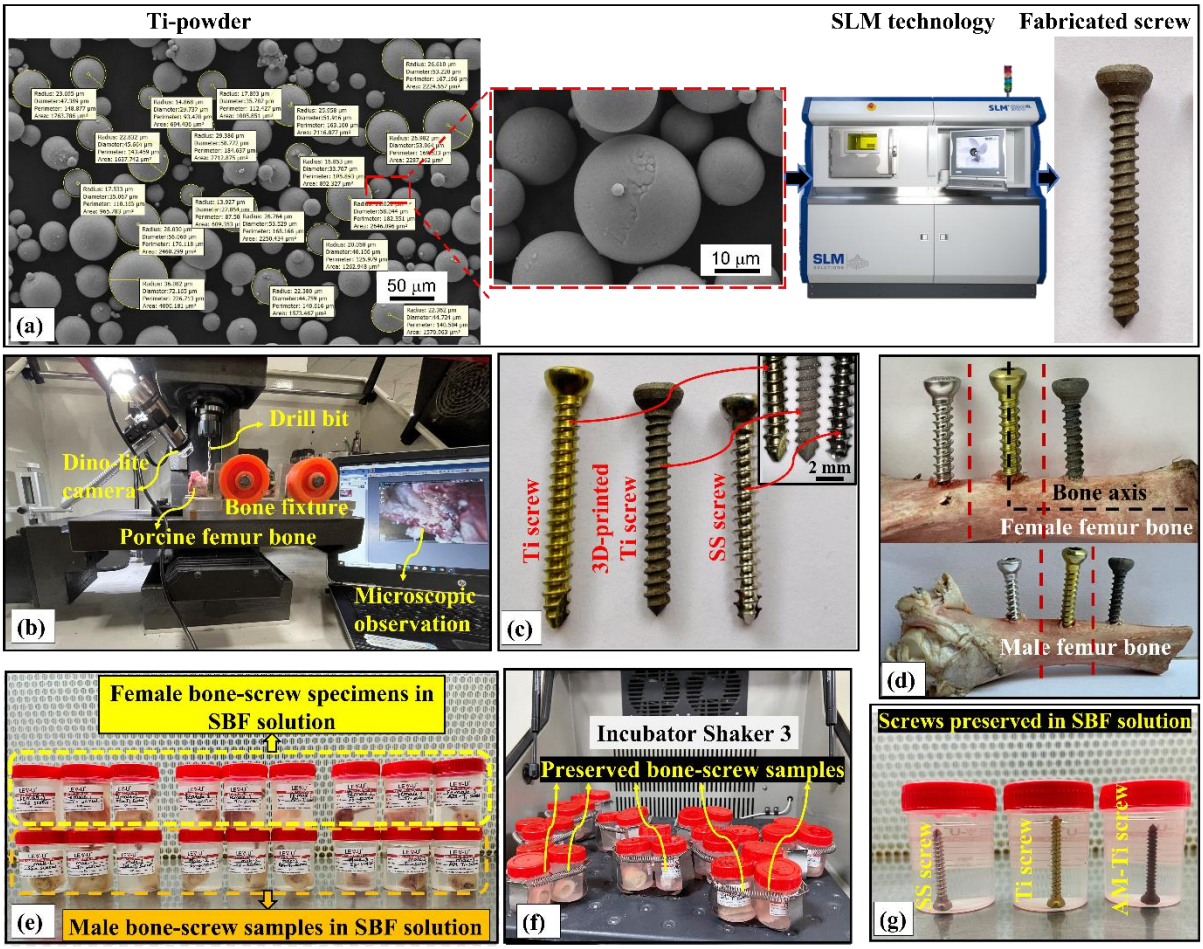


Figure 7.3. (a) Titanium powder for 3D printing of cortical screw, (b) experimental bone drilling setup, (c) 3D-printed titanium, titanium, and stainless-steel cortical screws, (d) different cortical screws insertion in female and male femur bones with different densities, (e) immersion of male/female bone-screws specimens in SBF solution, (f) preservation of samples in an incubator for 60 days, (g) different screws immersed in SBF solution for biological assessment.

7.2.5. Biomechanical pullout strength setup

The biomechanical pullout testing of bone-screw specimens was conducted to observe the resisting holding strength and required force to pull the cortical screws out from the bone surface. The universal testing machine (*UTM-series 7200, DAK system*) was used to perform the biomechanical pullout testing of cortical screws. The bone-screw specimens were held in the centre, and both ends of the fixture were rested in the upper jaw and lower jaw of the UTM machine. The lower jaw of the machine was fixed, whereas the upper jaw was actioned in an upward direction. The biomechanical pullout strength of different bone-screw samples was assessed as the maximum load applied till the extraction of the screw from bone integrity.

7.3 Results and Discussions

7.3.1. Micromorphology of different cortical screws

The surface topology and micromorphology of different cortical screws were examined by SEM micrography. The SBF-preserved screws were also observed in SEM for their microstructure and hydroxyapatite growth observation. It is expected that during the same interval of time in SBF solution, different bone-screw samples will have similar biological behaviour, as the screws preserved in SBF solution. The surface morphology and microstructure of the 3D-printed screws, titanium screws and stainless-steel cortical screws are illustrated in Figure 7.4(a)(b)(c). It was observed that 3D-printed cortical screw has roughened threads due to the sintering of Ti6Al4V powder via high-power laser for melting and fabrication of screws as depicted in Figure 7.4(a). Moreover, it was also observed at microscopic levels, that 3D-printed titanium cortical screws have a microporous structure due to the fusion of titanium powder. Whereas in the case of titanium and stainless-steel cortical screws, sharp-edged threads with solid structures are witnessed due to subtractive manufacturing of screws as illustrated in Figure 7.4(b) and Figure 7.4(c) respectively.

After observing the surface morphology and microstructure of screws, the biological assessment of different metallic orthopaedic screws was done with preservation in SBF solution. After 60 days of screw preservation in SBF solution, the samples were observed for SEM micrographs as represented in Figure 7.4(d)(e)(f). The hydroxyapatite coating was observed on all the metallic bone screws, confirming the biocompatible behaviour of all metallic screws. Further, it was witnessed that 3D-printed cortical screws have higher hydroxyapatite growth on the surface of screws compared to conventional surgical metallic

screws. This is due to the laser powder bed fusion-based 3D-printing technology that fabricates microporous and microroughened threads of cortical screws. Hefty-edged hydroxyapatite was accumulated in the threads of the 3D-printed titanium cortical screw as depicted in Figure 7.4(d) due to microporous structure of 3D-printed titanium cortical screws.

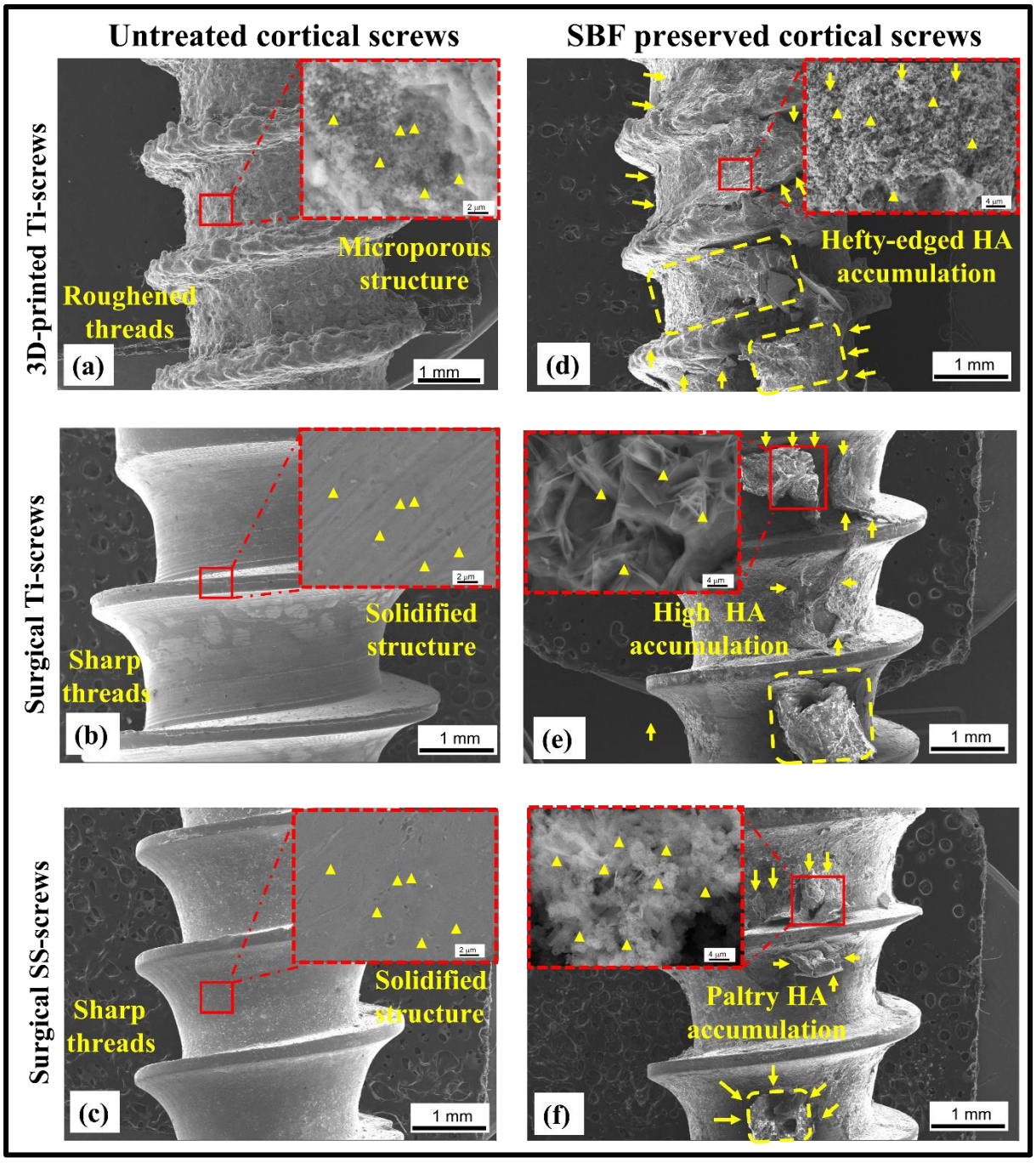


Figure 7.4. Micrographs of untreated cortical screws (a) 3D-printed titanium cortical screw, (b) surgical titanium cortical screw, (c) surgical stainless-steel cortical screw; SBF immersed cortical screws (d) 3D-printed titanium cortical screw, (e) surgical titanium cortical screw, (f) surgical stainless-steel cortical screw.

Whereas in the case of conventional medical titanium screws, less hydroxyapatite accumulation was observed compared to 3D-printed titanium cortical screws as depicted in Figure 7.4(e). This is due to solidified structure of conventional titanium screws manufactured via subtractive manufacturing. Partly hydroxyapatite accumulation was witnessed in conventional stainless-steel cortical screws as depicted in Figure 7.4(f). This is due to the high iron content and subtractive manufacturing of stainless-steel cortical screws. As 3D-printed cortical screws have higher hydroxyapatite growth on the periphery of the screw, it is expected that 3D-printed titanium cortical screws may enhance bone-screw integration. Higher bone-screw bonding and hydroxyapatite assimilation is expected that can ameliorate the pullout strength at the bone-screw interface in osteoporotic bones.

7.3.2. Analysis of hydroxyapatite formation

After the preservation of samples in SBF solution, hydroxyapatite coating was observed at a microscopic level to observe the structure and elements present in the accumulated hydroxyapatite. To observe the elements, present in accumulated hydroxyapatite over the periphery of screw threads of different screws, elemental energy-dispersive spectroscopy (EDS) was observed as illustrated in Figure 7.5. The micrographs of accumulated hydroxyapatite depict the surface geometry and texture morphology of hydroxyapatite in different cortical screws. With different SEM micrographs presented in Figure 7.5, it is witnessed that spiked hefty-edged hydroxyapatite growth is observed in 3D-printed titanium cortical screws as observed in Figure 7.5(a). The accumulated hydroxyapatite on the surface of different cortical screws replicates the composition of human plasma and bone-like biomimetic hydroxyapatite.

The EDS spectrums of different cortical screws display various elements present in the hydroxyapatite coating on the surface of different cortical screws. The calcium (Ca) contribution of titanium screws was higher than stainless-steel cortical screws as shown in Figure 7.5(b). The calcium (Ca) contribution by the stainless-steel cortical screws were minimum as compared to titanium and 3D-printed titanium cortical screws as depicted in Figure 7.5(c). The calcium phosphate (CaP) deposition in different screws was monitored using the weight percentage of elements present in hydroxyapatite growth. The bone-like hydroxyapatite surface enrichment of 3D-printed titanium cortical screws was significantly higher compared to conventional surgical titanium and stainless-steel cortical screws.

Therefore, 3D-printed titanium cortical screws are expected to improve the bone-screw-bonding ability at the bone-screw interface.

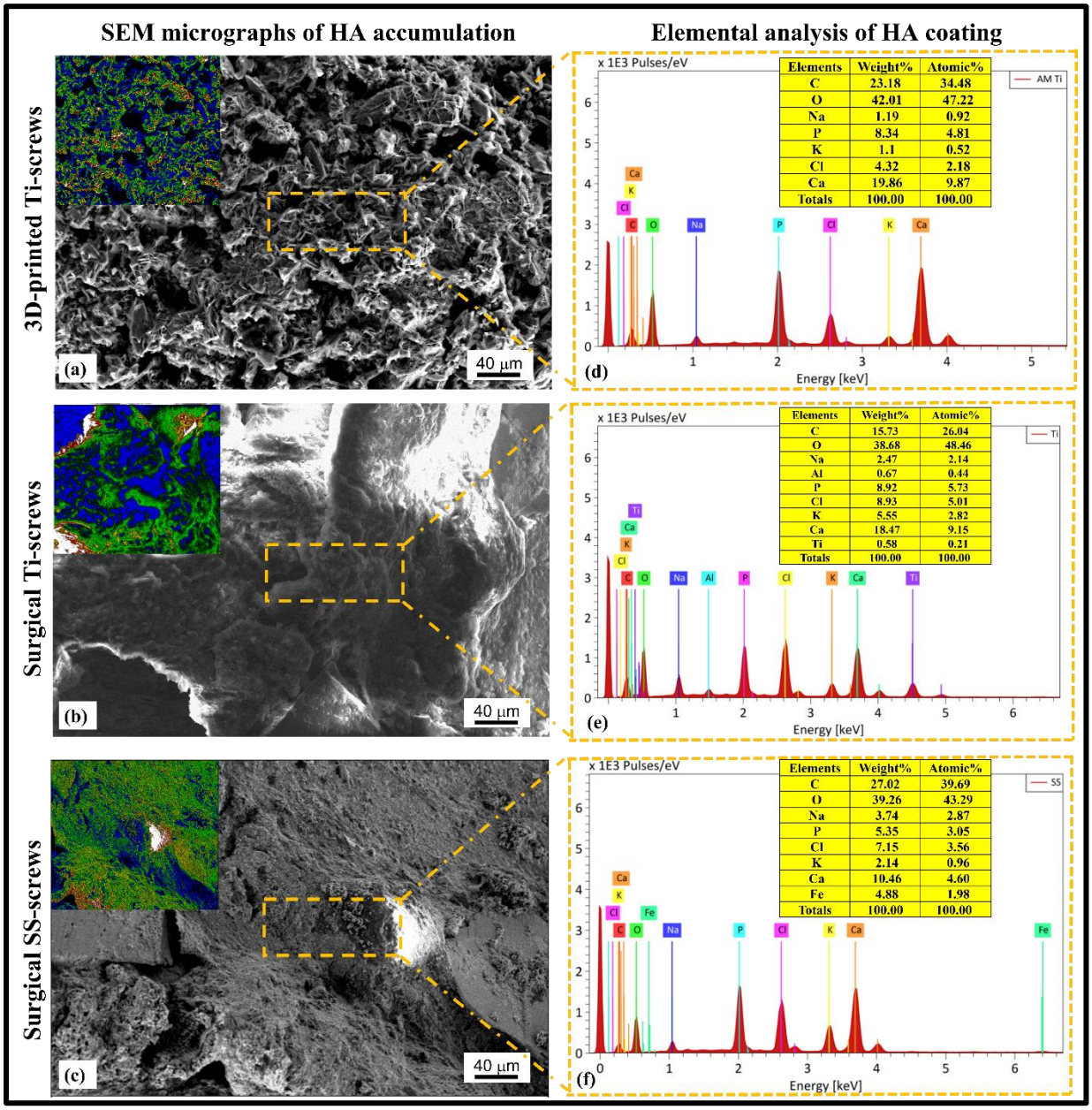


Figure 7.5. Micrographs of HA accumulation in (a) 3D-printed titanium cortical screw, (b) surgical titanium cortical screw, (c) surgical stainless-steel cortical screw; elements present in accumulated HA in (d) 3D-printed titanium cortical screw, (e) surgical titanium cortical screw, (f) surgical stainless-steel cortical screw.

7.3.3. Elemental analysis of hydroxyapatite coating

After observing the elements present in the bone-like hydroxyapatite coating of different screws, the elemental area mapping analysis of different screws was observed as illustrated in

Figure 7.6. The elemental area mapping of the tip of different cortical screws can be used to represent the spatial distribution and specific elemental composition of cortical screws. The texture content and composition zonation of elements replicate the level of hydroxyapatite formation on the tip of screws. The untreated tip of cortical screws replicates the base metallic elements present in the cortical screws as depicted in Figure 7.6.

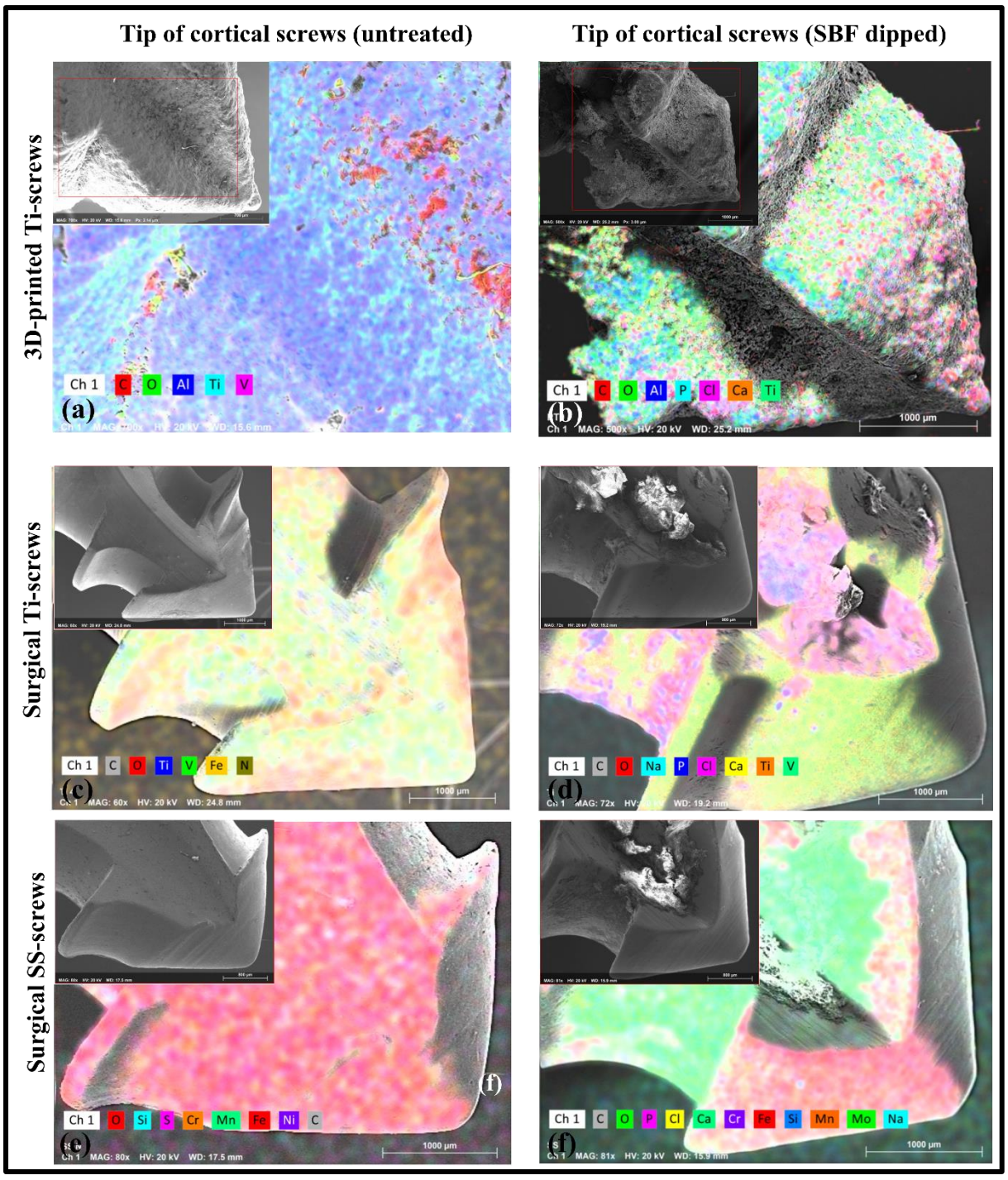


Figure 7.6. Elemental area mapping of the tip of cortical screws for (a) untreated, (b) SBF immersed for 3D-printed titanium screws; (c) untreated, (d) SBF immersed for surgical titanium screws; (e) untreated, and (f) SBF immersed for surgical stainless-steel screws.

The 3D-printed untreated cortical screw shows the presence of titanium (Ti), aluminium (Al), vanadium (V), carbon (C) and oxygen (O) as shown in Figure 7.6(a). The SBF-treated 3D-printed screw enriched hydroxyapatite with additional elements of calcium (Ca), chlorine (Cl) and phosphate (P) in high weight percentage as shown in Figure 7.6(b). The conventional surgical titanium cortical screws replicate the presence of base elements as shown in Figure 7.6(c), whereas the SBF-treated titanium screw has the presence of Ca, Cl, P, and sodium (Na) as shown in Figure 7.6(d). It was observed the tip of the 3D-printed cortical screw has a high accumulation of hydroxyapatite compared to conventional surgical titanium screws. The surgical stainless-steel cortical screw reveals the presence of C, O, iron (Fe), manganese (Mn), chromium (Cr), silicon (Si) and nickel (Ni) as shown in Figure 6(e). Due to the high presence of heterogenous metals in the stainless-steel cortical screws, very few hydroxyapatites were witnessed with additional elements of Ca, Cl and P as shown in Figure 6(f). The hydroxyapatite growth of 3D-printed titanium screws was significantly higher compared to surgical titanium and stainless-steel cortical screws. It is expected that similar biological behaviour of screws was indicated at the bone-screws interface in the SBF solution. Also, with higher hydroxyapatite accumulation, the pullout strength of the screw is expected to be advanced.

7.3.4. Biomechanical pullout strength of cortical screws

The biomechanical pullout strength of different bone-screw specimens was evaluated based on the axial pullout strength of screws embedded in the bone periphery. Pullout strength was observed as the maximum force required by different cortical screws inserted in different densities and genders of porcine femur bones. This section explains the influence of BMD, gender, and different surgical biomaterials on the pullout strength of cortical screws.

7.3.4.1. Effect of BMD on pullout strength of cortical screws

It was observed that BMD influences the biomechanical pullout strength of cortical screws inserted in different age groups of porcine femur bones. Figure 7 illustrates the influence of different age groups of porcine bones on the pullout strength of cortical screws. It was witnessed that with an increase in BMD, the pullout strength of all screws (SS, Ti, 3D-printed Ti cortical screws) increases as depicted in Figure 7. This increase in pullout strength is due to higher surface area provided with an increase in thickness and quality of bone, enhancing the holding power at the bone-screw interface. A higher density of bone increases the strength and stability of fixation which improves the rigid immobilization that enhances the biomechanical

pullout strength of cortical screws. A similar trend was observed after immersion of bone screw samples in SBF solution for 60 days of intervals. 48 months old femur bone-screw samples have the highest biomechanical pullout strength for all (3D-printed titanium, surgical titanium and stainless-steel) cortical screws.

7.3.4.2. Effect of gender on pullout strength of cortical screws

The influence of bone gender plays a vital role that affecting the BMD and pullout strength of cortical screws. It is witnessed from DEXA scans that with similarly aged femur bones of male and female porcine, the BMD of male femur bones were higher compared to the BMD of female bones. Therefore, the biomechanical pullout strength of cortical screws inserted in male femur bones is expected to be higher compared to female femur bones. It was witnessed from Figure 7.7 that for different age groups and different screws, the pullout strength of male bone-screw samples was higher compared to female bones. This is due to differences in their bone mineral densities for similar age groups. With the increase in BMD, the grasping power and holding capacity at the bone-screw interface increases. Therefore, in this study, it can be observed the gender and BMD of bone influences the biomechanical pullout strength at the bone-screw interface.

7.3.4.3. Effect of biomaterials on pullout strength of cortical screws

The selection of biomaterial is important to accelerate the holding strength at the bone-screw interface. The mechanical properties of biomaterial play a significant role that influencing the pullout strength and holding power at the bone-screw interface. During the present in-vitro investigation, it was observed that titanium screws have higher pullout strength as compared to stainless steel cortical screws as observed in Figure 7.7. This is due to changes in the element percentages of stainless steel and titanium screws.

Titanium screws have 89% of titanium with 6% aluminium and 4% vadnium, whereas in stainless steel screws 59.8-68% of iron, 16-18% of chromium, 10-16% nickel, 2-3% of molybdenum and less than 1% of carbon and nitrogen [196–198]. It is also reported in the literature that titanium screws are superior and expensive compared to stainless steel screws due to better biocompatibility, fatigue resistance, osseointegration and better bone-tissue reaction **[39, 40]**. Therefore, titanium bone screws are better as compared to stainless steel bone screws for accelerating the bone-screw holding strength and promoting the biomechanical pullout strength at the bone-screw iterface.

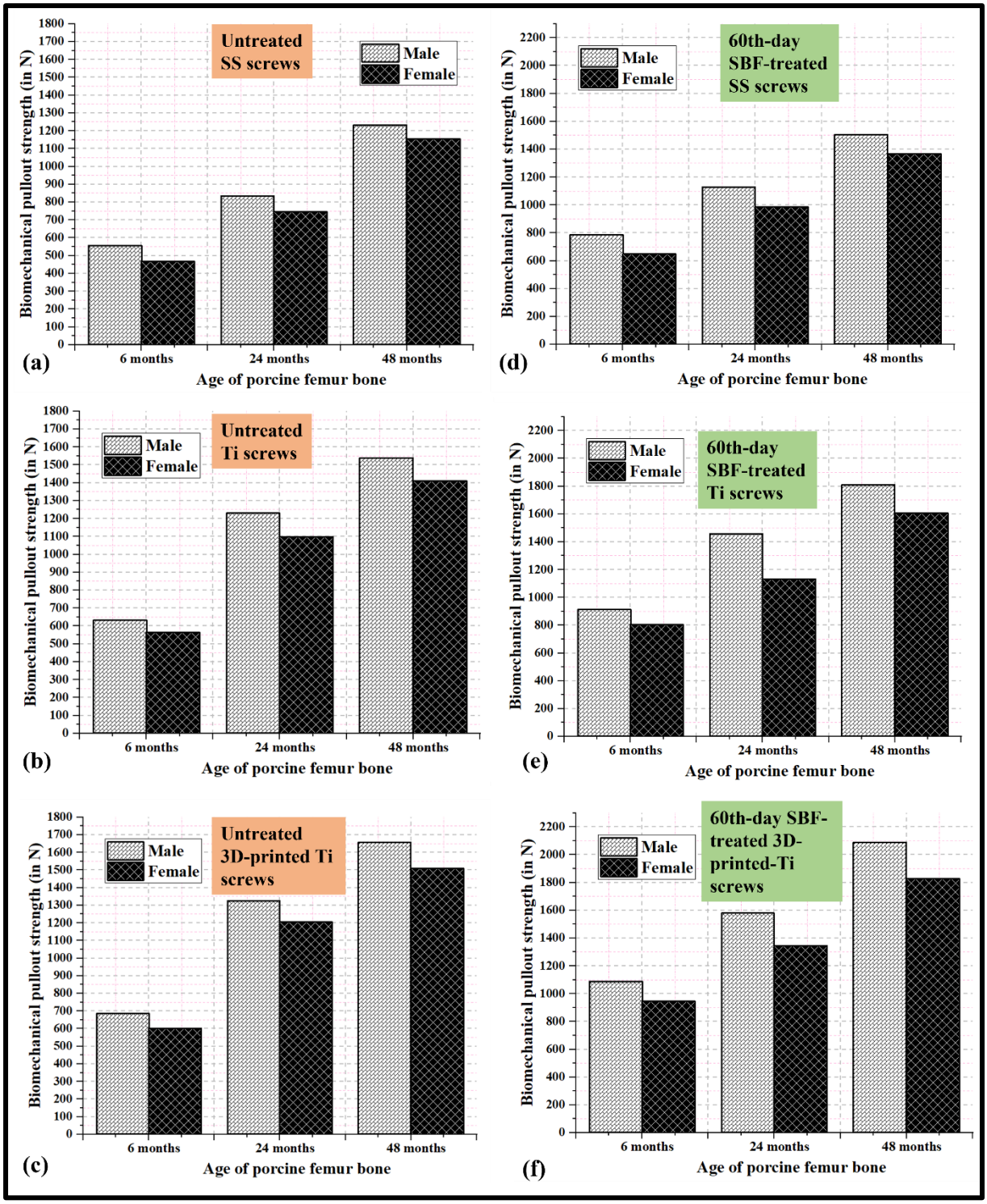


Figure 7.7. Untreated bone-screws pullout strength at 1st day for (a) surgical SS screws, (b) surgical Ti-screws, (c) 3D-printed titanium screws; SBF immersed bone-screws pullout strength at 60th day for (d) surgical SS screws, (e) surgical Ti-screws screws, and (f) 3D-printed titanium screws.

Titanium bone screws were fabricated using powder bed fusion-based metal 3D printing technology that provides microporous and micro-roughened surfaces. Therefore, 3D-

printed titanium screws have the higher bone-bonding ability and hefty-edged bone-like hydroxyapatite accumulation. Hence, 3D-printed orthopaedic cortical screws may improve the biomechanical pullout strength as compared to conventional surgical titanium cortical screws.

7.3.4.4. Effect of immersion period on pullout strength of cortical screws

It is elucidated that with an increase in the immersion period of different cortical screws in SBF solution, the bone-like hydroxyapatite bioactive coating of screws increases. A similar hydroxyapatite growth is anticipated in bone-screw samples. Higher biomechanical pullout strength of all bone-screw samples was observed after 60 days of immersion of samples in SBF solution as compared to 1st day of bone-screw samples. This is due to the reason of increase in bone-like hydroxyapatite bioactive coating that improves the bone-bonding ability after 60 days of immersion. 3D-printed titanium cortical screws have the highest hydroxyapatite formation. This increase in hydroxyapatite coating enhances the osteoconductive behaviour and holding strength at the bone screw interface promoting the biomechanical pullout strength of 3D-printed titanium cortical screw. The 3D-printed screws increase the contact area at the bone-screw interface with the hefty-edged surrounding bone-like hydroxyapatite accumulation that enhances the initial stability, holding potential and re-strict the micromovement at the bone-screw interface that ameliorates the biomechanical pullout strength of screw.

7.3.5. Fractured bone morphologies after screw extractions

After pullout testing of different screws from bone-screw samples, the hole quality of bone was observed to monitor the morphology of fractured bones. The axial pullout strength of the screw replicates the separation of the screw from the bone surface. The pullout force required for the push-out of the screw from the bone surface elucidates the holding strength of the screw and elongation of the bone. The morphology of bone evaluates the initial stability, bone-screw interface bonding, and damaged bone periphery during the extraction of the screw. The fractured bone morphologies after screw extractions for different age groups with surgical stainless steel, titanium and 3D-printed titanium screws are illustrated in Figure 7.8. During the extraction of surgical stainless-steel screws, the fractured bone hole quality is shown by mini-arrows as depicted in Figure 7.8(a). For 6-month-old femur bone, the conventional stainless-steel screws replicate clean separation with a little bone debris in the surroundings as depicted in Figure 7.8(a). Similar separation with some extra bone debris was witnessed with surgical titanium cortical screws as presented in Figure 7.8(b).

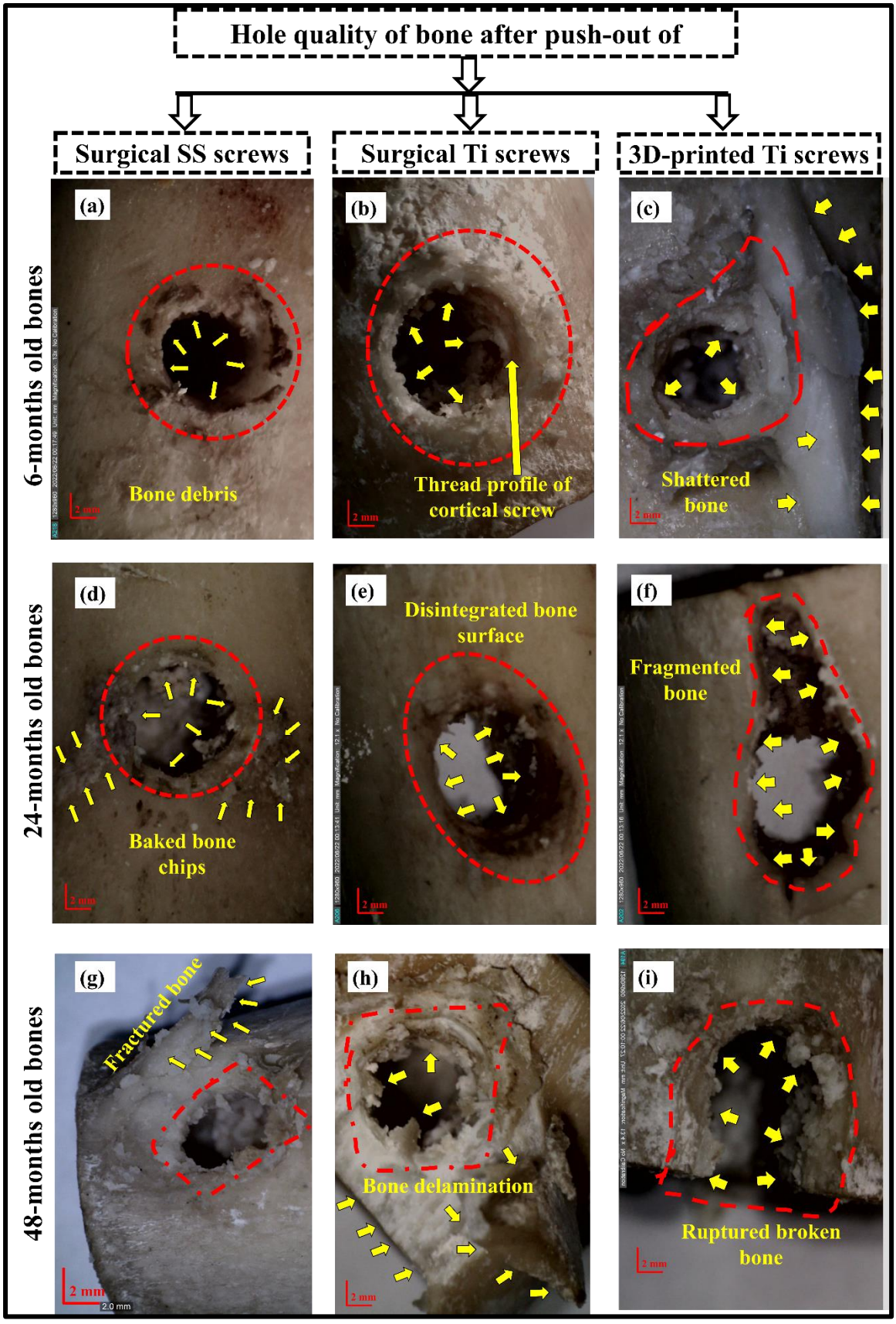


Figure 7.8. Fractured bone morphologies after push-out of cortical screws from bone periphery for 6 months, 24 months and 48 months old for (a) (d) (g) surgical SS screws, (b) (e) (h) surgical Ti-screws, (c) (f) (i) 3D-printed titanium cortical screws.

The 3D-printed titanium screws show shattered bone with fractured bone pieces highlighted with macro-arrows as illustrated in Figure 7.8(c). This is due to high bone-screw holding strength at the bone-screw interface. For 24-month-old porcine femur bones, heavy baked bone chips were witnessed with stainless steel screws as depicted in Figure 7.8(d). These baked bone chips are affixed with the bone periphery representing higher pullout force compared to 6-months old femur bones. The surgical titanium screws show a disintegrated bone surface with a damaged bone surface as illustrated in Figure 7.8(e). Whereas the 3D-printed titanium screws show fragmented bone surface with fractured bone affixed with 3D-printed screw as displayed in Figure 7.8(f). Due to the high bone-screw holding strength with 3D-printed screw, the bone was abandoned from the bone-screw periphery.

In the case of 48-month-old porcine femur bones, surgical stainless-steel screws show fractured bone surface with fragmented hole quality as illustrated in Figure 7.8(g) representing high pullout force compared to 6-month and 24-month-old femur bones. Surgical titanium screw samples appear to be a high pullout force as hole quality represents an elevated degree of bonding as depicted in Figure 7.8(h). The 3D-printed titanium screw samples represented ruptured broken bone found to be superior with high bonding force as depicted in Figure 7.8(i). The ruptured bone indicates high stability, bone-bonding strength and holding power at the bone-screw interface. Therefore, 3D-printed screws are prominent for accelerating pullout strength for all bone types.

7.4 Conclusions

In the present chapter, the influence of BMD and gender of porcine femur bones were observed on the biomechanical pullout strength of surgical metallic (titanium and stainless-steel) cortical screws. Three different ages of male and female porcine femur bones were used for their BMDs measurement. Selective laser melting based 3D printing technology is used to fabricate Ti6Al4V cortical screws. All bone-screw samples were preserved in SBF solution for their biological assessment. The influence of BMD, gender, immersion time of different bone-screw samples were observed on the biomechanical pullout strength. The fractured bone surface after the pullout testing of bone screws were observed to understand the holding strength at the bone-screw interface. Following conclusions were made based on this chapter.

- The hydroxyapatite formation of 3D-printed Ti6Al4V cortical screws were significantly higher as compared to conventional metallic screws. This is due to microporous structure of 3D-printed cortical screws.

- Male porcine femur bones have higher BMD as compared to female porcine femur bones.
- Surgical titanium cortical screws have higher pullout strength as compared to surgical stainless-steel cortical screws due to high hydroxyapatite accumulation at titanium cortical screws.
- The biomechanical pullout strength of 3D-printed Ti6Al4V cortical screws were substantially higher as compared to surgical metallic screws. This is due to higher hydroxyapatite accumulation and micro-roughened surface.
- 3D-printed Ti6Al4V cortical screws show ruptured bone surface in all groups of different BMDs of male and female porcine femur bones.
- With increasing the BMD of bone, the biomechanical pullout strength at bone-screw interface also increases. Hence, BMD and gender of bone play a vital role in affecting the biomechanical pullout strength of orthopaedic bone screws.

Chapter VIII

Summary, conclusions and the future scope

Chapter 8

Summary, conclusions, and the future scope

8.1 Summary

Bone fracture is a universal phenomenon which may occur due to accident or age factors. Orthopaedic bone screws have been used for the internal fixation of bone fractures for more than 100 years. For fixing the fractured bone, bone screws will always be used during the surgery. The most commonly used surgical metallic bone screws are titanium and stainless steel which are strong [199], ductile [50], fatigue-resistant [183], and highly biocompatible [102]. However, due to the high stiffness and high strength of metallic screws, they may cause stress corrosion [200], the stress-shielding effect [46], tear and wear in the neighbouring tissues [96]. Further, strong integration at the bone-screw interface by sharp threads and soft bony tissues complicates the post-operative revision surgery while removing the metallic screws [201]. These problems caused by metallic screws can be overcome with biodegradable bone screws. It is reported that the implant failure rate for the lower leg due to osteosynthesis is around 2.1 - 7.1% [30]. The reported rate of screw misplacement pedicle fixation ranges from 21 to 40% [32]. Hence, there is a necessity to use biodegradable bone screws for better osteosynthesis and reduce bone-screw-related complications. Therefore, attempts have been made to fabricate cortical bone screws using fused filament fabrication-based 3D printing technology to that the above-mentioned problem can be eliminated. 3D-printed biodegradable screws are MRI compatible, reduce the stress-shielding effect, and degrade in the body so no revision surgery is required for the removal of the implanted screw.

8.2 Conclusions

In the present work, orthopaedic cortical bone screws were designed in Creo Parametric 7.0 and fabricated using fused filament fabrication-based 3D printing technology. The effect of different process parameters of the 3D printer was observed on the mechanical strength of the screw. Different machine-learning models were leveraged to optimize the input process parameters of 3D-printed cortical screws. Different drilling angles were explored for the maximum pullout strength of the cortical screw. The degradation behaviour of 3D-printed screws was monitored in different biological solutions. Finally, histopathology was conducted to observe the viable osteocytes and surface damage at the bone-screw interface with surgical

metallic and 3D-printed screws. Based on the results presented in the chapters following conclusions have been made:

- In the 3D-printed cortical screws, the infill pattern and infill percentage significantly influence the mechanical compressive strength. Honeycomb-patterned cortical screws have 17% higher mechanical compressive strength as compared to triangular-patterned cortical screws due to higher bonding surface area at the intercalated layers. With increasing infill percentage, the compressive strength increases up to 17%, as increasing the infill increases the weight and reduces porosity.
- It was witnessed that ensemble ML models have higher adequacy and minimum error metrics compared to base ML models. It was observed that the XGBoost ensemble machine learning model has the least error metrics for training dataset with mean absolute error of 2.04 ± 0.94, root mean square error of 2.24 ± 0.92 and coefficient of determination of 0.94 ± 0.042.
- It was observed that with increasing the inclination angle, the biomechanical pullout strength at the bone-screw interface reduces. Highest pullout strength was witnessed with the drilling of bone at 0^0 due to an increase in stiffness that reduces microcracks at the bone-tool interface. With variation in inclination angle from 40^0 to 0^0, the biomechanical pullout strength of cortical screws can be increased up to 18%.
- RUABD is preferred drilling technique as compared to CBD. With RUABD, the induced cutting force can be reduced up to 35%, temperature elevations can be minimized up to 40% and pullout strength can be increased up to 50% as compared to CBD. Also, the SEM micrographs illustrate visible osteocyte tracks during RUABD, whereas no osteocyte tracks and microcracks were observed during CBD.
- Biological assessment of 3D-printed bone screws in different biological solutions illustrates biocompatible and biodegradable behaviour. Hydroxyapatite formation and biodegradation rate of 3D-printed PLA cortical screws were higher in the SBF solution compared to PBS and HBSS solutions.
- Histopathological evaluations at the drill edge site after the extraction of the 3D-printed PLA cortical screw illustrates less surface damage and highly viable osteocytes at the bone surface. Whereas the hole edge quality after extraction of metallic screws indicates empty lacuna, high surface damage, tissue injuries and high Haversian canals at the bone surface.

- The biomechanical pullout strength at bone-screw interface is significantly influenced by bone mineral density and gender of bone. 3D-printed Ti6Al4V cortical screws was observed to have microporous and micro-roughed surface that improve hydroxyapatite accumulation during preservation in SBF solution. 3D-printed orthopaedic cortical screws may improve the biomechanical pullout strength, promote bone regeneration, accelerate osseointegration, and reduce the loosing rate.

8.3 Future scope

The in vitro study presented in this thesis may be extended further in the following ways:

- In the present work, FFF-based 3D technology is used to fabricate cortical bone screws. Further based on that new screw designs can be proposed and fabricated for orthopaedic and trauma surgery.
- During the present work, four process parameters were considered, further the influence of printing speed, nozzle temperature, raster angle and building orientation can be considered on the 3D-printed bone screws.
- In this work in-vitro study was performed using the porcine cortical bone further study can be explored for the in-vivo study on animal bone or human bone.
- The mathematical or finite element models may be developed for the examination of biomechanical pullout strength at the bone-screw interface.
- The effect of bone mineral densities and gender of porcine femur bones on the biomechanical pullout strength can also be studied.

References

References

1. Abdel-Wahab AA, Alam K, Silberschmidt V V. (2011) Analysis of anisotropic viscoelastoplastic properties of cortical bone tissues. J Mech Behav Biomed Mater 4:807–820. https://doi.org/10.1016/j.jmbbm.2010.10.001

2. Li S, Abdel-Wahab A, Silberschmidt V V. (2013) Analysis of fracture processes in cortical bone tissue. Eng Fract Mech 110:448–458. https://doi.org/10.1016/j.engfracmech.2012.11.020

3. Jamil M, Rafique S, Khan AM, et al (2020) Comprehensive analysis on orthopedic drilling: A state-of-the-art review. Proc. Inst. Mech. Eng. Part H J. Eng. Med. 234:537–561

4. Tlili B, Guizani H, Aouadi K, Nasser M (2021) Multi-Scale Modeling of Mechanobiological Behavior of Bone. In: Biomechanics and Functional Tissue Engineering. IntechOpen, pp 225–240

5. Alam K, Khan M, Silberschmidt V V. (2014) 3D finite-element modelling of drilling cortical bone: Temperature analysis. J Med Biol Eng 34:618–623. https://doi.org/10.5405/jmbe.1585

6. Alam K, Mitrofanov AV, Silberschmidt VV (2010) Thermal analysis of orthogonal cutting of cortical bone using finite element simulations. Int J Exp Comput Biomech 1:236. https://doi.org/10.1504/ijecb.2010.035259

7. Noordin MY, Jiawkok N, Ndaruhadi PYMW, Kurniawan D (2015) Machining of bone: Analysis of cutting force and surface roughness by turning process. Proc Inst Mech Eng Part H J Eng Med 229:761–768. https://doi.org/10.1177/0954411915606169

8. Huiyu H, Chengyong W, Yue Z, et al (2017) Investigating bone chip formation in craniotomy. Proc Inst Mech Eng Part H J Eng Med 231:959–974. https://doi.org/10.1177/0954411917727245

9. Singh A, Singla E, Soni S, Singla A (2018) Kinematic modeling of a 7-degree of freedom spatial hybrid manipulator for medical surgery. Proc Inst Mech Eng Part H J Eng Med 232:12–23. https://doi.org/10.1177/0954411917741331

10. Singh A, Singla A, Soni S (2015) Extension of D-H parameter method to hybrid manipulators used in robot-assisted surgery. Proc Inst Mech Eng Part H J Eng Med 229:703–712. https://doi.org/10.1177/0954411915602289

11. Hillery MT, Shuaib I (1999) Temperature effects in the drilling of human and bovine bone. J Mater Process Technol 92:302–308. https://doi.org/10.1016/S0924-0136(99)00155-7

12. Li S, Shu L, Kizaki T, et al (2021) Cortical bone drilling: A time series experimental analysis of thermal characteristics. J Manuf Process 64:606–619. https://doi.org/10.1016/j.jmapro.2021.01.046

13. Zdero R, Aziz MSR, Nicayenzi B (2017) Pullout Force Testing of Cortical and Cancellous Screws in Whole Bone. Elsevier Inc.

14. Sharp JW, Kani KK, Gee A, et al (2018) Anterior cruciate ligament fixation devices: Expected imaging appearance and common complications. Eur J Radiol 99:17–27. https://doi.org/10.1016/j.ejrad.2017.12.006

15. Loving VA, Richardson ML (2006) Scaphoid Fracture Fixation with an Acutrak® Screw. Radiol Case Reports 1:58–60. https://doi.org/10.2484/rcr.v1i2.13

16. DeVries JG, Cuttica DJ, Hyer CF (2011) Cannulated screw fixation of jones fifth metatarsal fractures: A comparison of titanium and stainless steel screw fixation. J Foot Ankle Surg 50:207–212. https://doi.org/10.1053/j.jfas.2010.12.019

17. Goldstein IM, Singh R, Agarwal N (2017) Resolution of screw radiolucency following instrumentation with a hybrid rigid to dynamic stabilization system. Interdiscip Neurosurg Adv Tech Case Manag 9:71–75. https://doi.org/10.1016/j.inat.2017.03.009

18. Moser JE, Kunkel KAR, Gerard PD (2017) Pullout strength of 2.0 mm cancellous and cortical screws in synthetic bone. Vet Surg 46:1110–1115. https://doi.org/10.1111/vsu.12692

19. Hughes AN, Jordan BA (1972) The mechanical properties of surgical bone screws and some aspects of insertion practice. Injury 4:25–38. https://doi.org/10.1016/S0020-1383(72)80007-X

20. Miyawaki, Shouichi and Koyama, Isao and Inoue, Masahide and Mishima, Katsuaki and

Sugahara, Toshio and Takano-Yamamoto T (2003) Factors associated with the stability of titanium screws placed in the posterior region for orthodontic anchorage. Am J Orthod Dentofac Orthop 124:373–378. https://doi.org/10.1016/S0889-5406(03)00565-1

21. Stahel PF, Alfonso NA, Henderson C, Baldini T (2017) Introducing the "Bone-Screw-Fastener" for improved screw fixation in orthopedic surgery : a revolutionary paradigm shift? patient Saf Surg 11:1–8. https://doi.org/10.1186/s13037-017-0121-5

22. Chandra G, Pandey A (2020) Biodegradable bone implants in orthopedic applications: a review. Biocybern Biomed Eng 40:596–610. https://doi.org/10.1016/j.bbe.2020.02.003

23. Singh RP, Gupta V, Pandey PM, Mridha RA (2020) Effect of Drilling Techniques on Microcracks and Pull-Out Strength of Cortical Screw Fixed in Human Tibia: An In-Vitro Study. Ann Biomed Eng 49:382–393. https://doi.org/10.1007/s10439-020-02565-2

24. Li J, Qin L, Yang K, et al (2019) Materials evolution of bone plates for internal fixation of bone fractures, a review. J Mater Sci &Technology. https://doi.org/10.1016/j.jmst.2019.07.024

25. Panagiotopoulou VC, Varga P, Richards RG, et al (2019) Late screw-related complications in locking plating of proximal humerus fractures: A systematic review. Injury 50:2176–2195. https://doi.org/10.1016/j.injury.2019.11.002

26. Shen F, Kim H, Kang K, Yeom JS (2019) Comparison of the Pullout Strength of Pedicle Screws According to the Thread Design for Various Degrees of Bone Quality. Appl Sci 9:1–11. https://doi.org/10.3390/app9081525

27. Wu ZX, Gong FT, Liu L, et al (2012) A comparative study on screw loosening in osteoporotic lumbar spine fusion between expandable and conventional pedicle screws. Arch Orthop Trauma Surg 132:471–476. https://doi.org/10.1007/s00402-011-1439-6

28. Paul RA, Maldonado-Rodriguez N, Docter S, et al (2019) Glenoid bone grafting in primary reverse total shoulder arthroplasty: a systematic review. J Shoulder Elb Surg 28:2447–2456. https://doi.org/10.1016/j.jse.2019.05.011

29. Born C, Long WG De (2007) Two-screw femoral neck fracture fixation: A

biomechanical analysis of 2 different configurations. Am J Orthop (BELLE MEAD NJ) 36:481. https://doi.org/17948152

30. Eyal Y, Daniela S, Hemil M, S HD (2017) Surgical treatment of osteoporotic fractures : An update on the principles of management. Injury 48:1–7. https://doi.org/10.1016/j.injury.2017.08.036

31. Dhandapani R, Krishnan PD, Zennifer A, et al (2020) Additive manufacturing of biodegradable porous orthopaedic screw. Bioact Mater 5:458–467. https://doi.org/10.1016/j.bioactmat.2020.03.009

32. Shi S, Ying X, Zheng Q, et al (2018) Application of Cortical Bone Trajectory Screws in Elderly Patients with Lumbar Spinal Tuberculosis. World Neurosurg 117:e82–e89. https://doi.org/10.1016/j.wneu.2018.05.168

33. SHERMAN WO (1912) Operative treatment of fractures: report of fifty-five cases in which lane bone plates and screws were employed. J Am Med Assoc 58:1557–1561. https://doi.org/10.1001/jama.1912.04260050233001

34. Marko AR and ZS and BV and B (2012) The development of internal fixation- historical overview. Acta Chir Iugosl 59:9–13. https://doi.org/10.2298/ACI1203009L

35. Roberts, Timothy T and Prummer, Christoph M and Papaliodis, Dean N and Uhl, Richard L and Wagner TA (2013) History of the Orthopedic Screw. Orthopedics 36:12–14. https://doi.org/10.3928/01477447-20121217-02

36. Huang YM, Huang CC, Tsai PI, et al (2020) Three-dimensional printed porous titanium screw with bioactive surface modification for bone–tendon healing: A rabbit animal model. Int J Mol Sci 21:1–14. https://doi.org/10.3390/ijms21103628

37. Nurmi, J.T., Itälä, A., Sihvonen, R., Sillanpää, P., Kannus, P., Sievänen, H. and Järvinen TL (2017) Bioabsorbable versus metal screw in the fixation of tibial tubercle transfer: a cadaveric biomechanical study. Orthop J Sport Med 5:1–5. https://doi.org/10.1177/2325967117714433

38. van Arkel RJ, Ghouse S, Milner PE, Jeffers JRT (2018) Additive manufactured push-fit implant fixation with screw-strength pull out. J Orthop Res 36:1508–1518. https://doi.org/10.1002/jor.23771

39. Suryavanshi A, Khanna K, Sindhu KR, et al (2019) Development of bone screw using novel biodegradable composite orthopedic biomaterial: From material design to in vitro biomechanical and in vivo biocompatibility evaluation. Biomed Mater 14:045020. https://doi.org/10.1088/1748-605X/ab16be

40. Tappa K, Jammalamadaka U, Weisman JA, et al (2019) 3D printing custom bioactive and absorbable surgical screws, pins, and bone plates for localized drug delivery. J Funct Biomater 10:1–13. https://doi.org/10.3390/jfb10020017

41. Lee BS, Lee HJ, Lee KS, et al (2020) Enhanced osseointegration of Ti6Al4V ELI screws built-up by electron beam additive manufacturing: An experimental study in rabbits. Appl Surf Sci 508:145160. https://doi.org/10.1016/j.apsusc.2019.145160

42. Yao Y, Wang L, Li J, et al (2020) A novel auxetic structure based bone screw design: Tensile mechanical characterization and pullout fixation strength evaluation. Mater Des 188:108424. https://doi.org/10.1016/j.matdes.2019.108424

43. Del L, Silva R, Borges GA, et al (2020) 3D metal printing in dentistry: An in vitro biomechanical comparative study of two additive manufacturing technologies for full-arch implant-supported prostheses. J Mech Behav Biomed Mater 108:103821. https://doi.org/10.1016/j.jmbbm.2020.103821

44. Luan H, Yu Z, Li J, et al (2020) Effects of different concentrations of TiAl6V4 particles on MC3T3-E1 cells and bone in rats. Med Nov Technol Devices 7:100044. https://doi.org/10.1016/j.medntd.2020.100044

45. Yao Y, Yuan H, Huang H, et al (2021) Biomechanical design and analysis of auxetic pedicle screw to resist loosening. Comput Biol Med 133:104386. https://doi.org/10.1016/j.compbiomed.2021.104386

46. Hanawa T (2019) Overview of metals and applications. In: Niinomi M (ed) Metals for Biomedical Devices, 2nd ed. Woodhead Publishing, pp 3–29

47. Tigani D, Fosco M, Ayad R, Fantasia R (2012) Orthopaedic implant materials and design. In: Saverio Affatato (ed) Wear of orthopaedic implants and artificial joints. Woodhead Publishing, pp 133–177

48. Gulati K, Hamlet SM, Ivanovski S (2018) Tailoring the immuno-responsiveness of

anodized nano-engineered titanium implants. J Mater Chem B 6:2677–2689. https://doi.org/10.1039/c8tb00450a

49. Zindani D, Kumar K, Davim JP (2019) Metallic biomaterials—A review. Elsevier Ltd.

50. Liu S, Shin YC (2019) Additive manufacturing of Ti6Al4V alloy: A review. Mater Des 164:107552. https://doi.org/10.1016/j.matdes.2018.107552

51. Diomidis N (2013) Wear phenomena of metal joints. In: Affatato S (ed) Wear of Orthopaedic Implants and Artificial Joints. Woodhead Publishing, pp 246–277

52. Lee B, Lee H, Lee K, et al (2020) Enhanced osseointegration of Ti6Al4V ELI screws built-up by electron beam additive manufacturing: An experimental study in rabbits. Appl Surf Sci 508:145160. https://doi.org/10.1016/j.apsusc.2019.145160

53. Ernberg JJ, Asnis SE (1996) Materials and Manufacturing of Orthopaedic Bone Screws. Cannulated Screw Fixat 1–14. https://doi.org/10.1007/978-1-4612-2326-9_1

54. Affatato S, P. T (2013) Wear phenomena of ceramic joints. In: Affatato S (ed) Wear of Orthopaedic Implants and Artificial Joints. Woodhead Publishing, pp 278–297

55. Meng C, Ho B, Ng SH, Yoon Y (2015) A Review on 3D Printed Bioimplants. Int J Precis Eng Manuf 16:1035–1046. https://doi.org/10.1007/s12541-015-0134-x

56. Karakurt I, Lin L (2020) 3D printing technologies: techniques, materials, and post-processing. Curr Opin Chem Eng 28:134–143. https://doi.org/10.1016/j.coche.2020.04.001

57. Bai H, Cui Y, Wang C, et al (2020) 3D printed porous biomimetic composition sustained release zoledronate to promote osteointegration of osteoporotic defects. Mater Des 189:108513. https://doi.org/10.1016/j.matdes.2020.108513

58. Kok Y, Tan XP, Wang P, et al (2018) Anisotropy and heterogeneity of microstructure and mechanical properties in metal additive manufacturing : A critical review. Mater Des 139:565–586. https://doi.org/10.1016/j.matdes.2017.11.021

59. Gupta M (2017) 3D printing of metals. In: Gupta M (ed) Metals. Multidisciplinary Digital Publishing Institute, p 403

60. Yadroitsava I, Yadroitsev I (2020) Effects of defects on mechanical properties in metal

additive manufacturing : A review focusing on X-ray tomography insights. Mater Des 187:108385. https://doi.org/10.1016/j.matdes.2019.108385

61. Tilton M, Lewis GS, Bok Wee H, et al (2020) Additive manufacturing of fracture fixation implants: Design, material characterization, biomechanical modeling and experimentation. Addit Manuf 33:. https://doi.org/10.1016/j.addma.2020.101137

62. Buchanan C, Gardner L (2019) Metal 3D printing in construction: A review of methods, research, applications, opportunities and challenges. Eng Struct 180:332–348. https://doi.org/10.1016/j.engstruct.2018.11.045

63. Singh D, Babbar A, Jain V, et al (2019) Synthesis, characterization, and bioactivity investigation of biomimetic biodegradable PLA scaffold fabricated by fused filament fabrication process. J Brazilian Soc Mech Sci Eng 41:1–13. https://doi.org/10.1007/s40430-019-1625-y

64. Majeed A, Ahmed A, Lv J, et al (2020) A state-of-the-art review on energy consumption and quality characteristics in metal additive manufacturing processes. J Brazilian Soc Mech Sci Eng 42:1–25. https://doi.org/10.1007/s40430-020-02323-4

65. Ahangar P, Cooke ME, Weber MH, Rosenzweig DH (2019) Current biomedical applications of 3D printing and additive manufacturing. Appl Sci 9:1713. https://doi.org/10.3390/app9081713

66. Calignano, Flaviana and Manfredi, Diego and Ambrosio, Elisa Paola and Biamino, Sara and Lombardi, Mariangela and Atzeni, Eleonora and Salmi, Alessandro and Minetola, Paolo and Iuliano, Luca and Fino P (2017) Overview on Additive Manufacturing Technologies. Proc IEEE 105:593–612. https://doi.org/10.1109/JPROC.2016.2625098

67. Kansal A, Dvivedi A, Kumar P (2022) Development and performance study of biomedical porous zinc scaffold manufactured by using additive manufacturing and microwave sintering. Mater. Manuf. Process. 1–13

68. Anadioti E, Kane B, Soulas E (2018) Current and Emerging Applications of 3D Printing in Restorative Dentistry. Curr Oral Heal Reports 5:133–139. https://doi.org/10.1007/s40496-018-0181-3

69. Chang JZC, Tsai PI, Kuo MYP, et al (2019) Augmentation of DMLS biomimetic dental

implants with weight-bearing strut to balance of biologic and mechanical demands: From bench to animal. Materials (Basel) 12:. https://doi.org/10.3390/ma12010164

70. Ganguli, Anurup and Pagan-Diaz, Gelson J and Grant, Lauren and Cvetkovic, Caroline and Bramlet, Mathew and Vozenilek, John and Kesavadas, Thenkurussi and Bashir R (2018) 3D printing for preoperative planning and surgical training: a review. Biomed Microdevices 20:1–24. https://doi.org/10.1007/s10544-018-0301-9

71. Sharma GK, Pant P, Jain PK, et al (2021) On the suitability of induction heating system for metal additive manufacturing. Proc Inst Mech Eng Part B J Eng Manuf 235:219–229. https://doi.org/10.1177/0954405420937854

72. Kumar A, Shukla M (2022) Numerical Modeling of Selective Laser Melting: Influence of Process Parameters on the Melt Pool Geometry. J Mater Eng Perform. https://doi.org/10.1007/s11665-022-07693-5

73. Elgazzar H, Abdelghany K (2022) Recent Research Progress and Future Prospects in the Additive Manufacturing of Biomedical Magnesium and Titanium Implants. In: Shunmugam, M., Kanthababu M (ed) Additive and Subtractive Manufacturing Processes. Springer Singapore, pp 145–161

74. Altıparmak SC, Yardley VA, Shi Z, Lin J (2021) Challenges in additive manufacturing of high-strength aluminium alloys and current developments in hybrid additive manufacturing. Int J Light Mater Manuf 4:246–261. https://doi.org/10.1016/j.ijlmm.2020.12.004

75. Guo N, Leu MC (2013) Additive manufacturing: Technology, applications and research needs. Front Mech Eng 8:215–243. https://doi.org/10.1007/s11465-013-0248-8

76. Majeed A, Muzamil M, Lv J, et al (2019) Heat treatment influences densification and porosity of AlSi10Mg alloy thin-walled parts manufactured by selective laser melting technique. J Brazilian Soc Mech Sci Eng 41:1–13. https://doi.org/10.1007/s40430-019-1769-9

77. Al-Sayed Ali SR, Hussein AHA, Nofal A, et al (2019) A contribution to laser cladding of Ti-6Al-4V titanium alloy. Metall Res Technol 116:. https://doi.org/10.1051/metal/2019060

78. Al-Sayed SR, Elgazzar H, Nofal A (2022) Microstructure Evaluation and High-Temperature Wear Performance of Hard Protective Layer Deposited on Titanium Alloy via Laser Metal Deposition. Met Mater Int 28:2822–2835. https://doi.org/10.1007/s12540-021-01160-x

79. Park J, Kim K, Ph D, et al (2017) Biomechanical Comparison of Inter-fragmentary Compression Pressures : Lag Screw versus Herbert Screw for Anterior Odontoid Screw Fixation. Anterior Odontoid Screw Fixat 60:498–503. https://doi.org/10.3340/jkns.2017.0202.011

80. Sandeep R, Arivazhagan N (2021) Innovation of thermoplastic polymers and metals hybrid structure using friction stir welding technique: challenges and future perspectives. Springer Berlin Heidelberg

81. Chan CM, Vandi LJ, Pratt S, et al (2018) Composites of Wood and Biodegradable Thermoplastics: A Review. Polym Rev 58:444–494. https://doi.org/10.1080/15583724.2017.1380039

82. Diez-Pascual AM (2017) Tissue engineering bionanocomposites based on poly(propylene fumarate). Polymers (Basel) 9:1–19. https://doi.org/10.3390/polym9070260

83. Sinha AK, Narang HK, Bhattacharya S (2020) Mechanical properties of hybrid polymer composites: a review. J Brazilian Soc Mech Sci Eng 42:1–13. https://doi.org/10.1007/s40430-020-02517-w

84. Thakur RK, Singh KK (2021) Influence of fillers on polymeric composite during conventional machining processes: a review. J Brazilian Soc Mech Sci Eng 43:1–20. https://doi.org/10.1007/s40430-021-02813-z

85. Rahman MM, Olabi AG, Hashmi MSJ (2012) Finite element modelling of rheological property of curing PMMA bone cement. Part 1 : Effect of prosthesis insertion velocity. J Biomim Biomater Tissue Eng 12:83–90. https://doi.org/10.4028/www.scientific.net/JBBTE.12.83

86. Najeeb S, Khurshid Z, Matinlinna JP, et al (2015) Nanomodified Peek Dental Implants: Bioactive Composites and Surface Modification-A Review. Int J Dent 2015:. https://doi.org/10.1155/2015/381759

87. Yoshimura S, Ikuse K, Tsukazaki Y, et al (2009) Effect of ultraviolet light irradiation on etching process of poly(methyl methacrylate) by ion beam injections. J Phys Conf Ser 191:012030. https://doi.org/10.1088/1742-6596/191/1/012030

88. Kasper FK, Tanahashi K, Fisher JP, Mikos AG (2009) Synthesis of poly(propylene fumarate). Nat Protoc 4:518–525. https://doi.org/10.1038/nprot.2009.24

89. Ahmed KK, Tamer MA, Ghareeb MM, Salem AK (2019) Recent Advances in Polymeric Implants. AAPS PharmSciTech 20:1–10. https://doi.org/10.1208/s12249-019-1510-0

90. Nair NR, Sekhar VC, Nampoothiri KM, Pandey A (2017) Biodegradation of Biopolymers. In: Pandey A, Negi S, Soccol CR (eds) Current Developments in Biotechnology and Bioengineering. Elsevier, pp 739–755

91. Dandy LO, Oliveux G, Wood J, et al (2015) Accelerated degradation of Polyetheretherketone (PEEK) composite materials for recycling applications. Polym Degrad Stab 112:52–62. https://doi.org/10.1016/j.polymdegradstab.2014.12.012

92. Gentile P, Chiono V, Carmagnola I, Hatton P V (2014) An overview of poly (lactic-co-glycolic) acid (PLGA)-based biomaterials for bone tissue engineering. Int J Mol Sci 15:3640–3659. https://doi.org/10.3390/ijms15033640

93. Little, H and Clarke, SA and Cunningham, E and Buchanan F (2018) Process-induced degradation of bioresorbable PDLGA in bone tissue scaffold production. J Mater Sci Mater Med 29:14. https://doi.org/10.1007/s10856-017-6019-z

94. Zhuang X, Yu B, Zheng Z, et al (2010) Effect of the Degree of Osteoporosis on the Biomechanical Anchoring Strength of the Sacral Pedicle Screws An In Vitro Comparison Between Unaugmented Bicortical Screws. Spine (Phila Pa 1976) 35:925–931. https://doi.org/10.1097/BRS.0b013e3181c5fb21

95. Moore WR, Graves SE, Bain GI (2001) Synthetic bone graft substitutes. ANZ J Surg 71:354–361. https://doi.org/10.1046/j.1440-1622.2001.02128.x

96. Ramos DM, Dhandapani R, Subramanian A, et al (2020) Clinical complications of biodegradable screws for ligament injuries. Mater Sci Eng C 109:110423. https://doi.org/10.1016/j.msec.2019.110423

97. Diekmann J, Bauer S, Weizbauer A, et al (2016) Examination of a biodegradable magnesium screw for the reconstruction of the anterior cruciate ligament: A pilot in vivo study in rabbits. Mater Sci Eng C 59:1100–1109. https://doi.org/10.1016/j.msec.2015.11.037

98. Ricardo M, Oliveira D, Misquita F De, et al (2016) The performance of bone tissue engineering scaffolds in in vivo animal models : A systematic review. J Biomater Appl 0:1–12. https://doi.org/10.1177/0885328216656476

99. Ji Y, Xu GP, Zhang ZP, et al (2010) BMP-2/PLGA delayed-release microspheres composite graft, selection of bone particulate diameters, and prevention of aseptic inflammation for bone tissue engineering. Ann Biomed Eng 38:632–639. https://doi.org/10.1007/s10439-009-9888-6

100. Kim Y, Kim S, Lee SH, et al (2020) Stabilized Loading of Hyaluronic Acid-Containing Hydrogels into Magnesium-Based Cannulated Screws. ACS Biomater Sci Eng 6:715–726. https://doi.org/10.1021/acsbiomaterials.9b01057

101. Xu J, Ge H, Zhou X, et al (2005) Prediction of vascular tissue engineering results with artificial neural networks. J Biomed Inform 38:417–421. https://doi.org/10.1016/j.jbi.2005.03.002

102. Ratner BD (2019) Biomaterials : Been There , Done That , and Evolving into the Future. Annu Rev Biomed Eng 21:171–191. https://doi.org/10.1146/annurev-bioeng-062117-120940

103. Tripathi Y, Shukla M, Bhatt AD (2019) Implicit-Function-Based Design and Additive Manufacturing of Triply Periodic Minimal Surfaces Scaffolds for Bone Tissue Engineering. J Mater Eng Perform 28:7445–7451. https://doi.org/10.1007/s11665-019-04457-6

104. Ganguli A, Pagan-Diaz GJ, Grant L, et al (2018) 3D printing for preoperative planning and surgical training: a review. Biomed Microdevices 20:. https://doi.org/10.1007/s10544-018-0301-9

105. Dommati H, Ray SS, Wang JC, Chen SS (2019) A comprehensive review of recent developments in 3D printing technique for ceramic membrane fabrication for water purification. RSC Adv 9:16869–16883. https://doi.org/10.1039/c9ra00872a

106. Chang D-Y, Lin C-H, Wu X-Y, et al (2021) Cutting force, Vibration, and Temperature in Drilling on a Thermoplastic Material of PEEK. J Thermoplast Compos Mater 08927057211052325. https://doi.org/10.3390/polym12112703

107. Singh S, Prakash C, Ramakrishna S (2019) 3D printing of polyether-ether-ketone for biomedical applications. Eur Polym J 114:234–248. https://doi.org/10.1016/j.eurpolymj.2019.02.035

108. Kumar R, Kumar M, Chohan JS (2021) The role of additive manufacturing for biomedical applications: A critical review. J Manuf Process 64:828–850. https://doi.org/10.1016/j.jmapro.2021.02.022

109. Justin Stiltner L, Elliott AM, Williams CB (2011) A method for creating actuated joints via fiber embedding in a polyjet 3D printing process. 22nd Annu Int solid Free Fabr Symp 583–592

110. Francis V, Garg S, Saxena KK, et al (2022) Effect of chemical and heat treatment on 3D printed parts: nanoparticles embedment approach. Adv Mater Process Technol 8:2277–2288. https://doi.org/10.1080/2374068X.2022.2037876

111. Daminabo SC, Goel S, Grammatikos SA, et al (2020) Fused deposition modeling-based additive manufacturing (3D printing): techniques for polymer material systems. Mater Today Chem 16:100248. https://doi.org/10.1016/j.mtchem.2020.100248

112. Francis V, Jain PK (2018) A filament modification approach for in situ ABS/OMMT nanocomposite development in extrusion-based 3D printing. J Brazilian Soc Mech Sci Eng 40:1–13. https://doi.org/10.1007/s40430-018-1282-6

113. Anoop MS, Senthil P, Sooraj VS (2021) An investigation on viscoelastic characteristics of 3D-printed FDM components using RVE numerical analysis. J Brazilian Soc Mech Sci Eng 43:1–13. https://doi.org/10.1007/s40430-020-02724-5

114. Kumar R, Chohan JS, Kumar R, et al (2020) Hybrid fused filament fabrication for manufacturing of Al microfilm reinforced PLA structures. J Brazilian Soc Mech Sci Eng 42:1–13. https://doi.org/10.1007/s40430-020-02566-1

115. Sai T, Pathak VK, Srivastava AK (2020) Modeling and optimization of fused deposition modeling (FDM) process through printing PLA implants using adaptive neuro-fuzzy

inference system (ANFIS) model and whale optimization algorithm. J Brazilian Soc Mech Sci Eng 42:1–19. https://doi.org/10.1007/s40430-020-02699-3

116. Guessasma S, Zhang W, Zhu J, et al (2015) Challenges of additive manufacturing technologies from an optimisation perspective. Int J Simul Multidiscip Des Optim 6:A9. https://doi.org/10.1051/smdo/2016001

117. Korkut V, Yavuz H (2020) Enhancing the tensile properties with minimal mass variation by revealing the effects of parameters in fused filament fabrication process. J Brazilian Soc Mech Sci Eng 42:1–18. https://doi.org/10.1007/s40430-020-02610-0

118. Taufik M, Jain PK (2022) Part surface quality improvement studies in fused deposition modelling process: a review. Aust J Mech Eng 20:527–551. https://doi.org/10.1080/14484846.2020.1723342

119. Taufik M, Jain PK (2016) A study of build edge profile for prediction of surface roughness in fused deposition modeling. J Manuf Sci Eng Trans ASME 138:1–11. https://doi.org/10.1115/1.4032193

120. Taufik M, Jain PK (2017) Characterization, modeling and simulation of fused deposition modeling fabricated part surfaces. Surf Topogr Metrol Prop 5:045003. https://doi.org/10.1088/2051-672x/aa7da7

121. Dixit N, Jain PK (2022) Effect of Fused Filament Fabrication Process Parameters on Compressive Strength of Thermoplastic Polyurethane and Polylactic Acid Lattice Structures. J Mater Eng Perform 31:5973–5982. https://doi.org/10.1007/s11665-022-06664-0

122. Jain R, Nauriyal S, Gupta V, Khas KS (2021) Effects of Process Parameters on Surface Roughness, Dimensional Accuracy and Printing Time in 3D Printing. In: Advances in Production and Industrial Engineering. Springer, pp 187–197

123. Bajpai A, Jain PK (2022) Investigation on 3D Printing of Graphene and Multi-walled Carbon Nanotube Mixed Flexible Electrically Conductive Parts Using Fused Filament Fabrication. J Mater Eng Perform. https://doi.org/10.1007/s11665-022-07574-x

124. Singh M, Kumar S, Singh R, et al (2021) On shear resistance of almond skin reinforced PLA composite matrix-based scaffold using cancellous screw. Adv Mater Process

Technol 11:1–24. https://doi.org/10.1080/2374068X.2021.1912528

125. Chia HN, Wu BM (2015) Recent advances in 3D printing of biomaterials. J Biol Eng 9:1–14. https://doi.org/10.1186/s13036-015-0001-4

126. Hsu C, Chao C, Wang J, et al (2005) Increase of pullout strength of spinal pedicle screws with conical core : biomechanical tests and finite element analyses. J Orthop Res 23:788–794. https://doi.org/10.1016/j.orthres.2004.11.002

127. Augustin G, Davila S, Mihoci K, et al (2008) Thermal osteonecrosis and bone drilling parameters revisited. Arch Orthop Trauma Surg 128:71–77. https://doi.org/10.1007/s00402-007-0427-3

128. Beran T, Mulholland T, Henning F, et al (2018) Nozzle clogging factors during fused filament fabrication of spherical particle filled polymers. Addit Manuf 23:206–214. https://doi.org/10.1016/j.addma.2018.08.009

129. Singh J, Singh G, Pandey PM (2021) Multi-objective optimization of solvent cast 3D printing process parameters for fabrication of biodegradable composite stents. Int J Adv Manuf Technol 115:3945–3964. https://doi.org/10.1007/s00170-021-07423-6

130. Sharma S, Gupta V, Mudgal D (2022) Current trends, applications, and challenges of coatings on additive manufacturing based biopolymers: A state of art review. Polym Compos 43:1–33. https://doi.org/10.1002/pc.26809

131. Singh J, Pandey PM, Kaur T, Singh N (2021) Surface characterization of polycaprolactone and carbonyl iron powder composite fabricated by solvent cast 3D printing for tissue engineering. Polym Compos 42:865–871. https://doi.org/10.1002/pc.25871

132. Singh J, Pandey PM, Kaur T, Singh N (2021) A comparative analysis of solvent cast 3D printed carbonyl iron powder reinforced polycaprolactone polymeric stents for intravascular applications. J Biomed Mater Res - Part B Appl Biomater 109:1344–1359. https://doi.org/10.1002/jbm.b.34795

133. Limmahakhun S, Oloyede A, Sitthiseripratip K, et al (2017) 3D-printed cellular structures for bone biomimetic implants. Addit Manuf 15:93–101. https://doi.org/10.1016/j.addma.2017.03.010

134. Dixit N, Sharma V, Kumar P (2022) Experimental investigations into abrasive flow machining (AFM) of 3D printed ABS and PLA parts. Rapid Prototyp J 28:161–174. https://doi.org/10.1108/RPJ-01-2021-0013

135. Choudhary N, Sharma V, Kumar P (2022) Polylactic acid-based composite using fused filament fabrication: Process optimization and biomedical application. Polym Compos 1–20. https://doi.org/10.1002/pc.27027

136. Choudhary N, Sharma V, Kumar P (2021) Reinforcement of polylactic acid with bioceramics (alumina and YSZ composites) and their thermomechanical and physical properties for biomedical application. J Vinyl Addit Technol 27:612–625. https://doi.org/10.1002/vnl.21837

137. Moetazedian A, Gleadall A, Han X, Silberschmidt V V. (2020) Effect of environment on mechanical properties of 3D printed polylactide for biomedical applications. J Mech Behav Biomed Mater 102:103510. https://doi.org/10.1016/j.jmbbm.2019.103510

138. Ansari MAA, Jain PK, Nanda HS (2023) Preparation of 3D printed calcium sulfate filled PLA scaffolds with improved mechanical and degradation properties. J Biomater Sci Polym Ed 0:1–22. https://doi.org/10.1080/09205063.2023.2167374

139. Dave HK, Patel BH, Rajpurohit SR, et al (2021) Effect of multi-infill patterns on tensile behavior of FDM printed parts. J Brazilian Soc Mech Sci Eng 43:1–15. https://doi.org/10.1007/s40430-020-02742-3

140. Jang BZ, Uhlmann DR, Sande JBV (1984) Ductile–brittle transition in polymers. J Appl Polym Sci 29:3409–3420. https://doi.org/10.1002/app.1984.070291118

141. Amulani A, Pratap H, Thomas B, Thomas B (2021) Investigation of static and fatigue behavior of honeycomb sandwich structure : a computational approach. J Brazilian Soc Mech Sci Eng 43:1–19. https://doi.org/10.1007/s40430-021-03195-y

142. Thomas T, Tiwari G (2019) Crushing behavior of honeycomb structure: a review. Int J Crashworthiness 24:555–579. https://doi.org/10.1080/13588265.2018.1480471

143. Wang Z (2019) Recent advances in novel metallic honeycomb structure. Compos Part B Eng 166:731–741. https://doi.org/10.1016/j.compositesb.2019.02.011

144. Pouyanfar N, Harofte SZ, Soltani M, et al (2022) Artificial intelligence-based

microfluidic platforms for the sensitive detection of environmental pollutants: Recent advances and prospects. Trends Environ Anal Chem 34:e00160. https://doi.org/10.1016/j.teac.2022.e00160

145. Narayan J, Singla E, Soni S, Singla A (2018) Adaptive neuro-fuzzy inference system–based path planning of 5-degrees-of-freedom spatial manipulator for medical applications. Proc Inst Mech Eng Part H J Eng Med 232:726–732. https://doi.org/10.1177/0954411918781418

146. Wang C, Tan XP, Tor SB, Lim CS (2020) Machine learning in additive manufacturing: State-of-the-art and perspectives. Addit Manuf 36:101538. https://doi.org/10.1016/j.addma.2020.101538

147. Goh GD, Sing SL, Yeong WY (2021) A review on machine learning in 3D printing: applications, potential, and challenges. Springer Netherlands

148. Lee J, Ni J, Singh J, et al (2020) Intelligent Maintenance Systems and Predictive Manufacturing. J Manuf Sci Eng 142:. https://doi.org/10.1115/1.4047856

149. Ding H, Yuan Y (2020) Industrial Artificial Intelligence. Zhongguo Kexue Jishu Kexue/Scientia Sin Technol 50:1413. https://doi.org/10.48550/arXiv.1908.02150

150. Lee J, Davari H, Singh J, Pandhare V (2018) Industrial Artificial Intelligence for industry 4 . 0-based manufacturing systems. Manuf Lett 18:20–23. https://doi.org/10.1016/j.mfglet.2018.09.002

151. Onan A (2019) Topic-Enriched Word Embeddings for Sarcasm Identification. Adv Intell Syst Comput 984:293–304. https://doi.org/10.1007/978-3-030-19807-7_29

152. Onan A (2021) Ensemble of Classifiers and Term Weighting Schemes for Sentiment Analysis in Turkish. Sci Res Commun 1:1–12. https://doi.org/10.52460/src.2021.004

153. Podgorelec V, Kokol P, Stiglic B, Rozman I (2002) Decision trees: An overview and their use in medicine. J Med Syst 26:445–463. https://doi.org/10.1023/A:1016409317640

154. Bustillo A, Reis R, Machado AR, Pimenov DY (2022) Improving the accuracy of machine-learning models with data from machine test repetitions. J Intell Manuf 33:203–221. https://doi.org/10.1007/s10845-020-01661-3

155. Joodaki H, Gepner B, Kerrigan J (2020) Leveraging machine learning for predicting human body model response in restraint design simulations. Comput Methods Biomech Biomed Engin 0:1–15. https://doi.org/10.1080/10255842.2020.1841754

156. Guo G, Wang H, Bell D, et al (2003) KNN model-based approach in classification. Lect Notes Comput Sci 986–996. https://doi.org/10.1007/978-3-540-39964-3_62

157. Onan A (2018) An ensemble scheme based on language function analysis and feature engineering for text genre classification. J Inf Sci 44:28–47. https://doi.org/10.1177/0165551516677911

158. Onan, Korukoğlu S, Bulut H (2016) A multiobjective weighted voting ensemble classifier based on differential evolution algorithm for text sentiment classification. Expert Syst Appl 62:1–16. https://doi.org/10.1016/j.eswa.2016.06.005

159. Deo TY, Patange AD, Pardeshi SS, et al (2021) A white-box SVM framework and its swarm-based optimization for supervision of toothed milling cutter through characterization of spindle vibrations. arXiv Prepr arXiv211208421

160. Khade HS, Patange AD, Pardeshi SS, Jegadeeshwaran R (2021) Design of bagged tree ensemble for carbide coated inserts fault diagnosis. Mater Today Proc. https://doi.org/10.1016/j.matpr.2021.02.128

161. Khairnar A, Patange A, Pardeshi, Sujit Jegadeeshwaran R (2021) Supervision of Carbide Tool Condition by Training of Vibration-based Statistical Model using Boosted Trees Ensemble. Int J Performability Eng 7:229–240. https://doi.org/10.1002/polb.24610

162. Bajaj NS, Patange AD, Jegadeeshwaran R, et al (2022) A Bayesian Optimized Discriminant Analysis Model for Condition Monitoring of Face Milling Cutter Using Vibration Datasets. J Nondestruct Eval Diagnostics Progn Eng Syst 5:1–9. https://doi.org/10.1115/1.4051696

163. Ibrahem Ahmed Osman A, Najah Ahmed A, Chow MF, et al (2021) Extreme gradient boosting (Xgboost) model to predict the groundwater levels in Selangor Malaysia. Ain Shams Eng J 12:1545–1556. https://doi.org/10.1016/j.asej.2020.11.011

164. Baturynska I, Martinsen K (2021) Prediction of geometry deviations in additive manufactured parts: comparison of linear regression with machine learning algorithms.

J Intell Manuf 32:179–200. https://doi.org/10.1007/s10845-020-01567-0

165. Tama BA, Rhee KH (2019) Tree-based classifier ensembles for early detection method of diabetes: an exploratory study. Artif Intell Rev 51:355–370. https://doi.org/10.1007/s10462-017-9565-3

166. Hambali MA, Saheed YK, Oladele TO, Gbolagade MD (2019) Adaboost Ensemble Algorithms for Breast Cancer Classification. J Adv Comput Res Q 10:1–10

167. Mustaqeem, Ishaq M, Kwon S (2021) Short-Term Energy Forecasting Framework Using an Ensemble Deep Learning Approach. IEEE Access 9:94262–94271. https://doi.org/10.1109/ACCESS.2021.3093053

168. Chen T, Guestrin C (2016) XGBoost: A Scalable Tree Boosting System. In: Proceedings of the 22nd acm sigkdd international conference on knowledge discovery and data mining. pp 785–794

169. Chen Y, Cheng A, Zhang C, et al (2021) Rapid mechanical evaluation of the engine hood based on machine learning. J Brazilian Soc Mech Sci Eng 43:1–17. https://doi.org/10.1007/s40430-021-03070-w

170. Cui W, Zhang Y, Zhang X, et al (2020) Metal additive manufacturing parts inspection using convolutional neural network. Appl Sci 10:. https://doi.org/10.3390/app10020545

171. Dong W, Huang Y, Lehane B, Ma G (2020) XGBoost algorithm-based prediction of concrete electrical resistivity for structural health monitoring. Autom Constr 114:103155. https://doi.org/10.1016/j.autcon.2020.103155

172. Gok K, Erdem M, Kisioglu Y, et al (2021) Development of bone chip - vacuum system in orthopedic drilling process. J Brazilian Soc Mech Sci Eng 43:1–11. https://doi.org/10.1007/s40430-021-02959-w

173. Huja SS, Litsky AS, Beck FM, et al (2005) Pull-out strength of monocortical screws placed in the maxillae and mandibles of dogs. Am J Orthod Dentofac Orthop 127:307–313. https://doi.org/10.1016/j.ajodo.2003.12.023

174. Qasemi M, Tahmasbi V, Sheikhi M, Zolfaghari M (2022) An effect of osteon orientation in end milling operation of cortical bone based on FEM and experiment. J Manuf Process 81:141–154. https://doi.org/10.1016/j.jmapro.2022.06.068

175. Liu Z, Chen H, Sui J, et al (2021) Failure behavior and influence of surgical tool edges in soft tissue cutting. J Manuf Process 68:69–78. https://doi.org/10.1016/j.jmapro.2021.07.025

176. Yang M, Li C, Said Z, et al (2021) Semiempirical heat flux model of hard-brittle bone material in ductile microgrinding. J Manuf Process 71:501–514. https://doi.org/10.1016/j.jmapro.2021.09.053

177. Gupta V, Pandey PM, Silberschmidt V V. (2017) Rotary ultrasonic bone drilling: Improved pullout strength and reduced damage. Med Eng Phys 41:1–8. https://doi.org/10.1016/j.medengphy.2016.11.004

178. Vafadar S, Rouhi G (2017) The Effects of Geometrical Parameters of the Pedicle Screw on Its Pullout Strength: In-Vitro Animal Tests. J Orthop Spine Trauma 3:74189. https://doi.org/10.5812/jost.74189

179. Singh N, Singh G (2021) Advances in polymers for bio-additive manufacturing: A state of art review. J Manuf Process 72:439–457. https://doi.org/10.1016/j.jmapro.2021.10.045

180. Sharma V, Pandey PM (2016) Optimization of machining and vibration parameters for residual stresses minimization in ultrasonic assisted turning of 4340 hardened steel. Ultrasonics 70:172–182. https://doi.org/10.1016/j.ultras.2016.05.001

181. Singh G, Pandey PM (2021) Design and analysis of long-stepped horn for ultrasonic-assisted sintering. Adv Mater Process Technol 7:216–226. https://doi.org/10.1080/2374068X.2020.1758604

182. Varghese V, Ramu P, Krishnan V, Saravana Kumar G (2016) Pull out strength calculator for pedicle screws using a surrogate ensemble approach. Comput Methods Programs Biomed 137:11–22. https://doi.org/10.1016/j.cmpb.2016.08.023

183. Gupta V, Singh RP, Pandey PM, Gupta R (2020) In vitro comparison of conventional surgical and rotary ultrasonic bone drilling techniques. Proc Inst Mech Eng Part H J Eng Med 234:398–411. https://doi.org/10.1177/0954411919898301

184. Alam K, Silberschmidt V V. (2014) Analysis of temperature in conventional and ultrasonically-assisted drilling of cortical bone with infrared thermography. Technol

Heal Care 22:243–252. https://doi.org/10.3233/THC-140813

185. Alam K, Mitrofanov A V, Silberschmidt V V (2011) Experimental investigations of forces and torque in conventional and ultrasonically-assisted drilling of cortical bone. Med Eng Phys 33:234–239. https://doi.org/10.1016/j.medengphy.2010.10.003

186. Boiadjiev T, Boiadjiev G, Delchev K, et al (2021) Feed rate control in robotic bone drilling process. Proc Inst Mech Eng Part H J Eng Med 235:273–280. https://doi.org/10.1177/0954411920975890

187. Singh RP, Pandey PM, Behera C, Mridha AR (2020) Effects of rotary ultrasonic bone drilling on cutting force and temperature in the human bones. Proc Inst Mech Eng Part H J Eng Med 234:829–842. https://doi.org/10.1177/0954411920925254

188. Gupta V, Pandey MP (2016) Experimental investigation and statistical modeling of temperature rise in rotary ultrasonic bone drilling. Med Eng Phys Phys 38:1330–1380. https://doi.org/10.1007/s11668-020-00943-5

189. Singh G, Jain V, Gupta D, Sharma A (2018) Parametric effect of vibrational drilling on osteonecrosis and comparative histopathology study with conventional drilling of cortical bone. Proc Inst Mech Eng Part H J Eng Med 232:975–986. https://doi.org/10.1177/0954411918794983

190. Alam K, Khan M, Silberschmidt V V. (2013) Analysis of forces in conventional and ultrasonically assisted plane cutting of cortical bone. Proc Inst Mech Eng Part H J Eng Med 227:636–642. https://doi.org/10.1177/0954411913485042

191. Baino F, Yamaguchi S (2020) The use of simulated body fluid (SBF) for assessing materials bioactivity in the context of tissue engineering: Review and challenges. Biomimetics 5:1–19. https://doi.org/10.3390/biomimetics5040057

192. Yilmaz B, Pazarceviren AE, Tezcaner A, Evis Z (2020) Historical development of simulated body fluids used in biomedical applications: A review. Microchem J 155:104713. https://doi.org/10.1016/j.microc.2020.104713

193. Cesur S, Küçükgöksel Y, Taşdemir Ş, Ürkmez AŞ (2018) Polycaprolactone-hydroxy apatite composites for tissue engineering applications. J Vinyl Addit Technol 24:248–261. https://doi.org/10.1002/vnl.21569

194. Das A, Shukla M (2017) Hydroxyapatite Coatings on High Nitrogen Stainless Steel by Laser Rapid Manufacturing. Jom 69:2292–2296. https://doi.org/10.1007/s11837-017-2529-x

195. Das A, Shukla M (2020) Multifunctional hydroxyapatite and hopeite coatings on SS254 by laser rapid manufacturing for improved osseointegration and antibacterial character: A comparative study. Proc Inst Mech Eng Part H J Eng Med 234:720–727. https://doi.org/10.1177/0954411920917851

196. Singh M, Gill AS, Deol PK, et al (2022) Drug eluting titanium implants for localised drug delivery. J Mater Res 37:2491–2511. https://doi.org/10.1557/s43578-022-00609-y

197. Morshed MM, Daniels SM, Hashmi MSJ (2011) Finite element method for predicting the cohesive strength of DLC film on 316L stainless steel by four point bend test and validation with experimental results. Adv Mater Res 264–265:1823–1831. https://doi.org/10.4028/www.scientific.net/AMR.264-265.1823

198. Ali SRAS, Hussein AHA, Nofal AAMS, et al (2017) Laser powder cladding of Ti-6Al-4V α/β alloy. Materials (Basel) 10:. https://doi.org/10.3390/ma10101178

199. Haase K, Rouhi G (2013) Prediction of stress shielding around an orthopedic screw: Using stress and strain energy density as mechanical stimuli. Comput Biol Med 43:1748. https://doi.org/10.1016/j.compbiomed.2013.07.032

200. Galbusera F, Volkheimer D, Reitmaier S, et al (2015) Pedicle screw loosening: a clinically relevant complication? Eur Spine J 24:1005–1016. https://doi.org/10.1007/s00586-015-3768-6

201. Gupta V, Pandey PM (2018) An in-vitro study of cutting force and torque during rotary ultrasonic bone drilling. Proc Inst Mech Eng Part B J Eng Manuf 232:1549–1560. https://doi.org/10.1177/0954405416673115

Publications

List of Publications

International journal papers accepted

1. Raj Agarwal, Jaskaran Singh, Vishal Gupta. “Mechanical and biological behaviour of additive manufactured biomimetic biodegradable orthopaedic cortical screws”. *Rapid Prototyping Journal*. (2022). **[SCI: Impact Factor 4.043]**.

2. Raj Agarwal, Jaskaran Singh, Vishal Gupta. “Predicting the compressive strength of additively manufactured PLA-based orthopaedic bone screws: A machine learning framework”. *Polymer Composites*. (2022). **[SCI: Impact Factor 3.531]**.

3. Raj Agarwal, Jaskaran Singh, Vishal Gupta. “An intelligent approach to predict thermal injuries during orthopaedic bone drilling using machine learning”. *Journal of the Brazilian Society of Mechanical Sciences and Engineering*. (2022). **[SCI: Impact Factor 2.361]**.

4. Raj Agarwal, Jaskaran Singh, Vishal Gupta. “Prediction of Temperature Elevation in rotary ultrasonic bone drilling using machine learning models: An in-vitro experimental study”. *Medical Engineering & Physics*. (2022). **[SCI: Impact Factor 2.356]**.

5. Raj Agarwal, Vishal Gupta, Jaskaran Singh. “Additive manufacturing-based design approaches and challenges for orthopaedic bone screws: a state-of-the-art review”. *Journal of the Brazilian Society of Mechanical Sciences and Engineering*. (2022). **[SCI: Impact Factor 2.361]**.

6. Raj Agarwal, Hitesh Kumar Mehtani, Jaskaran Singh, Vishal Gupta. “Post-yielding fracture mechanics of 3D printed polymer-based orthopedic cortical screws”. *Polymer Composites*. (2022). **[SCI: Impact Factor 3.531]**.

National conference paper accepted

1. Raj Agarwal, Vishal Gupta, Jaskaran Singh. “A novel drill bit design for reducing bone-chip morphology in orthopaedic bone drilling”. *Materials Today: Proceedings,* presented on 18.2.2022 in ICAMEN-2022. **[SCOPUS INDEXED]**.

International journal papers under review

1. Raj Agarwal, Jaskaran Singh, Vishal Gupta. “Additively manufactured orthopaedic Ti6Al4V cortical bone screws to improve the biomechanical pullout strength”. *Rapid Prototyping Journal. (2022).* [**SCI: Impact Factor 4.043**].
2. Raj Agarwal, Jaskaran Singh, Vishal Gupta. “Leveraging ultrasonic actuation during inclined orthopaedic bone drilling: An Experimental and Histological study”. *Applied Acoustics*. (2023). **[SCI: Impact Factor 3.614]**.
3. Raj Agarwal, Jaskaran Singh, Vishal Gupta. “A data-driven ensemble machine learning approach for predicting the mechanical strength of 3D printed orthopaedic bone screws”. *Proceedings of the Institution of Mechanical Engineers, Part E: Journal of Process Mechanical Engineering*. (2023). **[SCI: Impact Factor 1.822]**.

International journal papers under preparation

1. Raj Agarwal, Jaskaran Singh, Vishal Gupta. “The application of machine learning in rotary ultrasonic-assisted orthopaedic bone drilling: A Biomechanical in-vitro study”.
2. Raj Agarwal, Jaskaran Singh, Vishal Gupta. “Histopathological evaluations of bone surface after extraction of 3D-printed cortical bone screw”.